



---

# **Experimental Study of Spin Waves in Magnetic Thin Films and Nanostructures**

---

Thesis submitted for the degree of  
**Doctor of Philosophy (Science)**

in

**Physics (Experimental)**

by

**Chandrima Banerjee**



**Department of Physics**

**Jadavpur University**

**2017**

CERTIFICATE FROM THE SUPERVISOR(S)

This is to certify that the thesis entitled "Experimental Study of Spin Waves in Magnetic Thin Films and Nanostructures" submitted by Smt. Chandrima Banerjee who got her name registered on 2<sup>nd</sup> May, 2014 for the award of Ph. D. (Science) degree of Jadavpur University, is absolutely based upon her own work under the supervision of Prof. Anjan Barman and that neither this thesis nor any part of it has been submitted for either any degree / diploma or any other academic award anywhere before.

Anjan Barman 18/7/2017

(Signature of the Supervisor(s) date with official seal)

**DR. ANJAN BARMAN**  
*Professor*  
S. N. Bose National Centre for Basic Sciences  
Block - JD, Sector- III, Salt Lake,  
Kolkata - 700 098, India

*To Maa, Bapi and Roon .....*

## Abstract

In view of increasing demand for computational resources, the electronic circuits are reaching their limits in terms of miniaturization, performance and energy consumption. The spintronic and magnonic devices, instead, potentially offer a replacement of electric charges as information carriers which could satisfy those demands. Besides magnetic data storage, where the presence or orientation of magnetic moment define the data bit, transfer of information is also possible via spin waves (SWs). Especially interesting are patterned magnetic nanostructures, such as magnonic crystals (MCs), metamaterials where magnetic properties are modulated in periodic manners. However, many obstacles need to be overcome before SW devices become technologically relevant.

The main objectives of this doctoral research are to elucidate the spin dynamics in different magnonic systems including layered and patterned structures. We have employed Brillouin light scattering spectroscopy and time-resolved magneto optical Kerr effect measurement for the wave vector resolved and time resolved dynamics respectively. The topic of modification of magnetic properties was explored in three main categories of systems: i) magnetic layered structures: We have measured the magnetization dynamics in  $[\text{Co}/\text{NiFe}]_n$ ,  $[\text{Co}/\text{Pd}]_n/\text{NiFe}$ , and  $[\text{Co}/\text{Pd}]_n$  multilayers by varying the stack number, layer thickness and wave vector orientation respectively. The interlayer interactions at the magnetic/magnetic and magnetic/non-magnetic interfaces significantly affect the effective magnetic anisotropy as well as the spin texture across the system. In addition to that, in the latter two cases, the competition between the in-plane and out-of-plane anisotropies offers exotic tunability of spin wave damping and magnonic band structure. ii) patterned magnetic film: We have investigated the effects of geometrical parameters and the applied magnetic field orientation on the spin wave properties in a two-dimensional array of NiFe square nanorings and an array of corrugated NiFe stripes respectively. By varying the width of each ring, it is possible to significantly tune the nature of spin wave confinement. For the other case, a change in the applied magnetic field direction changes the magnonic band gap and spin wave propagation properties. iii) single ferromagnetic layer with varying adjacent layers: We have further studied the dynamic magnetic properties in Co-Fe-Al-Si Heusler alloy thin film by varying the non-magnetic layers adjacent to it. In case of Heusler alloy film, the magnetic behavior is strongly dependent on the structural and chemical order, which can be

altered by external depositional parameters. Our results demonstrate that by merely changing the adjacent layer coupling with the magnetic film, one can effectively manipulate the magnetic anisotropy and the spin wave damping properties. All the observations are important in terms of their potential applications in future data storage and nanoscale microwave communication systems.

# List of publications

## Included in This Thesis:

1. Brillouin light scattering study of spin waves in NiFe/Co exchange spring bilayer films  
A. Haldar, **C. Banerjee**, P. Laha, and A. Barman  
*J. Appl. Phys.* **115**, 133901 (2014).
2. Width dependent transition of quantized spin-wave modes in Ni<sub>80</sub>Fe<sub>20</sub> square nanorings  
**C. Banerjee**, S. Saha, S. Barman, O. Rousseau, Y. Otani, and A. Barman  
*J. Appl. Phys.* **116**, 163912 (2014).
3. Tunable spin wave properties in [Co/Ni<sub>80</sub>Fe<sub>20</sub>]<sub>r</sub> multilayers with the number of bilayer repetition  
**C. Banerjee**, A. K. Chaurasiya, S. Saha, J. Sinha and A. Barman  
*J. Phys. D: Appl. Phys.* **48**, 395001 (2015).
4. Improvement of chemical ordering and magnetization dynamics of Co–Fe–Al–Si Heusler alloy thin films by changing adjacent layers  
**C. Banerjee**, L. M. Loong, S. Srivastava, S. Pal, X. Qiu, H. Yang and A. Barman  
*RSC Adv.* **6**, 77811 (2016).
5. All-optical study of tunable ultrafast spin dynamics in [Co/Pd]/NiFe systems: the role of spin-twist structure on Gilbert damping  
**C. Banerjee**, S. Pal, M. Ahlberg, T. N. A. Nguyen, J. Akerman and A. Barman  
*RSC Adv.* **6**, 80168 (2016).
6. Development of Pseudo One-Dimensional Magnonic Crystal for High Frequency Nanoscale Devices  
**C. Banerjee**, S. Choudhury, J. Sinha and A. Barman  
(Accepted in *Phys. Rev. Applied*)

7. Magnonic band structure in a Co/Pd stripe domain system investigated by Brillouin light scattering and micromagnetic simulations.

**C. Banerjee**, P. Gruszecki, J. W. Klos, O. Hellwig, M. Krawczyk and A. Barman

(Accepted in Phys. Rev. B)

**Not Included in This Thesis:**

1. Improved magnetic damping in CoFeB|MgO with an N-doped Ta underlayer investigated using the Brillouin light scattering technique

J. Sinha, **C. Banerjee**, A. K. Chaurasiya, M. Hayashi and A. Barman

*RSC Adv.* **5**, 57815 (2015).

2. Direct Observation of Interfacial Dzyaloshinskii-Moriya Interaction from Asymmetric Spin-wave Propagation in W/CoFeB/SiO<sub>2</sub> Heterostructures Down to Subnanometer CoFeB Thickness

A. K. Chaurasiya, **C. Banerjee**, S. Pan, S. Sahoo, S. Choudhury, J. Sinha and A. Barman

*Sci. Rep* **6**, 32592 (2016).

3. Perpendicular Standing Spin Wave and Magnetic Anisotropic Study on Amorphous FeTaC Films

A. Samantaray, A. K. Singh, **C. Banerjee**, A. Barman, A. Perumal, and P. Mandal

*IEEE Trans. Magn.* **52**, 2003104 (2016).

## Acknowledgements

The journey of my PhD started in 2012 and now it ends after five years. In this respect, it is a pleasure for me to express my gratitude to all the people who were a part of my PhD life including the CMPMS department of S N Bose Centre, our collaborators and our funding agencies.

I will start with expressing my deepest gratitude and respect to my supervisor, Prof. Anjan Barman, for his tolerance, insight, patience and for his constant help throughout my PhD work. He is a perfect combo of positivity, professionalism and intelligence who can tackle a big group of twelve people, giving attention to every individual's work. I remember when I joined his group, there was a junkyard in place of the present BLS lab. I evidenced what a tremendous effort he gave to set up the lab and to get things going. When I by fault misaligned the optics of tandem Fabry Perot interferometer box, I thought I will be expelled. But it was only his trust and motivation, which kept me positive to finally get back the alignment after three months of incessant effort! Overall, apart from doing research, he taught me to grow a proper research attitude, which will be a big lesson for my future life.

I am grateful to Dr. Arabinda Haldar, my junior mentor. In the initial phase of my PhD life, he helped me a lot to build up professional skills which were very useful for my experimental and analysis work. Also thanks to Dr. Jaivardhan Sinha and Dr. Saswati Barman for their help and discussions.

I convey my heartiest gratitude to my family, for their unconditional love, support and trust. My parents are my strength and inspiration. My younger sister is my best friend, philosopher and playmate. She is quite matured from childhood and I have learnt many important life lessons from her. I also thank my fiancé Rajan for his constant support and motivation.

I thank Prof. Yoshichika Otani, Prof. Maciej Krawczyk, Prof. Olav Hellwig, Prof. HyunSoo Yang and Prof. Johan Åkerman for providing us with various samples and helping me with the analysis of results. I thank my seniors of lab, Bivasda, Dheerajda, Susmitadi, Rumadi, Debanjanda, Arnabda and specially Semantidi for their affection, help and discussion. My dear juniors, Samiran, Sucheta, Anulekha, Sourav, Kartik, Avinash, Santanu, Sudip, Panda have never

let my PhD life get boring. There are many fun moments with my labmates which I will cherish for life. I should also acknowledge my very close childhood friends Sumana and Shilpa, for growing up together and making life tolerable.

Finally, I thank the S. N. Bose National Centre for Basic Sciences for giving me an opportunity to work. Thanks to Council of Scientific and Industrial Research for providing me with junior and senior research fellowships. Thanks to various funding agencies including Department of Science and Technology, Government of India for the funding towards development of experimental set ups I used during my Ph.D. study.

Chandrima Banerjee

S. N. Bose National Centre for Basic Sciences,  
Salt Lake, Kolkata, India.

## List of Abbreviations

|        |   |
|--------|---|
| AFM    | : Atomic force microscopy               |
| ASW    | : Asymmetric sawtooth-shaped waveguide  |
| AR     | : Anti reflection                       |
| BLS    | : Brillouin light scattering            |
| CPW    | : Coplanar waveguide                    |
| DC     | : Direct current                        |
| DE     | : Damon–Eshbach                         |
| DMI    | : Dzyaloshinskii Moriya interaction     |
| DW     | : Domain wall                           |
| EBL    | : Electron beam lithography             |
| EDX    | : Energy dispersive x-ray spectroscopy  |
| ES     | : Exchange spring                       |
| FDM    | : Finite difference method              |
| FEM    | : Finite element method                 |
| FM     | : Ferromagnet                           |
| FMR    | : Ferromagnetic resonance               |
| fs     | : Femtosecond                           |
| FSR    | : Free spectral range                   |
| GMR    | : Giant magnetoresistance               |
| HA     | : Heusler alloy                         |
| HAMR   | : Heat assisted magnetic recording      |
| IP     | : In plane                              |
| (I)SHE | : (Inverse) spin Hall effect            |
| LLG    | : Landau-Lifshitz-Gilbert               |
| MC     | : Magnonic crystal                      |
| MO     | : Microscope objective                  |
| MOKE   | : Magneto-optical Kerr effect           |
| MRAM   | : Magnetoresistive random access memory |

|         |   |
|---------|---|
| MS      | :Micromagnetic simulation                   |
| MSBVW   | : Magnetostatic backward volume wave        |
| MSSW    | : Magnetostatic surface wave                |
| NA      | : Numerical aperture                        |
| OBD     | : Optical bridge detector                   |
| OOP     | : Out of plane                              |
| PBS     | : Polarizing beam splitter                  |
| PhC     | : Photonic crystal                          |
| ps      | : Picosecond                                |
| PSSW    | : Perpendicular standing spin waves         |
| PVD     | : Plasma vapor deposition                   |
| PWM     | : Plane wave method                         |
| RF      | : Radio frequency                           |
| RMS     | : Root mean square                          |
| RR      | : Retro reflector                           |
| RT      | : Room temperature                          |
| SEM     | : Scanning electron microscopy              |
| SSE     | : Spin Seebeck effect                       |
| STO     | : Spin-torque oscillator                    |
| STT     | : Spin transfer torque                      |
| SW      | : Spin wave                                 |
| TEM     | : Transmission electron microscopy          |
| TFPI    | : Tandem Fabry-Pérot interferometer         |
| TMR     | : Tunnel magnetoresistance                  |
| TR-MOKE | : Time-resolved magneto-optical Kerr effect |
| VSM     | : Vibrating sample magnetometry             |
| XRD     | : X-ray diffraction                         |
| YIG     | : Yittrium iron garnet                      |

# List of Figures

| <b>Figure number and caption</b>   | <b>Page no.</b> |
|--|-----------------|
| Figure 2.1: The precessional motion of the magnetization around the effective magnetic field.  | 26              |
| Figure 2.2: Semiclassical representation of spin wave in a ferromagnet: (a) the ground state (b) a spin wave of precessing magnetic moments and (c) the spin wave (viewed from above) showing a complete wavelength.                                   | 28              |
| Figure 2.3: Schematics of (a) perpendicular standing spin wave mode (PSSW) and magnetostatic surface spin wave mode (MSSW) are shown for a ferromagnetic thin film. (b) The dispersion relations for three different types of magnetostatic SWs modes. | 30              |
| Figure 2.4: (a) Geometry of the Kerr rotation ( $\theta_k$ ) and Kerr ellipticity ( $\varepsilon_k$ ). (b) Schematics of polar, longitudinal and transverse MOKE geometries are shown.   | 33              |
| Figure 3.1: Schematic of the sputtering technique.   | 38              |
| Figure 3.2: Schematic diagram of electron beam lithography process.  | 39              |
| Figure 3.3: Schematic diagram of electron beam evaporation technique.  | 40              |
| Figure 3.4: Schematic diagram of Scanning Electron Microscope.   | 41              |
| Figure 3.5: (a) Schematic of EDX spectrometer. (b) Interaction of accelerated electrons with sample and emission of X-rays.  | 43              |
| Figure 3.6: Schematic diagram of X-ray diffraction (left panel) and X-ray diffractometer (right panel).  | 44              |
| Figure 3.7: Schematic diagram of Vibrating Sample Magnetometer (VSM).  | 46              |
| Figure 3.8: Schematic diagram of Atomic Force Microscope.  | 47              |
| Figure 3.9: Schematic diagram of static magneto-optical Kerr effect (Static MOKE) microscope in longitudinal geometry.   | 49              |
| Figure 3.10: The scattering geometry showing the incident, reflected and scattered beams, the direction of magnon wave vectors for Stokes and anti Stokes process in BLS. The measurement geometry shown is DE geometry.                               | 52              |

- Figure 3.11: Schematic of the (a) Stokes and (b) anti Stokes Scattering processes occurring in BLS. 53
- Figure 3.12: Scattering of laser beam by (a) bulk magnon and (b) surface magnon. The direction of  $q$  corresponds to the anti Stokes process. 54
- Figure 3.13: Schematic of the interaction between p-polarized incident beam and the precessing magnetization. 55
- Figure 3.14: The set up and optical pathway for conventional BLS set up. The notation for the components is given in the text. 57
- Figure 3.15: A Schematic view of the pinhole and light modulator system. 59
- Figure 3.16: The part of the BLS spectrum that corresponds to when SH1 is open (a) and SH2 is open (b). A superposition of the spectra in (a) and (b) is what is obtained when SH1 and SH2 operates in synchronization. 60
- Figure 3.17: Schematic of the optical arrangement of TFPI. 61
- Figure 3.18: Periodic transmission spectrum depicting the FSR. 62
- Figure 3.19: Transmission Spectra of FP1 and FP2 and in tandem operation. 64
- Figure 3.20: Optical arrangement inside TFPI box in (a) tandem and (b) alignment mode. Figure is taken from reference [19]. 66
- Figure 3.21: GHOST software interface for single scan measurement of BLS signal showing the data for plexi glass. The reference beam suppressing the elastic peak is shown in purple color. The Stokes and anti Stokes peaks along with two ghost peaks (higher orders of the central peak) are also indicated. 69
- Figure 3.22: BLS spectra for  $\text{Ni}_{80}\text{Fe}_{20}$  thin film at (a) different in-plane bias magnetic field and (b) wave vector. 70
- Figure 3.23: BLS spectrum of bare laser beam. 70
- Figure 3.24: Schematics of the optical set up of micro-BLS required for the transformation from conventional BLS. 71
- Figure 3.25: Schematic diagram of the time-resolved magneto-optical Kerr effect (TR-MOKE) microscope. 76
- Figure 3.26: (a) Typical time-resolved Kerr rotation data taken from a  $\text{Ni}_{80}\text{Fe}_{20}$  (7 nm)/[Co

- (0.5 nm)/Pd (1 nm)]<sub>5</sub> multilayered sample with an out of plane bias field of 2.5 kOe. (b) precessional oscillation part of the time-resolved data and (c) fast Fourier transform of Fig. 3.26b. 77
- Figure 4.1: A rectangular MC formed by circular ferromagnetic elements A embedded in matrix B. 86
- Figure 5.1: AFM images of (a) Py (10nm)/Co (10nm), (b) Py (20 nm)/Co (10nm) bilayer films. 95
- Figure 5.2: Magnetic hysteresis loops for all the Co (10nm)/ Py (10–30nm) bilayer films measured with static MOKE experiment. 96
- Figure 5.3: BLS spectra for Co (10nm)/ Py (25nm) film at different in-plane bias magnetic fields. Angle of incidence is  $\theta = 45^\circ$ . The measurement geometry is shown in the inset. 97
- Figure 5.4: Spin wave frequencies of mode 1 and mode 2 as a function of magnetic field for Co (10 nm)/ Py (25 nm) film (symbols) along with the fits (line). Dispersions ( $f(q)$ ) of the two modes have been shown in one of the insets. The symbols correspond to the experimental data while the lines joining the symbols are only guide to the eyes. Other inset shows the field hysteresis of mode 2 in low field regime. 98
- Figure 5.5: Thickness dependence of  $\Delta f \times f$  for Co (10 nm)/ Py ( $t$ ) films (symbols). A fit to Eq. (5.3) has also been shown (line). Inset shows the Lorentzian fit to experimental BLS spectrum obtained for Co (10 nm)/ Py (25 nm) film at  $H = 2800$  Oe. 100
- Figure 6.1: AFM images of [Co (10 nm)/Py (10 nm)] <sub>$r$</sub>  multilayers for a)  $r=1$  and b)  $r=4$ . 107
- Figure 6.2: Magnetic hysteresis loops of [Co (10 nm)/Py (10 nm)] <sub>$r$</sub>  multilayers, measured for the magnetic field applied parallel to the film plane. Different cycles refer to samples with different numbers of repetition ( $r$ ). 108
- Figure 6.3: BLS spectra for [Co (10 nm)/Py (10 nm)] <sub>$r$</sub>  multilayers with  $r = 1-4$  taken for (a)  $q = 1.1 \times 10^7$  rad/m and (b)  $q = 0$ . The measurement geometry is shown at the inset of (a) where the parameters are the same as described in the text. The arrows indicate the spin wave peak frequencies. 109
- Figure 6.4: Measured spin wave frequencies (symbols) as a function of in-plane wave vector for the [Co (10 nm)/Py (10 nm)] <sub>$r$</sub>  multilayers with (a)  $r = 1$ , (b)  $r = 2$ , (c)  $r = 3$  and (d)  $r = 4$ , respectively. The solid lines are calculated frequencies. 110
- Figure 6.5: Dependence of effective magnetization on the number of repeats ( $r$ ). The line is a guide to the eyes. 114

Figure 7.1: (a) In plane AFM images and (b) magnetic hysteresis loops (in-plane and out of plane) for the exchange spring systems with  $t = 5.5$  nm, 7 nm, 20 nm. (c) Typical EDX spectrum of the exchange spring systems.

123

Figure 7.2: (a) Schematic of the two-color pump-probe measurement of the time-resolved magnetization dynamics of exchange-spring systems. The bias field is applied with a small angle to the normal of the sample plane. (b) Typical time-resolved Kerr rotation data revealing ultrafast demagnetization, fast and slow relaxations, and precession of magnetization for the exchange-spring system with  $t = 7.5$  nm at  $H = 2.5$  kOe. (c) FFT spectrum of the background-subtracted time-resolved Kerr rotation. (d) Variation of demagnetization time with  $t$ .

124

Figure 7.3: (a) Background-subtracted time-resolved Kerr rotation and the corresponding FFT spectra for samples with different  $t$  values at  $H = 2.5$  kOe. The black lines show the fit according to Eqn. 7.1. (b) Simulated static magnetic configurations for samples with  $t = 20$ , 10, and 6 nm with a bias field  $H = 2.5$  kOe in the experimental configuration. The simulated samples are not to scale. The color map is shown at the bottom of the figure.

126

Figure 7.4: (a) Dependence of spin wave frequency on NiFe layer thickness ( $t$ ) at a magnetic field of 2.5 kOe. The inset shows the frequency dependence on  $t$  when the magnetic field (of 2.5 kOe) is applied in-plane, as obtained from BLS measurements. (b) Evolution of Gilbert damping constant as a function of  $t$  at  $H = 1.3$  kOe (green circles) and 2.5 kOe (violet circles).

127

Figure 7.5: Dependence of Gilbert damping coefficient on soft layer thickness ( $t$ ) for (a) 7–10 nm and (b) 5–7 nm, respectively.

130

Figure 8.1: (a) MFM image in the demagnetized state showing the parallel (left panel) and labyrinth (right panel) stripe domains of the Co/Pd multilayered system, obtained after IP and OOP AC demagnetization, respectively. (b) Magnetic hysteresis loops of the multilayers with IP and OOP applied magnetic fields. (c) The domain configuration (cross-sectional view) obtained from micromagnetic simulations. Arrows correspond to the magnetization vector and colors spanning between blue and red correspond to the OOP component of the magnetization. The bottom panel schematically visualizes static magnetization with clockwise and anticlockwise domain walls. The  $x$  and  $z$  axes are assumed to be parallel to domain walls and multilayered system thickness, respectively.

140

Figure 8.2: (a)-(c) The measurement geometries for the saturated state,  $\varphi = 90^\circ$  in (a) and (b), and  $\varphi = 0^\circ$  in (c). (d)-(f) Corresponding typical BLS spectra at  $q = 1.2 \times 10^7$  rad/m and (g)-(i) dispersion curves. Measured in BLS dispersions and modes are labeled with M and marked with the color points in (g)-(i). Simulation results are shown by the gray scale map, the orange stars labeled with S represent modes visualized in Fig. 8.3.

142

Figure 8.3: The amplitude and phase maps of  $m_z$  for different SW modes (as marked with

orange stars in Fig. 8.2) calculated at  $q=2 \times 10^7$  rad/m for the saturated state (a), and domain structure with  $\varphi=90^\circ$  (b) and  $\varphi=0^\circ$  (c). The corresponding color scale is shown at the top of the figure. Dark solid lines in (b) and (c) correspond to the OOP component of the static magnetization at the top surface of the structure.

145

Figure 8.4: Dispersion relation obtained from MSs for the DE configuration in the stripe domain structure without external magnetic field (a), (b) and with external magnetic field of 0.01 T and 0.005 T along the  $x$ -axis (parallel to the domains) and  $z$ -axis (perpendicular to the film plane) in (c) and (d), respectively. In (b) the aggregated dynamics from all three magnetization components is used in the calculation of the dispersion relation, whereas in all other figures only OOP magnetization component was used. In order to visualize as much as possible SWs resonances, the power of the presented signals is shown in logarithmic scale.

146

Figure 8.5: (a) Dispersion relation obtained from MSs for the SW propagating along domains (along the  $x$ -axis). (b) The amplitude and phase of SWs from the first band at the wave number close to zero  $q \approx 0$ , marked by blue circle in (a).

147

Figure 8.6: (a) MFM image of the labyrinth stripe domain sample. (b) The BLS spectra taken at different values of the in-plane transferred wave vector  $q$  (denoted in units of  $10^7$  rad/m) for labyrinth stripe domain sample. The mode numbers are assigned in accordance with the aligned stripe domain sample.

148

Figure 9.1: (a) Typical time-resolved Kerr rotation data revealing ultrafast demagnetization, fast and slow relaxations, and precession of magnetization for Py square ring array with ring width  $w=300$  nm at  $H=550$  Oe. (b) Background subtracted time-resolved Kerr rotation. (c) Scanning electron micrographs of the ring arrays of different ring width. (d) Experimental and (e) simulated FFT spectra.

158

Figure 9.2: (a) Static magnetic configuration of a single ring with  $w=300$  nm at  $H=550$  Oe. The component of magnetization perpendicular to the bias magnetic field is represented by a blue-white-red colormap. (b) MFM image of this nanoring array in presence of  $H=550$  Oe. (c) Simulated MFM image. (d) Simulated power and phase maps of the observed resonant modes. The color maps for the power and phase distributions are shown at the bottom of (d).

159

Figure 9.3: (a) The simulated static magnetic configuration (left panel) and simulated MFM image (right panel) of a single nanoring with  $w=200$  nm at  $H=550$  Oe. (b) Experimental MFM image. (c) Power and phase maps for mode 2. (d) Simulated power maps corresponding to the resonant peaks from mode 3 to mode 12. The colormap for power and phase distributions are shown at the bottom of (d).

161

Figure 9.4: (a) Static magnetic configuration of the ring with  $w=100$  nm at  $H=550$  Oe. The circles denote the pole regions. (b) Experimental and (c) simulated MFM image of the ring array, respectively. (d) Simulated power maps corresponding to the resonant peaks in the FFT spectra. The simulated phase profile of mode 10 is also shown in lower panel. The

colormap for power and phase distributions are shown at the bottom of (d). 162

Figure 9.5: (a) Contour maps of the simulated magnetostatic stray field distribution and (b) line scans of simulated magnetostatic fields from various ring arrays as obtained from the positions indicated by horizontal dashed lines in (a). 164

Figure 10.1: (a) Scanning electron microscope (SEM) image of the studied ASW array. The co-ordinate axes are shown by the white arrows. The unit cell considered for PWM calculations is marked by dashed box. (b) Schematic of the BLS measurement geometry used, showing the incident and scattered light beams and the in-plane angle  $\varphi$  between the magnon wave vector  $q$  and applied magnetic field  $H$ , with both vectors lying in the sample plane. (c) Simulated static magnetic configurations (shown in red-white-blue colour map) for  $\varphi = 90^\circ$  and  $\varphi = 70^\circ$  configurations (left and right panel, respectively) for  $H = 850$  Oe. The magnetic field direction is shown by blue arrows. 171

Figure 10.2: (a) The Stokes side of BLS spectra taken at different values of the in-plane transferred wave vector  $q$  (denoted in units of  $10^7$  rad/m) for  $\varphi = 90^\circ$  geometry. The spectra are horizontally flipped for convenience. The SW peaks are indicated by the arrows. (b) Relative values of BLS intensities as calculated by PWM for different values of  $q$  given in (a). (c) Magnonic band structure in  $\varphi = 90^\circ$  geometry. Thin blue lines are PWM results. Bold green lines emphasize intense excitations as predicted by PWM. Red solid circles represent peaks in the BLS spectra. The dashed vertical line is the boundary of first BZ. The bandgap is shown by shaded region. 175

Figure 10.3: Spatial profiles of the selected modes for (a)  $q = 0$  and (b)  $q = \pi/a$  and (b)  $q = 2\pi/a$  for the geometry with  $\varphi = 90^\circ$ . 176

Figure 10.4: (a) The Stokes side of BLS spectra taken at different values of the in-plane transferred wave vector  $q$  (denoted in units of  $10^7$  rad/m) for  $\varphi = 70^\circ$  geometry. The spectra are horizontally flipped for convenience. The SW peaks are indicated by the arrows. (b) Relative values of BLS intensities as calculated by PWM for different values of  $q$  given in (a). (c) Magnonic band structure in  $\varphi = 70^\circ$  geometry. Thin blue lines are PWM results. Bold green lines emphasize intense excitations as predicted by PWM. Red solid circles represent peaks in the BLS spectra. The dashed vertical line is the boundary of first BZ. The bandgap is shown by shaded region. 178

Figure 10.5: Spatial profiles of the selected modes for (a)  $q = 0$  and (b)  $q = \pi/a$  and (b)  $q = 2\pi/a$  for the geometry with  $\varphi = 70^\circ$ . 179

Figure 10.6: Amplitude profiles of different spin wave modes excited locally at the shaded region for (a)  $\varphi = 90^\circ$  and (b)  $\varphi = 70^\circ$  geometry. 181

Figure 10.7: BLS spectra measured at two different values of the in-plane transferred wave vector  $q$  (denoted in units of  $10^7$  rad/m) for (a)  $\varphi = 90^\circ$  and (b)  $\varphi = 70^\circ$  geometry. The spectra

in red and black stand for two counter propagating directions of wave vector. 182

Figure 11.1: (a) Three-dimensional and (b) in-plane view of AFM images for S1, S2 and S3. (c) Cross-sectional TEM images for all three samples. The lower panels show high resolution images of the diffraction fringes of CFAS films. 191

Figure 11.2: (a) XRD patterns for all three samples. The arrows indicate the CFAS peaks, while peaks corresponding to other materials are indicated by symbols. (b) Lorentzian fit to the characteristic CFAS peaks of S1, S2 and S3 which is used in the text to find out the crystallite size of the CFAS thin films. 192

Figure 11.3: (a) Magnetic hysteresis loops of S1 (upper panel) and S3 (lower panel), measured for magnetic field applied parallel to the film surface, at various angles with respect to the edges of the MgO substrate ([100] and [010]). The results for S3 are also representative of S2. (b) Typical BLS spectra of all samples taken for  $q = 0$  at  $H = 2$  kOe. The arrows indicate the peak frequencies of PSSW modes. The measurement geometry is shown in the inset. 193

Figure 11.4: (a) Evolution of the frequencies (symbols) of the Kittel mode (F1) and PSSW mode (F2) with respect to the bias magnetic field. (b) Dependence of F1 on the azimuthal angle of the applied bias magnetic field. The solid lines correspond to fits to Eqn. 11.2 and 11.3 for F1 and F2, respectively. 196

Figure 11.5: Measured spin wave frequencies (symbols) as a function of in-plane wave vector at a magnetic field of 2 kOe. The solid lines are calculated frequencies. 198

Figure 11.6: Linewidth of the  $q = 0$  mode as a function of the mode frequency for different samples. Inset shows typical anti-Stokes peaks for all three samples, taken for  $q = 0$  at  $H = 1500$  Oe. 199

# Contents

|   |      |
|---|------|
| Abstract.....   | iv   |
| List of Publications.....                                   | vi   |
| Acknowledgements.....                                       | viii |
| List of abbreviations.....                                  | x    |
| List of Figures.....  | xii  |
| 1. Introduction.....  | 1    |
| References.....   | 9    |
| 2. Theoretical Background.....                              | 20   |
| 2.1. Introduction.....                                      | 20   |
| 2.2. Magnetic Energies and Fields.....                      | 21   |
| 2.2.1. Zeeman Energy.....                                   | 21   |
| 2.2.2. Exchange Energy.....                                 | 21   |
| 2.2.3. Magnetic dipolar interaction.....                    | 22   |
| 2.2.4. Magnetic Anisotropy.....                             | 23   |
| 2.3. Magnetization Dynamics and Spin Waves.....             | 25   |
| 2.3.1. Exchange Spin Waves.....                             | 30   |
| 2.3.2. Confined Spin Wave Modes in Magnetic Structures..... | 31   |
| 2.4. Magneto-Optical Kerr Effect (MOKE).....                | 32   |
| 2.4.1. Origin of Magneto-Optical Kerr Effect.....           | 33   |
| 2.4.2. MOKE Geometries.....                                 | 34   |
| References.....   | 35   |

|  |    |
|--|----|
| 3. Experimental Techniques.....  | 37 |
| 3.1. Introduction.....   | 37 |
| 3.2. Fabrication Techniques.....   | 38 |
| 3.2.1. Sputtering.....   | 38 |
| 3.2.2. Electron Beam Lithography (EBL) and Electron Beam Deposition.....   | 39 |
| 3.3. Characterization Techniques.....  | 41 |
| 3.3.1. Scanning Electron Microscopy (SEM).....   | 41 |
| 3.3.2. Transmission Electron Microscopy (TEM).....   | 42 |
| 3.3.3. Energy-dispersive X-ray spectroscopy (EDX).....   | 43 |
| 3.3.4. X-ray diffraction (XRD) Analysis.....   | 44 |
| 3.3.5. Vibrating Sample Magnetometer (VSM).....  | 45 |
| 3.3.6. Atomic Force Microscopy (AFM) and Magnetic Force Microscopy (MFM).....  | 46 |
| 3.3.7. Static Magneto-Optical Kerr Effect (Static-MOKE) Magnetometer.....  | 48 |
| 3.4. Measurement Techniques.....   | 50 |
| 3.4.1. Brillouin Light Scattering.....   | 50 |
| 3.4.1.1. Principles.....   | 51 |
| 3.4.1.2 Uncertainty in the Selected SW Wave Vector.....  | 54 |
| 3.4.1.3. Polarization of Scattered Beam.....   | 55 |
| 3.4.1.4. Experimental Setup.....   | 56 |
| 3.4.1.5. Instrumentation.....  | 58 |
| 3.4.1.6. Optimization of the BLS set up Using Plexi Glass, Ni <sub>80</sub> Fe <sub>20</sub> Thin Film and<br>Bare Laser Beam..... | 68 |
| 3.4.1.7. BLS Microscopy.....   | 71 |

|   |     |
|---|-----|
| 3.4.2. Time-resolved Magneto-optical Kerr Effect (TR-MOKE) Microscope.....  | 73  |
| 3.4.2.1. Different Time Scales of Magnetization Dynamics.....   | 74  |
| 3.4.2.2. Primary Components of the Setup.....   | 74  |
| 3.4.2.3. Experimental Setup.....  | 76  |
| 3.4.2.4. Some Routine Alignments.....   | 78  |
| References.....   | 79  |
| 4. Numerical Methods.....   | 82  |
| 4.1. Introduction.....  | 82  |
| 4.2. Micromagnetic Simulations.....   | 83  |
| 4.2.1. Calculation of Power and Phase Profiles of the Resonating Modes.....   | 85  |
| 4.3. Plane Wave Method (PWM).....   | 86  |
| References.....   | 92  |
| 5. Investigation of spin waves in Co/ NiFe exchange spring bilayer films using Brillouin light scattering.....                                  | 93  |
| 5.1. Introduction.....  | 93  |
| 5.2. Experimental Details.....  | 94  |
| 5.3. Results and Discussions.....   | 95  |
| 5.4. Conclusions.....   | 101 |
| References.....   | 102 |
| 6. Brillouin light scattering study of $[\text{Co}/\text{Ni}_{180}\text{Fe}_{20}]_r$ multilayers with varying number of bilayer repetition..... | 105 |
| 6.1. Introduction.....  | 105 |
| 6.2. Experimental Details.....  | 106 |

|   |     |
|---|-----|
| 6.3. Results and Discussions.....   | 107 |
| 6.4. Conclusions.....   | 115 |
| References.....   | 116 |
| 7. All-optical study of ultrafast spin dynamics in [Co/Pd]/NiFe exchange spring systems with tunable tilted anisotropy..... | 119 |
| 7.1. Introduction.....  | 119 |
| 7.2. Experimental Details.....  | 121 |
| 7.2.1. Sample Fabrication.....  | 121 |
| 7.2.2. Measurement Technique.....   | 121 |
| 7.3. Results and Discussions.....   | 123 |
| 7.4. Conclusions.....   | 130 |
| References.....   | 131 |
| 8. Investigation of Magnonic Band Structure in Co/Pd Stripe Domain System.....  | 134 |
| 8.1. Introduction.....  | 134 |
| 8.2. Experimental Details.....  | 136 |
| 8.3. Micromagnetic Simulations.....   | 138 |
| 8.3.1. Discretization.....  | 138 |
| 8.3.2. Stripe Domain Pattern Relaxation.....  | 138 |
| 8.3.3. Dispersion Relation and Resonant Mode Profiles Calculation.....  | 139 |
| 8.4. Results and Discussions.....   | 139 |
| 8.5. Conclusions.....   | 149 |
| References.....   | 149 |
| 9. Width dependent transition of quantized spin wave modes in Ni <sub>80</sub> Fe <sub>20</sub> square                      |     |

|  |     |
|--|-----|
| nanorings.....   | 155 |
| 9.1. Introduction.....   | 155 |
| 9.2. Experimental Details.....   | 156 |
| 9.3. Results and Discussions.....  | 157 |
| 9.4. Conclusions.....  | 164 |
| References.....  | 165 |
| 10. Reconfigurable spin wave propagation in pseudo one-dimensional nanoscale<br>magnonic crystal.....                      | 168 |
| 10.1. Introduction.....  | 168 |
| 10.2. Experimental Details and Definition of Measurement Geometries.....   | 170 |
| 10.3. Theoretical Approach.....  | 172 |
| 10.4. Results and Discussions.....   | 174 |
| 10.5. Conclusions.....   | 183 |
| References.....  | 183 |
| 11. Effects of adjacent layers on the structure and magnetization dynamics of Co-Fe-Al-Si<br>Heusler alloy thin films..... | 187 |
| 11.1. Introduction.....  | 187 |
| 11.2. Experimental Details.....  | 189 |
| 11.3. Results and Discussions.....   | 191 |
| 11.4. Conclusions.....   | 200 |
| References.....  | 201 |
| 12. Summary and outlook.....   | 204 |
| 12.1. Summary.....   | 204 |

12.2. Future Perspectives..... 207

# Chapter 1

## 1. Introduction

---

In 1947, the invention of transistor [1] ignited a series of radical and phenomenological change in the world of communication and technology. The ability of on-chip digitization has fueled the information-age, whose fundamental sources of economical wealth are knowledge and communication rather than natural resources and physical labor. In present days, if we look around, people are seen communicating with others by cell phone, working on laptops, or performing their household duties using world-wide-web. There are several other applications in devices as diverse as video cameras, jumbo jets, modern automobiles, manufacturing equipments etc. Overall, the explosive growth and development of high performance electronic devices and integrated circuits have transformed the foundation of the world economy and have increasing impact on all areas from everyday life to the most advanced science, technology and business.

The evolution of semiconductor based technology has always been boosted by the ever increasing data processing capability, together with astonishingly high integration density and faster speed. Combined with advances in optical communication, these advantages have enabled easy and affordable storage, processing, and transmission of massive amount of information. Nevertheless, according to the International Technology Roadmap for Semiconductors, the semiconductor based technology will face serious obstacles hindering downscaling and power reduction in the near future, since both the miniaturization of single-element size and the operational speed will reach their ultimate limits within next few years [2]. Another fundamental drawback, inherent in electronics, is the generation of waste heat during switching (since it is associated with a translational motion of electrons), which is responsible for an increase in the power consumption of electronic devices. Consequently, the challenge not only becomes to develop new particle-less technologies to accommodate increasing information, but also how to organize information in the new media. A possible way out is to bend towards all-optical integrated circuits, which employ photons, the quanta of electromagnetic waves as the information carrier and has opened a new dimension in the field of nanophotonics research: photonic crystal [3-5]. Photonic crystals (PhCs) are a class of artificial optical materials with periodically modulated refractive indices. In a semiconductor, the periodic lattice of atoms causes electrons to have energy bands and energy gaps; in a PhC, the periodic dielectric lattice causes photons to have frequency

bands and frequency gaps, the latter often being called photonic bandgap. If the frequency of light (or photon) falls in the gap, the PhC will reflect the light totally irrespective of its angle of incidence. The properties of the band gaps can reliably be controlled and manipulated by changing physical parameters of the structure such as dielectric constant of the used materials or lattice parameters of the structure. In other words, PhC structures suggest high spectral selectivity that has led to various applications of the photonic crystal to optical nanodevices such as photonic waveguides [6-10] and integrated circuits [11-13].

In the meantime, the areas of nanomagnetism and magnetization dynamics, a popular sub-area of spintronics [14], have become a subject of growing interest, owing to its promising applications in nanoscale signal processing and information transfer devices [15-17] such as filters [18], delay lines [19] and storage elements [20-21]. This field encompasses the transmission, storage and processing of information based on the magnetization state of a system (The term Spintronics originally was an acronym for SPIN TRansport electrONICS). Historically, the concept of associating the spin degree of freedom with electric signals (i.e. electronic charge) came with the experimental observation of giant magnetoresistance (GMR) effect in Fe/Cr multilayered system by Fert and Grunberg [22-23], for which they were awarded Noble prize in 2007. The phenomenon is based on the fact that for a spin-polarized current, i.e. a current which is not carried by an equal amount of up- and down-spins, flowing from one ferromagnetic layer into another, the resistance depends on the relative orientation of the two ferromagnetic layers. This was a major breakthrough in the technological industry and led to the possibility of novel non-volatile magnetic memories, like Magnetoresistive Random Access Memory (MRAM) [15] and magnetic hard disk drives, in which each bit can be separately manipulated by means of current controlled write or read. Later on, the discoveries like Spin Transfer Torque (STT) [24-25], which allows for current assisted magnetization switching, (Inverse) Spin Hall Effect ((I)SHE) [26-27], which provides new ways to create and detect spin currents, Spin Pumping Effect [28], Spin Seebeck Effect (SSE) [29] and the Dzyaloshinskii Moriya Interaction (DMI) [30-32], have added interesting perspectives to the field of spintronics.

Besides using electrical current, the transfer of magnetic moment or spin can also occur with the help of spin waves [33-34] or magnons (the quanta of spin waves with spin 1 obeying Bose – Einstein statistics) in magnetic materials--giving rise to the nascent scientific field, so-called magnonics. From a classical point of view, the Spin wave (SW) represents a phase-coherent

precession of microscopic vectors of magnetization of the magnetic medium. The concept of spin wave was first introduced by F. Bloch in 1930 [35] and presently is considered as potential data carriers for computing devices, providing the elemental base for Joule-heat-free transfer of spin information over macroscopic distances. In that sense, the SW is equivalent to the electromagnetic waves in photonics, however having wavelengths that are a few orders of magnitude shorter than that of electromagnetic waves at the same frequency. Magnonics thus inherently fosters the miniaturization of microwave devices towards nanoscale. Ultimate control and functionality of SW based logic is expected from the so-called magnonic crystal (MC) (the magnetic counter part of photonic crystal) [36-40], which is formed by periodic magnetic nanostructures, resulting in allowed and partially or fully forbidden SW modes which can be manipulated via a wide range of parameters, including the choice of magnetic material, the size and shape of the sample and the orientation and magnitude of applied bias magnetic field. A striking example is given by the recently discovered magnetic lattices created by skyrmions [41-42] and artificial spin ice [43-44], which stimulated abundant new physics and many new applications. Further advantages of magnonic devices lie in the fact that, perhaps more than any other kind of wave (for example electromagnetic or acoustic), spin waves display a diversity of dispersion characteristics. For example, the dispersion of dipole-dominated spin waves in thin ferromagnetic films strongly depends on their propagation direction with respect to an in-plane magnetic field, giving rise to Damon-Eshbach modes for wave vector perpendicular to magnetic field, backward-volume modes for wave vector parallel to magnetic field, or a combination of both. Overall, the concept of magnonics provides an unprecedented controllability in terms of ultrafast information transmission and processing and therefore a thorough understanding of the fundamental SW properties (such as the frequency, amplitude, phase, velocity, non-reciprocity etc.) is necessary to mould the SWs for the next generation multifunctional frequency-agile computing devices.

In the following paragraphs, a brief overview of a few aspects of the research field of magnon-spintronics will be presented, which has motivated the present thesis work. Finally, an outline of the content of this thesis will be given.

### **Thin Films for Magnetic Storage Media**

Since the discovery of GMR, the area of spintronics has remarkably flourished, driven by the urge to develop high density magnetic recording media, combined with controlled magnetization switching that is fast and reproducible. This has triggered a considerable interest in magnetic switching properties, magnetic anisotropy, interlayer interactions and magnetic damping in different magnetic nanostructures. Initially, in the beginning of the nineteenth century, the concept of conventional magnetic storage was limited with the magnetic drum, tape, disk and bubble memory, where the data was stored as the presence or absence of magnetic spots or domains. These were basically the precursors of the subsequent longitudinal recording media [45-46], where the orientation of magnetization in each grain or domain (with magnetization in plane) contributes to single bit of information and the data was written and retrieved using GMR or TMR (tunnel magnetoresistance) based read head. However, the progress in this field was hindered due to superparamagnetic effect (causes instability of magnetization state at room temperature) and cross talk between the data bits. Instead, it was found that magnetic materials with high perpendicular magnetic anisotropies (PMA) are superior candidates for this field [47-49]. The magnetic anisotropy may originate from different sources, e.g., the crystalline structure (like in Co, CoPt, CoCrPt), the shape and aspect ratio in case of structured magnetic media. The PMA media offers a higher areal density of data (340GB/in<sup>2</sup>) [50] along with the bit patterns which are magnetostatically and thermally more stable. Consequently, a thorough study of the magnetic properties was carried out in Co [51], CoCr [52], CoPt [53], CoCrPt films and Co/Pd [54], Co/Pt [55] and Co/Ni [56] multilayers. In case of multilayers, a higher grain density, together with the interface anisotropy promote a higher and tunable PMA. Nevertheless, the PMA has to compete with the magnetostatic energy of the system which may eventually give rise to exotic phenomena like stripe domain structures, if the film thickness is higher than a critical value. So far, formation and evolution of stripe domains and their spin wave excitations are reported for NiFe [57], Co [58], CoFeSiB [59], FeSiB [60], FeCoAlON [61], FeCoZr [62], FePd [63] films. However, a detailed study of the periodic internal field and its impact on the spin dynamics is still scarce in the literature.

The most crucial problem with the application of the high anisotropy materials is the requirement of very high field to switch the magnetization [64]. One of the proposed techniques to overcome this difficulty is heat assisted magnetic recording (HAMR) [65]. Here, a reduction of

the anisotropy at the time of switching is achieved by a local heating. Another way out to get around the issue is to use exchange spring (ES) magnetic media [66-69]. ES systems consist of hard and soft magnetic materials strongly exchange coupled at the interface. By selecting the anisotropy direction in the hard layer, one can have parallel or perpendicular ES magnet. Because of the high anisotropy in the hard layer, its spins are pinned, while the amount of pinning in the soft layer decreases with increasing distance from the interface, due to reduced exchange coupling. This eventually leads to a characteristic spin-twist structure under the application of an external field, which strongly depends on the soft layer thickness. Such combination of tunable magnetic anisotropy and thermal stability makes this system attractive for magnetic storage, spin transfer torque (STT) devices and other spintronics applications [66, 70-72].

In addition to the magnetic anisotropy and thermal stability, the technological possibilities also demand for a material with low magnetic damping. The material so far known for the lowest Gilbert damping is Yttrium Iron Garnet (YIG) [73]. However, its complicated crystal structure does not allow for patterning at microscale and therefore inhibits its practical implementation for information processing. The issue therefore boils down to the utilization of metallic ferromagnets. In this aspect, Heusler alloy (HA) [74-75] compounds are very important. The HA compounds are known as half metals which exhibit spin dependent band structure: while the majority spin band exhibits a metallic behavior, the minority electrons show a semiconducting behavior. Such band structure suppresses the spin flip processes and thereby reduces the damping of magnetization precession. Moreover, the resulting spin polarization makes it a potential candidate as a high spin polarized current source for giant and tunnel magnetoresistance devices [76-77]. Interestingly, here the magnetic properties such as magnetic anisotropy and damping are strongly dependent on the crystalline structure and the degree of chemical order which in turn depend on the substrate material as well as other deposition conditions. These facts have spurred interest in different ternary (like  $\text{Ni}_2\text{MnSn}$  [78],  $\text{Co}_2\text{FeSi}$  [79],  $\text{Co}_2\text{MnSi}$  [80],  $\text{Co}_2\text{FeAl}$  [81], and  $\text{Co}_2\text{CrAl}$  [82]) and quaternary (like Co-Cr-Fe-Al [81, 83], Co-Fe-Mn-Si [84] and Co-Fe-Al-Si [76, 85]) HA compounds, where the tunability and optimization of structural properties and deposition parameters have been explored.

## Magnonic Crystals

As mentioned earlier, MCs are anticipated to be a great promise in a wide range of magnetic device applications such as in magneto-electronic devices, magnonic waveguides and magnetic logic devices, where the SWs are used to carry and process information at nanoscale. The surge of interest in the static and dynamic magnetic properties of MCs started almost two decades ago [39-40, 86]. Later on, numerous theoretical and experimental studies have been conducted on one dimensional (e.g. arrays of stripes) [87-88], two-dimensional (e.g. arrays of dots) [89-90] or three dimensional (e.g. arrays of nanospheres) [91] MCs, in the form of periodic distribution of different materials or specific material parameters (e.g. saturation magnetization  $M_S$  or magnetocrystalline anisotropy [92-93]), or other modulated parameters (such as external magnetic field or stress [94]) modifying the propagation of SWs. Materials that have been mostly exploited for these studies are YIG [73] (an insulating ferrimagnet, provides smallest SW damping) and metallic ferromagnets such as  $\text{Ni}_{80}\text{Fe}_{20}$  (Permalloy) (soft magnet, negligible magnetocrystalline anisotropy) [90], Co (reasonably hard magnet, moderate magnetocrystalline anisotropy) [95] and CoFeB [96-97] for micro and nanostructured devices. In general, the modulation of magnetic properties brings about changes in coercivity and switching field, induced anisotropies, and collective behaviors of the elements in magnetization reversal. SWs form localized or standing modes in the periodic distribution of local magnetic fields, coherent coupling between which (due to exchange interaction or anisotropic dipolar interaction) leads to the creation of dispersive energy bands when arranged in an appropriate lattice. These waves may also undergo coherent scattering and Bragg reflection at specific wave vectors, giving rise to a modified band structure with partial or complete bandgaps.

In the literature, artificial tailoring of the magnonic bands in 1D MCs were studied in the form of arrays of stripes of ferromagnetic materials [86-87, 98-99] and stripes of two different ferromagnetic materials (bicomponent MCs) [88, 100], where the dynamic dipolar stray fields due to precessing magnetic moments provide the relevant interaction which is responsible for collective SW excitations across the array. Here the magnetic shape anisotropy plays a significant role which often leads to the intriguing bistable magnetic states [101]. In addition to alternating stripes, 1D MC consisted also of single magnetic stripe with periodic modulation of geometrical parameters (such as thickness or width) [18, 102] or magnetic properties (such as the magnetic anisotropy, saturation magnetization, size and orientation of internal magnetic field) [93-94],

which show effective band engineering. Waveguide structures made up of chains of magnetic dots [103-104] or periodic sequences of holes [105] along a ferromagnetic stripe can also be considered as 1D MC, where the spin wave spectra are significantly dependent on the geometrical parameters of the magnetic elements, as well as on their arrangement.

The progress in recent lithography and deposition techniques has enabled the practical realization of more complex 2D MCs comprising of magnetic dot arrays (2D periodic array of magnetic elements in non-magnetic matrix) [39-40, 106-107], antidot arrays (periodic holes arranged in homogeneous magnetic film) [95, 108-110] and arrays of magnetic rings (magnetic dot without its core) [111-114]. Periodic Array of non-interacting elements can be used in bit-patterned media where single bit of information can be stored as the magnetization state of a single dot or can be trapped between the consecutive holes along the intrinsic hard axis in an antidot nanostructure. On the other hand, when the elements are interacting, the periodic distribution of magnetostatic and dynamic dipolar stray field (arising from the unsaturated or demagnetized regions) leads to the splitting of single SW mode into multimodes. In particular, the formation of band structure is governed by the dynamic dipolar interactions between standing waves in case of nanodisks or between gyroscopic modes of the vortex core motion, if the discs are in the vortex state, or between the adjacent SW nanochannels for antidot arrays. In all cases the magnonic band width is a direct measure of the strength of coupling, which depends on the shape and size of the element, its magnetic configuration, the edge to edge separation, lattice arrangement and the magnitude and orientation of external bias magnetic field. Noticably, the antidot lattices, being exchange-coupled magnetic systems, offer higher SW propagation velocity as compared to dot arrays, which can be further improved by introducing dots of another magnetic material inside the antidots (bi-component MC [115-116]), thereby providing additional tunability in the magnonic band structures.

Another example of a combination of dot and antidot is magnetic ring arrays. Such ring array can possess different magnetic ground states, namely, the vortex state [117] in which the magnetization is circumferential to the ring (without vortex core), and the onion state [118] with two opposite head-on-head domain walls. In case of vortex, interestingly, the absence of core impedes any magnetostatic field leakage (cross talk) and reduces the influence of edge domains. This makes them good candidates as building blocks for high density magnetic random access memories and magnetosensors. Moreover, the smooth and controlled transition between the vortex

and onion states, together with their rich eigenmodes, has boosted the interest in the static and dynamic magnetic properties of arrays of circular [118-119], elliptical [120], rectangular [121-122], triangular [123] and asymmetric rings [124] of different size and composition.

Based on the study of fundamental SW properties in magnetic nanostructures, many novel SW based devices have been proposed, accompanied by their prospectives and challenges, such as magnonic waveguides [125], filters [126], splitters, grating coupler [127], SW emitters [128], SW amplifier, SW multiplexer [129] and SW interferometer [130]. In a MC, SWs of different frequencies can be used for parallel logic operations where information or data is coded into magnon phase or density. On the other hand, the intermediate gaps are important for SW filter [18] and transistor [131], which can be tailored by applying electric fields to construct SW logic gates [132]. In case of reconfigurable or dynamic MC [133-134], which forms a fascinating class of MC, it is possible to realize universal data processing units with switchable SW properties. Apart from periodic systems, single microstructured SW waveguide are also interesting, where the SW channeling along the distribution of local magnetic field can be manipulated by inducing different potentials such as magnetostatic potential [135], domain wall [136-137], local Oersted field [138], interfacial interactions etc. The application of electric field further modifies the SW phase, which can be implemented in SW logic gates, where the output is processed by SW interference [139-141]. In addition to magnon-based elements, another important requirement is converter devices which efficiently interface the magnonic circuitry with spintronic and electronic environments. So far, the techniques that have been successfully used for magnon excitation (SW source) are inductive microwave technique, STT and SHE based magnon injection.

### **Objectives of Thesis**

The framework of this thesis consist in experimental and theoretical investigation of dynamic magnetization in a variety of magnetic thin films, multilayers and 2-D patterned nano-structured elements using time resolved (time resolved magneto optical Kerr effect microscopy) and wave vector resolved (conventional Brillouin light scattering) techniques. The specific objectives of this research are to study the magnetic parameters and characteristics of SWs under various potentials (demagnetizing field, interlayer interactions, chemical ordering). Broadly, the studied systems can be classified as follows:

- i) **Magnetic multilayered structures:** The spin wave dispersions are measured to study the strength of interlayer interactions and their impact on specific magnetic parameters.
- ii) **Magnetic/non-magnetic multilayered stripe domain system:** the magnonic band structure in presence and absence of stripe domains are investigated from which the analogy between periodic stripe domains and one dimensional magnonic crystals are addressed.
- iii) **Magnonic crystals in the form of array of asymmetric stripes and square rings:** the role of complex distribution of demagnetizing field on the spin wave spectra and its tunability is investigated.
- iv) **Co-Fe-Al-Si Heusler alloy thin film:** The influence of the adjacent layers (top and bottom) on the structural and magnetic parameters as well as on the spin wave excitations are demonstrated.

## References

- [1] J. Bardeen and W. H. Brattain, "The Transistor, a Semi-conductor Triode," *Phys. Rev.* **75**, 1208 (1948).
- [2] Semiconductor Industry and Association., "International Technology Roadmap for Semiconductors," <http://www.itrs.net/Links/2011ITRS/2011Chapters/2011ERD.pdf>, (2011).
- [3] S. S. Oh, C. S. Kee, J.-E. Kim, *et al.*, "Duplexer using microwave photonic band gap structure," *Appl. Phys. Lett.* **76**, 2301 (2000).
- [4] A. D'Orazio, M. D. Sario, V. Petruzzelli, *et al.*, "Photonic band gap filter for wavelength division multiplexer," *Opt. Express* **11**, 230 (2003).
- [5] M. Loncar, T. Doll, J. Vuckovic, *et al.*, "Design and Fabrication of Silicon Photonic Crystal Optical Waveguides," *J. Lightwave Technol.* **18**, 10 (2000).
- [6] J. Li and K. S. Chiang, "Guided modes of one-dimensional photonic bandgap waveguides," *J. Opt. Soc. Am. B* **24**, 1942 (2007).
- [7] J. Li and K. S. Chiang, "Light guidance in a photonic bandgap slab waveguide consisting of two different Bragg reflectors," *Opt. Commun.* **281**, 5797 (2008).

- [8] J. Li, T. P. White, L. O'Faolain, *et al.*, "Systematic design of flat band slow light in photonic crystal waveguides," *Opt. Express* **16**, 6227 (2008).
- [9] J. C. Knight, "Photonic crystal fibres," *Nature* **424**, 847 (2003).
- [10] A. Petrov and M. Eich, "Dispersion compensation with photonic crystal line-defect waveguides," *IEEE J. Sel. Area. Commun.* **23**, 1396 (2005).
- [11] S. J. McNab, N. Moll, and Y. A. Vlasov, "Ultra-low loss photonic integrated circuit with membrane-type photonic crystal waveguides " *Opt. Express* **11**, 2927 (2003).
- [12] F. V. Laere, T. Stomeo, C. Cambournac, *et al.*, "Nanophotonic Polarization Diversity Demultiplexer Chip," *J. Lightwave Technol.* **27**, 417 (2009).
- [13] F. V. Laere, G. Roelkens, M. Ayre, *et al.*, "Compact and Highly Efficient Grating Couplers Between Optical Fiber and Nanophotonic Waveguides," *J. Lightwave Technol.* **25**, 151 (2007).
- [14] S. A. Wolf, D. D. Awschalom, R. A. Buhrman, *et al.*, "Spintronics: A Spin-Based Electronics Vision for the Future," *Science* **294**, 1488 (2001).
- [15] S. Tehrani, E. Chen, M. Durlam, *et al.*, "High density submicron magnetoresistive random access memory (invited)," *J. Appl. Phys.* **85**, 5822 (1999).
- [16] A. Imre, G. Csaba, L. Ji, *et al.*, "Majority Logic Gate for Magnetic Quantum-Dot Cellular Automata," *Science* **311**, 205 (2006).
- [17] D. A. Allwood, G. Xiong, C. C. Faulkner, *et al.*, "Magnetic Domain-Wall Logic," *Science* **309**, 1688 (2005).
- [18] K.-S. Lee, D.-S. Han, and S.-K. Kim, "Physical Origin and Generic Control of Magnonic Band Gaps of Dipole-Exchange Spin Waves in Width-Modulated Nanostrip Waveguides," *Phys. Rev. Lett.* **102**, 127202 (2009).
- [19] Y. L. Etko and A. B. Ustinov, "Broadband spin-wave delay lines with slot antennas," *Tech. Phys. Lett.* **37**, 1015 (2011).
- [20] S. S. P. Parkin, M. Hayashi, and L. Thomas, "Magnetic Domain-Wall Racetrack Memory," *Science* **320**, 190 (2008).
- [21] T. Thomson, G. Hu, and B. D. Terris, "Intrinsic Distribution of Magnetic Anisotropy in Thin Films Probed by Patterned Nanostructures," *Phys. Rev. Lett.* **96**, 257204 (2006).
- [22] M. N. Baibich, J. M. Broto, A. Fert, *et al.*, "Giant magnetoresistance of (001) Fe/(001) Cr magnetic superlattices," *Phys. Rev. Lett.* **61**, 2472 (1988).

- [23] G. Binasch, P. Grünberg, F. Saurenbach, *et al.*, "Enhanced magnetoresistance in layered magnetic structures with antiferromagnetic interlayer exchange," *Phys. Rev. B* **39**, 4828 (1989).
- [24] L. Berger, "Emission of spin waves by a magnetic multilayer traversed by a current," *Phys. Rev. B* **54**, 9353 (1996).
- [25] J. Slonczewski, "Current-driven excitation of magnetic multilayers," *J. Magn. Magn. Mater.* **159**, L1 (1996).
- [26] J. E. Hirsch, "Spin Hall Effect," *Phys. Rev. Lett.* **83**, 1834 (1999).
- [27] Y. K. Kato, R. C. Myers, A. C. Gossard, *et al.*, "Observation of the Spin Hall Effect in Semiconductors," *Science* **306**, 1910 (2004).
- [28] A. Brataas, A. D. Kent, and H. Ohno, "Current-induced torques in magnetic materials," *Nat. Mater.* **11**, 372 (2012).
- [29] K. Uchida, S. Takahashi, K. Harii, *et al.*, "Observation of the spin Seebeck effect," *Nature*. **455**, 778 (2008).
- [30] I. E. Dzyaloshinskii, "Thermodynamic theory of weak ferromagnetism in antiferromagnetic substances," *Sov. Phys. JETP* **5**, 1259 (1957).
- [31] T. Moriya, "Anisotropic superexchange interaction and weak ferromagnetism," *Phys. Rev.* **120**, 91 (1960).
- [32] S. Emori, U. Bauer, S.-M. Ahn, *et al.*, "Current-driven dynamics of chiral ferromagnetic domain walls," *Nat. Mater.* **12**, 611 (2013).
- [33] A. I. Akhiezer, V. G. Bar'yakhtar, and S. V. Peletminskii, "Spin Waves," Amsterdam, North-Holland, (1968).
- [34] A. G. Gurevich and G. A. Melkov, "Magnetization Oscillations and Waves," New York, Chemical Rubber Corp., (1996).
- [35] F. Bloch, "Zur theorie des ferromagnetismus," *Z. Phys.* **61**, 206 (1930).
- [36] S. A. Nikitova, P. Tailhadesa, and C. S. Tsai, "Spin waves in periodic magnetic structures-magnonic crystals," *J. Magn. Magn. Mater.* **236**, 320 (2001).
- [37] J. Jorzick, S. O. Demokritov, B. Hillebrands, *et al.*, "Spin Wave Wells in Nonellipsoidal Micrometer Size Magnetic Elements," *Phys. Rev. Lett.* **88**, 4 (2002).
- [38] G. Gubbiotti, L. Albini, G. Carlotti, *et al.*, "Finite size effects in patterned magnetic permalloy films," *J. Appl. Phys.* **87**, 5633 (2000).

- [39] B. Hillebrands, C. Mathieu, C. Hartmann, *et al.*, "Static and dynamic properties of patterned magnetic permalloy films," *J. Magn. Magn. Mater.* **175**, 10 (1997).
- [40] M. Grimsditch, Y. Jaccard, and I. K. Schuller, "Magnetic anisotropies in dot arrays: Shape anisotropy versus coupling," *Phys. Rev. B* **58**, 11539 (1998).
- [41] S. Mühlbauer, B. Bin, F. Jonietz, *et al.*, "Skyrmion Lattice in a Chiral Magnet," *Science* **323**, 915 (2009).
- [42] A. Fert, V. Cros, and J. Sampaio, "Skyrmions on the track," *Nat. Nanotechnol.* **8**, 152 (2013).
- [43] R. F. Wang, C. Nisoli, R. S. Freitas, *et al.*, "Artificial 'spin ice' in a geometrically frustrated lattice of nanoscale ferromagnetic islands," *Nature* **439**, 303 (2006).
- [44] G. Moller and R. Moessner, "Artificial Square Ice and Related Dipolar Nanoarrays," *Phys. Rev. Lett.* **96**, 237202 (2006).
- [45] A. Moser and D. Weller, "Thermal processes and stability of longitudinal magnetic recording media," *IEEE Trans. Magn.* **35**, 2808 (1999).
- [46] H. N. Bertram, H. Zhou, and R. Gustafson, "Signal to noise ratio scaling and density limit estimates in longitudinal magnetic recording," *IEEE Trans. Magn.* **34**, 1845 (1998).
- [47] S. Iwasaki and K. Ouchi, "Co-Cr recording films with perpendicular magnetic anisotropy," *IEEE Trans. Magn.* **14**, 849 (1978).
- [48] S. Iwasaki, "Perpendicular magnetic recording," *IEEE Trans. Magn.* **16**, 71 (1980).
- [49] M. Albrecht, C. T. Rettner, A. Moser, *et al.*, "Recording performance of high-density patterned perpendicular magnetic media," *Appl. Phys. Lett.* **81**, 2875 (2002).
- [50] Y. Hsu, V. Nikitin, D. Hsiao, *et al.*, "Challenges for perpendicular write heads at high recording density," *IEEE Trans. Magn.* **43**, 605 (2007).
- [51] C. Chappert, P. Beauvillain, P. Bruno, *et al.*, "Magnetization, coercive forces and magnetoresistance in simple and double Co films with perpendicular magnetization " *J. Magn. Magn. Mater.* **93**, 319 (1991).
- [52] K. Kobayashi and G. Ishida, "Magnetic and Structural Properties of Rh Substituted CoCr Alloy Films with Perpendicular Magnetic Anisotropy," *J. Appl. Phys.* **52**, 2453 (1981).
- [53] D. Makarov, E. Bermúdez-Ureña, O. G. Schmidt, *et al.*, "Nanopatterned CoPt Alloys with Perpendicular Magnetic Anisotropy," *Appl. Phys. Lett.* **93**, 153112 (2008).

- [54] O. Hellwig, T. Hauet, T. Thomson, *et al.*, "Coercivity Tuning in Co/Pd Multilayer Based Bit Patterned Media," *Appl. Phys. Lett.* **95**, 232505 (2009).
- [55] O. Hellwig, S. Maat, J. B. Kortright, *et al.*, "Magnetic Reversal of Perpendicular-biased Co/Pt Multilayers," *Phys. Rev. B.* **65**, 144418 (2002).
- [56] F. J. A. d. Broeder, E. Janssen, A. Mud, *et al.*, "Co/Ni multilayers with perpendicular magnetic anisotropy " *J. Magn. Magn. Mater.* **126**, 563 (1993).
- [57] N. Amos, R. Fernandez, R. Ikkawi, *et al.*, "Magnetic force microscopy study of magnetic stripe domains in sputter deposited Permalloy thin films," *J. Appl. Phys.* **103**, 07E732 (2008).
- [58] M. Hehn, S. Padovani, K. Ounadjela, *et al.*, "Nanoscale magnetic domain structures in epitaxial cobalt films," *Phys. Rev. B.* **54**, 3428 (1996).
- [59] J. Yoon, S.-y. Park, Y. Jo, *et al.*, "Dense stripe domains in a nanocrystalline CoFeSiB thin film," *Curr. Appl. Phys.* **9**, 688 (2009).
- [60] M. Coïsson, C. Appino, F. Celegato, *et al.*, "Magnetic properties of FeSiB thin films displaying stripe domains," *Phys. Rev. B.* **77**, 214404 (2008).
- [61] D. Wu, T. Jin, Y. Lou, *et al.*, "Understanding the dense stripe domains in soft magnetic film," *Appl. Surf. Sci.* **346**, 567 (2015).
- [62] F. Luo, F. Zheng, G. Yin, *et al.*, "Approximate Solution of the Magnetostatic Property of FeCoZr Thin Films with Stripe Domain," *Appl. Phys. Express* **6**, 073003 (2013).
- [63] N. Vukadinovic, H. L. Gall, J. B. Youssef, *et al.*, "Magnetization dynamics and relaxation in epitaxial FePd thin flms with a stripe domain structure," *Eur. Phys. J. B* **13**, 445 (2000).
- [64] S. -I. Iwasaki, "Discoveries that Guided the Beginning of Perpendicular Magnetic Recording," *J. Magn. Magn. Mater.* **235**, 227 (2001).
- [65] A. Moser, K. Takano, D. T. Margulies, *et al.*, "Magnetic Recording: Advancing into the Future," *J. Phys. D: Appl. Phys.* **35**, R157 (2002).
- [66] E. F. Kneller and R. Hawig, "The exchange-spring magnet: a new material principle for permanent magnets," *IEEE Trans. Magn.* **27**, 3588 (1991).
- [67] E. E. Fullerton, J. S. Jiang, M. Grimsditch, *et al.*, "Exchange-spring Behavior in Epitaxial Hard/Soft Magnetic Bilayers," *Phys. Rev. B* **58**, 12193 (1998).

- [68] O. Hellwig, J. B. Kortright, K. Takano, *et al.*, "Switching Behavior of Fe-Pt/Ni-Fe Exchange-spring Films Studied by Resonant Soft-X-ray Magneto-optical Kerr Effect," *Phys. Rev. B* **62**, 11694 (2000).
- [69] R. Röhlberger, H. Thomas, K. Schlage, *et al.*, "Imaging the Magnetic Spin Structure of Exchange-Coupled Thin Films," *Phys. Rev. B* **89**, 237201 (2002).
- [70] S. N. Gordeev, J. M. L. Beaujour, G. J. Bowden, *et al.*, "Giant Magnetoresistance by Exchange Springs in DyFe<sub>2</sub>/YFe<sub>2</sub> Superlattices," *Phys. Rev. Lett.* **87**, 186808 (2001).
- [71] D. Suess, T. Schrefl, S. Fähler, *et al.*, "Exchange spring media for perpendicular recording," *Appl. Phys. Lett.* **87**, 012504 (2005).
- [72] Y. Zhou, C. L. Zha, S. Bonetti, *et al.*, "Spin-torque oscillator with tilted fixed layer magnetization," *Appl. Phys. Lett.* **92**, 262508 (2008).
- [73] A. A. Serga, A. V. Chumak, and B. Hillebrands, "YIG Magnonics," *J. Phys. D: Appl. Phys.* **43**, 264002 (2010).
- [74] C. Liu, C. K. A. Mewes, M. Chshiev, *et al.*, "Origin of low Gilbert damping in half metals," *Appl. Phys. Lett.* **95**, 022509 (2009).
- [75] M. Oogane, T. Kubota, Y. Kota, *et al.*, "Gilbert magnetic damping constant of epitaxially grown Co-based Heusler alloy thin films," *Appl. Phys. Lett.* **96**, 252501 (2010).
- [76] R. Shan, H. Sukegawa, W. H. Wang, *et al.*, "Demonstration of Half-Metallicity in Fermi-Level-Tuned Heusler Alloy Co<sub>2</sub>FeAl<sub>0.5</sub>Si<sub>0.5</sub> at Room Temperature," *Phys. Rev. Lett.* **102**, 246601 (2009).
- [77] H. Sukegawa, W. Wang, R. Shan, *et al.*, "Spin-polarized tunneling spectroscopy of fully epitaxial magnetic tunnel junctions using Co<sub>2</sub>FeAl<sub>0.5</sub>Si<sub>0.5</sub> Heusler alloy electrodes," *Phys. Rev. B* **79**, 184418 (2009).
- [78] J. Dubowika, I. Goscianska, K. Z. H. Glowinski, *et al.*, "Epitaxial Growths and Magnetization Dynamics of Ni<sub>2</sub>MnSn Heusler Alloy Films," *Acta. Phys. Pol. A.* **121**, 1121 (2012).
- [79] D. Steil, O. Schmitt, R. Fetzner, *et al.*, "Ultrafast magnetization dynamics in Co-based Heusler compounds with tuned chemical ordering," *New J. Phys.* **16**, 063068 (2014).
- [80] Y. Liu, L. R. Sheldford, V. V. Kruglyak, *et al.*, "Optically induced magnetization dynamics and variation of damping parameter in epitaxial Co<sub>2</sub>MnSi Heusler alloy films," *Phys. Rev. B* **81**, 094402 (2010).

- [81] O. Gaier, J. Hamrle, S. Trudel, *et al.*, "Brillouin light scattering study of  $\text{Co}_2\text{Cr}_{0.6}\text{Fe}_{0.4}\text{Al}$  and  $\text{Co}_2\text{FeAl}$  Heusler compounds," *J. Phys. D: Appl. Phys.* **42**, 084004 (2009).
- [82] E. Şaşıoğlu, L. M. Sandratskii, P. Bruno, *et al.*, "Exchange interactions and temperature dependence of the magnetization in half-metallic Heusler alloys," *Phys. Rev. B* **72**, 184415 (2015).
- [83] J.-P. Wustenberg, D. Steil, S. Alebrand, *et al.*, "Ultrafast magnetization dynamics in the half-metallic Heusler alloy  $\text{Co}_2\text{Cr}_{0.6}\text{Fe}_{0.4}\text{Al}$ ," *Phys. Status Solidi B* **248**, 2330 (2011).
- [84] T. Seki, H. Yako, T. Yamamoto, *et al.*, "Spin torque-induced magnetization dynamics in giant magnetoresistance devices with Heusler alloy layers," *J. Phys. D: Appl. Phys.* **48**, 164010 (2015).
- [85] W. Wang, H. Sukegawa, R. Shan, *et al.*, "Preparation and characterization of highly  $L_{21}$ -ordered full-Heusler alloy  $\text{Co}_2\text{FeAl}_{0.5}\text{Si}_{0.5}$  thin films for spintronics device applications," *Appl. Phys. Lett.* **92**, 221912 (2008).
- [86] C. Mathieu, J. Jorzick, A. Frank, *et al.*, "Lateral Quantization of Spin Waves in Micron Size Magnetic Wires," *Phys. Rev. Lett.* **81**, 3968 (1998).
- [87] M. Kostylev, P. Schrader, R. L. Stamps, *et al.*, "Partial frequency band gap in one-dimensional magnonic crystals," *Appl. Phys. Lett.* **92**, 132504 (2008).
- [88] Z. K. Wang, V. L. Zhang, H. S. Lim, *et al.*, "Nanostructured Magnonic Crystals with Size-Tunable Bandgaps," *ACS Nano* **4**, 643 (2010).
- [89] V. V. Kruglyak, A. Barman, R. J. Hicken, *et al.*, "Precessional dynamics in microarrays of nanomagnets," *J. Appl. Phys.* **97**, 10A706 (2005).
- [90] B. Rana, D. Kumar, S. Barman, *et al.*, "Detection of picosecond magnetization dynamics of 50 nm magnetic dots down to the single dot regime," *ACS Nano* **5**, 9559 (2011).
- [91] J. R. Vivas, S. Mamica, M. Krawczyk, *et al.*, "Investigation of spin wave damping in three-dimensional magnonic crystals using the plane wave method," *Phys. Rev. B* **86**, 144417 (2012).
- [92] N. I. Polushkin, S. A. Michalski, L. Yue, *et al.*, "Evidence of Long-Wavelength Collective Excitations in Magnetic Superlattices," *Phys. Rev. Lett.* **97**, 256401 (2006).
- [93] B. Obry, P. Pirro, T. Bracher, *et al.*, "A micro-structured ion-implanted magnonic crystal," *Appl. Phys. Lett.* **102**, 202403 (2013).

- [94] L. Bai, M. Kohda, and J. Nitta, "Observation of spin wave modes depending on a tunable periodic magnetic field," *Appl. Phys. Lett.* **98**, 172508 (2011).
- [95] R. Mandal, S. Saha, D. Kumar, *et al.*, "Optically Induced Tunable Magnetization Dynamics in Nanoscale Co Antidot Lattices," *ACS Nano* **6**, 3397 (2012).
- [96] H. Ulrichs, B. Lenk, and M. Münzenberg, "Magnonic spin-wave modes in CoFeB antidot lattices," *Appl. Phys. Lett.* **97**, 092506 (2010).
- [97] T. Schwarze and D. Grundler, "Magnonic crystal wave guide with large spin-wave propagation velocity in CoFeB," *Appl. Phys. Lett.* **102**, 222412 (2013).
- [98] M. P. Kostylev, G. Gubbiotti, J.-G. Hu, *et al.*, "Dipole-exchange propagating spin-wave modes in metallic ferromagnetic stripes," *Phys. Rev. B* **76**, 054422 (2007).
- [99] G. Gubbiotti, S. Tacchi, G. Carlotti, *et al.*, "Collective spin modes in monodimensional magnonic crystals consisting of dipolarly coupled nanowires," *Appl. Phys. Lett.* **90**, 092503 (2007).
- [100] Z. K. Wang, V. L. Zhang, H. S. Lim, *et al.*, "Observation of frequency band gaps in a one-dimensional nanostructured magnonic crystal," *Appl. Phys. Lett.* **94**, 083112 (2009).
- [101] J. Topp, D. Heitmann, M. P. Kostylev, *et al.*, "Making a Reconfigurable Artificial Crystal by Ordering Bistable Magnetic Nanowires," *Phys. Rev. Lett.* **104**, 207205 (2010).
- [102] A. V. Chumak, A. A. Serga, B. Hillebrands, *et al.*, "Scattering of backward spin waves in a one-dimensional magnonic crystal," *Appl. Phys. Lett.* **93**, 022508 (2008).
- [103] D.-S. Han, A. Vogel, H. Jung, *et al.*, "Wave modes of collective vortex gyration in dipolar-coupled-dot-array magnonic crystals," *Sci. Rep.* **3**, 2262 (2013).
- [104] A. Haldar, D. Kumar, and A. O. Adeyeye, "A reconfigurable waveguide for energy-efficient transmission and local manipulation of information in a nanomagnetic device," *Nat. Nanotechnol.* **11**, 437 (2016).
- [105] J. W. Klos, D. Kumar, M. Krawczyk, *et al.*, "Magnonic Band Engineering by Intrinsic and Extrinsic Mirror Symmetry Breaking in Antidot Spin-Wave Waveguides," *Sci. Rep.* **3**, 2444 (2013).
- [106] B. Hillebrands, S. O. Demokritov, C. Mathieu, *et al.*, "Arrays of Interacting Magnetic Dots and Wires: Static and Dynamic Properties," *J. Mag. Soc. Jpn.* **23**, 670 (1999).
- [107] K. Y. Guslienko and A. N. Slavin, "Spin-wave excitations in cylindrical magnetic dot arrays with in-plane magnetization," *J. Magn. Magn. Mater.* **215**, 576 (2000).

- [108] C. Yu, M. J. Pechan, W. A. Burgei, *et al.*, "Lateral standing spin waves in permalloy antidot arrays," *J. Appl. Phys.* **95**, 6648 (2004).
- [109] M. J. Pechan, C. Yu, R. L. Compton, *et al.*, "Direct measurement of spatially localized ferromagnetic-resonance modes in an antidot lattice (invited)," *J. Appl. Phys.* **97**, 10J903 (2005).
- [110] O. N. Martyanov, V. F. Yudanov, R. N. Lee, *et al.*, "Ferromagnetic resonance study of thin film antidot arrays: Experiment and micromagnetic simulations," *Phys. Rev. B* **75**, 174429 (2007).
- [111] P. Vavassori, M. Grimsditch, V. Novosad, *et al.*, "Magnetization switching in Permalloy square ring magnets," *J. Appl. Phys.* **93**, 7900 (2003).
- [112] D. R. Lee, J. W. Freeland, G. Srajer, *et al.*, "Domain-specific magnetization reversals on a Permalloy square ring array," *J. Appl. Phys.* **95**, 7016 (2004).
- [113] X. Zhu, M. Malac, Z. Liu, *et al.*, "Broadband spin dynamics of Permalloy rings in the circulation state," *Appl. Phys. Lett.* **86**, 262502 (2005).
- [114] H. Schultheiss, C. W. Sandweg, B. Obry, *et al.*, "Dissipation characteristics of quantized spin waves in nano-scaled magnetic ring structures," *J. Phys. D: Appl. Phys.* **41**, 164017 (2008).
- [115] F. S. Ma, H. S. Lim, Z. K. Wang, *et al.*, "Micromagnetic study of spin wave propagation in bicomponent magnonic crystal waveguide," *Appl. Phys. Lett.* **98**, 153107 (2011).
- [116] G. Duerr, M. Madami, S. Neusser, *et al.*, "Spatial control of spin-wave modes in Ni<sub>80</sub>Fe<sub>20</sub> antidot lattices by embedded Co nanodisks," *Appl. Phys. Lett.* **99**, 202502 (2011).
- [117] M. Madami, S. Tacchi, G. Gubbiotti, *et al.*, "Spin Modes in Elliptical Nanorings in the Vortex State: Two-Dimensional Mapping by Micro-Focused Brillouin Light Scattering," *IEEE Trans. Magn.* **46**, 199 (2010).
- [118] H. Schultheiss, S. Schafer, P. Candeloro, *et al.*, "Observation of Coherence and Partial Decoherence of Quantized Spin Waves in Nanoscaled Magnetic Ring Structures," *Phys. Rev. Lett.* **100**, 047204 (2008).
- [119] I. Neudecker, M. Klaui, K. Perzlmaier, *et al.*, "Spatially Resolved Dynamic Eigenmode Spectrum of Co Rings," *Phys. Rev. Lett.* **96**, 057207 (2006).
- [120] L. J. Chang, C. Yu, T. W. Chiang, *et al.*, "Magnetic interaction in nanometer line width elliptical ring arrays," *J. Appl. Phys.* **103**, 07C514 (2008).

- [121] F. S. Ma, V. L. Zhang, Z. K. Wang, *et al.*, "Magnetic-field-orientation dependent magnetization reversal and spin waves in elongated permalloy nanorings," *J. Appl. Phys.* **108**, 053909 (2010).
- [122] Y. Ren and A. O. Adeyeye, "Magnetic spin states and vortex stability control in elongated Ni<sub>80</sub>Fe<sub>20</sub> nanorings," *J. Appl. Phys.* **105**, 063901 (2009).
- [123] J. Ding, M. Kostylev, and A. O. Adeyeye, "Broadband ferromagnetic resonance spectroscopy of permalloy triangular nanorings," *Appl. Phys. Lett.* **100**, 062401 (2012).
- [124] T. M. Nguyen and M. G. Cottam, "Spin-wave excitations in arrays of asymmetric ferromagnetic nanorings," *J. Appl. Phys.* **103**, 07C503 (2008).
- [125] V. E. Demidov, S. O. Demokritov, K. Rott, *et al.*, "Mode interference and periodic self-focusing of spin waves in permalloy microstripes," *Phys. Rev. B* **77**, 064406 (2008).
- [126] S.-K. Kim, K.-S. Lee, and D.-S. Han, "A gigahertz-range spin-wave filter composed of width-modulated nanostrip magnonic-crystal waveguides," *Appl. Phys. Lett.* **95**, 082507 (2009).
- [127] H. Yu, G. Duerr, R. Huber, *et al.*, "Omnidirectional spin-wave nanograting coupler," *Nat. Commun.* **4**, 2702 (2013).
- [128] S. Kaka, M. R. Pufall, W. H. Rippard, *et al.*, "Mutual phase-locking of microwave spin torque nano-oscillators," *Nature* **437**, 389 (2005).
- [129] K. Vogt, F. Y. Fradin, J. E. Pearson, *et al.*, "Realization of a spin-wave multiplexer," *Nat. Commun.* **5**, 3727 (2014).
- [130] N. Kanazawa, T. Goto, K. Sekiguchi, *et al.*, "Demonstration of a robust magnonic spin wave interferometer," *Sci. Rep.* **6**, 30268 (2016).
- [131] A. V. Chumak, A. A. Serga, and B. Hillebrands, "Magnon transistor for all-magnon data processing," *Nat. Commun.* **5**, 4700 (2014).
- [132] A. A. Nikitin, A. B. Ustinov, A. A. Semenov, *et al.*, "A spin-wave logic gate based on a width-modulated dynamic magnonic crystal," *Appl. Phys. Lett.* **106**, 102405 (2015).
- [133] A. V. Chumak, T. Neumann, A. A. Serga, *et al.*, "A current-controlled, dynamic magnonic crystal," *J. Phys. D: Appl. Phys.* **42**, 205005 (2009).
- [134] A. V. Chumak, V. S. Tiberkevich, A. D. Karenowska, *et al.*, "All-linear time reversal by a dynamic artificial crystal," *Nat. Commun.* **1**, 141 (2010).

- [135] V. E. Demidov, J. Jersch, S. O. Demokritov, *et al.*, "Transformation of propagating spin-wave modes in microscopic waveguides with variable width," *Phys. Rev. B* **79**, 054417 (2009).
- [136] P. Pirro, T. Koyama, T. Bracher, *et al.*, "Experimental observation of the interaction of propagating spin waves with Neel domain walls in a Landau domain structure," *Appl. Phys. Lett.* **106**, 232405 (2015).
- [137] K. Wagner, A. Kákay, K. Schultheiss, *et al.*, "Magnetic domain walls as reconfigurable spin-wave nanochannels," *Nat. Nanotechnol.* **11**, 432 (2016).
- [138] V. E. Demidov, S. Urazhdin, and S. O. Demokritov, "Control of spin-wave phase and wavelength by electric current on the microscopic scale," *Appl. Phys. Lett.* **95**, 262509 (2009).
- [139] M. P. Kostylev, A. A. Serga, T. Schneider, *et al.*, "Spin-wave logical gates," *Appl. Phys. Lett.* **87**, 153501 (2005).
- [140] T. Schneider, A. A. Serga, B. Leven, *et al.*, "Realization of spin-wave logic gates," *Appl. Phys. Lett.* **92**, 022505 (2008).
- [141] K.-S. Lee and S.-K. Kima, "Conceptual design of spin wave logic gates based on a Mach–Zehnder-type spin wave interferometer for universal logic functions," *J. Appl. Phys.* **104**, 053909 (2008).

## Chapter 2

# 2. Theoretical background

---

### 2.1. Introduction

The fundamental origin of the intrinsic magnetic properties of a material lies in its molecular structure as well as in its electronic arrangement. The spin of the electrons, together with the number of unpaired electrons and the interactions between their spin and orbital momenta determine the magnetic response both in microscopic and macroscopic level. Based on that, materials can be classified as diamagnet, paramagnet, ferromagnet, ferrimagnet, and antiferromagnet. Amongst them, the ferromagnetic and ferrimagnetic materials are especially interesting because they possess spontaneous magnetic polarization. This thesis will focus on the properties of ferromagnetic (FM) materials. The transition metals (to which iron, cobalt and nickel belong) are characterized by partially filled internal electron shell corresponding to the 3d levels. The 3d band is very narrow and hence the kinetic energy of 3d electrons is small while the density of states is very high. These facts lead to the intricate interaction between the 3d electrons of neighboring atoms (known as exchange interaction) which is responsible for the molecular spin alignment of the material. According to the Weiss theory [1], this exchange interaction has to compete with the dipolar interaction caused by the free magnetic poles on the surface (demagnetizing field), which ends up with the FM to break up into small domains for the minimization of the free energy.

The individual moments of a FM material collectively contribute to a volume magnetization  $\mathbf{M}$ , which is maximum when the moments are fully aligned under a large enough external magnetic field. In presence of magnetic field, the coupled moments precess about the field direction, which is called ferromagnetic resonance (FMR) in case of uniform precession (the moments have same frequency and phase) [2]. When the precession is not uniform, each individual dipole precesses slightly out-of-phase with its nearest neighbor. This produces a propagating wave, known as spin-wave (SW) [3], with its energy and momentum related by characteristic dispersion relations. The parameter that describes the rate of energy loss of precessing magnetization, is called magnetic damping, which can be intrinsic (e.g. due to spin-orbit coupling) or extrinsic (e.g. due to

two-magnon scattering) depending upon its origin. Another exotic property observed in FM materials is magnetic anisotropy that is the dependence of magnetic energy on the direction of the spins with respect to the crystal lattice, or, in patterned structures, with respect to the geometrical axes.

This chapter starts off with an overview of the energies that play a role in the dynamics of a ferromagnetic system. Next, we describe the magnetization dynamics followed by the illustration of different aspects of spin waves.

## 2.2. Magnetic Energies and Fields

The static and dynamic magnetic properties of a magnetic material are dependent on the relative contribution of different energy terms, such as Zeeman energy, magnetostatic self-energy (also known as demagnetizing energy), exchange energy, and magnetic anisotropy energy. In equilibrium the system is in a local minimum of the total free energy. This section presents a brief outline of some of the vital energy factors.

### 2.2.1. Zeeman Energy

The Zeeman energy describes the interaction of the magnetization  $M$  with an external magnetic field  $H_0$ . The energy is given by:

$$E_{Zee} = -\mu_0 \int_V M \cdot H_0 d\tau \quad \dots\dots\dots(2.1)$$

where  $V$  is the volume occupied by the magnetic structure and  $d\tau$  the volume element. This equation states that in presence of magnetic field, the magnetization tends to align along  $H_0$  to make the energy minimum.

### 2.2.2. Exchange Energy

The interaction which is quantum-mechanical in nature and is responsible for the long range magnetic order in ferromagnets is the so called exchange interaction [4]. Besides ferromagnets, this interaction is pronounced in ferrimagnets and antiferromagnets as well, where the exchange interaction between the neighboring magnetic ions will force the moments into parallel or antiparallel alignment. It actually stems from the Coulombic interaction energy and Pauli exclusion

principle, which can be phenomenologically described by the Heisenberg exchange Hamiltonian, given by

$$H_{ex} = -2J \sum_{i \neq j} S_i \cdot S_j \quad \dots\dots\dots(2.2)$$

where  $S_i$  is the spin operator of the  $i$ -th atom and  $J$  is known as exchange integral. In the continuum model, the above equation can be written as:

$$E_{ex} = A \int (\nabla m)^2 dV \quad \dots\dots\dots(2.3)$$

where the magnetic moment  $m$  is a continuous vector quantity and  $A$  is called the exchange stiffness constant presented as:

$$A = \frac{2JS^2}{a} \quad \dots\dots\dots(2.4)$$

where  $a$  is the lattice constant.

The aforementioned exchange is also known as direct exchange interaction, where the electrons of magnetic atoms interact with its nearest neighbors. Apart from that, exchange can also occur in indirect ways, which couples moments over relatively larger distances. For example, RKKY exchange, where the metallic ions are coupled via itinerant electrons, super-exchange, where the exchange is mediated via different non-magnetic ion, anisotropic exchange interaction (also known as Dzyaloshinsky-Moriya interaction) [5], where the spin orbit interaction plays a major role and often leads to canting of spins by small angle.

### 2.2.3. Magnetic Dipolar Interaction

The dipolar interaction between two magnetic dipoles is common for any magnetic dipole, irrespective of whether it is in ferromagnetic system or not. The corresponding energy term reads as

$$E_{dipole} = \frac{\mu_0}{4\pi r^3} \left[ \mu_1 \cdot \mu_2 - \frac{3}{r^2} (\mu_1 \cdot r)(\mu_2 \cdot r) \right] \quad \dots\dots\dots(2.5)$$

where  $\mu_0$  is the permeability,  $\mu_1$  and  $\mu_2$  are the moments of the two magnetic dipoles and  $r$  is the vector connecting the two dipoles, which experience the magnetic field generated by each other. The above equation tells that the energy decreases with the 3rd order of their distance. In case of

ferromagnets, although this interaction does not contribute to magnetic ordering, but it plays an important role in a number of phenomena such as formation of domains, demagnetizing field and spin waves in the long wavelength regime.

#### 2.2.4. Magnetic Anisotropy

Magnetic anisotropy [6] is the directional dependence of material's magnetic properties. Because of this, there are preferential directions in space (known as easy magnetization axes) in which a magnetic system is easier to magnetize than in other ones. Deviation from these directions imposes an energy penalty, called the anisotropy energy. The origin of magnetic anisotropy lies in multiple factors, such as:

i) **Magnetocrystalline anisotropy:-**

The magneto crystalline anisotropy is an intrinsic property of the material which is caused by the spin-orbit interaction of the electrons. The spatial arrangement of the electron orbitals are strongly linked to the crystallographic structure. Consequently, when they interact with the spins they force the latter to align along well defined crystallographic axes. The symmetry of the lattice structure is responsible for the 'foldedness' of the magnetic anisotropy. For instance, in cubic systems the energy density due to crystal anisotropy reads

$$E_{ani} = K_0 + K_1(\alpha_x^2\alpha_y^2 + \alpha_y^2\alpha_z^2 + \alpha_z^2\alpha_x^2) + K_2\alpha_x^2\alpha_y^2\alpha_z^2 \quad \dots\dots\dots(2.6)$$

where  $\alpha_i$  are the direction cosines of the normalized magnetization  $\mathbf{m}$  with respect to the Cartesian axes of the lattice.  $K_i$ 's are the magnetocrystalline anisotropy constants,  $K_0$ ,  $K_1$ , and  $K_2$  are the crystalline anisotropy constants of zero, first and second order, respectively. On the other hand, for crystals having uniaxial anisotropy, the energy density is given by

$$E_{ani} = K_U\alpha_x^2 \quad \dots\dots\dots(2.7)$$

where  $K_U$  is the uniaxial anisotropy constant.

## ii) Shape anisotropy and demagnetizing energy:-

Another very common origin of magnetic anisotropy belongs to the anisotropic shape of the magnetic element. It is basically the anisotropic dipolar interaction of free magnetic poles (stray and demagnetization fields) which comes into play when the geometry of submicron sized magnetic elements is not symmetric.

A magnetic system with finite boundaries exhibits poles at its surfaces which lead to a stray field outside the sample. This in effect gives rise to demagnetizing field inside the sample. The energy corresponding to the stray field is given by

$$E_{dem} = -\frac{1}{2} \int \mu_0 M \cdot H_{dem} dV \quad \dots\dots\dots(2.8)$$

In case of a homogeneously magnetized ellipsoid the demagnetizing field is uniform which is given by

$$H_{dem} = -NM \quad \dots\dots\dots(2.9)$$

where  $N$  is called the demagnetizing tensor. Thus, the stray field energy (demagnetizing energy) reduces to

$$E_{dem} = \frac{1}{2} \mu_0 \int MNM dV \quad \dots\dots\dots(2.10)$$

$$E_{dem} = \frac{1}{2} V \mu_0 MNM \quad \dots\dots\dots(2.11)$$

where  $V$  is the volume of the sample. For an arbitrary shaped element,  $N$  is strongly dependent on the shape and geometry of the element and forms a complex function of position. Finally, the preferred orientation of magnetization is the one for which  $E_{dem}$  is minimum.

## iii) Surface and interface anisotropy:-

The broken symmetry at surfaces and interfaces of magnetic thin films and multilayers often induces some anisotropy in the system. This results in the effective anisotropy ( $K^{eff}$ ) constant to be divided into two parts:

$$K^{eff} = K^V + \frac{2K^S}{d} \quad \dots\dots\dots(2.12)$$

with  $K^V$  being the volume dependent magneto crystalline anisotropy constant and  $K^S$  is the surface anisotropy. The latter exhibits an inverse dependence on the thickness  $d$  of the system and prefers an out of plane magnetization of the sample. The competition between volume and surface anisotropy gives rise to a dependence of the magnetization on the film thickness. Below a critical thickness  $d_c$  (given by  $d_c = \frac{-2K^S}{K^V}$ ), the magnetization favors out of plane orientation and vice versa.

In case of few multilayered systems (like Co/Pd and Co/Pt multilayers), the observed interfacial anisotropy is rooted in the interfacial hybridization of electronic band-structure [7-8]. These hybridizations are sensitive to the local interface structure and affect the spin orbit coupling strength, which in turn changes the magnetocrystalline anisotropy energy.

## 2.3. Magnetization Dynamics and Spin Waves

In presence of an external magnetic field, the magnetic moments of a magnetic material experience a torque which induces a precessional motion about the direction of the external field. In addition, the moments try to align themselves along the external field to minimize the Zeeman energy. Effectively, they execute a damped spiral motion about the field direction which is referred to as magnetization dynamics (See Fig. 2.1). The net behavior of dynamic magnetization is phenomenologically illustrated by the Landau-Lifshitz and Gilbert equation of motion. The Landau-Lifshitz-Gilbert (LLG) equation is a torque equation which was first introduced by Lev Landau and Evgeny Lifshitz in 1935 as Landau-Lifshitz (LL) equation [9]. Later, Gilbert modified it by inserting a Gilbert damping term [10].

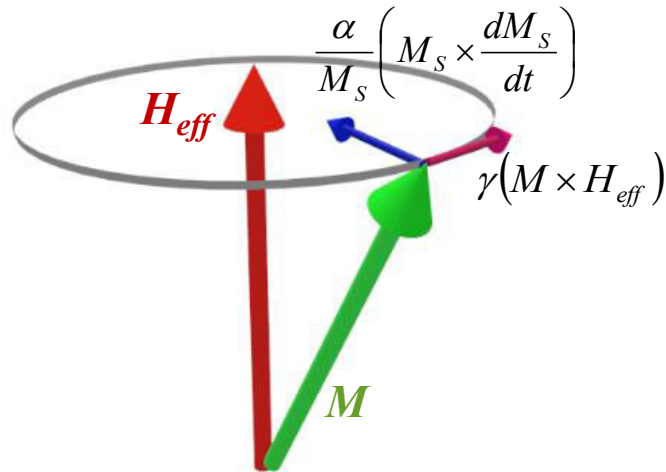


Figure 2.1: The precessional motion of the magnetization around the effective magnetic field direction.

When a magnetic moment  $\mu_m$  is placed in an effective magnetic field  $H_{eff}$ , it experiences a torque given as:

$$\tau = \mu_m \times H_{eff} \tag{2.13}$$

In a semiclassical approach, the magnetic moment  $\mu_m$  can be related to the angular momentum  $L$  of electrons as follows:

$$\mu_m = -\gamma L \tag{2.14}$$

where  $\gamma = \frac{g\mu_B}{\hbar}$  is the gyromagnetic ratio,  $g$  is the Landé-factor ( $g \approx 2$ ),  $\mu_B$  is the Bohr magnetron and  $\hbar$  is the reduced Planck constant. By applying the momentum theorem one can express Eqn. 2.13 as the rate of change of angular momentum  $L$ :

$$\frac{dL}{dt} = \mu_m \times H_{eff} \tag{2.15}$$

Using Eqn. 2.14 the above expression reduces to

$$\frac{d\mu}{dt} = -\gamma\mu \times H_{eff} \tag{2.16}$$

Here, the effective magnetic field  $H_{eff}$  is a sum of all external and internal magnetic fields:

$$H_{eff} = H_0 + h(t) + H_{ex} + H_{dem} + H_{ani} \quad \dots\dots\dots(2.17)$$

$H_0$  is the applied bias magnetic field,  $h(t)$  is the dynamic component,  $H_{ex}$  is the exchange field and  $H_{dem}$  represents the demagnetization field created by the dipolar interaction of magnetic surface and volume charges. The field  $H_{ani}$  includes all kinds of anisotropic fields described above.

In the continuum limit, the atomic magnetic moment can be replaced by the macroscopic magnetization  $M$  resulting in the equation of motion, i.e., Landau-Lifshitz (LL) equation:

$$\frac{dM}{dt} = -\gamma M \times H_{eff} \quad \dots\dots\dots(2.18)$$

Physically, the above equation features a continuum precession which means that the system is non-dissipative. To avoid this impractical situation, Landau and Lifshitz proposed the damping term to be

$$-\lambda m \times (m \times H_{eff})$$

Later, Gilbert introduced another damping term into the LL equation resulting in the so called Landau-Lifshitz-Gilbert (LLG) equation as:

$$\frac{dM}{dt} = -\gamma M \times H_{eff} + \frac{\alpha}{M_S} \left( M \times \frac{dM}{dt} \right) \quad \dots\dots\dots(2.19)$$

Here  $\alpha$  is the dimensionless Gilbert damping parameter. An interesting aspect of this parameter is its viscous nature, i.e. an increase in rotation of magnetization  $dM_S/dt$  increases the damping of the system.

Figure 2.1 schematically illustrates the interplay between different torques acting on the magnetization vector. The precessional torque (the first term on the right hand side of Eqn. 2.19) acts tangentially to the circle traced by the tip of the magnetization vector, while the damping torque (the second term) acts radially to align the magnetization along the effective magnetic field. The mechanism of damping primarily arises from the spin orbit interaction [11] and therefore the damping parameter  $\alpha$  is a material property. Other than spin orbit interaction, different external channels, namely, magnon-electron scattering [12], eddy currents [13], spin pumping [14], multi-magnon scattering [15-16] etc., may also take part in the relaxation of magnetization precession amplitude.

In 1930, the idea of spin waves (SWs) was introduced by Bloch [3] in order to describe the reduction of the spontaneous magnetization in a ferromagnet. At absolute zero temperature, all the atomic magnetic moments of a ferromagnet are aligned in the same direction (as shown in Fig. 2.2a), which is the ground state of the system. As the temperature rises, the thermal agitation perturbs the spontaneous magnetization causing a deviation of the spins from the aligned direction. This phase of the disturbance propagates through the system in the form of a wave as depicted in Fig. 2.2b and 2.2c.

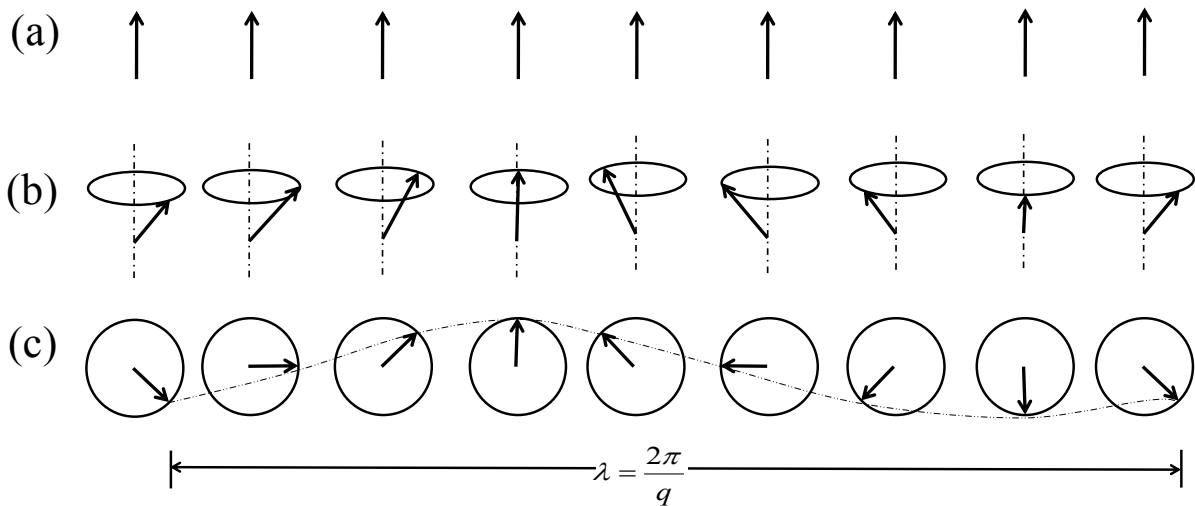


Figure 2.2: Semiclassical representation of spin wave in a ferromagnet: (a) the ground state (b) a spin wave of precessing magnetic moments and (c) the spin wave (viewed from above) showing a complete wavelength.

In case of uniform precession in presence of a magnetic field, the spins of the system precess in phase about the field direction, i.e. the wavelength (wave vector) of SW is nearly infinity (zero). By solving LLG equation (Eqn. 2.19) the frequency of uniform precession (known as Ferromagnetic Resonance or FMR frequency) can be obtained by setting  $\frac{dM}{dt}$  equal to zero. For a thin magnetic film, the corresponding solutions were calculated by Kittel [2] and is given by,

$$\omega^2 = \gamma [H + (N_y - N_x)4\pi M_s] [H + (N_z - N_x)4\pi M_s] \dots\dots\dots(2.20)$$

Here  $N_x$ ,  $N_y$  and  $N_z$  are the demagnetizing factors in the x, y and z directions respectively and the magnetic field is applied along the z axis.

On the other hand, the non-uniform precession is signified as the propagation of phase shift across the spin system and hence the mutual interactions between the moments play a crucial role in determining the wavelength, frequency and overall dispersion behavior of the SW. In the long wavelength regime, the phase difference between consecutive spins is rather small, the SW energy is primarily dominated by dipolar energy and the SWs are referred to as dipolar-dominated or magnetostatic SWs. In contrast, the short wavelength SWs are governed by exchange interaction and known as exchange SWs.

The characteristics of magnetostatic SWs were first reported by Damon and Eshbach [17] in 1961. The dipolar interaction being anisotropic, the frequency, amplitude and propagation properties of magnetostatic modes strongly depend on the geometry of their propagation direction with respect to the applied field and the film plane. When both the applied field and the SW wave vector lie in the film plane and are perpendicular (parallel) to each other, a magnetostatic surface mode (magnetostatic backward volume mode) appears. On contrary, if the magnetic field is applied out of the film plane and SW propagates parallel to the surface, it is known as magnetostatic forward volume mode. In this thesis, the SWs were investigated for the bias field applied in plane. Therefore, the discussion is limited to the former two cases only. The frequency vs. wave vector dispersion characteristics of these modes are presented in Fig. 2.3. The magnetostatic surface wave (MSSW) mode, also known as Damon and Eshbach mode (DE), shows a positive dispersion starting from the Kittel mode at zero wave vector. This mode is further characterized by the localization of SW amplitude in the vicinity of the top and bottom surfaces along with its nonreciprocal behavior, i.e. the propagation is possible for either positive or negative direction of the wave vector for each surface. In absence of any exchange interaction and magnetic anisotropy, the dispersion relation of the DE mode is given by [18],

$$f_{DE} = \frac{\gamma}{2\pi} \left[ H_0 (H_0 + M_S) + (2\pi M_S)^2 (1 - e^{-2q_{||}d}) \right]^{\frac{1}{2}} \dots\dots\dots(2.21)$$

where  $q_{||}$  is the in-plane component of the wave vector and  $d$  in the thickness of the film.

In case of magnetostatic backward volume waves (MSBVW), the SW amplitude prevails throughout the thickness of the sample and the dispersion features a negative slope (group and phase velocities are in opposite directions). The corresponding dispersion relation is given by [19]

$$f_{MSBVM} = \frac{\gamma}{2\pi} \left[ H_0 \left( H_0 + 4\pi M_s \frac{1 - e^{-q_{\parallel}d}}{q_{\parallel}d} \right) \right]^{\frac{1}{2}} \dots\dots\dots(2.22)$$

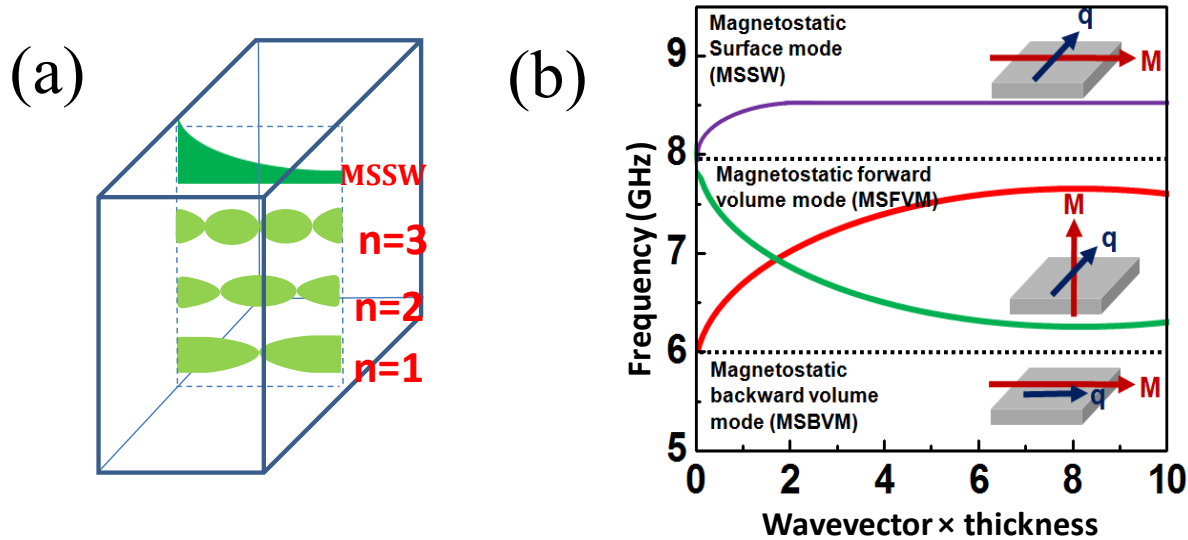


Figure 2.3: Schematics of (a) perpendicular standing spin wave mode (PSSW) and magnetostatic surface spin wave mode (MSSW) are shown for a ferromagnetic thin film. (b) The dispersion relations for three different types of magnetostatic SWs modes.

### 2.3.1. Exchange Spin Waves

When the wave vector of SW is increased (wavelength is decreased), the exchange interaction comes into play. Basically, the exchange interaction becomes dominant when the SW wavelength is of the order of the exchange length which is given by

$$l_{ex}(r) = \sqrt{\frac{2A}{\mu_0 M_s^2}} \dots\dots\dots(2.23)$$

where  $A$  is the exchange constant. It is worth to note that the exchange dominated SW mode does not depend on the relative orientation of the wave vector and magnetic field. The SW dispersion relation with dipolar-exchange interactions taken into account is given by [15]

$$f = \frac{\gamma}{2\pi} \left[ \left( H_0 + 2\pi M_S q_{\parallel} d \sin^2 \phi_{q_{\parallel}} + \frac{2A}{M_S} q_{\parallel}^2 \right) \left( H_0 + 4\pi M_S - 2\pi M_S q_{\parallel} d + \frac{2A}{M_S} q_{\parallel}^2 \right) \right]^{\frac{1}{2}} \dots\dots\dots(2.24)$$

where  $\phi_{q_{\parallel}}$  is the angle between the applied field  $H_0$  and  $q_{\parallel}$ .

In addition to  $q_{\parallel}$  it is also possible to excite SWs which propagate perpendicular to the film plane to form perpendicular standing spin waves (PSSW) (Fig. 2.3a). For a film of thickness  $d$ , the wave vector of PSSW mode can be written as

$$q_{\perp} = \frac{n\pi}{d} \dots\dots\dots(2.25)$$

Their dynamic magnetization profile is sinusoidal and depends on their quantization number  $n$ :

$$m_n(z) = a_n \cdot \cos \left[ q_{\perp, n} \left( z + \frac{d}{2} \right) \right], \quad -\frac{d}{2} < z < \frac{d}{2} \dots\dots\dots(2.26)$$

where  $z$  denotes the coordinate along the film thickness. The above equation actually describes a standing mode consisting of two counter propagating waves with quantized wave vectors. Without considering the contribution of in-plane wave vector, the frequency for the PSSW mode is given by [20]

$$f = \frac{\gamma}{2\pi} \left\{ \left( H_{eff} + \frac{2A}{M_S} q_{\perp}^2 \right) \times \left( H_{eff} + 4\pi M_{eff} + \frac{2A}{M_S} q_{\perp}^2 \right) \right\}^{1/2} \dots\dots\dots(2.27)$$

### 2.3.2. Confined Spin Wave Modes in Magnetic Structures

In the discussion above, we have dealt with the properties of SWs in infinite thin film. In case of a confined structure, the spectrum of SW is modified by the boundary conditions imposed by the lateral dimensions [21]. In particular, the SW finds a propagation channel [22] or form standing waves [23] in the distribution of ‘potential wells’ defined by the geometry of the structure. The formation of standing wave often leads to localized mode or quantized mode (with multiple quantization numbers) when the feature dimensions are of the order of the wavelength of the SW. Overall, the number of SW modes increases whose properties are strongly dependent on the system

geometry as well as on the orientation of the magnetic field. The structural confinement also affects the dispersion relation, resulting in a number of allowed and forbidden magnonic bands in case of periodic patterning (Magnonic crystal or MC) [24]. The band structure of MC consists of several Brillouin Zones, which provides the flexibility to mould the SW properties by changing the external structuring. Nevertheless, the estimation of the magnonic band structure in a MC is not trivial. In this thesis, we have used plane wave method to numerically calculate the magnonic band structure of a MC which will be described in subsequent chapter.

## 2.4. Magneto-Optical Kerr Effect (MOKE)

The phenomenon of magneto-optical effect was first discovered by Michael Faraday in 1845, when he observed that the magnetic moment of a material have influence on the polarization of light wave. He observed that the plane of polarization of a linearly polarized light is rotated when the light is transmitted through a magnetized material. Later on John Kerr observed a similar rotation of polarization in reflected light as well [25]. Upon reflection from a magnetized sample, a plane polarized light is converted to an elliptically polarized light, which is known as Kerr effect and the corresponding rotation of the plane of polarization (i.e. the major axis of the ellipse) is called the Kerr rotation. Since its discovery, the Kerr effect has been widely embraced to study the quasistatic and dynamic properties of magnetic systems. Figure 2.4a schematically depicts the Kerr rotation ( $\theta_k$ ) and ellipticity ( $\varepsilon_k$ ), which are proportional to the magnetization of the sample. If  $r$  and  $k$  denote the parallel and perpendicular electric vector components of the reflected light with respect to that of the incident light, then the following relation is satisfied:

$$\theta_k + i\varepsilon_k = \frac{k}{r}, \text{ where } k \ll r. \quad \dots\dots\dots(2.28)$$

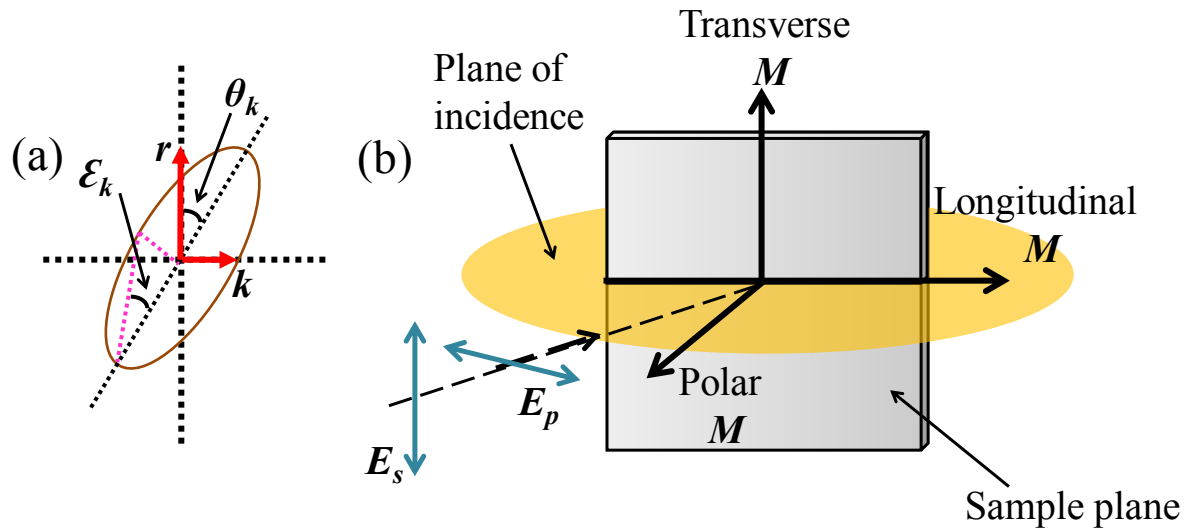


Figure 2.4: (a) Geometry of the Kerr rotation ( $\theta_k$ ) and Kerr ellipticity ( $\epsilon_k$ ). (b) Schematics of polar, longitudinal and transverse MOKE geometries are shown.

### 2.4.1. Origin of Magneto-Optical Kerr Effect

The origin of magneto-optical Kerr effect can be described in the context of either macroscopic dielectric theory or microscopic quantum theory. Macroscopically, magneto-optic effects arise from the antisymmetric, off-diagonal elements in the dielectric tensor. The dielectric tensor plays a role in determining the optical properties of a medium which are associated with the motion of its electrons. When a light propagates through a medium, the movement of its electrons follows the electrical field of the light. Thus for a linearly polarized light, the response of the electrons can be conceived as a combination of left and right circular motions, the radii of the circles being equal. Since the electric dipole moment is proportional to the radius of the circular orbit, it will be same for the left- and right-circularly polarized light and hence no Faraday rotation will be there. Now, in presence of a magnetic field, there will be an additional Lorentz force acting on the electrons. This force acts on the left and right circular motions of electrons in the opposite ways, pointing towards or away from the center of the circle. Thus, the radius for left circular motion will be reduced and that for right circular motion will expand, or vice versa, depending on the direction of magnetic field. The difference in the radii of left and right circularly polarized light will give a finite difference in dielectric constants which leads towards the magneto-optical Kerr effect (MOKE). The difference in the dielectric constants also affects the refractive indices for the two

circularly polarized lights, which is responsible for the phase difference between the orthogonal components of the reflected light (Eqn. 2.28).

The quantum mechanical description, on contrary, stresses on the spin-orbit interaction that couples the electron spin to its motion to give rise to the Kerr effect in a ferromagnetic. The movement of electrons under the influence of the electric field vector of light affects the spin-orbit interaction, which can be thought of as an effective magnetic field vector potential  $\sim s \times \nabla V$ ,  $s$  and  $\nabla V$  being the electron spin and the electric field respectively, acting on the motion of the electron. This effect is present in all materials, however not so prominent in non-magnets, because of the presence of equal amount of up and down spins canceling the effect. For ferromagnetic materials, the effect manifests itself because of the unbalanced population of electron spins.

### 2.4.2. MOKE Geometries

There are three types of MOKE geometry, namely, polar, longitudinal and transverse, which are classified depending upon the orientation of magnetization with respect to the sample surface and plane of incidence. Figure 2.4b shows the relative orientations of the magnetization, plane of incidence and polarization direction in different MOKE geometries.

In polar MOKE, the magnetization is perpendicular to the sample surface and parallel to the plane of incidence. Since the plane of polarization of both p-polarized light (polarization parallel to the plane of incidence) and s-polarized light (polarization perpendicular to the plane of incidence) is always perpendicular to the magnetization, irrespective of the angle of incidence, a Lorentz force always exists and hence Kerr rotation occurs. The polar configuration is generally used to study thin films, which exhibit perpendicular magnetic anisotropy. During the experiments, light is incident normal to the sample surface.

In the longitudinal Kerr effect, the magnetization lies in the plane of the sample and parallel to the plane of incidence. Unlike the polar geometry, the longitudinal Kerr effect depends upon the angle of incidence. In case of normal incidence, the Kerr effect is absent because either the Lorentz force vanishes (for p-polarized light) or points along the direction of the light (for s-polarized light). The measurements are performed by keeping the angle of incidence in between  $5^\circ$  and  $60^\circ$ .

The transverse MOKE geometry occurs when the magnetization ( $M$ ) is perpendicular to the plane of incidence and parallel to the reflection surface. Here also no Kerr effect is observed for normal incidence of light. Moreover, in case of oblique incidence, the polarization does not change, since there is either no Lorentz force present (for s-polarized light) or the direction of polarization of the induced component is same as the incident polarization (for p-polarized light). Instead, the transverse effect is associated with a change in the intensity of the reflected light when magnetization changes its orientation. The change in the intensity is dependent upon the component of magnetization perpendicular to the plane of incidence.

## References

- [1] P. Weiss, "L'hypothèse du Champ Moléculaire et la Propriété Ferromagnétique," *J. Phys. Theor. Appl.* **6**, 661 (1907).
- [2] C. Kittel, "On the theory of ferromagnetic resonance absorption," *Phys. Rev.* **73**, 155 (1948).
- [3] F. Bloch, "Zur theorie des ferromagnetismus," *Z. Phys.* **61**, 206 (1930).
- [4] A. H. Morrish, "The Physical Principles of Magnetism," IEEE Press, New York, United States, (2001).
- [5] T. Moriya, "Anisotropic superexchange interaction and weak ferromagnetism," *Phys. Rev.* **120**, 91 (1960).
- [6] P. Bruno, "Physical Origins and Theoretical Models of Magnetic Anisotropy," Jürich, (1993).
- [7] N. Nakajima, T. Koide, T. Shidara, *et al.*, "Perpendicular Magnetic Anisotropy Caused by Interfacial Hybridization via Enhanced Orbital Moment in Co/Pt Multilayers: Magnetic Circular X-Ray Dichroism Study," *Phys. Rev. Lett.* **81**, 5229 (1998).
- [8] S. Pal, B. Rana, O. Hellwig, *et al.*, "Tunable magnonic frequency and damping in [Co/Pd]<sub>8</sub> multilayers with variable Co layer thickness," *Appl. Phys. Lett.* **98**, 082501 (2011).
- [9] L. Landau and E. Lifshits, "On the theory of the dispersion of magnetic permeability in ferromagnetic bodies," *Phys. Z. Sowjet.* **8**, 153 (1935).
- [10] T. Gilbert, "A phenomenological theory of damping in ferromagnetic materials," *IEEE. Trans. Magn.* **40**, 3443 (2004).

- [11] H. Suhl, "Theory of the magnetic damping constant," *IEEE Trans. Magn.* **34**, 1834 (1998).
- [12] V. Kambersky and C. Patton, "Spin-wave relaxation and phenomenological damping in ferromagnetic resonance," *Phys. Rev. B.* **11**, 2668 (1975).
- [13] B. Heinrich, R. Urban, and G. Woltersdorf, "Magnetic relaxation in metallic films: Single and multilayer structures," *J. Appl. Phys.* **91**, 7523 (2002).
- [14] J. Z. Sun, B. Ozyilmaz, W. Chen, *et al.*, "Spin-transfer-induced magnetic excitation: The role of spin-pumping induced damping," *J. Appl. Phys.* **97**, 10C714 (2005).
- [15] R. Arias and D. L. Mills, "Extrinsic contributions to the ferromagnetic resonance response of ultrathin films," *Phys. Rev. B.* **60**, 7395 (1999).
- [16] H. Schultheiss, K. Vogt, and B. Hillebrands, "Direct observation of nonlinear four-magnon scattering in spin-wave microconduits," *Phys. Rev. B.* **86**, 054414 (2012).
- [17] R. W. Damon and J. R. Eshbach, "Magnetostatic Modes of a Ferromagnetic Slab," *J. Phys. Chem. Solids.* **19**, 308 (1961).
- [18] S. O. Demokritov, B. Hillebrands, and A. N. Slavin, "Brillouin Light Scattering Studies of Confined Spin Waves: Linear and Non Linear Confinement," *Phys. Rep.* **348**, 441 (2001).
- [19] B. A. Kalinikos and A. N. Slavin, "Theory of dipole-exchange spin wave spectrum for ferromagnetic films with mixed exchange boundary conditions," *J. Phys. C* **19**, 7013 (1986).
- [20] M. Cottam and D. Lockwood, "Light Scattering in Magnetic Solids," Wiley, New York, (1986).
- [21] K. Y. Guslienko and A. N. Slavin, "Boundary conditions for magnetization in magnetic nanoelements," *Phys. Rev. B* **72**, 014463 (2005).
- [22] R. Mandal, S. Saha, D. Kumar, *et al.*, "Optically Induced Tunable Magnetization Dynamics in Nanoscale Co Antidot Lattices," *ACS Nano.* **6**, 3397 (2012).
- [23] C. Yu, M. J. Pechan, W. A. Burgei, *et al.*, "Lateral standing spin waves in permalloy antidot arrays," *J. Appl. Phys.* **95**, 6648 (2004).
- [24] Z. K. Wang, V. L. Zhang, H. S. Lim, *et al.*, "Nanostructured Magnonic Crystals with Size-Tunable Bandgaps," *ACS Nano.* **4**, 643 (2010).
- [25] J. Kerr, "On Rotation of the Plane of Polarization by Reflection from the Pole of a Magnet," *Philos. Mag. Series 5.* **3**, 321 (1877).

## Chapter 3

# 3. Experimental techniques

---

### 3.1. Introduction

This chapter provides an overview over the fabrication, characterization and experimental techniques that have been employed in the course of present thesis work. For the successful implementation of nano-magnetic systems in the future technology, it is very crucial to fabricate good quality thin films and confined structures with minimum structural and compositional defects. Essentially, at nanoscale, the intrinsic magnetic properties of a material strongly depend upon the surface quality, combined with the microstructure and chemical order. Hence, a detailed characterization is also necessary to examine and optimize the respective magnetic parameters.

For the works presented in this thesis, the thin films were grown by magnetron sputtering and e-beam evaporation technique while the patterning is done using electron beam lithography. The crystal structure, surface morphology and the chemical purity of the nanostructures were characterized by using X-ray diffraction (XRD), scanning electron microscopy (SEM), transmission electron microscopy (TEM), atomic force microscopy (AFM) and energy dispersive x-ray spectroscopy (EDX). On the other hand, the static and quasistatic magnetic properties of the nanomagnets were studied using magnetic force microscopy (MFM), magneto-optical Kerr effect magnetometry (MOKE) and vibrating sample magnetometry (VSM). We have further employed the Brillouin Light Scattering (BLS) and time-resolved magneto optical Kerr effect microscope (TR-MOKE) to investigate the magnetization dynamics. The BLS set up can additionally be equipped so as to observe the spin dynamics with space, time and phase resolution. Both these techniques rely on magneto-optical interactions, which are different from electrical characterization methods (like Ferromagnetic Resonance or FMR) which does not allow for a space resolution on the microscale. In the following, we briefly discuss the principles and advantages of the aforementioned techniques.

## 3.2. Fabrication Techniques

### 3.2.1. Sputtering

The sputtering is a Plasma Vapor Deposition (PVD) technique which is used to deposit good quality thin films and multilayers [1]. It is a multiple collision process where the positive ions of a gaseous plasma are accelerated and used to dislodge and eject atoms from source (target) material. These eroded atoms (or cluster of atoms) then condense over the substrate to form a thin film of desired parameters. The sputtering process is schematically shown in Fig. 3.1.

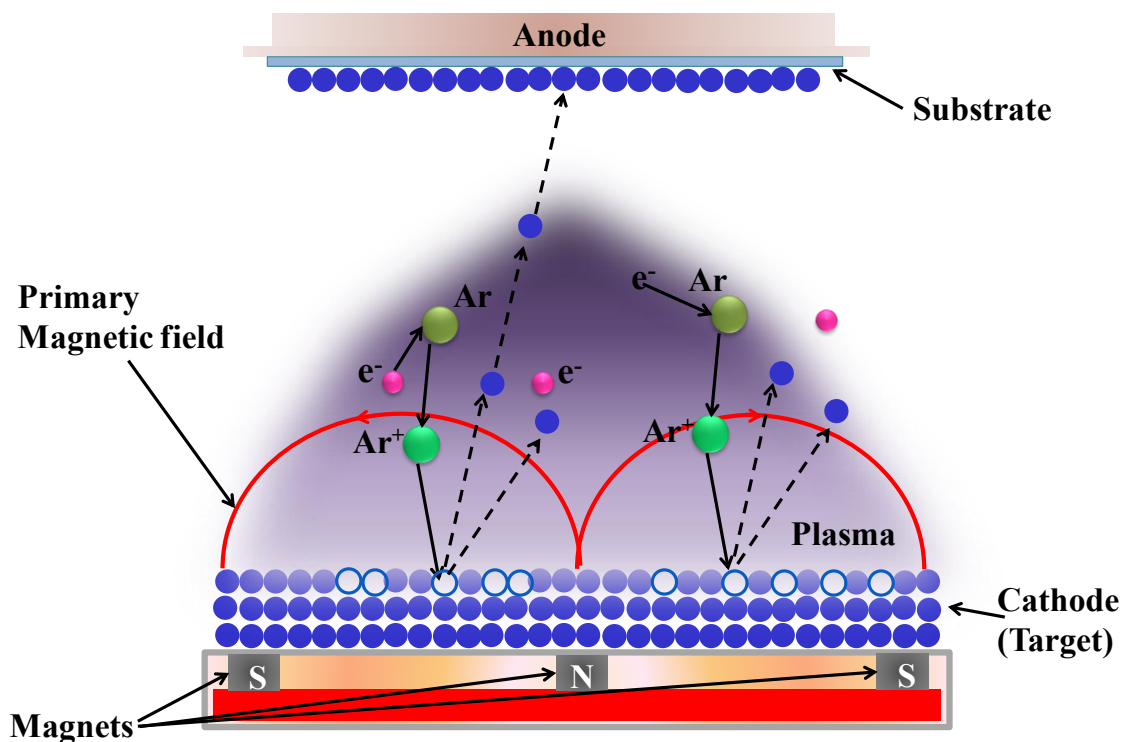


Figure 3.1: Schematic of the sputtering technique.

At the beginning, an inert gas (generally Ar) is introduced into a pre-pumped vacuum chamber. In the next step, a gaseous plasma is created and sustained inside the chamber using a high energy source (ranging from a few hundred to a few thousand electron volts). Here the cathode or target is composed of the material or alloy to be deposited and the substrate serves as the anode. Depending on whether the target material is conductive or non-conductive, a direct current (DC) or radio frequency (RF) power supply can be used. The plasma is described as the

fourth state of matter where neutral gas atoms, ions, electrons and photons exist in a nearly balanced state simultaneously. As soon as the power supply is on, the free electrons present in the plasma immediately accelerates away from the negatively charged cathode. The accelerated electrons then collide with the neutral gas atoms in their path, driving them off their electrons, therefore leaving the positively charged ions (i.e.  $\text{Ar}^+$ ). At this point the positively charged ions are accelerated into the target to strike its surface and eject neutral atoms and electrons (which further feed the formation of ions and the continuation of the plasma) out of it. These ejected atoms then travel in a typical line-of-sight cosine path and gets subsequently deposited on the substrate which is kept in proximity with the target.

This conventional sputtering technique suffers from two major problems of slow deposition rate and overheating of the target (due to extensive electron bombardment). One way to address these issues is to use magnetron sputtering. In this case magnets are used behind the cathode to trap the free electrons in a cyclic path just above the cathode. This way not only the probability of ionizing neutral gas molecules increases (this in turn enhances the deposition rate) but also the velocity of electrons near the target decreases. As a result, it is possible to deposit layered structures in lesser time and with lower substrate temperature.

### 3.2.2. Electron Beam Lithography (EBL) and Electron Beam Deposition

Lithography technique is popular for fabricating fine structures onto a substrate. Typically, different kinds of radiation, such as optical, electron beam, X-ray and ion beam are exposed to a medium known as resist to draw the pattern of ordered arrays of nanostructures. Later on, the desired material is deposited which follows the footprint of the patterned resist to render the final structure.

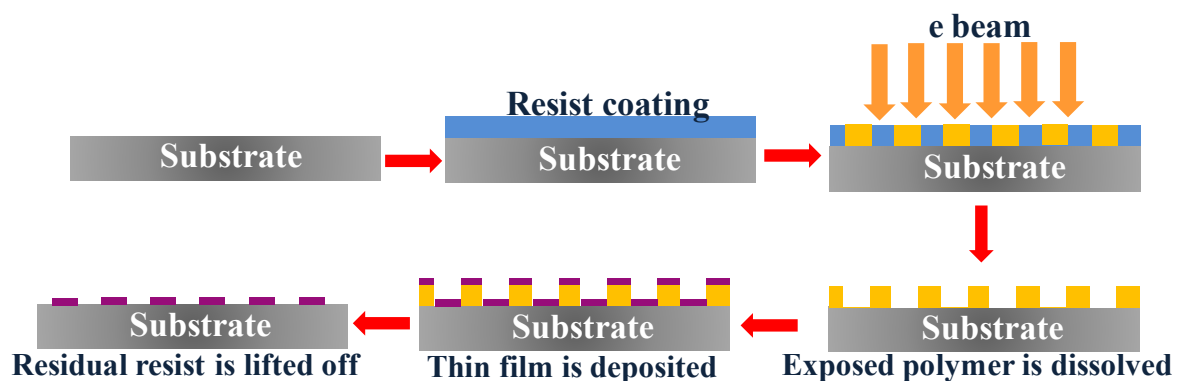


Figure 3.2: Schematic diagram of electron beam lithography process.

The electron beam lithography technique (EBL) is widely used for the fabrication of two dimensional arrays with submicron features. The fact that high energy electron beam possesses much shorter wavelength than that of light is responsible for the resolution as high as tens of nanometers. This technique is composed of the following fundamental steps (See Fig. 3.2): i) Firstly, a pre-cleaned substrate is spin-coated with bilayer polymethyl methacrylate (PMMA 495K and 950K) positive tone e-beam resist. The coating of two layers actually helps in achieving an undercut edge profile of the resist after development of the pattern onto it. ii) Then this resist is exposed to focused electron beams inside a scanning electron microscope connected with a computer. In this step the desired structure is drawn using commercially available design software (Auto CAD). Subsequently, this design is printed onto the resist layers by accelerated electron beam controlled by the computer. iii) After writing, the resist is developed in methyl isobutyl ketone (MIBK) and isopropyl alcohol (IPA), MIBK:IPA :: 1:3, solution, followed by rinsing in water. iv) Next the desired material is deposited on top of the developed resist. v) Finally, the lift off is done in acetone using ultrasonic agitation to remove the unexposed resist along with the film deposited on it.

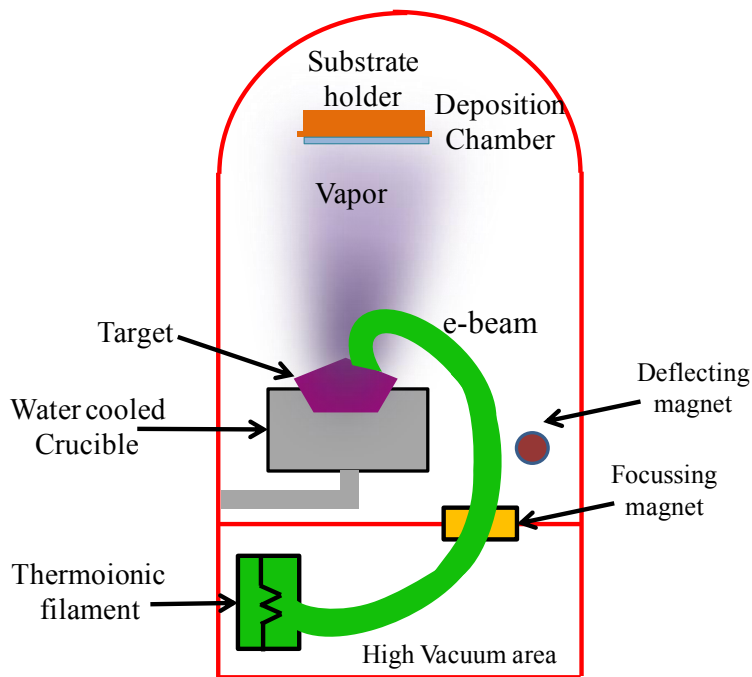


Figure 3.3: Schematic diagram of electron beam evaporation technique.

In this thesis, the material used for the studied patterned structures is Permalloy (NiFe), which was deposited using electron beam (e-beam) evaporation process. The e-beam evaporation technique is a kind of physical vapor deposition technique and is schematically shown in Fig 3.3. Here the material to be deposited is kept in a water cooled graphite crucible which is placed inside an evacuated chamber. A beam of electron generated by a hot tungsten filament by thermoionic emission is guided and focused onto the material with the help of deflecting and focusing magnets. The focused beam heats the sample to its boiling point. The vapor of the material moves towards the substrate which is loaded on a sample holder and gets condensed all over its surface. The sample holder is mounted on a rotation motor, which rotates during the deposition, in order to obtain a uniform deposition.

### 3.3. Characterization Techniques

#### 3.3.1. Scanning Electron Microscopy (SEM)

A scanning electron microscope (SEM) [2] is used to characterize the surface topography and morphology of samples by scanning it with a focused beam of electrons. The electrons in the beam interact with the sample, producing various signals which provide the information about the surface texture and composition. The advantage of this tool over the conventional optical microscopy lies in its high resolution ( $\sim 1$  nm), owing to the much shorter de Broglie wavelength of electrons.

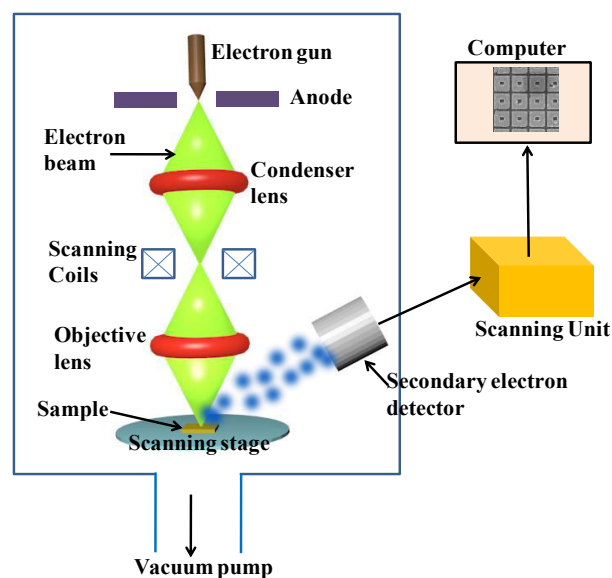


Figure 3.4: Schematic diagram of Scanning Electron Microscope.

In a typical SEM, a stream of accelerated electrons is generated from a cathode either by using thermionic emission or an electric field (See Fig. 3.4). The beam is then focused by one or two electromagnetic condenser lenses. Subsequently, the beam passes through pair of scanning coils or deflector plates, which can deflect the beam inside a two dimensional rectangular region of the sample surface so as to scan it in a raster fashion. As the electrons hit the sample surface, they lose energy due to scattering and absorption within the interaction volume. This leads to the generation of variety of signals, which can be detected by specialized detectors. These signals include secondary electrons (that produce SEM images), backscattered electrons (due to elastic scattering), auger electrons, transmitted electrons, photons (characteristic X-rays that are used for elemental analysis and continuum X-rays), visible light (cathodoluminescence–CL), and heat. Finally, a two-dimensional image is generated for the selected area of the sample surface, which displays the spatial variations of the intensity of secondary electrons *w.r.t.* that of the incident electrons. Due to the very narrow electron beam, SEM micrographs have a large depth of field, rendering the capability of producing three-dimensional images useful for understanding the surface structure of a sample. However, to prevent any scanning faults and other image artifacts the specimens should be electrically conductive at the surface and electrically grounded, because a nonconductive surface accumulates electric charge when scanned by the electron beam.

### **3.3.2. Transmission Electron Microscopy (TEM)**

The transmission electron microscope (TEM) operates on the same basic principles as SEM, however, rather than scattered electrons, it works on the electrons transmitted through ultra-thin specimens, which can be analyzed to observe features such as the crystal structures and their defects, grain boundaries, layer growth and compositions. Therefore, preparation of TEM specimen is a crucial job to make the sample cross section equivalent to the mean free path of the electron beam. Here the beam of electrons, focused by the condenser lens strikes the specimen where parts of it are transmitted depending upon the thickness and electron transparency of the specimen. This transmitted part has an imprint of the sample, which can be detected and imaged using fluorescence or CCD camera. While the electron beam passes through the sample, they are scattered by the electrostatic potential of the constituent elements in the specimen. This is manifested as diffraction pattern on the TEM micrograph, which can be a measure of the periodicity of the atomic arrangement of the sample. Finally, a two or three dimensional image of

the specimen profile is formed, where the image contrast can be varied by varying the mode of operation, such as bright field mode, dark field mode, phase contrast mode etc. Lastly, although this technique facilitates the inspection of the finer details of the sample even down to atomic level, the facts like extensive sample preparation, relatively small field of view, potential of damaging the sample (especially biological samples) limit its wide range application.

### 3.3.3. Energy-Dispersive X-ray Spectroscopy (EDX)

This technique is a powerful tool for the elemental analysis and chemical characterization of a sample. Generally, it is used in conjunction with electron microscopes or x-ray spectrometers. The schematic of an EDX spectrometer is illustrated in Fig. 3.5.

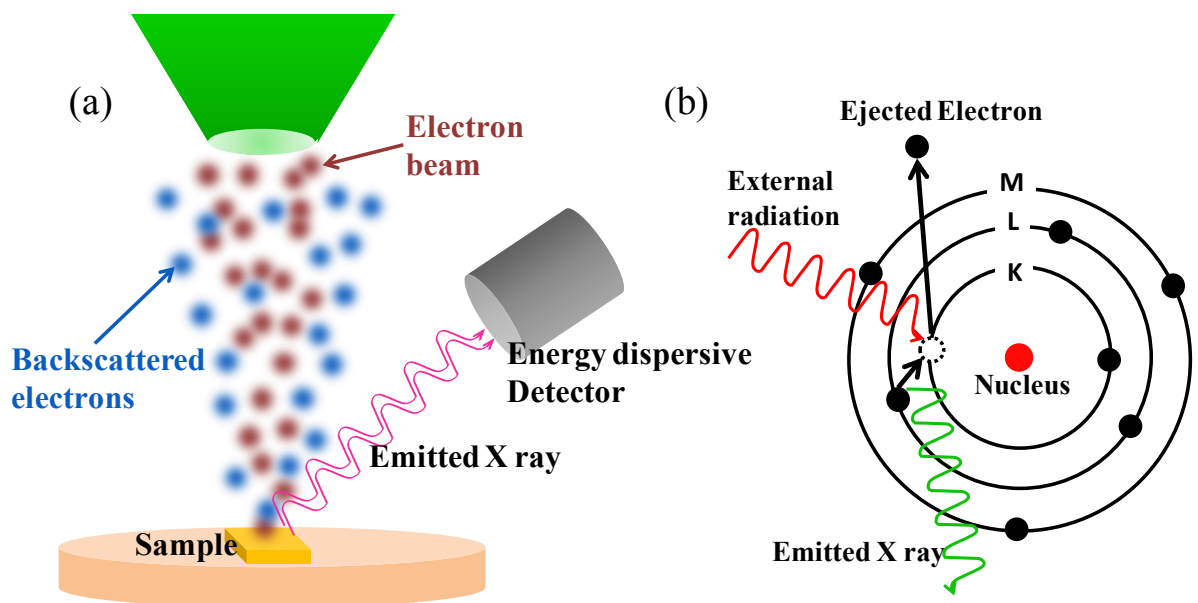


Figure 3.5: (a) Schematic of EDX spectrometer. (b) Interaction of accelerated electrons with sample and emission of X-rays.

The principle of operation relies on the phenomenon that each element possesses a unique atomic structure as well as emission spectrum, which can be utilized to recognize the elements present in the specimen. Basically, at ground state, an atom contains a number of electrons moving around the nucleus while arranged in discrete characteristic shells. As a high energy beam of charged particles (like electrons, protons or x-ray) hits the sample, it excites and ejects out electrons from an inner shell and creates electron-hole. The electrons from outer, high energy shells then jump to the inner shell to fill the hole where the difference in the two energy shells is emitted

in the form of an X-ray. A Si (or Li) detector is used as an energy dispersive spectrometer to measure the energy and number of the emitted X-rays. The elements are identified from the peak energy values of the X-rays and the relative heights of the peaks give the atomic percentage of the elements in the sample.

### 3.3.4. X-ray Diffraction (XRD) Analysis

The XRD technique [3] investigates the crystalline material structure, including atomic arrangement, crystallite size and imperfections. Here a beam of X-rays (wavelength  $\sim 1.5418 \text{ \AA}$ ) is incident on the sample and is diffracted by the crystalline atoms. By measuring the angles and intensities of these diffracted beams, one can determine the atomic arrangement, its disorder and various other information.

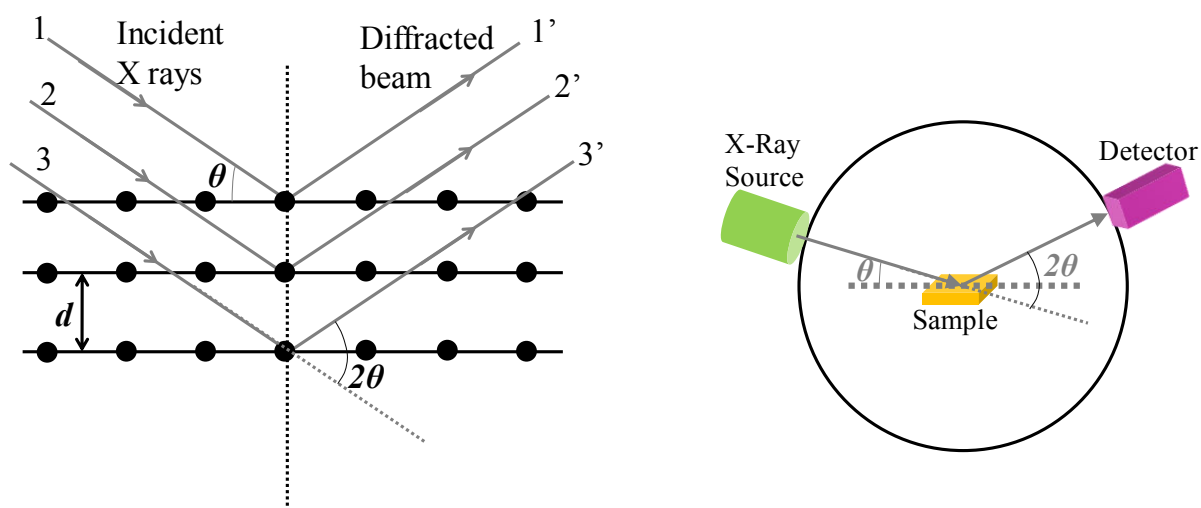


Figure 3.6: Schematic diagram of X-ray diffraction (left panel) and X-ray diffractometer (right panel).

Figure 3.6 presents a schematic of the XRD technique. A crystal can be considered as a regular array of atoms, which can elastically scatter electromagnetic waves like x-rays. The scattered beams form secondary waves which can interfere constructively at certain directions according to the Bragg's condition:

$$2d \sin \theta = n\lambda \quad \dots\dots(3.1)$$

Here  $d$  is the spacing between the atomic planes,  $\theta$  is the incident angle,  $n$  is any integer and  $\lambda$  is the wavelength of the X-ray beam. Therefore, for a certain lattice structure (that corresponds to  $d$ ), the diffraction spots appear only at certain angles of incidence. In the measurement, the incident

angle of X-ray is varied between a range of angles in small steps and the corresponding reflected intensities are measured as a function of the angle of the reflected beam with respect to the direction of the incident beam ( $2\theta$ ). Subsequently, the diffraction peaks are converted to d-spacings to identify the elements present in the sample. Typically, this is accomplished by tallying the data with standard reference patterns (i.e. ICSD or Inorganic Crystal Structure Database).

### 3.3.5. Vibrating Sample Magnetometer (VSM)

The VSM technique [4] is employed to measure the magnetic properties of a sample including the magnetic moment, its behavior as a function of applied magnetic field ( $H$ ) and temperature ( $T$ ). It operates on the Faraday's law of induction, which states that a changing magnetic flux through a coil gives rise to an electric field induced in the coil. Mathematically,

$$E_{in} = -n_w A \frac{dB}{dt} \quad \dots\dots\dots(3.2)$$

where  $E_{in}$  is the induced electric field,  $A$  is the area of the coil with number of turns  $n_w$ . Using  $B = \mu_0(H + M)$ , we get for constant magnetic field

$$E_{in} = -n_w A \frac{dM}{dt} \quad \dots\dots\dots(3.3)$$

Since the magnetization  $M$  depends on the total magnetic moment ( $m$ ) and several other factors, Eqn. 3.3 finally reduces to

$$E_{in} \propto -mwzy_0 n_w n_c G \cos(wt) \quad \dots\dots\dots(3.4)$$

where  $w$  and  $z$  are frequency and amplitude of vibration respectively,  $y_0$  is the distance to pick up coils,  $n_c$  is the number of pick up coils and  $G$  is geometric factor of the sample.

This electric field can be used to examine the magnetic moment of a sample. The schematic diagram of the set up is shown in Fig. 3.7. For the measurement, the sample under study is first placed in a constant magnetic field. The magnetic dipole moment of the sample then creates a stray magnetic field around the sample. The sample is actually attached to a piezoelectric transducer assembly, which converts sinusoidal electric signal (generated by an oscillator/amplifier) into a sinusoidal vertical vibration of the sample rod which results in a sinusoidal oscillation of the sample. The resulting oscillation in the sample's magnetic moment induces a voltage in the pick-up coil (located close to the sample) which is independent of the applied field. This way the VSM

technique converts the dipole field of the sample into an ac electrical signal, which can be amplified and measured using a lock in amplifier where the output of the piezoelectric signal serves as the reference signal. Any change in the applied magnetic field or temperature brings about changes in the magnetic dipole moment of the sample, which can be traced to inspect the  $M-H$  or  $M-T$  curves of a ferromagnetic material.

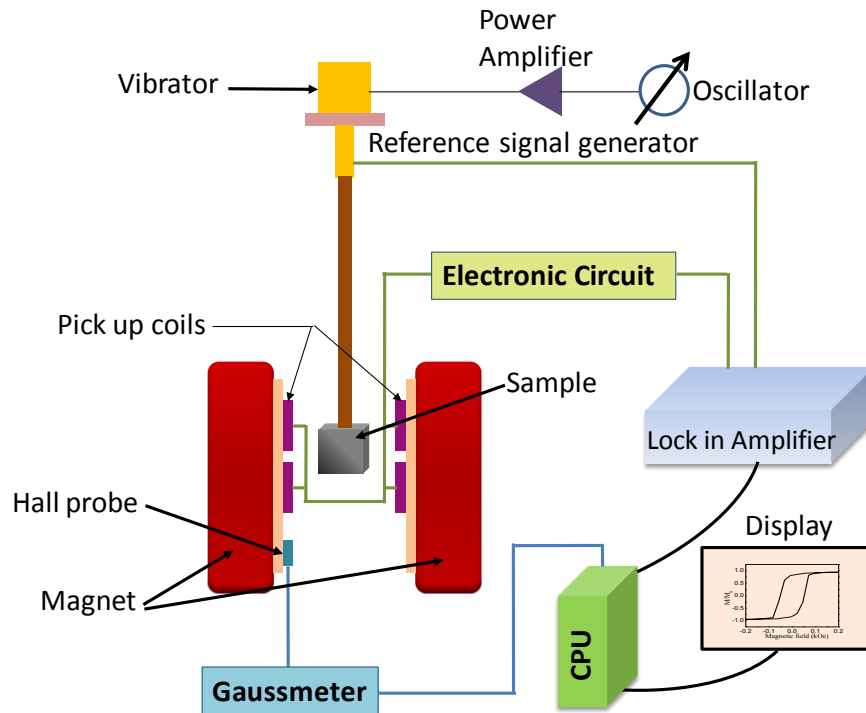


Figure 3.7: Schematic diagram of Vibrating Sample Magnetometer (VSM).

### 3.3.6. Atomic Force Microscopy (AFM) and Magnetic Force Microscopy (MFM)

The atomic force microscope [5] (AFM) is one kind of scanning probe microscope (schematically shown in Fig. 3.8), which are designed to measure local properties, such as morphology, roughness, magnetism etc. The information is acquired by measuring the force between a probe and the sample. Piezoelectric devices enabling small and accurate movements of the sample at nanoscale facilitates very precise scanning, with resolution more than 1000 times of the optical diffraction limit. Normally, the AFM probe consists of a cantilever with a sharp tip at its end. As

the tip is brought into proximity of the sample surface, it experiences vertical and lateral deflections due to forces such as van der Waals forces, capillary forces, chemical bonding, electrostatic forces and magnetic forces. The deflection is mapped by using a laser spot reflected from the top surface of the cantilever. The reflected laser beam strikes a position-sensitive photo-detector consisting of four-segments. The differences between the signals of different segments of photo detector give the estimate of the angular deflections of the cantilever. A two dimensional image of the local properties can then be acquired by performing a raster-scan over a small area of the sample.

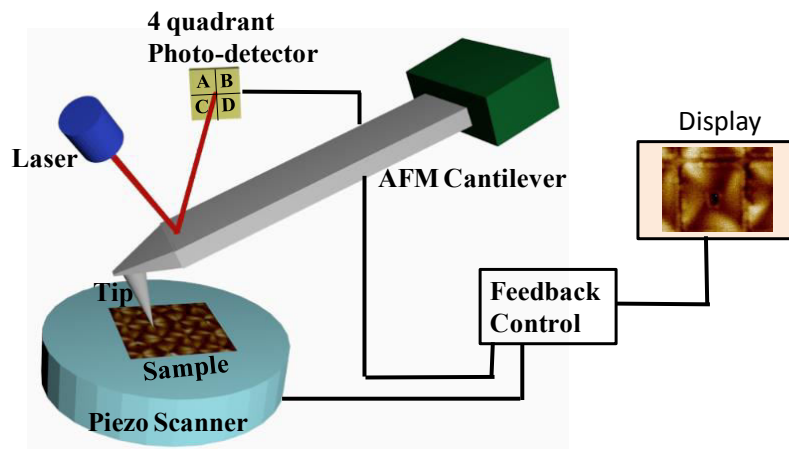


Figure 3.8: Schematic diagram of Atomic Force Microscope.

Depending on the sample surface and the acting force between the probe and the sample, AFM can be operated in one of the three modes, namely

- i) **Contact mode:** The contact mode is also known as static mode AFM, where the tip scans the sample in close contact with its surface, and a constant repulsive force between the tip and the surface is maintained throughout. A feedback amplifier is used to apply feedback voltage to the piezo to sustain this condition during scanning, which determines the height of features on the sample surface. Since such measurement of static signal can cause damage to the sample, low stiffness cantilevers are used to achieve a large enough deflection signal while keeping the interaction force low.
- ii) **Non-Contact Mode:** The non-contact AFM mode is used in situations where tip contact might cause any sample degradation. In this mode the tip hovers few tens of Angstroms above the sample and attractive forces like Van der Waals force is probed to construct

the topographical image of the sample. Because such forces are substantially weaker than the forces in contact mode, the tip is given a small oscillation and the small forces between the tip and the sample is measured by measuring the change in amplitude, phase, or frequency of the oscillating cantilever in response to force gradients from the sample.

- iii) **Tapping Mode:** The tapping mode is the most commonly used AFM mode in ambient conditions. It is implemented by oscillating the cantilever at or near its resonant frequency using a piezoelectric crystal. The tip is then brought close to the sample until it begins to lightly touch, or tap the surface. The intermittent contact of the tip with the surface affects the cantilever oscillation causing an energy loss. The resulting change in oscillation amplitude is used to identify and measure surface features.

As mentioned earlier in this paragraph, AFM imaging technique is capable of measuring a number of forces other than the atomic forces. Amongst them, one popular variant is magnetic force microscopy (MFM), where the tip-sample magnetic interactions are perceived to construct the magnetic structure of the sample surface. Here the cantilever tip is coated with a thin magnetic layer of high coercivity (like Co) so that magnetization state of the tip does not change during imaging. As this tip is brought close to the sample, it senses the magnetic forces as well as the atomic and electrostatic forces. However, to increase the magnetic contrast of the image, the AFM image is first taken. The tip is then lifted further away and scanned again over the sample at that particular height to extract the magnetic signal. Depending on the strength of the stray field from the sample, MFM can operate in static and dynamic mode.

### **3.3.7. Static Magneto-Optical Kerr Effect (Static-MOKE) Magnetometer:**

The static-MOKE technique employs the magneto-optical Kerr Effect and is used for the measurement of magnetic hysteresis loops in continuous and patterned thin films. The basic difference of this technique from VSM is that static-MOKE is a surface sensitive technique and it allows to perform localized measurement of magnetization characteristics in case of non-uniform distribution. The schematic of this set up in our laboratory is shown in Fig. 3.9.

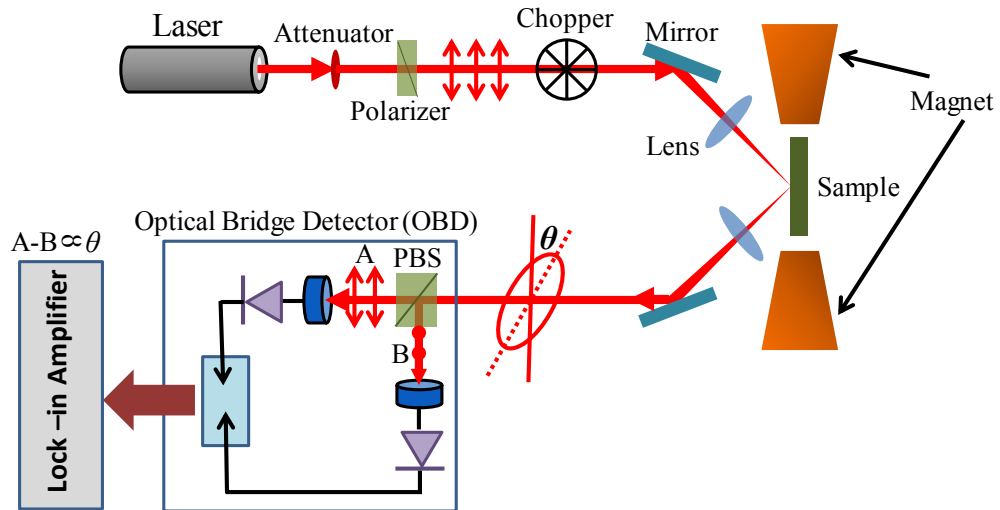


Figure 3.9: Schematic diagram of static magneto-optical Kerr effect (Static MOKE) microscope in longitudinal geometry.

The laser beam from a He-Ne laser (wavelength= 632 nm, power 30 mW) passes through an attenuator and a Glan-Thompson polarizer consecutively. This polarized beam is then chopped at 2 kHz frequency by a mechanical chopper controlled by a controller unit. The signal of the chopper is later used as a reference signal in the lock in amplifier. The chopped beam is then guided to a lens (L1) which focuses the beam onto the sample. The sample is mounted in between the pole pieces of a magnet and the measurement is taken in longitudinal geometry, i.e. the plane of incidence is parallel to the magnetic field direction. The magnetic moment of the sample causes the polarization of the reflected beam to rotate from its initial direction due to Kerr rotation. The reflected beam is then collected by another lens L2 by which the beam is fed to the detector, known as optical bridge detector (OBD). The OBD consists of a polarizing beam splitter (PBS), which splits the beam in two perpendicularly polarized components A and B, two Si-photodiode detectors, to convert the incident light to voltage, and electronic circuitry to obtain the electrical signal via lock in amplifier. In absence of any magnetic field, the OBD is brought to its balanced condition (i.e.  $A=B$ ) by rotating the axis of the polarized beam splitter. As the magnetic field is applied, the detector is no longer balanced (as the polarization of the beam is now changed) and the difference signal  $A-B$ , which is proportional to the magnetization of the sample, is measured as a function of the bias magnetic field to obtain the hysteresis loop. The OBD signal can further be converted to Kerr rotation. To achieve this, the polarizing beam splitter is rotated  $1^\circ$  away from

its balanced condition and the equivalent voltage is recorded, which can be subsequently used as the calibration factor. The hysteresis loop obtained from static-MOKE technique helps to get information like switching field, coercivity, remanence, domain property and anisotropy, which are useful for the sample characterization.

## **3.4. Measurement Techniques**

### **3.4.1. Brillouin Light Scattering**

The light scattering technique has been used for many decades to measure the coherent dynamic properties in gases, liquids, and solids. In this technique, the properties of the scattered light from the sample is characterized and compared to that of the incident light which gives information about the mechanisms that play a role in the scattering process. In the so-called Raman Scattering [6], light interacts with rotational or vibrational degree of freedom of the system. The Brillouin Light Scattering (BLS), named after its inventor, deals with the inelastic scattering of photons from a rather lower frequency (in the order of GHz) excitations, viz, phonons, magnons, plasmons. For instance, using this non-contact and thus non-invasive tool it has been possible to measure the elastic properties in water [7-8], solids [9], as well as organic materials (like eyes lens [10]). Nevertheless, in this thesis our focus will be on the use of BLS to measure spin wave excitations in ferromagnetic structures, such as thin films, multilayers and magnetic nanoelements.

The theoretical prediction of light scattering from acoustic waves was given independently by Léon Brillouin in 1922 [11] and Mandelstam in 1926 [12]. Subsequently after few years in 1930, Gross experimentally confirmed the observation of scattering of light in liquids [13]. Later on, the invention of laser in the 1960s revolutionized this area of research, however, the investigation of acoustic waves and spin waves in optically opaque material became possible only after Sandercock in 1971 developed a highly sophisticated spectrometer [14]. The key to this development was noticing the fact of dramatic enhancement of sensitivity of a Fabry-Perot interferometer if the scattered light passes multiple times through it [15]. Both surface and bulk spin waves were detected in polycrystalline films of Fe and Ni by Sandercock and Wettling using tandem operation of two interferometers [16-17]. In succeeding years, BLS has developed to be a very powerful and versatile tool in magnetic research because of its degree of flexibility in samples, frequency-, phase-, time-resolution, and localized spatial resolution. The other advantages include

(i) the ability to measure the thermal excitations (without any external stimulation), that even upto a frequency range as high as 500 GHz, with a resolution of 50 MHz. (ii) the potential to investigate dispersion of SWs with different absolute values and orientations of their wave vectors. (iii) Further, one can extract rich information about the magnetic properties of magnetic layers, such as saturation magnetization, magnetic anisotropy and coupling parameter between different magnetic layers.

### **3.4.1.1. Principles**

BLS is a spectroscopic technique where a beam of highly monochromatic laser light is incident on the surface of the sample under study. The scattering geometry depicting the incident and scattered beam, the incidence angle and the direction of wave vectors is shown in Fig. 3.10. Although most of the light is specularly reflected or absorbed, a small fraction of the light is scattered from the thermally excited SWs, which can be divided into two main categories: the elastic and inelastic scattering. In the elastic scattering (like Rayleigh scattering) of photons the photon's energy or frequency is unchanged. However in case of inelastic scattering, a shift in the angular frequency takes place, which forms the basis of the spin wave detection in this technique. The scattered light is collected (using the same lens as that used for incident beam) within a solid angle in the direction  $180^\circ$  from the incident light, which is known as the  $180^\circ$ -backscattering geometry. The backscattered geometry has the advantage that it maximizes the magnitude of the SW wave vector taking part in the scattering process. The light is then frequency analyzed using a multi-pass Fabry-Perot (FP) interferometer to extract the information about the surface and bulk magnons.

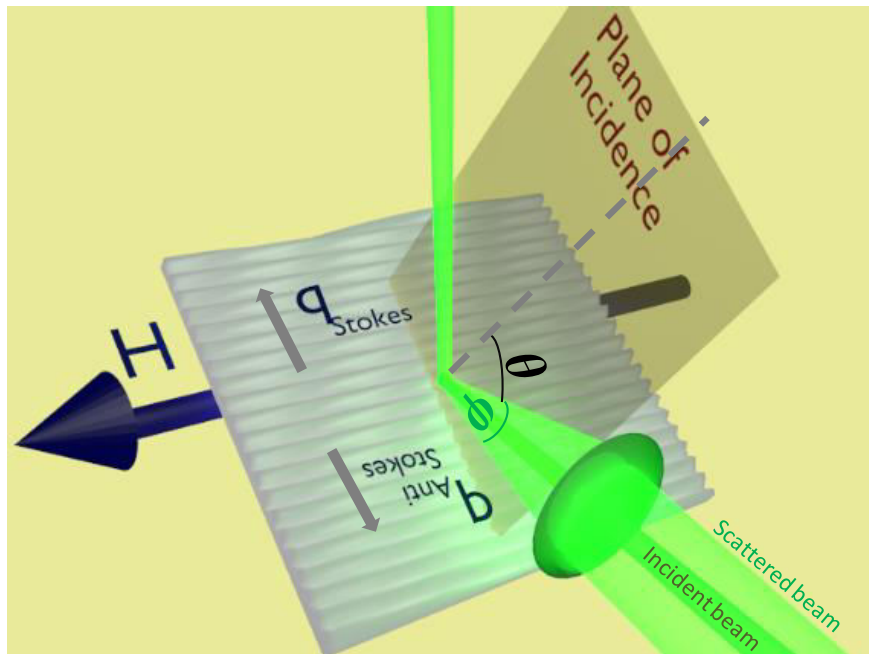


Figure 3.10: The scattering geometry showing the incident, reflected and scattered beams, the direction of magnon wave vectors for Stokes and anti Stokes process in BLS. The measurement geometry shown is DE geometry.

From a quantum mechanical viewpoint, the mechanism of inelastic scattering can be stated as a photon-magnon collision, i.e., in terms of the creation (Stokes process) and annihilation (anti-Stokes process) of a magnon of wave vector  $q$  and angular frequency  $\omega$ . The process is shown in Fig. 3.11. Considering the conservation of energy (frequency) and momentum (wave vector) between the magnon and the incident ( $i$ ) and scattered ( $s$ ) photons, it follows

$$\hbar\omega_s = \hbar\omega_i \pm \hbar\omega \quad \dots\dots\dots(3.5)$$

$$\hbar k_s = \hbar k_i \pm \hbar q \quad \dots\dots\dots(3.6)$$

where '+' ('-') sign stands for the anti-Stokes (Stokes) shift and  $\omega_i, k_i, \omega_s, k_s$  are the respective angular frequencies and wave vectors of the incident and scattered light. Note that, for light scattering from thin films the perpendicular component of the wave is not conserved because of translational symmetry breaking. Hence, the above equations are only valid for  $q$  which is the wave vector component parallel to the film plane.

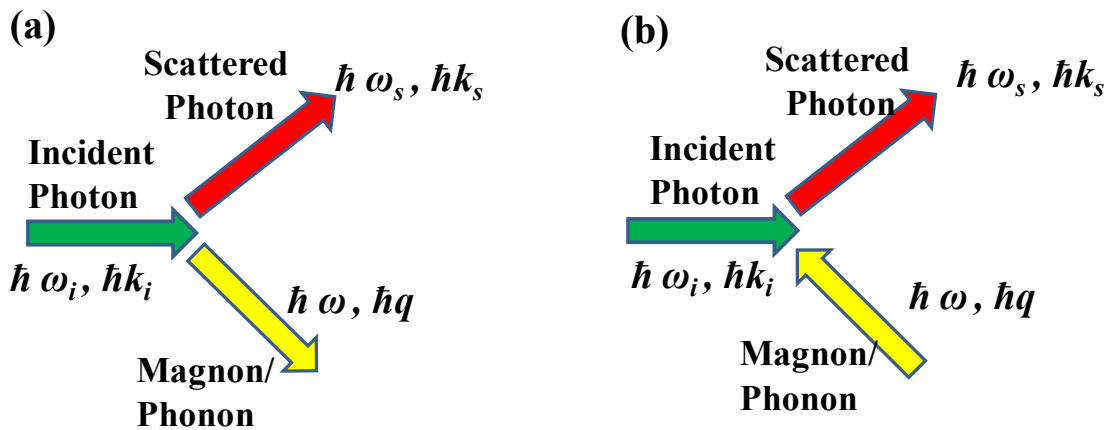


Figure 3.11: Schematic of the (a) Stokes and (b) anti Stokes Scattering processes occurring in BLS.

From the conservation of momentum described above, it is possible to determine the wave vector of SW taking part in the scattering process. Basically, the amount of energy of incident light exchanged with the system during the scattering (i.e., the energy of the magnon itself) is very small with respect to the incident photon energy. The energy of a visible photon is few eV whereas the energy of magnon observed in BLS is about  $\sim 10^{-4}$  eV. Consequently, the magnitude of the wave vector of the scattered photon ( $k_s$ ) should be very close to that of the wave vector  $k_i$  of the incident photon. Figure 3.12a schematically illustrates the scattering profile of a photon by a bulk magnon, which means that the SW taking part in the scattering has a component perpendicular to the surface. Here the scattered photon wave vector  $k_s$  must lie on the dashed circle line, whose radius is equal to the magnitude of incident photon wave vector ( $k_i$ ). Here the cone represents the collection angle of the scattered beam in the BLS experiment, whose central axis aligns with the incident photon wave vector. Therefore, by assuming that  $k_i$  and  $k_s$  are collinear ( $k_s = -k_i$ ), i.e., the backscattered geometry, the wave vector magnitude of the emitted or absorbed bulk magnon  $|q|$  is always equal  $2|k_i|$ .

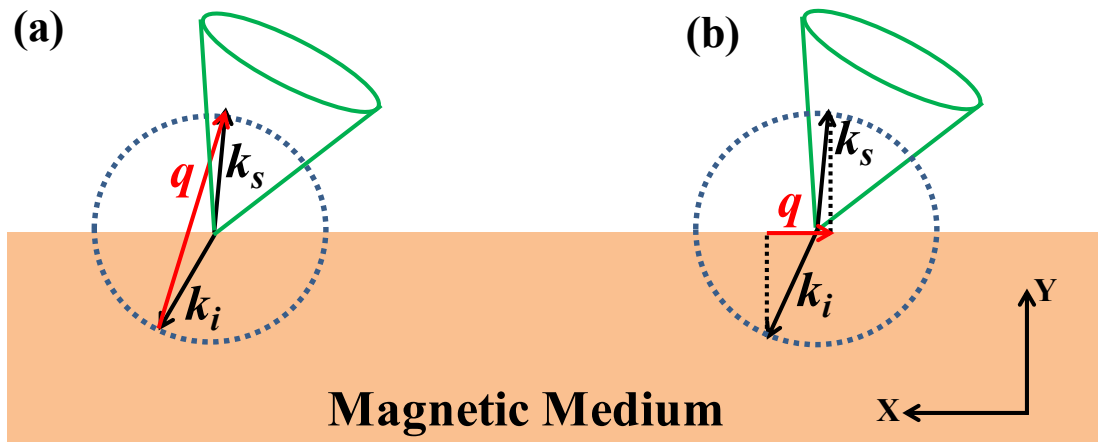


Figure 3.12: Scattering of laser beam by (a) bulk magnon and (b) surface magnon. The direction of  $q$  corresponds to the anti Stokes process.

On the other hand, the scattering of a photon by a surface magnon is illustrated in Fig. 3.12b. Here, since the direction of  $q$  lies in the horizontal plane, the momentum will be conserved only in the plane along the sample surface. In other words, the conserved component of the incident beam is equal to  $|k_i| \sin \theta$ , where  $\theta$  is the angle between  $k_i$  and sample surface normal (See Fig. 3.10). Therefore, the wave vector of the magnon probed by the experiment is given by

$$|\bar{q}| = |\bar{k}_i \sin \theta - \bar{k}_s \sin \theta| = 2|k_i| \sin \theta \quad \dots\dots\dots(3.7)$$

The above discussion suggests that, by varying the incident angle, no new information can be obtained about the bulk magnons, whereas the surface magnon reveals the important frequency-wave vector dispersion relation. Eq. 3.7 is known as the Bragg’s condition and provides an approximation for most of the light scattering experiments. According to Eqn. 3.7 one can vary the magnitude of  $q$  by varying either wavelength  $\lambda$  or  $\theta$ .

### 3.4.1.2 Uncertainty in the Selected Spin Wave Wave-Vector

Due to the finite aperture angle of the objective lens used for focusing and collecting light from the sample, an uncertainty is always induced in the selected SW wave vector. For finite angle of incidence  $\theta$ , the corresponding spread in  $q$  is given by,

$$\Delta q = 2k_i \cos \theta \sin\left(\frac{\phi}{2}\right) = 2 \frac{2\pi}{\lambda} \cos \theta NA \quad \dots\dots\dots(3.8)$$

where  $\phi$  is the collecting angle of the lens and  $NA = \sin(\phi/2)$  is its numerical aperture (See Fig. 3.10). Clearly, this uncertainty is maximum for normal incidence ( $\theta = 0$ ). Noticeably, a possible uncertainty can also be present in  $\theta$  due to the focusing of incident beam. However, to reduce this in the practical experiment, a very narrow beam (width  $\sim 500 \mu\text{m}$ ) is used, which in turn increases the focused spot size.

### 3.4.1.3. Polarization of Scattered Beam

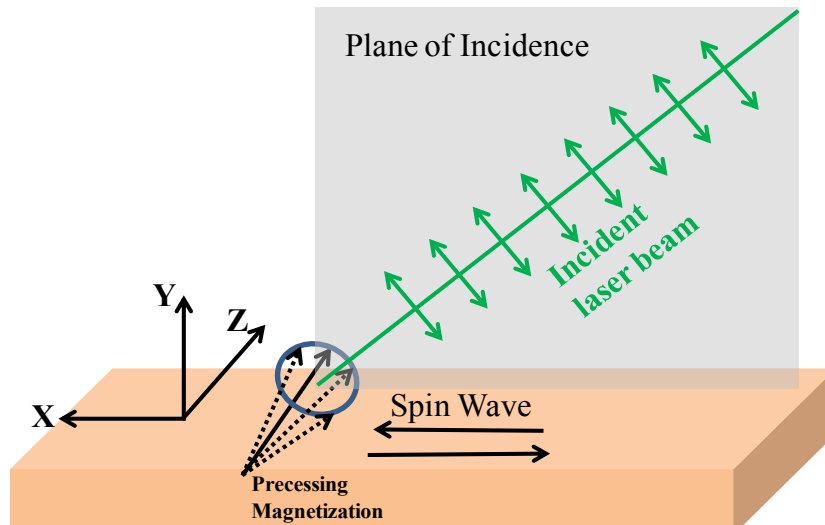


Figure 3.13: Schematic of the interaction between p-polarized incident beam and the precessing magnetization.

The scattering of light from the SWs can be viewed as a magneto-optic mechanism. Basically, in presence of precessing magnetization or SW the oscillating electric dipoles experience a Lorentz force which effectively causes a spatially periodic fluctuation in the polarizability of the medium. This leads to a scattered electromagnetic wave whose electric field vector is perpendicular to that of incident wave. This process is illustrated in Fig. 3.13 for an incident light which is p-polarized (polarization parallel to the plane of incidence). The geometry shown is the DE geometry where the propagation of SW is perpendicular to the magnetization direction. As the laser beam hits the sample, it provokes the electric dipoles to oscillate due to its oscillatory electric field, given by  $E = E_x e_x + E_y e_y$ . Now, say, magnetization  $\mathbf{M}$  also contains a dynamic component, then  $\mathbf{M}$  can be written as  $\mathbf{M} = \mathbf{M}_0 + \mathbf{m}$ , where  $\mathbf{m} = m_x e_x + m_y e_y$ . The fluctuating component of  $\mathbf{M}$  exerts a Lorentz force (proportional to  $E \times m$ ) on the electric dipoles, which in this case results in the polarization

pointing in the  $z$ . As a result, the radiated light wave has its electric field along the  $z$  direction, i.e., s-polarized. A similar argument for s-polarized incident light follows that the scattered light is p-polarized. Therefore we conclude that the polarization of light scattered by a magnon is perpendicular to the polarization of the incident light. This is different from the case when light is scattered by acoustic phonons, there the polarizations of incident and scattered beam lie in same direction. This helps to isolate the light scattered from magnons from that scattered from phonons by selecting proper orientation of the analyzing polarizer in the experiment.

#### 3.4.1.4. Experimental Setup

As illustrated in the previous section, the inelastically scattered beam carries information about the frequency and wave vector of the involved SW mode. Further, the intensity of the scattered light is proportional to the intensity of studied SW. In this section, we will explain how these quantities are accessed and analyzed experimentally. In general, the BLS technique offers two different measurement geometries: (i) Forward Scattering geometry, where the scattered beam is collected after transmission of the probing beam through a transparent sample, and (ii) Backscattered geometry, where the beams that are backscattered from the surface of opaque sample are investigated. The latter can be further extended to BLS microscopy (Micro-BLS), where the profile of SW can be mapped in a space-, time- and phase-resolved manner. In the following we will discuss the details of conventional backscattered geometry, followed by the distinguished features of the Micro-BLS technique.

Figure 3.14 presents the schematics of the optical beam path used for conventional Brillouin light scattering experimental arrangement. The main components constituting the BLS apparatus include:

- i) A continuous single mode solid state laser (A).
- ii) A beam splitter (BS)
- iii) A half wave plate (HWP)
- iv) Polarizing beam splitter (PBS)
- v) Mirrors (M and M').
- vi) Achromatic Doublet (L'1)
- vii) Polarizer (P)

- viii) Focusing lens (L'2)
- ix) The pinhole, the light diffuser and the shutter (C)
- x) The Tandem Fabry-Pérot Interferometer (TFPI) equipped with a single photon detector (D)
- xi) A computer equipped with a multi-channel analyzer software GHOST (not shown)
- xii) Magnet (F)

For the measurement of thermally excited magnons, a laser light emitted by a diode-pumped, frequency-doubled, single mode solid-state laser of wavelength  $\lambda = 532$  nm is used (the power of the emitted light is 300 mW). Right in front of the laser, the light is split into two beams using a 10:90 beam splitter (BS). The smaller part of the deflected beam is directed straight to the TFPI using mirrors M'1 and M'2, where it serves as a reference beam. The purpose of this reference beam is manifold:

- i) Firstly, this beam is used to stabilize the mirror spacing of the Fabry-Perot etalons.
- ii) This beam forms the central elastic peak in a BLS spectrum, where it is used to determine the frequency shift of the scattered beam *w.r.t.* the incident beam.
- iii) Also, reference beam is employed to estimate the transmission order of the Fabry-Perot etalon which in turn helps to deduce the frequencies present in the scattered light.

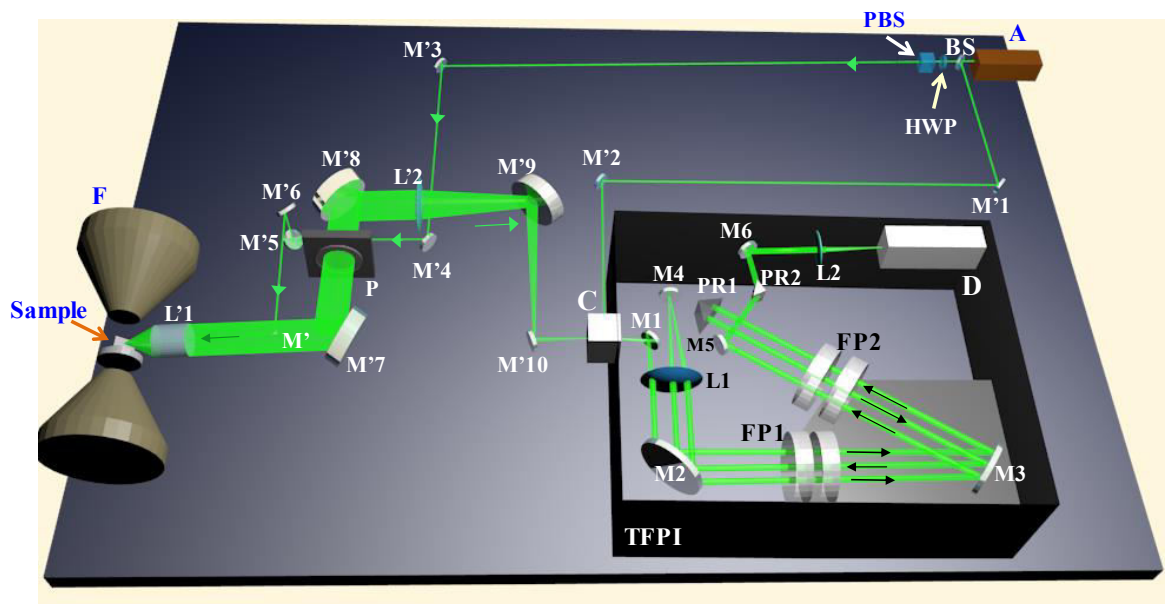


Figure 3.14: The set up and optical pathway for conventional BLS set up. The notation for the components is given in the text.

The other part of the beam is first sent through a HWP and a PBS, in order to eliminate the small in-plane polarized component from the partially polarized beam of the laser. The beam perpendicularly polarized to the optical table is then guided by the mirrors M'3, M'4, M'5, M'6 and M' towards the sample which is lying between the electromagnets. The mirror M' is taken as a tiny prism mirror so as to minimize the blocking of the backscattered beam by itself. Finally, the beam is focused onto the sample using an achromatic doublet lens. The sample is mounted on a rotation stage. The change in the rotation angle changes the angle of incidence, thereby addressing different transferred SW wave vector according to Eqn. 3.7. A magnetic field is applied perpendicular to the transferred wave vector direction, i.e. in the Damon-Eshbach (DE) geometry. The measurements are performed for various magnetic field values at different wave vectors of transferred SW. Subsequently, the scattered beam is collected by the same lens and continues its way towards the entrance pinhole of a JRS Scientific Instrument (3+3)-pass tandem FPI for frequency analysis, using the focusing lens L'2. In order to select the light scattered from SWs, a crossed polarizer *P* is inserted in the path of the scattered light. This allows for the suppression of the elastically scattered beam as well as the beam containing the signal from phonons. Inside the TFPI, the beam hits mirror M1 and then reaches FP1 via lens L1 and mirror M2. After passing through FP1, the beam undergoes its first pass (beam 1) until it is reflected from M3 (beam 2) and passes through FP2. Then the beam is reflected from PR1 and traces back its path via FP2 (beam 3) and FP1 (beam 4) and reaches M4. The beam is once again reflected at M4, and thus it gets redirected, passes through FP1 and FP2 for the third time (beam 5 and beam 6 respectively) to finally arrive at the single-photon counter (D). The resulting light has very low intensity which is detected by the photon detector and the signals are sent to a computer for storage and analysis.

### **3.4.1.5. Instrumentation**

#### **Laser**

For a precise and accurate measurement of SW frequencies, a laser light of single frequency mode with narrow bandwidth is essential. To meet this requirement, a 300 mW Excelsior solid state cw laser is used in the experiment. The laser system comprises of the laser head, together with a separate controller unit, which routes the electrical power and monitors the signal between the laser head and the master system. Here a diode laser is used to pump the Nd<sup>3+</sup> ions doped in the crystal of yttrium vanadate (Nd: YVO<sub>4</sub>), which emits photons at 1064 nm. This infrared output is

further converted to visible light by sending it through a non-linear crystal of lithium triborate (LBO) for frequency doubling (wavelength 532 nm). The emitted laser beam has a diameter of about 670  $\mu\text{m}$  with a beam divergence of about 1.03 mrad. Overall, the laser system is extremely reliable and steady in terms of output power and beam pointing and requires no external adjustments in normal operation.

### The Pinhole and Light Modulator

The light modulator, as shown in Fig. 3.15, is a double shutter system situated right behind the entrance pinhole of the TFP. Together with the TFPI in operation, the shutters SH1 and SH2 are alternately opened, thereby controlling the light intensity that ultimately reaches the photon detector. Since the detector is a single photon counter, a strong elastic light can damage the detector. Therefore to protect it, this device operates in synchronization with the scanning stage, which is illustrated in Fig. 3.16. Figure 3.16a presents the spectrum of the scattered signal captured by P1, while Fig. 3.16b depicts that of the reference beam entering through P2. During the scanning of the elastic peak (region I, IV and V), P1 is blocked and P2 is opened, allowing the reference beam to enter through it. This small intensity reference beam is further used to maintain the stabilization of the angular orientation of the FPIs. On contrary, while scanning for the Brillouin shifts (in regions II and III); pinhole 2 is closed while pinhole 1 is opened.

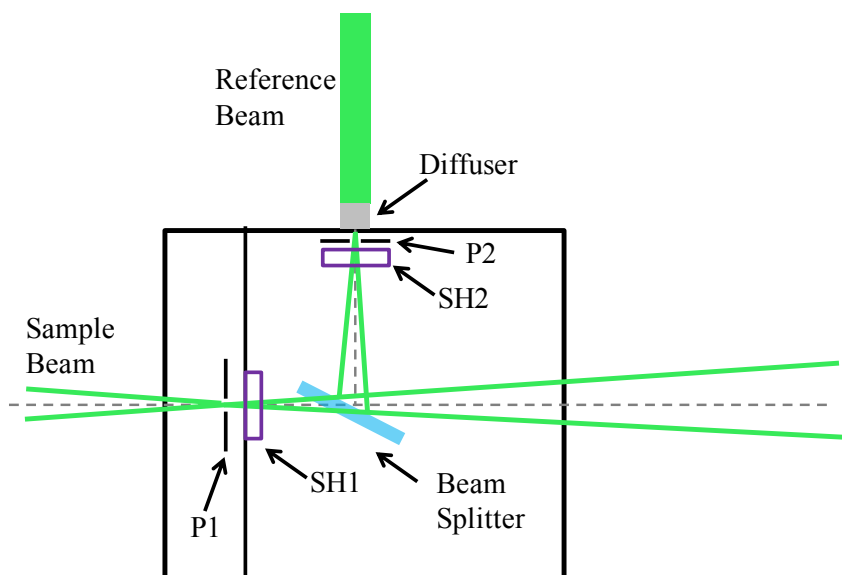


Figure 3.15: A Schematic view of the pinhole and light modulator system.

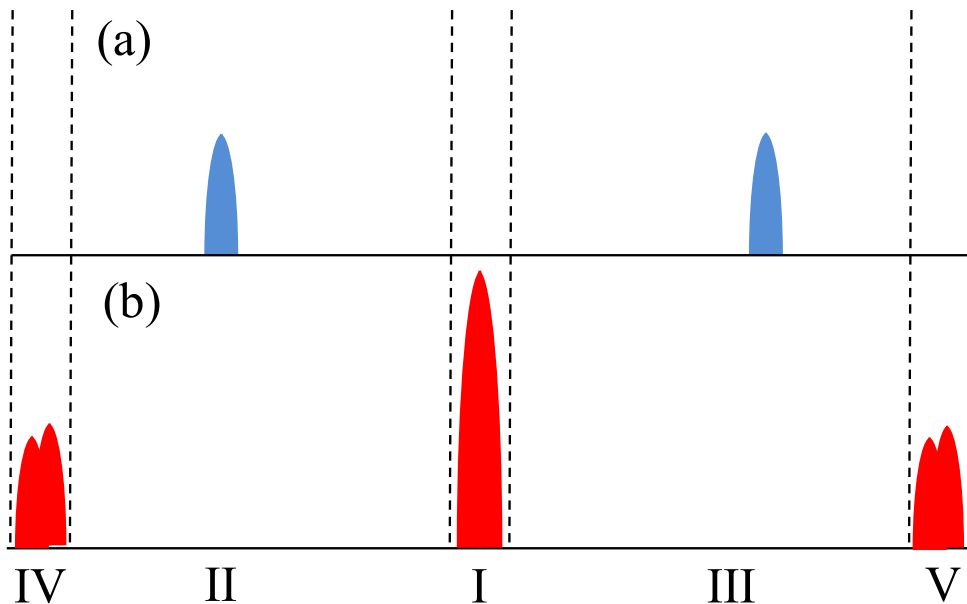


Figure 3.16: The part of the BLS spectrum that corresponds to when SH1 is open (a) and SH2 is open (b). A superposition of the spectra in (a) and (b) is what is obtained when SH1 and SH2 operates in synchronization.

### Tandem Fabry-Pérot Interferometer (TFPI)

One of the key issues of BLS spectroscopy is the frequency analysis of SWs, which requires very high spectral resolution. Basically, the observed frequency for magnons is, at most, 300 GHz, which is about  $10 \text{ cm}^{-1}$ . This is nearly  $10^{-5}$  times smaller than that of a typical excitation frequency of laser light. Moreover, the cross section of the inelastic scattering of photons is very small as compared to the elastic scattering. Therefore a high contrast is required for an efficient detection of the fractional amount of incident laser power with high signal to noise ratio. These conditions are fulfilled by the implementation of a triple pass Tandem Fabry-Pérot Interferometer (TPFI) in the BLS setup. The TFPI consists of two single Fabry-Pérot Interferometers (FPI) connected in series and the light passes each FPI three times, as can be seen in Fig. 3.17. In the following, first we address briefly the transmission characteristics of a single FPI and then the realization and the operations of the Tandem mode are discussed.

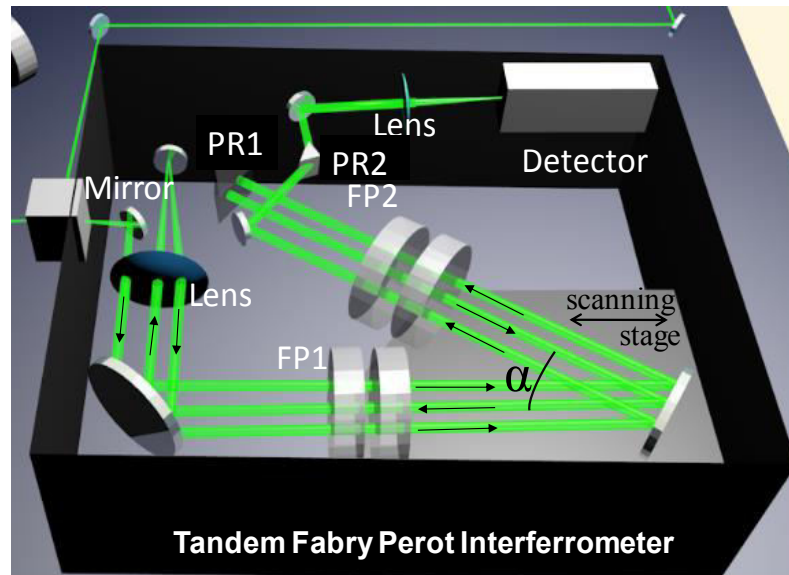


Figure 3.17: Schematic of the optical arrangement of TFPI.

### The Fabry-Pérot interferometer

A typical FPI [18], or etalon is constituted of two planar, partially reflecting mirrors mounted accurately parallel to each other at a distance ( $L$ ). The light entering the FPI, undergoes multiple back and forth reflections and transmissions. The transmitted beams interfere with each other and results in the condition for constructive interference under normal incidence given by:

$$L = \frac{n\lambda_0}{2} \quad \dots\dots\dots(3.9)$$

where  $n=1, 2, 3, \dots$  is an integer (transmission order) and  $\lambda$  is the wavelength of the light. Therefore, the consecutive orders of interference are separated by a frequency gap  $\Delta f$  as

$$\Delta f = \frac{c}{2L} = \frac{150}{L} \text{GHz.mm}^{-1} \quad \dots\dots\dots(3.10)$$

Here  $c$  denotes the velocity of light. This inter order spacing is known as the free spectral range (FSR) of the interferometer (See Fig. 3.18). The Finesse of the interferometer is related to FSR as

$$F = \frac{\Delta f_{FSR}}{\Delta f_{FWHM}} \quad \dots\dots\dots(3.11)$$

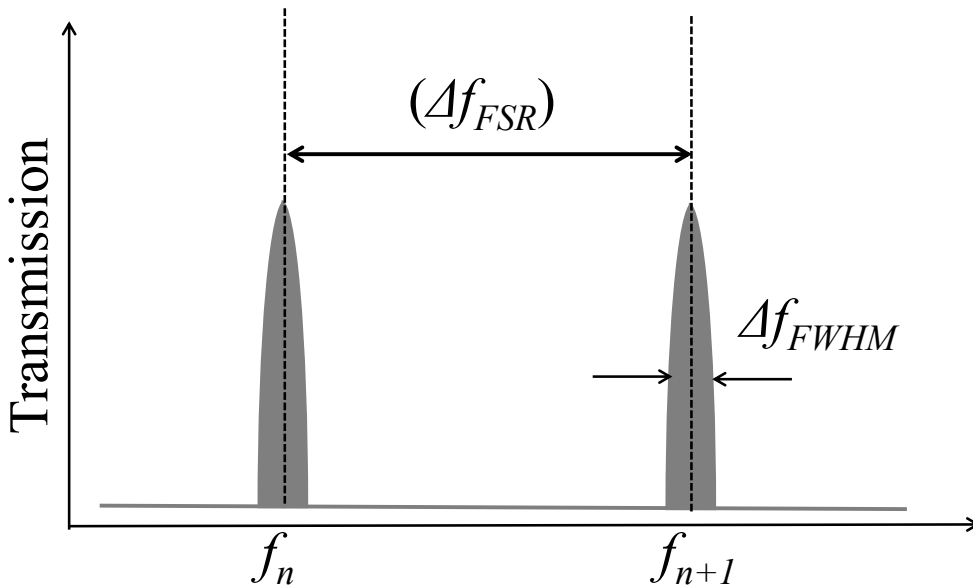


Figure 3.18: Periodic transmission spectrum depicting the FSR.

Where  $\Delta f_{FWHM}$  is the full width at half maximum of the transmission curve. The finesse  $F$  affects the transmitted intensity ( $I_t$ ) off the FPI via:

$$I_t = \frac{I_0}{1 + \left(\frac{4F^2}{\pi^2}\right) \sin^2\left(\frac{2\pi L}{\lambda_0}\right)} \dots\dots\dots(3.12)$$

where  $I_0$  is the intensity of the incident light. The above equation is known as Airy function which describes the periodicity of transmitted intensity with mirror spacing and frequency. The finesse can be regarded as a measure for the quality of the instrument, which is connected to the reflectivity  $R$  of the FP etalons, by the relation

$$F = \frac{\pi\sqrt{R}}{(1-R)} \dots\dots\dots(3.13)$$

Therefore a higher reflectivity enhances the finesse and as obtained from Eqn. 3.11, increases the frequency resolution, as  $f_{FWHM}$  decreases. On the other hand, for fixed  $R$ , an increase in  $L$  reduces the FSR, which improves the frequency resolution as the Finesse maintains constant.

The contrast of a FPI is defined as

$$C = 1 + \frac{4R}{(1-R)^2} \quad \dots\dots\dots(3.14)$$

The contrast for an  $n$ -pass interferometer is the  $n$ th power of that of a single-pass one. For example, a five-pass interferometer can achieve a contrast of at least five or six orders of magnitude greater than that of a single-pass interferometer.

### **Tandem Operation**

One issue inherent to FPI is the periodicity of transmitted intensity as a function of the mirror spacing. The fact that the transmission characteristic repeats every FSR creates certain problems in the identification of the frequencies present in the scattered light. For example, say, for a fixed mirror spacing  $L$ , there are two wavelengths present in the measured light beam, such that,

$$2L = m_1 \lambda_1 \quad \dots\dots\dots(3.15)$$

$$2L = m_2 \lambda_2 \quad \dots\dots\dots(3.16)$$

Therefore, the transmission condition is satisfied for both the wavelengths at different orders. Since the order of transmission spectrum is determined from the reference beam, the order of second wavelength (which does not match with that of the reference beam) and consequently, the wavelength itself, remains un-accessed. Moreover, it is difficult to unambiguously identify whether a peak signal belongs to the Stokes side of a specific transmission order or it is the anti-Stokes signal of the previous order. To address these shortcomings, the interferometer is used in a Tandem configuration, wherein the light passes consecutively through two interferometers, which are mounted under an angle  $\alpha$ . This arrangement was developed by Dr. J. R. Sandercock and is shown in Fig. 3.17. The right mirror of each FPI sits on the translation stages, and the other on a separate angular orientation device. The scanning stage can move the right mirror of each pair along the optical axis of FP1. A displacement  $d$  of the translation stage leads to a change of the mirror distance in FP1 by  $\Delta L_1 = d$ , while the change for FP2 is given by:

$$\Delta L_2 = \Delta L_1 \cos(\alpha) \quad \dots\dots\dots(3.17)$$

This also satisfies the synchronization condition as

$$\frac{\delta L_1}{\delta L_2} = \frac{L_1}{L_2} \quad \dots\dots\dots(3.18)$$

Now this can be used to suppress the intermixing of different orders. To do that, before the scanning of linear stage, each FPI is adjusted to transmission separately. Although their

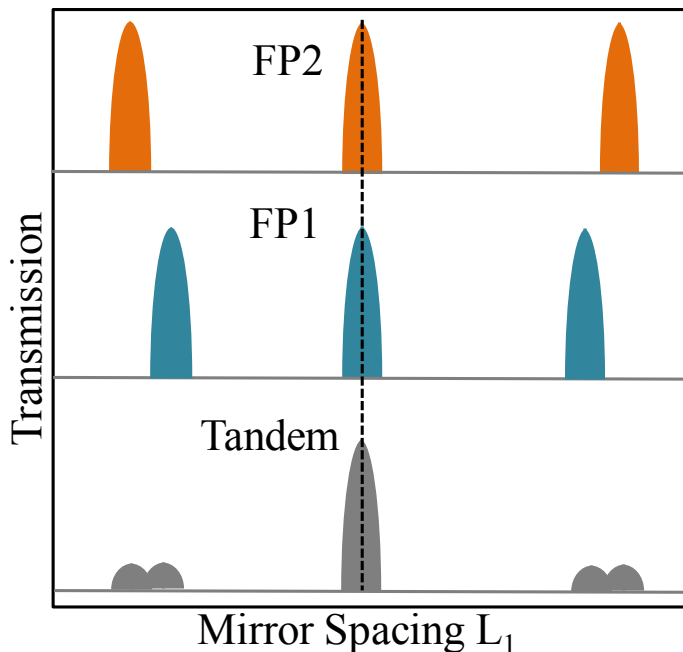


Figure 3.19: Transmission Spectra of FP1 and FP2 and in tandem operation.

transmission orders are different, but they together provide a central transmission order, which can be adjusted by changing the mirror spacing of FP2 (See Fig. 3.19). At the same time, the other orders are suppressed, since the FSR of the two FPIs are now different. This arrangement also increases the FSR of the final spectrum, without affecting the resolution. Now when the stage is moved, the mirror spacing changes by

$$l_1 = (L_{10} + d) \tag{3.19}$$

$$l_2 = (L_{10} + d)\cos \alpha \tag{3.20}$$

for FP1 and FP2 respectively, where  $L_{10}$  is the initial mirror spacings of FP1, i.e., at  $d=0$ . This removes the aforementioned ambiguities since the transmission order is now fixed. As mentioned earlier, the light additionally passes through each FPI three times to enhance the contrast. Finally, after the 6 passes through the FPIs, the light is directed to a photomultiplier, which counts the number of transmitted photons as a function of the mirror-spacing, and consequently, as a function of the frequency shift. To achieve this, the scanning stage constantly sweeps the distance which corresponds to the required frequency window and the data is recorded for long time to attain

sufficient statistics. In this way, the obtained BLS intensity is proportional to the spin wave intensity at a given frequency.

### **Alignment of TFP Interferometer**

The proper alignment of optics inside TFP interferometer box is extremely crucial for BLS experiments. In general, one should not tamper with the alignment of TFP optics in any situation. In case of any accidental misalignment, one may follow the steps described below [19]:

1. Before proceeding with the alignment, a proper source of light is required. The most convenient light source for aligning is an expanded laser beam which provides a uniform wave front to view the interference fringes easily. For that purpose, the direct laser beam was sent through the input pinhole P1 (refer to Fig. 3.20a) using two steering mirrors (not shown in the figure). The tilt angles of these mirrors can be adjusted so that the beam enters the TFPI box even for the smallest pinhole. To confirm this alignment, one can hold a flat mirror against the pinhole cover and check that the reflected laser beam traces back its path.
2. Now open the pinhole cover. Mount a 10 mm focal length lens attached to XYZ stage (this was provided with the TFPI accessories) in its place. Adjust the X-Y stage until the beam passes through the largest pinhole. Turn to successively smaller pinholes and re-adjust as necessary. With the smallest pinhole check that the lens is focused correctly (as X or Y is moved the light spot should vanish suddenly). If the focus is incorrect adjust by turning the knurled knob. At this point the aperture A1 is symmetrically illuminated. Note that this lens can only be used for direct laser beam. In case of any other beam, the focal length of the required lens is 18 times the beam width.
3. At this point the aim is to make sure that the beam falling on FPI is collimated, perpendicular to the mirror surface and at right location. Start with adjusting the focus of L1. Using a mirror the beam after L1 is reflected onto a distant wall and the focus of L1 is adjusted for parallel light. Otherwise one can look for the back reflected beam from FP1 coming back out of the TFP. When L1 is in focus, this beam will be visible even for smallest pinhole. Remember that the back reflected beam will disappear when FP1 is in transmission. Use Z-control to restrict the transmission from FP1.

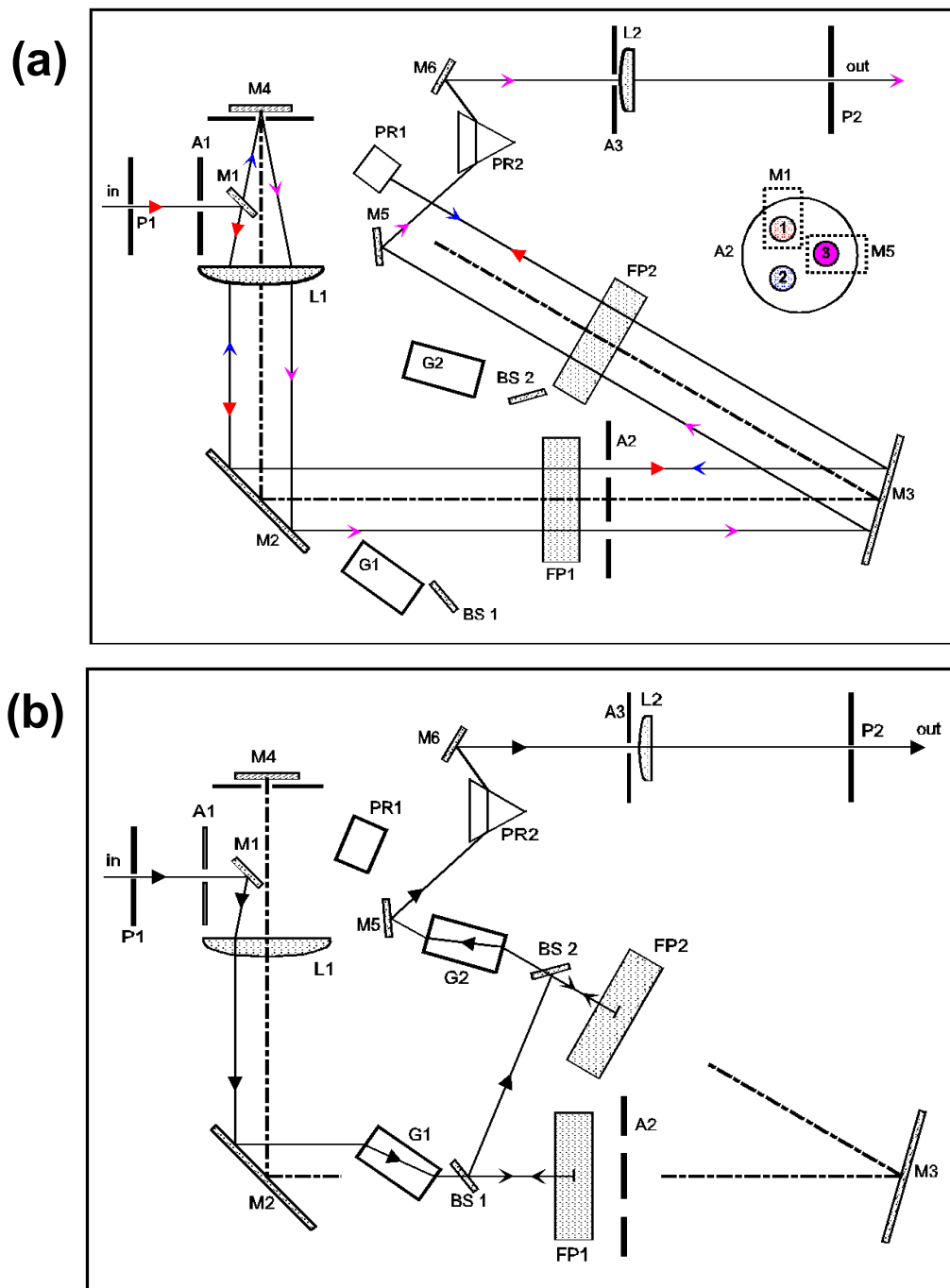


Figure 3.20: Optical arrangement inside TFPI box in (a) tandem and (b) alignment mode. Figure is taken from reference [19].

4. Now one can proceed to align the mirrors M1 and M2. Make sure that the right hand edge of M1 is about 41 mm from the aperture A1 and slide the base of M1 so that the input beam strikes M1 about 1 mm from its right hand edge. The orientation of M1 should be such that the vertical diameter of L1 touches the right hand edge of the beam. Slide the base of M2 so that the beam passes through the correct aperture of A2.
5. Adjust M1 so that the beam cleanly fills the aperture A2. Then adjust M2 so that the beam is again reflected back out of the pinhole. One may have to repeat the sequence until the beam is properly aligned.
6. The next step is to adjust the multiple passes through the interferometers. Align FP1 and adjust for steady transmission. Then use M3 to direct the beam 1 onto FP2 so that the back reflected beam returns through the aperture 1 of A2. It is very crucial to achieve a good alignment of this beam as the alignment of the higher passes depends on it. One can cut a fine slit in a piece of card and place it over A2. Then it is easier to drive the reflected beam onto the slit itself. Finally look for fringes on the surface of M3, or on the ghost beam on A2, or after transmission through FP2, and slightly tweak M3 to give about 5 fringes.
7. Now Align FP2 and using the  $\Delta Z$  control, adjust for steady transmission. Beam 3 should now be visible. Now adjust for the translation and rotation of PR1 so that the beam cleanly falls on the aperture 2 of A2 along with visible fringes.
8. Since the alignment of the FPIs are very sensitive to any room temperature fluctuation, intermittent adjustment is necessary to achieve good transmission for all the passes. Once beam 4 is visible, it should strike M4. Adjust the position and tilt of M4 so that the bright spot seen on its surface is as small as possible and beam 5 becomes visible after aperture 3 of A2. Alternatively, one can observe beam 5 on M3 using a card. When M4 is properly aligned, similar fringes as mentioned in step 6 are visible for beam 5.
9. The beam 6 should now be aligned. Adjust the position of M5 so that beam 6 strikes its right hand edge. Rotate M5 to guide the reflected beam to the middle of the side of the prism PR2. Adjust the rotation of PR2 slightly if the beam falling on M6 is not circular in cross-section.

10. Finally, adjust the orientation of M6 (and M5, if necessary) and the focus of L2, so that the beam passes through the output pinhole P2.

The optics for tandem-multipass operation is now aligned. The alignment mode optics should now be adjusted as described below (See Fig. 3.20b):

11. Switch the optics to the ALIGN mode. The glass block G1 deflects the beam to the axis of FP1. Note that, the glass blocks G1 and G2 are hard to move by light push. In addition, the optics from M5 to the output pinhole P2 in the beam path must not be tampered once they are adjusted for tandem operation. Therefore, one is left with the adjustment of the beam splitters BS1 and BS2.
12. Align FP1 for steady transmission. Adjust BS1 so that the transmitted beam strikes A2 in the center.
13. In reflection (one can switch between reflection and transmission by adjusting Z), the beam should strike BS2 in the middle. Now adjust BS2 so that the beam passes via G2 and M5 to the output pinhole P2.
14. One may need to repeat step 12 and 13 several times to optimize the alignment.
15. Under proper alignment, the ratio of the peak height in the tandem mode to the background level in the alignment mode should lie between 3 and 6 (in our setup it is 4). One can finely tune this ration in the following way:
  - i) In the tandem mode, with a small output pinhole, adjust mirror M6 for maximum detector signal.
  - ii) In alignment mode, with the same pinhole, maximize the background signal by tweaking BS1.

#### **3.4.1.6. Optimization of the BLS Set up Using Plexi Glass, Ni<sub>80</sub>Fe<sub>20</sub> Thin Film and Bare Laser Beam**

After the BLS spectroscope was set up in our laboratory, we verified its alignment by first measuring the phonon signal from a piece of plexi glass. In principle, the phonons from plexi glass should produce 3-6 BLS counts/mW laser beam/ms (In the measurement, selecting 1024 channels will correspond to 0.5 ms) for a single scan. The corresponding frequency should lie around 16

GHz. Figure 3.21 shows the computer screenshot of the observed BLS signal for 50 mW of laser power falling on the sample, which indicates a reasonably good alignment.

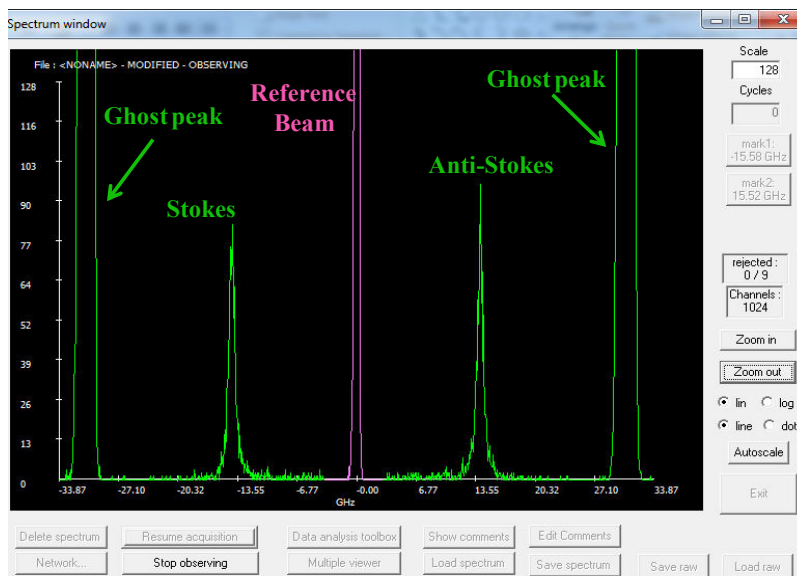


Figure 3.21: GHOST software interface for single scan measurement of BLS signal showing the data for plexi glass. The reference beam suppressing the elastic peak is shown in purple color. The Stokes and anti Stokes peaks along with two ghost peaks (higher orders of the central peak) are also indicated.

known magnetic parameters. Figure 3.22 presents the series of BLS spectra measured in Damon Eshbach geometry by varying the magnetic field (Fig. 3.22a) as well as the transferred wave vector (Fig. 3.22b). The data is fitted with the equation given by

$$f = \gamma \left[ H(H + 4\pi M_S) + (2\pi M_S)^2 (1 - e^{-2q_{\parallel}d}) \right]^{1/2} \dots \dots \dots (3.21)$$

Where  $q_{\parallel} = 2k_i \sin \theta$ ,  $k_i$  is the wave vector of laser beam,  $\theta$  is the angle of incidence,  $d$  is film thickness,  $M_S$  is the saturation magnetization,  $H$  is the applied magnetic field. The data show a good fitting for the parameters  $\gamma = 2.78$  GHz/kOe and  $M_S = 800$  Gauss.

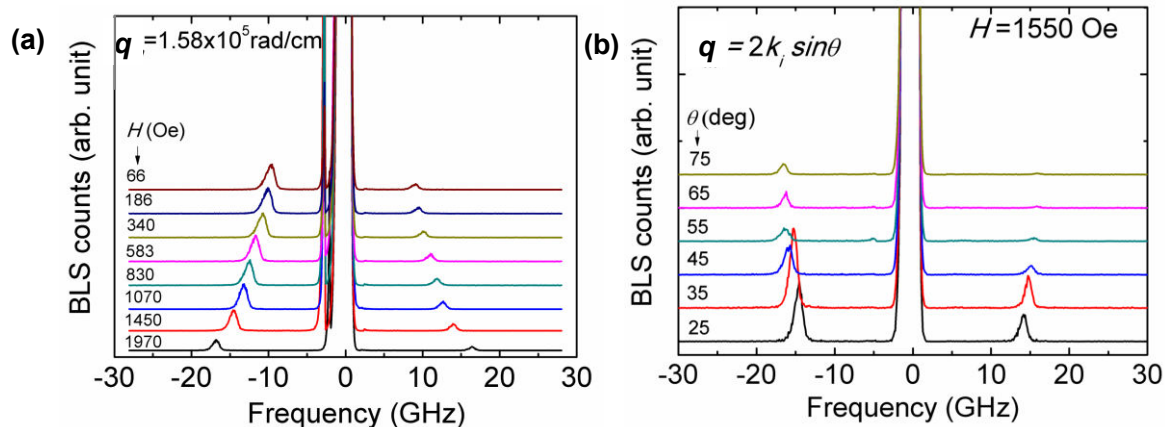


Figure 3.22: BLS spectra for  $\text{Ni}_{80}\text{Fe}_{20}$  thin film at (a) different in-plane bias magnetic field and (b) wave vector.

We have also measured the BLS spectrum of bare laser beam and the data is shown in Fig. 3.23. The measurement was performed by focusing the attenuated laser light normally onto the surface of a mirror. The back reflected beam was then fed to TFPI. The result reveals the presence of higher order harmonics of the fundamental laser frequency on the anti-Stokes side of BLS spectrum. The corresponding signal on the Stokes side is comparatively much lower.

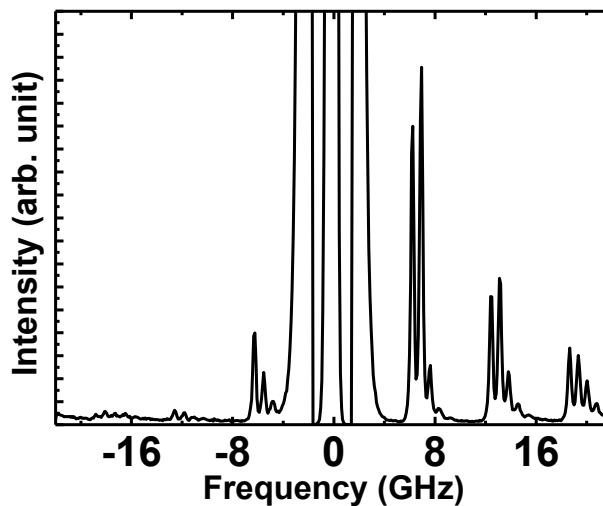


Figure 3.23: BLS spectrum of bare laser beam.

### 3.4.1.7. BLS Microscopy

#### Micro BLS—Space Resolved BLS

The micro-BLS is an extension of conventional BLS which was developed in the past decade [20-21]. The conventional BLS is an efficient technique for examining spin waves in thin films and large arrays of micro-structures but is limited when single micrometer-sized elements are introduced. This is because the spot size of the focused laser is as large as tens of micrometers. In micro-BLS, the laser is focused down to a small spot ( $\sim 250$  nm) on the sample, which allows for a spatial sensitivity, however at the cost of wave vector resolution. The reason is the Heisenberg's uncertainty principle, which prohibits the simultaneous access to position and wave vector with arbitrary high precision. The components needed to transform the BLS to a micro-BLS are shown in Fig. 3.24. The additional important components are: a microscope objective, a CMOS camera, a set of high precision three-dimensional translation stages and a number of steering optics.

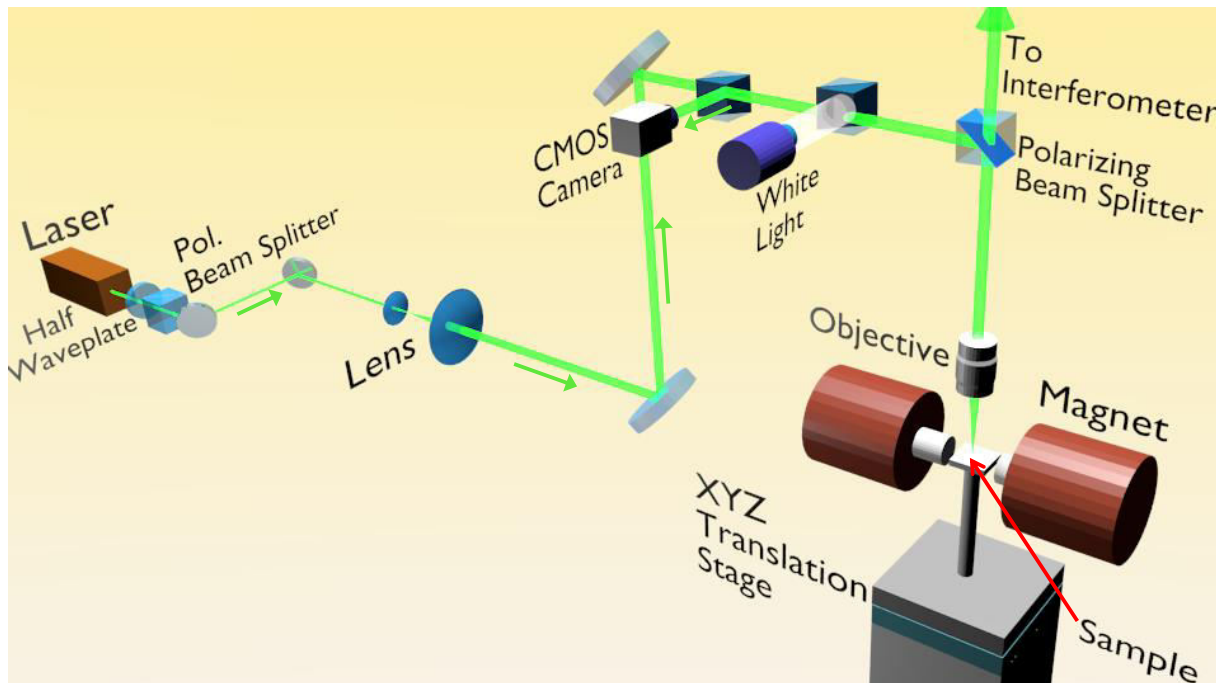


Figure 3.24: Schematics of the optical set up of micro-BLS required for the transformation from conventional BLS.

Here the laser beam is broadened using two lenses of small and large focal lengths in succession placed in telescopic arrangement, which subsequently fills the back aperture of the microscope objective of magnification of 100x, a numerical aperture (NA) of 0.75, and a long working distance

of 4 mm. Finally, the beam hits the sample in a range of angle of incidence depending on the numerical aperture  $NA = n \sin \theta$ , where  $n$  is the index of refraction of the medium (1.00 for air) and  $\theta$  is the angle of incidence. In the set-up developed at S N Bose National Centre for Basic Sciences Kolkata,  $NA = 0.75$  and the maximum angle of incidence is given by  $48.6^\circ$ . This corresponds to a range of transferred wave vector from 0 to  $1.77 \times 10^7$  rad/m. The scattered beam is collected by the same objective lens (back scattered geometry) and sent to the TFPI for frequency analysis. The purpose of the CMOS camera is twofold: i) it helps to locate the laser spot on the sample, and ii) it allows for the stabilization of the sample position with respect to the thermal drift.

In order to conduct a fine spatial scan and for thermal stabilization, the sample is mounted on a set of very high precision translation stages. The spatial resolution of lateral and vertical stages are 1 nm and 50 nm, respectively. By moving the position of the laser onto the sample, the spatially dependent amplitude of scattered light is measured for a given-frequency. To enhance the signal to noise ratio, the density of measured magnons is increased by electrical excitation with a RF frequency sent through a Coplanar Waveguide (CPW).

### Phase Resolved Micro BLS

As pointed out above, due to Heisenberg's uncertainty principle, the spatial resolution in micro BLS comes with an uncertainty in the measurement of the wave vector of the spin wave. This limitation can be countered by analyzing the spin wave phase [22-24]. Probing the propagating spin wave phases is basically equivalent to the measurement of wavelength and thus the wave vector of spin wave. The information about the spin wave phase is extracted by analyzing the phase of the scattered beam. This is realized via the interference of the scattered beam with a temporally coherent reference beam that is generated using an electro-optical modulator (EOM). By changing the probing position across the sample, the propagation of the spin wave phase can be monitored. The intensity of the corresponding interference signal can be expressed as

$$I_{\text{int}} \propto E_S^2 + 2E_R E_S \cos(\Delta\phi_0 + q.r) + E_R^2 \quad \dots\dots\dots(3.22)$$

Where  $E_S$  and  $E_R$  are the electric fields corresponding to the sample and the reference beam, respectively,  $\Delta\phi_0$  is the initial phase difference between the reference beam and the sample beam. The argument of the cosine function indicates the corresponding phase difference as the spin wave of wave vector  $q$  advances by a distance  $r$ .

### **Time Resolved Micro BLS**

In BLS technique, it is possible to examine the propagation and relaxation characteristics of spin wave eigen modes via time-resolved analysis [25-27]. The main idea is to excite the spin waves externally at a time  $t_0$  and then to measure the temporal evolution of the spin wave intensity as it propagates through the sample. For this purpose the spin wave mode is repeatedly excited using a train of microwave pulses. The leading edge of the pulse defines the starting time  $t_0$  and the data is acquired at different point of times  $t_i$  w.r.t.  $t_0$ . The corresponding counts for subsequent pulses are added up which finally renders the matrix formed by the intensity of total accumulated photons and the associated time  $t_i$ . Further, one can acquire a two-dimensional intensity map of a spin wave pulse excited at a fixed frequency for different delays, which basically presents the spatial and temporal advancement of the corresponding wave packet.

### **3.4.2. Time-resolved Magneto-optical Kerr Effect (TR-MOKE) Microscope**

The Kerr rotation caused by the magneto-optical Kerr Effect [28] is proportional to the magnetization of the system and as mentioned earlier, this phenomenon can be used to extract the information about the local magnetization state. The time-resolved magneto-optical Kerr effect (TR-MOKE) [29] technique additionally features a very powerful means to study the magnetization dynamics at a very fast time scale [30-31]. Amongst a number of variants of TR-MOKE, the all-optical TR-MOKE is based upon both the excitation and detection of the magnetization dynamics in optical manner, along with the advantages of very high temporal resolution (down to sub-100 femtoseconds) and the ease of sample fabrication (no additional waveguide structures are required). Its working principle stands upon the two-color collinear pump-probe geometry where the data is recorded in a stroboscopic fashion. A pulsed laser beam (also known as pump beam) hits the sample to rupture its equilibrium magnetization state (ultrafast demagnetization). As the probe beam (another laser beam) approaches the sample, it undergoes the Kerr rotation depending upon the current magnetization state (which is actually trying to recover its equilibrium) and the data is collected with respect to the time delay between pump and probe pulses. This way the temporal resolution is solely limited by the pulse width of the laser and one can measure the ultrafast demagnetization, different relaxation processes and coherent precession of magnetization in a single measurement. In the following, we will briefly discuss the

different timescales of magnetization dynamics, followed by the description of primary optical components and the optical setup.

### **3.4.2.1. Different Time Scales of Magnetization Dynamics**

The term magnetization dynamics covers a broad range of phenomena occurring at different timescales starting from few femtoseconds (fs) to micro seconds ( $\mu\text{s}$ ). The fastest dynamics which typically cover the time scales in fs range include fundamental exchange interaction ( $\sim 10$  fs), spin-transfer-torque ( $\sim 10$  fs – 1 ps) and laser induced ultrafast demagnetization (100s of fs). The relatively slower phenomena are precession of magnetization (characteristic time scale 10-100 picoseconds, causes the propagation of spin-waves in ferromagnetic materials before it gets damped in sub-ns to tens of ns), damping, reversal of spins (characteristic time scale few ps – few hundred ps, useful for in magnetic recording technology) and vortex core switching (few tens of ps – several ns). Finally, the slowest one is the domain wall dynamics which typically occurs between few nanoseconds (ns) to few  $\mu\text{s}$ .

When a very short (in order of fs) high energy laser pulse falls on a magnetized ferromagnetic sample, it causes an ultrafast demagnetization within about 500 fs. The physical origin behind this effect is still a topic of intense debate. However, broadly, different physical mechanisms namely, excitation of stoner pairs, Spin Orbit coupling, coupling with the electromagnetic field via a terahertz emission, and scattering of spins with impurity centers or phonons are responsible for the demagnetization process. As soon as the laser pulse is withdrawn, the system tries to get back its equilibrium state via remagnetization process. This initially occurs via fast relaxation (within 1-10 ps) due to the exchange of energy from hot electrons and spins to the lattice which can be phenomenologically described by a three-temperature model. Subsequently, there is a slow recovery of magnetization via the diffusion of electron and lattice heat to the surroundings. In the course of the slow relaxation process, the system also undergoes a precessional motion about the effective magnetic field, which eventually damps out within few ns.

### **3.4.2.2. Primary Components of the Setup**

#### **Laser System**

The generation of ultrashort laser pulses of required wavelength involves a composite laser system consisting of three lasers [32-34]. First, an array of twenty diode lasers is used to pump a solid

state laser. The CW output of the diode laser bars, after collimated with a cylindrical micro-lens, is coupled to an optical fiber bundle which efficiently directs the beam towards the solid state laser.

The diode pumped solid state laser (also known as DPSS or Millennia) uses  $\text{Nd}^{3+}$  ions doped in a Yttrium Vanadate crystalline matrix ( $\text{Nd:YVO}_4$ ) to serve as the gain medium. The monochromatic output of the diode laser overlaps with the absorption spectra of the  $\text{Nd}^{3+}$  ion. The  $\text{Nd}^{3+}$  is a four level system which primarily emits photons of wavelength 1064 nm due to the transition of electron from  $4F_{3/2}$  level to  $4I_{1/2}$  level. Subsequently, a lithium triborate (LBO) nonlinear crystal is used for frequency doubling to convert the output wavelength to  $\lambda = 532$  nm. A temperature regulator and a shutter are also attached to the cavity to ensure constant  $\lambda$  at the output (with maximum power 10 W) and to block the beam when necessary.

The output of DPSS finally pumps a Ti-sapphire oscillator (Tsunami). Here the lasing medium is titanium ions ( $\text{Ti}^{3+}$ ) doped sapphire ( $\text{Al}_2\text{O}_3$ ) crystal. Tsunami employs regenerative acousto-optic mode locking mechanism to produce the output laser pulses of  $\sim 70$  fs pulse width at 80 MHz repetition rate, with output wavelength tunable between 700 nm to 1080 nm. To achieve that, a longer cavity is required, which is obtained by a ten-mirror folded arrangement. However, the generation of a shorter pulse comes with a greater frequency distribution within a pulse, due to the Heisenberg uncertainty principle (time-bandwidth product of a Gaussian pulse is 0.441). As the refractive index ( $n$ ) depends on frequency, there is a distribution of  $n$  in a pulse resulting in a variation of velocity. The variation is called as the group velocity dispersion (GVD). In Tsunami, the intracavity GVD, the working frequency and corresponding bandwidth of the output laser can be controllably tuned using a four prism and slit arrangement. During the experiment, we keep the wavelength of the output beam constant at around 800 nm because our Si-based photo detectors are most sensitive near that wavelength.

### **Second Harmonic Generator (SHG)**

One part of the output beam from Tsunami is fed to a second harmonic generator (SHG) to produce the second harmonic beam of wavelength  $\lambda = 400$  nm, which is used to pump the sample. The pulses of the other part of the beam are time delayed and used to probe the dynamics. Inside the SHG cavity, a nonlinear crystal of barium betaborate (BBO) is utilized for the frequency doubling. The conversion efficiency of BBO is higher as compared to LBO crystal. A prism separates the second harmonic from the residual fundamental beam. The fundamental beam, however, cannot

pass through because of the high reflective coating on the prism at infrared wavelength. The second harmonic is then guided to the output end by a pair of prisms which make the beam roughly parallel to the fundamental beam and compensate the beam ellipticity. These prisms also have anti-reflection (AR) coating at second harmonic wavelength to minimize any reflection loss from prism surfaces.

### 3.4.2.3. Experimental Setup

The homebuilt TR-MOKE microscope in our laboratory [35] works on two color collinear pump-probe geometry, where the axis of the pump beam (the second harmonic output with wavelength 400 nm) and the probe beam (the fundamental beam) are superposed before the beams fall onto the sample. The schematic diagram of the setup is presented in Fig. 3.25.

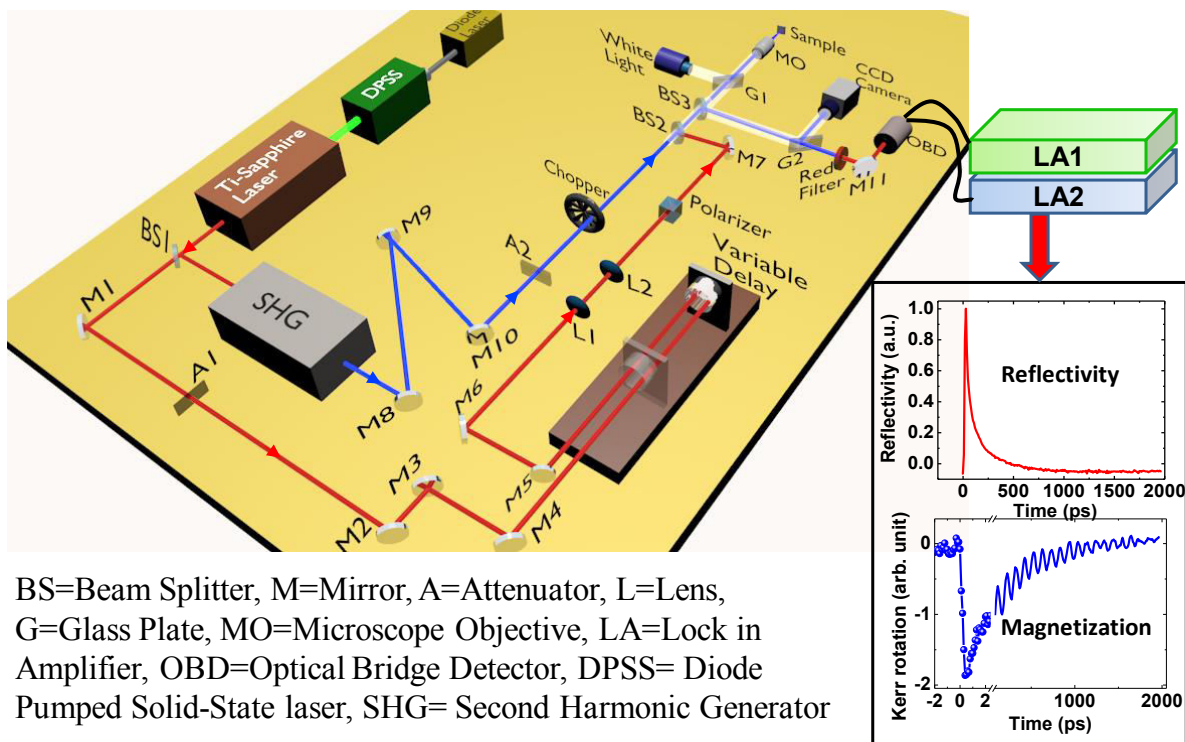


Figure 3.25: Schematic diagram of the time-resolved magneto-optical Kerr effect (TR-MOKE) microscope.

The fundamental beam from the Ti-sapphire pulsed laser source is divided into two parts by a 70:30 beam splitter. The intense part goes through the SHG to produce the pump beam, which is then guided towards the sample with the help of steering mirrors. The other part (the fundamental

probe beam) goes through a retro-reflector fixed on an automated variable delay stage on the path of the probe beam. By moving the retro-reflector back and forth it is possible to introduce the desired optical path difference between pump and probe beams, which actually corresponds to the time delay in this experiment. Subsequently, both the beams are spatially overlapped using a beam combiner and are collinearly focused onto the sample using a single microscope objective (MO: M-40X, N.A. = 0.65). The microscope objective focuses the probe beam to a diffraction limited spot size ( $\sim 800$  nm) on the sample surface while the other is slightly defocused with a spot size of  $\sim 1$   $\mu\text{m}$  because of chromatic aberration. The higher intensity of the pump beam perturbs the equilibrium magnetization of the sample, thereby inducing the dynamics. This dynamics affects the Kerr rotation of the reflected probe beam, which is in turn dependent on the time delay between pump and probe pulses. By changing the retro-reflector position on the delay stage by small steps, the time evolution of the magnetization dynamics (along with the total reflectivity signal) is measured by an optical bridge detector (OBD) in a phase-sensitive manner (the operation of OBD is described in static-MOKE section). The direction of the applied bias magnetic field is slightly tilted with respect to the magnetic anisotropy direction, so as to get a finite demagnetizing field along the direction of the pump pulse.

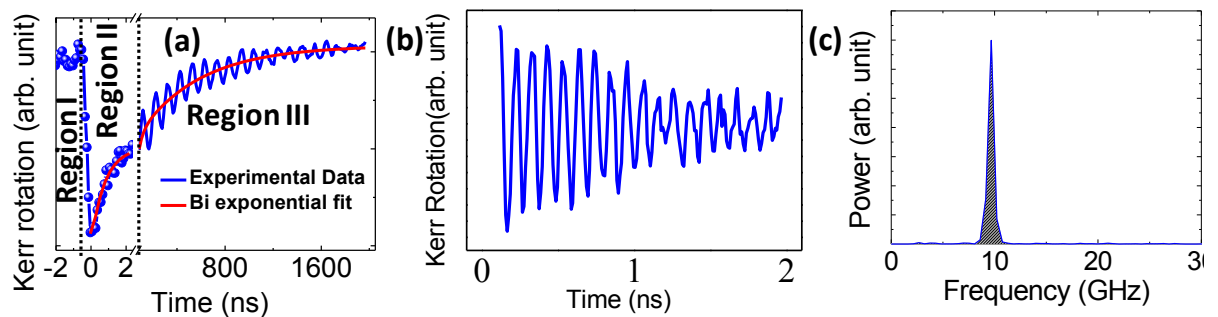


Figure 3.26: (a) Typical time-resolved Kerr rotation data taken from a  $\text{Ni}_{80}\text{Fe}_{20}$  (7 nm)/[Co (0.5 nm)/Pd (1 nm)]<sub>5</sub> multilayered sample with an out of plane bias field of 2.5 kOe. (b) precessional oscillation part of the time-resolved data and (c) fast Fourier transform of Fig. 3.26b.

Figure 3.26a shows a typical time-resolved Kerr rotation data where the different temporal regions are indicated. The Region I ( $t < 0$ ) is also known as negative delay region where the sample is probed before the arrival of pump pulse and the equilibrium magnetization under external bias field is obtained. Region II (up to few tens of ps) contains a sharp demagnetization (within 500 fs) followed by a fast relaxation. In Region III, a slower relaxation is observed together with a

precession of magnetization around its new equilibrium position. Figure 3.26b presents the precessional oscillation data extracted by subtracting the bi-exponential background. The corresponding fast Fourier transform (FFT) spectrum is depicted in Fig. 3.26c which gives the precession frequency.

#### **3.4.2.4. Some Routine Alignments**

The collinear alignment of the pump and probe beam is very crucial in this experiment. Therefore, some routine alignment procedures are practiced before each experiment is started:

1. Firstly, using external micrometer controllers of Tsunami, the power of the Tsunami output is maximized while optimizing the spectrum for desired central wavelength ( $\lambda_0 = 800$  nm) and FWHM ( $\sim 12$  nm or more).
2. The retro-reflector (RR) alignment is checked by observing the position of the beam after RR. If the beam moves by moving the RR position, mirrors before RR are adjusted to stop the shift.
3. The overlap of the pump and probe beam is then checked after the beam combiner. If the alignment is correct, both the beams will follow the same path.
4. Next, we check whether the beams are co-axial with the microscope objective (MO). For that we check the beam positions at the back aperture of MO. Any misalignment of the beams is adjusted by changing the tilts of the respective mirrors. The adjustment is fine tuned by monitoring the pump and probe spots falling on to a substrate by a CCD camera. The MO is moved back and forth about its focus position and any consequent movement of the center(s) of the pump and/or probe spot(s) on the screen implies that the beam(s) is (are) not co-axial with the MO.
5. Finally, the alignment of the OBD is adjusted by superposing the back reflected beam from OBD with the incident beam.
6. After adjusting the optical components, the time-resolved reflectivity data from a test Si substrate is recorded and its relaxation rate is compared with the standard data to verify the alignment condition.

## References

- [1] "Sputtering by Particle Bombardment," Springer, (2007).
- [2] D. McMullan, "Scanning Electron Microscopy 1928–1965," *Scanning*. **17**, 175 (1995).
- [3] M. A. Moram and M. E. Vickers, "X-ray diffraction of III-nitrides," *Rep. Prog. Phys.* **72**, 036502 (2009).
- [4] S. Foner, "Versatile and Sensitive Vibrating-Sample Magnetometer," *Rev. Sci. Instrum.* **30**, 548 (1959).
- [5] G. Binnig, C. F. Quate, and C. Gerber, "Atomic Force Microscope," *Phys. Rev. Lett.* **56**, 930 (1986).
- [6] C. V. Raman, "A change of wave-length in light scattering," *Nature* **121**, 619 (1928).
- [7] P. H. Gammon, H. Kiefte, and M. J. Clouter, "Elastic constants of ice samples by Brillouin spectroscopy," *J. Phys. Chem.* **87**, 4025 (1983).
- [8] F. Li, Q. Cui, Z. He, *et al.*, "High pressure-temperature Brillouin study of liquid water: Evidence of the structural transition from low-density water to high-density water," *The J. Chem. Phys.* **123**, 17 (2005).
- [9] E. Courtens, J. Pelous, J. Phalippou, *et al.*, "Brillouin-scattering measurements of phonon-fracton crossover in silica aerogels," *Phys. Rev. Lett.* **58**, 128 (1987).
- [10] S. Reiss, G. Burau, O. Stachs, *et al.*, "Spatially resolved Brillouin spectroscopy to determine the rheological properties of the eye lens," *Biomedical Optics Express*. **2**, 2144 (2011).
- [11] L. Brillouin, "Diffusion of light and x-rays by a transparent homogeneous body," *Ann. Phys.* **17**, 88 (1922).
- [12] L. I. Mandelstam, *Zh. Russ. Fiz-Khim. Ova.* **58**, 381 (1926).
- [13] E. Gross, "Change of Wave-length of Light due to Elastic Heat Waves at Scattering in Liquids" *Nature* **126**, 201 (1930).
- [14] J. R. Sandercock, "Second Int. Conf. on Light Scattering in Solids, eds M. Balkanski," Flammarion, Paris, (1971).
- [15] R. Mock, B. Hillebrands, and J. R. Sandercock, "Construction and performance of a Brillouin scattering set-up using a triple-pass tandem Fabry-Perot interferometer," *J. Phys. E.* **20**, 656 (1987).

- [16] W. Wettling, R. S. Smith, W. Jantz, *et al.*, "Single Crystal Fe Films Grown on GaAs Substrates," *J. Magn. Magn. Mater.* **28**, 299 (1982).
- [17] J. R. Sandercock and W. Wettling, *IEEE Trans. Magn.* **14**, 442 (1978).
- [18] J. R. Sandercock, "Operator Manual for the Tandem Fabry-Perot Interferometer," (1999).
- [19] J. R. Sandercock, "Operator manual of TANDEM FABRY-PEROT INTERFEROMETER TFP-1," (2010).
- [20] V. E. Demidov, S. O. Demokritov, B. Hillebrands, *et al.*, "Radiation of spin waves by a single micrometer-sized magnetic element," *Appl. Phys. Lett.* **85**, 2866 (2004).
- [21] G. Gubbiotti, G. Carlotti, M. Madami, *et al.*, "Setup of a new Brillouin light scattering apparatus with submicrometric lateral resolution and its application to the study of spin modes in nanomagnets," *J. Appl. Phys.* **105**, 07D521 (2009).
- [22] A. A. Serga, T. Schneider, B. Hillebrands, *et al.*, "Phase-Sensitive Brillouin Light Scattering Spectroscopy from Spin-Wave Packets," *Appl. Phys. Lett.* **89**, 063506 (2006).
- [23] K. Vogt, H. Schultheiss, S. J. Hermsdoerfer, *et al.*, "All-Optical Detection of Phase Fronts of Propagating Spin Waves in a Ni<sub>81</sub>Fe<sub>19</sub> Microstripe," *Appl. Phys. Lett.* **95**, 182508 (2009).
- [24] F. Fohr, A. A. Serga, T. Schneider, *et al.*, "Phase-Sensitive Brillouin Scattering Measurements with a Novel Magneto-Optic Modulator," *Rev. Sci. Instrum.* **80**, 043903 (2009).
- [25] M. Bauer, O. Büttner, S. O. Demokritov, *et al.*, "Observation of Spatiotemporal Self-Focusing of Spin Waves in Magnetic Films," *Phys. Rev. Lett.* **81**, 3769 (1998).
- [26] A. Serga, S. Demokritov, B. Hillebrands, *et al.*, "Self-Generation of Two-Dimensional Spin-Wave Bullets," *Phys. Ref. Lett.* **92**, 117203 (2004).
- [27] H. Schultheiss, C. W. Sandweg, B. Obry, *et al.*, "Dissipation Characteristics of Quantized Spin Waves in Nano-Scaled Magnetic Ring Structures," *J. Phys. D: Appl. Phys.* **41**, 164017 (2008).
- [28] J. Kerr, "On Rotation of the Plane of Polarization by Reflection from the Pole of a Magnet," *Philos. Mag. Series 5.* **3**, 321 (1877).
- [29] M. Freeman, R. Ruf, and R. Gambino, "Picosecond pulsed magnetic fields for studies of ultrafast magnetic phenomena," *IEEE Trans. Magn.* **27**, 4840 (1991).

- [30] A. Barman, V. V. Kruglyak, R. J. Hicken, *et al.*, "Dependence of anisotropy and damping on shape and aspect ratio in micron sized Ni<sub>81</sub>Fe<sub>19</sub> elements," J. Appl. Phys. **95**, 6998 (2004).
- [31] A. Barman, S. Wang, and H. Schmidt, "Ultrafast Magnetization Dynamics in High Perpendicular Anisotropy [Co/Pt]<sub>n</sub> Multilayers," J. Appl. Phys. **101**, 09D102 (2007).
- [32] U. S. Manual, "Tsunami: Mode-locked Ti:sapphire Laser," (Spectra-Physics, California, USA, 2002).
- [33] U. S. Manual, "Model 3980: Frequency Doubler and Pulse Selector," (Spectra-Physics, California, USA, 2002).
- [34] U. S. Manual, "Millenia Pro s-Series: Diode-Pumped, CW Visible Laser System," (Spectra-Physics, California, USA, 2007).
- [35] A. Barman and A. Haldar, "Solid State Physics Vol. 65, eds E. Camley Robert & L. Stamps Robert (pp.1-108)," Academic Press, (2014).

## Chapter 4

# 4. Numerical methods

---

### 4.1. Introduction

In case of ferromagnetic thin films with uniform magnetization, the magnetization dynamics can be determined under the macrospin formalism as described in chapter 2. Here, the non-linear ordinary differential LLG equation is linearized under small angle approximation to extract the spin wave (SW) frequency and other material parameters. However, for materials with finite boundaries, e.g., in case of multilayered and/or patterned structures, the calculations are not straight forward. Basically, the finite magnetic boundaries are associated with the occurrence of uncompensated dipoles at the surface, which produce demagnetizing field opposite to the external bias field. The information about the distribution of demagnetizing field (which is in fact dependent on the geometry) is extremely crucial for a proper understanding of the magnetization dynamics. To determine the local demagnetizing field profile and to calculate the consequent spin wave properties of non-uniformly magnetized samples, various techniques have been developed. One of the most popular methods is micromagnetic simulations, where the magnetization is considered to be a continuous function of position, the sample is divided into large number of cells where the dynamic motion of each cell is considered as a macrospin interacting with the neighboring cells by short-range exchange and long-range dipolar interactions under the effect of magnetocrystalline anisotropy and external magnetic fields. Also, there exist other theoretical models, which, under certain assumptions, calculate the magnetic parameters. In this thesis work, we have employed both micromagnetic simulations (using object oriented micromagnetic simulator and Mumax3) and a combination of analytical and numerical technique (using plane wave method) to analyze the character of the dynamic magnetization of the studied systems.

## 4.2. Micromagnetic Simulations

Micromagnetic Simulations [1] is an efficient tool for studying a wide variety of magnetic phenomena including magnetization reversal and dynamics. Based on the finite difference method (FDM) or finite element method (FEM), this technique utilizes the continuum theory to estimate the magnetic features of several nanometers length scale in terms of the local arrangement of magnetic moments.

In case of FDM, The system space is discretized into a number ( $N$ ) of regular cubic cells. Thus the continuous solution domain is replaced by a discrete set of lattice points and the domain boundaries are replaced by their discrete counterparts. Subsequently, each cell is assigned with a magnetization vector and their relative interactions are taken into account by the minimization of total energy. Although FDM features a faster computation as compared to FEM, it is not applicable for complicated geometry like curved boundary or irregular microstructures. A few examples of FDM simulators are Object Oriented Micromagnetic Frameworks (OOMMF), LLG Simulator, MicroMagus, Mumax etc.

The above mentioned problem is solved by using FEM. Here the system is discretized into finite elements, which can be two dimensional (like triangles, squares, or rectangles) or three-dimensional (like tetrahedrons, cubes, or hexahedra) depending on the dimension and shape of the system. Despite reproducing complex geometries easily, this method is much slower as compared to the FDM. Examples of FEM simulators include NMAG, MAGPAR etc.

As stated earlier, we have used OOMMF [2] and Mumax3 [3] micromagnetic simulators during this thesis work. Although both OOMMF and Mumax3 use FDM based discretization, the latter is more advanced because of its faster speed, high performance and low memory requirements. Another difference between them is their programming language: while OOMMF is written in C++ and Tcl script, Mumax uses GO and CUDA. Here, the LLG equation is solved in space and time at temperature  $T=0$  K. The input parameters (like bulk saturation magnetization, exchange stiffness constant, magnetocrystalline anisotropy, Zeeman field, sample structure and dimensions and the magnetic field geometry) and the initial conditions of any problem are given using external script file. One of the advantages of using micromagnetic simulations is that one can feed the sample structure to the software by using an image file. This helps to incorporate any

structural artifacts of the system under consideration in the simulation. The sample space is divided into identical cuboidal cells with dimensions equal to or less than the exchange length. Each cell is then assigned with a single spin. Subsequently, the LLG equation (Eqn. 2.19) is solved assuming the magnetization to be a continuous function of position and deriving relevant expressions for different energy terms. Then the stable equilibrium state is achieved by minimizing the total Gibb's free energy with respect to the magnetization.

Before starting the calculations for magnetization dynamics, the system is brought to equilibrium under the effect of static bias magnetic field. First, a large enough bias field is applied to fully magnetize the sample and allow the magnetization to relax for a long time. The applied field is then reduced to the required bias field value and the magnetization is further allowed to relax for a longer time. During each step, the magnetization configuration is updated by two types of evolvers: first one is a time evolver which tracks the LLG dynamics and the second one is an energy minimization evolver which calculates the local minima in energy by using energy minimization techniques. A 4th order Runge Kutta evolver is used as a time evolver which solves LLG equation considering an ordinary differential equation in time. The evolvers are connected to corresponding drivers, namely, time driver and minimization driver, which control the time and minimization evolver, respectively. The job of the driver is to determine the completion of a simulation stage depending upon the stopping criteria described in the script file. The stopping criterion is determined by the convergence of the maximum torque  $\mathbf{m} \times \mathbf{H}$ , where  $\mathbf{m} = \mathbf{M}/M_s$ . In the script file, users provide either the stopping time or the stopping value of  $d\mathbf{m}/dt$ , which is set in such a way that the value of maximum torque ( $\mathbf{m} \times \mathbf{H}$ ) should be less than  $10^{-6}$  A/m. The simulation will terminate when the stopping criteria will match.

After the system acquires a stable, static equilibrium state under the bias magnetic field, the magnetization dynamics is triggered under a uniform excitation (spatially and temporally varying 'sinc' function) to simulate the TR-MOKE (BLS) results. In case of uniform excitation, the optical perturbation used in the experiment is mimicked in the form of a pulsed magnetic field of rise time of 50 ps and peak amplitude of 30 Oe applied perpendicular to the sample plane. The time evolution of the different components of dynamic magnetization averaged over the entire sample volume are then recorded for a total timescale of 4 ns at intervals of 10 ps. A small value for damping parameter (say 0.008 for  $\text{Ni}_{80}\text{Fe}_{20}$ ) was assumed during the dynamic simulation.

### 4.2.1. Calculation of Power and Phase Profiles of the Resonating Modes

To analyze the character of the resonant magnonic modes, we have further calculated the spatial profiles of the corresponding dynamic magnetization component [4]. The output files of the simulations actually consist of a number of ‘.omf’ files containing the information about the magnetization distribution ( $M(r, t)$ ) over the entire simulation volume at a particular instance of simulation time. These files can be used to inspect the time as well as spatial distribution of the spin wave amplitude, phase and propagation. For that, first, the  $M(r, t)$  is rearranged into three four dimensional (4-D) matrices, viz.,  $m_i(x, y, z, t)$ ,  $m_j(x, y, z, t)$  and  $m_k(x, y, z, t)$ , where each matrix corresponds to each component of magnetization. Subsequently, one spatial co-ordinate (say  $z$ ) of one of the 4-D matrices (say  $m_k$ ) is fixed, which reduces the matrix dimension to three ( $m_k(x, y, z_m, t)$ ). Then a discrete Fourier transform with respect to the time dimension  $t$  is performed for each elemental cell. Next, the power value of the FFT spectrum corresponding to the desired frequency is extracted and plotted for each cell. This gives the in-plane space dependent power profiles at a particular resonance frequency. Similarly, the phase profile can be plotted by extracting the phase of complex dynamic magnetization. The frequency resolution depends on the simulation time window and the spatial resolution depends on the discretization used during the micromagnetic simulations. The expressions for the power and phase profiles for a particular resonant mode at  $f=f_r$  can then be written as:

$$\text{Power: } P^{z_m, f_r}(x, y) = 20 \log_{10} |\tilde{M}^{z_m}(f_r, x, y)| \quad \dots\dots\dots(4.1)$$

$$\text{Phase: } \phi^{z_m, f_r}(x, y) = \tan^{-1} \left[ \frac{\text{Im}(\tilde{M}^{z_m}(f_r, x, y))}{\text{Re}(\tilde{M}^{z_m}(f_r, x, y))} \right] \quad \dots\dots\dots(4.2)$$

### 4.3. Plane Wave Method (PWM)

The PWM is extensively used to calculate the excitation spectra (band structure) for an inhomogeneous or periodic geometry, e.g., in electronic, photonic, phononic or magnonic crystals [5-8]. This is a simple method which can give a full spectra of eigen excitations for any type of lattice, any shape of scattering centres and for various dimensions of the periodicity. In magnonic crystals (MCs), the inhomogeneity of the internal magnetic field is taken into account in the form of the superposition of plane waves, which eventually converts the LLG equation to an eigenvalue problem. The problem is subsequently solved using standard numerical routines to find out the eigenvalues (SW frequencies) and eigen vectors (amplitude of the dynamical component of the magnetization vector).

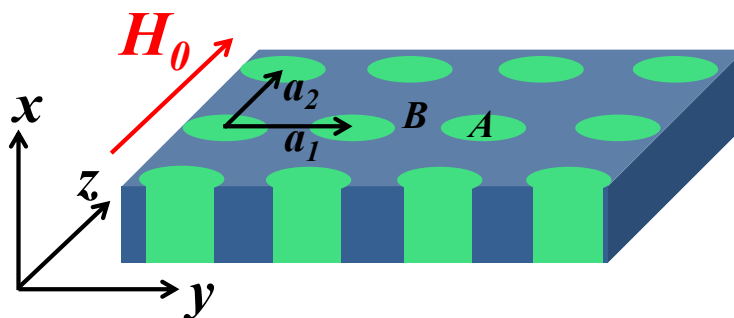


Figure 4.1: A rectangular MC formed by circular ferromagnetic elements A embedded in matrix B.

For the calculations of SW spectra, we assume the MC to be composed of an array of scattering centres of finite thickness made of ferromagnetic material *A* embedded in an infinite ferromagnetic matrix *B*. Figure 4.1 shows the schematic of a MC with circular scattering centers arranged in a rectangular array together with the co-ordinate axes. The x-axis is assumed to be normal to the surface plane and the external bias field  $H_0$  is applied in the sample plane along the z-axis. We solve the Landau–Lifshitz (LL) equation, i.e., the equation of motion of the magnetization vector  $M(r, t)$  in space and time, given by

$$\frac{\partial M(r, t)}{\partial t} = -\gamma\mu_0 M(r, t) \times H_{eff}(r, t) \quad \dots\dots\dots(4.3)$$

where  $\gamma$  and  $\mu_0$  are the gyromagnetic ratio and the permeability of vacuum, respectively ( $|\gamma|\mu_0 = 2.21 \times 10^5 \text{ (Am)}^{-1} \text{ s}^{-1}$ ).  $H_{eff}$  denotes the effective magnetic field acting on the magnetization. A negligible relaxation of magnetization is assumed in this case.

In the linear approximation, the component of the magnetization vector parallel to the static magnetic field (i.e., in  $z$  direction in this case) is constant in time  $t$ , and its magnitude is larger than the dynamic perpendicular components  $m(r,t)$ , i.e.,  $|m(r,t)| \ll M_z(r)$ , where  $M(r,t) = M_z(r) \hat{z} + m(r,t)$  and  $M_z \sim M_S$ . For monochromatic SWs,  $m(r,t)$  has the form  $m(r,t) = m(r)e^{i\omega t}$ , where  $\omega$  is the SW angular frequency. We further consider that the effective magnetic field  $H_{eff}$  consists of the uniform and constant external magnetic field  $H_0$  (which is strong enough to enforce parallel alignment of all the magnetic moments), the exchange field  $H_{ex}$  and the magnetostatic field  $H_{ms}$ . For simplicity, we neglect any contribution from the anisotropy field.

In classical limit, the time and space dependent exchange field can be written in terms of the exchange length  $l_{ex}$  as [9]:

$$H_{ex}(r,t) = (\nabla \cdot l_{ex}^2(r) \nabla m(r,t)) \quad \dots\dots\dots(4.4)$$

$$\text{where, } l_{ex}(r) = \sqrt{\frac{2A(r)}{\mu_0 M_S^2(r)}} \quad \dots\dots\dots(4.5)$$

$A(r)$  is the exchange stiffness constant.

The magnetostatic field can be divided into a static and a dynamic component,  $H_{ms}(r)$  and  $h_{ms}(r,t)$ , respectively:  $H_{ms}(r,t) = H_{ms,z} \hat{z} + h_{ms}(r) e^{i\omega t}$ . Finally,  $H_{eff}$  reads as:

$$H_{eff}(r,t) = H_0 \hat{z} + (\nabla \cdot l_{ex}^2(r) \nabla) m(r,t) + H_{ms,z} \hat{z} + h_{ms}(r) e^{i\omega t} \quad \dots\dots\dots(4.6)$$

The respective components of  $M(r,t)$  and  $H_{eff}(r,t)$  in different coordinate axes can be used to calculate the vector product on the right hand side of Eqn. 4.3, equating which with corresponding left hand side renders the expressions for the dynamic magnetization components  $m_x(r)$  and  $m_y(r)$  as follows:

$$m_x(r) = \frac{\mu_0 \gamma}{i\omega} (m_y(r) (H_0 + H_{ms}) - M_S h_{ms,y} - M_S \nabla \cdot l_{ex}^2(r) \nabla m_y(r)) \quad \dots\dots\dots(4.7)$$

$$m_y(r) = \frac{\mu_0 \gamma}{i\omega} (M_S h_{ms,y} + M_S \nabla \cdot l_{ex}^2(r) \nabla m_y(r) - m_x(r) (H_0 + H_{ms})) \quad \dots\dots\dots(4.8)$$

In the next step, all the periodic functions (both in time and space) are mapped onto the Fourier space. The material parameters  $M_S$ ,  $A$  and consequently  $l_{ex}^2$  have the periodicity of the lattice constant, i.e.,

$$M_S(\vec{r} + \vec{a}) = M_S(\vec{r}), \quad A(\vec{r} + \vec{a}) = A(\vec{r})$$

$$\text{And } l_{ex}^2(\vec{r} + \vec{a}) = l_{ex}^2(\vec{r})$$

where  $\vec{a}$  is a general lattice vector in the direction of periodicity. The Fourier transformation formulas for them are

$$M_S(r_{\parallel}) = \sum_G M_S(G) e^{iG \cdot r_{\parallel}}, \quad \dots\dots\dots(4.9)$$

$$l_{ex}^2(r_{\parallel}) = \sum_G l_{ex}^2(G) e^{iG \cdot r_{\parallel}}$$

where  $G = (G_y, G_z)$  denotes the reciprocal lattice vector of the periodic structure and  $M_S(G)$  ( $l_{ex}^2(G)$ ) is the Fourier co-efficient of  $M_S(r)$  ( $l_{ex}^2(r)$ ). The spatial dynamic components of  $M(r,t)$  and  $H_{ms}(r,t)$  can be converted by using the Bloch's theorem, i.e., as product of a plane wave with the wave vector  $q = (q_y, q_z)$  from the first Brillouin Zone and a periodic function, which can be expanded into Fourier series:

$$m(r_{\parallel}) = e^{iq_{\parallel} r_{\parallel}} \sum_G m_q(G) e^{iG \cdot r_{\parallel}} \quad \dots\dots\dots(4.10)$$

$$h_{ms}(r_{\parallel}) = e^{iq_{\parallel} r_{\parallel}} \sum_G h_{ms,q}(G) e^{iG \cdot r_{\parallel}} \quad \dots\dots\dots(4.11)$$

In general, the reciprocal lattice vector  $G$  can be calculated using the expression  $\vec{G} = (m\vec{a}^* + n\vec{b}^*)$ , where

$$\vec{a}^* = 2\pi \frac{\vec{b} \times \hat{n}}{|\vec{a} \times \vec{b}|} \quad \dots\dots\dots(4.12)$$

$$\vec{b}^* = 2\pi \frac{\hat{n} \times \vec{a}}{|\vec{a} \times \vec{b}|} \quad \dots\dots(4.13)$$

$m, n$  are integers,  $\vec{a}$  ( $\vec{a}^*$ ) and  $\vec{b}$  ( $\vec{b}^*$ ) are the lattice vectors of real (reciprocal) lattice.

The Fourier coefficient  $M_S(G)$  for  $G=0$  is given by  $M_S(G=0) = ff(M_{S,A} - M_{S,B}) + M_{S,B}$ . Here  $ff$  is the filling fraction defined as the ratio of the area of scattering centre to that of a unit cell. For  $G \neq 0$ ,  $M_S(G)$  can be calculated using the following analytical formula

$$M_S(G) = \frac{M_{S,A} - M_{S,B}}{|\vec{a} \times \vec{b}|} \int_S e^{-iGr} d^2r \quad \dots\dots(4.14)$$

Here  $M_{S,A}$  and  $M_{S,B}$  denote the magnetization of region A and B, respectively and the integration is performed over the cross-sectional area of element  $A$ . The formula for  $l_{ex}^2(G)$  has the same form as Eqn. 4.14.

On the other hand, the formulas for the Fourier coefficients of the static and dynamic magnetostatic fields,  $H_{ms,z}(r, x)$ ,  $h_{ms,x}(r, x)$  and  $h_{ms,y}(r, x)$  can be obtained by solving the Maxwell's equations with proper electromagnetic boundary conditions at both surfaces of the slab. According to Ref. [10], for the considered structure, the magnetostatic fields can be expressed as:

$$H_{ms,z}(r_{\parallel}, x) = -\sum_G \frac{M_S(G)}{G^2} G_z^2 \times (1 - \cosh(|G|x) e^{-|G|d/2}) e^{iG \cdot r_{\parallel}} \quad \dots\dots(4.15)$$

$$h_{ms,y}(r_{\parallel}, x) = -\sum_G \frac{m_y(G)}{|q+G|^2} (q_y + G_y)^2 \times (1 - \cosh(|q+G|x) e^{-|q+G|d/2}) e^{i(q+G) \cdot r_{\parallel}} \quad \dots\dots(4.16)$$

$$h_{ms,x}(r_{\parallel}, x) = -\sum_G m_x(G) \cosh(|q+G|x) \times e^{-|q+G|d/2} e^{i(q+G) \cdot r_{\parallel}} \quad \dots\dots(4.17)$$

where  $d$  is the thickness of the slab. In the works presented in this thesis, the above expressions are calculated at  $x=d/2$ , i.e., at the surface of the film.

The Eqns. 4.9 - 4.17 can be substituted into Eqns. 4.7 and 4.8 to obtain the dynamic magnetization components in the form of infinite system of equations in Fourier space:

$$\begin{aligned}
\frac{i\omega}{\gamma\mu_0} m_{x,\vec{q}}(\vec{G}) &= H_0 m_{y,\vec{q}}(\vec{G}) + \sum_{\vec{G}'} \frac{m_{y,q}(\vec{G})}{|q + \vec{G}'|^2} (q_y + \vec{G}'_y)^2 \times \left(1 - \cosh\left(|q + \vec{G}'|x\right) e^{-|q + \vec{G}'|d/2}\right) M_S(\vec{G} - \vec{G}') \\
&- \sum_{\vec{G}'} \frac{m_{y,\vec{q}}(\vec{G})}{|\vec{G} - \vec{G}'|^2} (\vec{G}_z - \vec{G}'_z)^2 \times \left(1 - \cosh\left(|\vec{G} - \vec{G}'|x\right) e^{-|\vec{G} - \vec{G}'|d/2}\right) M_S(\vec{G} - \vec{G}') \\
&+ \sum_{\vec{G}'} \sum_{\vec{G}''} (q + G')(q + G'')^2_{ex} (G'' - G') M_S(G - G'') m_{y,q}(\vec{G}) \quad \dots\dots\dots(4.18)
\end{aligned}$$

$$\begin{aligned}
\frac{i\omega}{\gamma\mu_0} m_{y,\vec{q}}(\vec{G}) &= -H_0 m_{x,\vec{q}}(\vec{G}) - \sum_{\vec{G}'} m_{x,q}(\vec{G}) \cosh\left(|q + \vec{G}'|x\right) e^{-|q + \vec{G}'|d/2} M_S(\vec{G} - \vec{G}') \\
&+ \sum_{\vec{G}'} \frac{m_{x,\vec{q}}(\vec{G})}{|\vec{G} - \vec{G}'|^2} (\vec{G}_z - \vec{G}'_z)^2 \times \left(1 - \cosh\left(|\vec{G} - \vec{G}'|x\right) e^{-|\vec{G} - \vec{G}'|d/2}\right) M_S(\vec{G} - \vec{G}') \\
&- \sum_{\vec{G}'} \sum_{\vec{G}''} (q + G')(q + G'')^2_{ex} (G'' - G') M_S(G - G'') m_{x,q}(\vec{G}) \quad \dots\dots\dots(4.19)
\end{aligned}$$

When a finite number  $N$  of reciprocal lattice vectors is considered, the above system of equations becomes finite. The problem then reduces to an eigen value problem with eigen values  $\frac{i2\pi f}{\gamma\mu_0 H_0}$  and eigen vectors  $m_{x,q}(G)$  and  $m_{y,q}(G)$ , which can be structured in a matrix form as follows:

$$\hat{M}m_q = \frac{i2\pi f}{\gamma\mu_0 H_0} m_q \quad \dots\dots\dots(4.20)$$

with the eigen vector defined as  $m_q^T = [m_{x,q}(G_1), \dots, m_{x,q}(G_N), m_{y,q}(G_1), \dots, m_{y,q}(G_N)]$ . The matrix  $\hat{M}$  is the following Block matrix

$$\hat{M} = \begin{pmatrix} \hat{M}^{xx} & \hat{M}^{xy} \\ \hat{M}^{yx} & \hat{M}^{yy} \end{pmatrix} \quad \dots\dots\dots(4.21)$$

The sub-matrices of  $\hat{M}$  are given by [8]

$$\hat{M}^{xx} = \hat{M}^{yy} = 0 \quad \dots\dots\dots(4.22)$$

$$\begin{aligned} \hat{M}_{ij}^{xy} = & \delta_{ij} + \sum_l \frac{(q + G_j)(q + G_l)}{H_0} l_{ex}^2 (G_l - G_j) M_S(G_i - G_l) \\ & + \frac{(q_y + G_{y,j})^2}{H_0 |q + G_j|^2} (1 - C(q + G_j, x)) M_S(G_i - G_j) - \frac{1}{H_0} \frac{(G_{z,i} - G_{z,j})^2}{|G_i - G_j|^2} M_S(G_i - G_j) (1 - C(G_i - G_j, x)) \end{aligned} \quad \dots\dots\dots(4.23)$$

$$\begin{aligned} \hat{M}_{ij}^{yx} = & -\delta_{ij} - \sum_l \frac{(q + G_j)(q + G_l)}{H_0} l_{ex}^2 (G_l - G_j) M_S(G_i - G_l) \\ & - \frac{1}{H_0} C(q + G_j, x) M_S(G_i - G_j) + \frac{1}{H_0} \frac{(G_{z,i} - G_{z,j})^2}{|G_i - G_j|^2} M_S(G_i - G_j) (1 - C(G_i - G_j, x)) \end{aligned} \quad \dots\dots\dots(4.24)$$

where reciprocal lattice vector indices  $i, j$ , and  $l$  are integers in the range  $\langle 1, N \rangle$ . One can solve the above system of equations for different SW wave vector  $q$  by standard numerical procedures to find the corresponding eigenvalues (which gives the SW frequency  $f$ ) and eigen vectors ( $m_q$ ). To tally the calculated dispersion with the experimentally obtained band structure via Brillouin light scattering (BLS) spectroscopy, it is required to estimate the square of the modulus of the fundamental harmonics of magnetization, i.e.,

$$I_{BLS} \propto |m_q(G = 0)|^2 \quad \dots\dots\dots(4.25)$$

Subsequently, the spatial mode profiles can also be calculated for a given wave vector and frequency, by determining the modulus of the dynamic magnetization ( $m_x(r)$ ) for each spatial point. It is noteworthy that the PWM calculations stand upon the consideration that both the scattering centre and the matrix consist of ferromagnetic materials. In case of dot or antidot array, where either the scattering centres or the matrix are made up of non-magnet, a very small value should be assigned to the material parameters in order to avoid any unphysical solutions.

## References

- [1] S.-K. Kim, "Micromagnetic Computer Simulations of Spin Waves in Nanometre-scale Patterned Magnetic Elements," *J. Phys. D: Appl. Phys.* **43**, 264004 (2010).
- [2] M. Donahue and D. G. Porter, "OOMMF User's guide, Version 1.0.," NIST Interagency Report No. 6376, National Institute of Standard and Technology, Gaithersburg, MD, URL: <http://math.nist.gov/oommf>, (1999).
- [3] A. Vansteenkiste, J. Leliaert, M. Dvornik, *et al.*, "The design and verification of MuMax3," *AIP Advances*. **4**, 107133 (2014).
- [4] D. Kumar, O. Dmytriiev, S. Ponraj, *et al.*, "Numerical Calculation of Spin Wave Dispersions in Magnetic Nanostructures," *J. Phys. D: Appl. Phys.* **45**, 015001 (2012).
- [5] V. Laude, M. Wilm, S. Benchabane, *et al.*, "Full Band Gap for Surface Acoustic Waves in a Piezoelectric Phononic Crystal," *Phys. Rev. E*. **71**, 036607 (2005).
- [6] J. O. Vasseur, P. A. Deymier, B. Djafari-Rouhani, *et al.*, "Absolute Forbidden Bands and Waveguiding in Two-dimensional Phononic Crystal Plates," *Phys. Rev. B*. **77**, 085415 (2008).
- [7] M. Krawczyk and H. Puzkarski, "Plane-wave Theory of Three-Dimensional Magnonic Crystals," *Phys. Rev. B*. **77**, 054437 (2008).
- [8] M. Krawczyk, S. Mamica, M. Mruczkiewicz, *et al.*, "Magnonic Band Structures in Two-dimensional Bi-component Magnonic Crystals with In-plane Magnetization," *J. Phys. D: Appl. Phys.* **46**, 495003 (2013).
- [9] M. Krawczyk, M. L. Sokolovskyy, J. W. Klos, *et al.*, "On the Formulation of the Exchange Field in the Landau-Lifshitz Equation for Spin-Wave Calculation in Magnonic Crystals," *Adv. Condens. Matter Phys.* **2012**, 764783 (2012).
- [10] J. Kaczer and L. Murtinova, "On the Demagnetizing Energy of Periodic Magnetic Distributions," *Phys. Status Solidi A*. **23**, 79 (1974).

## Chapter 5

# 5. Investigation of spin waves in Co/ NiFe exchange spring bilayer films using Brillouin light scattering

---

### 5.1. Introduction

The exchange spring systems are composite hard and soft magnetic systems, which are exchange coupled at their interface [1- 2]. They have been found to display characteristic structure in the magnetic hysteresis properties. The high saturation magnetization of the soft magnetic material and the high coercivity of the hard magnetic material improve the maximum energy product [3-5]. This high value of the maximum energy product and the information density that can be stored in a magnet make the exchange springs suitable candidates for the progress of both permanent magnets and recording media industry [6-8]. The strength of the exchange coupling interaction depends on the thickness of the soft magnetic material. When the thickness of the soft magnetic layer is small then the system behaves as a rigid magnet while for its higher thickness the system behaves as an exchange spring magnet. Therefore, the magnetic behaviors of the system are strongly influenced by the soft layer thickness, which allows the existence of three different magnetic regimes: the hard single-phase, the exchange coupled regime and the exchange decoupled regime. For all these behaviors, a decrease of coercivity is expected by increasing the soft layer thickness [5, 9]. However, in few cases an initial increase of coercivity has been observed, which finds no explanation [7, 10]. The understanding of this peculiar behavior is very important from the fundamental and technological viewpoints, allowing an improvement of the actual capabilities to finely tailor the properties of the material. In this respect understanding of surface and interface magnetism in multilayers is crucial. One of the proven methods for this is to probe spin waves as they are sensitive to exchange coupling and other effective fields in magnetic multilayer. Therefore, spin wave excitations in such systems reveal interlayer exchange, anisotropy energies and other important parameters. Spin wave investigations by light scattering experiments were reported in exchange coupled systems, e.g. Co/CoPt [11-12], FeTaN/FeSm/FeTaN [13], Co/Pd-NiFe [14]. On the other hand, time-resolved magneto-optical

Kerr effect measurements on FePt/NiFe exchange spring bilayers showed a strong variation in spin wave mode frequencies with variation of NiFe layer thickness due to the variation of exchange field and the ensuing spin twist structure in the NiFe layer [15]. Theoretical modelling of the spin twist structures in an exchange spring system and coupled multilayers have also been presented by several authors [16-18].

In this chapter, we report the investigation of Brillouin light scattering (BLS) study in Co/ Ni<sub>80</sub>Fe<sub>20</sub> (Py) exchange spring bilayer systems with varying Py layer thickness. As opposed to the previous reports on magnetization dynamics in Co (100nm)/ Py (50nm) bilayer films [19-20] we have used much thinner ferromagnetic layers and attempted to increase the anisotropy of the Cobalt layer by elevating the substrate temperature during deposition to assist greater differences in magnetic parameters of the constituent layers of the exchange spring bilayer system. Here, we have addressed the phenomena occurring at the soft/hard interface and their relation with the magnetic properties of the system, such as the degree of soft/hard exchange coupling and the coercivity behavior as a function of the Py film thickness.

## 5.2. Experimental Details

The Co/Py bilayers were grown by dc magnetron sputtering onto self-oxidized silicon [100] substrates at  $2 \times 10^{-8}$  Torr base pressure. First a 10 nm Co layer was deposited from a Co target (99.99%) at a substrate temperature 500° C. The optimum value of the substrate temperature for the Co layer was determined by a careful investigation of the substrate temperature dependence of its coercivity. Py layers with thickness varying between 10 and 30 nm were then grown at room temperature from Py target (99.99%) on the Co layer. All deposition was performed at working pressure of about 10 mTorr and at a dc power of 400 W for Co and 350 W for Py. The topography and roughness of the films were measured by atomic force microscopy (AFM). The quasistatic magnetization reversal properties were measured using a longitudinal magneto-optic Kerr effect (MOKE) magnetometer using a He-Ne laser operating at 632.8 nm. Thermal magnons were measured in these bilayer films using BLS technique to investigate the role of interfacial exchange coupling ( $J_I$ ). BLS is a powerful technique for the investigation of spin waves in magnetic thin films (transparent or opaque), multilayers and patterned magnetic structures [21-23]. This technique relies on inelastic light scattering process due to interaction between incident photons

and magnons. Magnons are created or annihilated during the interaction with photons. A frequency shift is observed along with the laser frequency taking into account energy and momentum conservation. The BLS experiments were performed in backscattering geometry using a single-mode solid state laser operated at 532 nm (wave number  $k_i = 1.181 \times 10^7$  rad/m) and a Sandercock-type six-pass tandem Fabry-Perot interferometer. It enables wave vector resolved measurements of the spin waves by changing the angle of incidence ( $\theta$ ) of the laser beam.

### 5.3. Results and Discussions

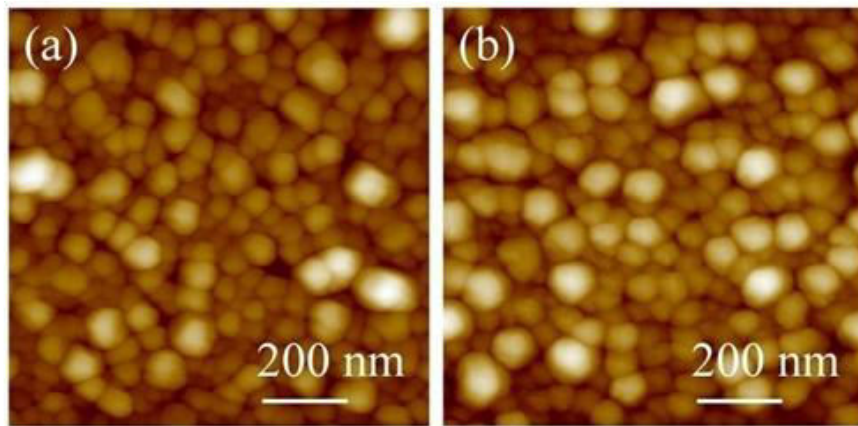


Figure 5.1: AFM images of (a) Co (10nm)/ Py (10nm), (b) Co (10nm)/ Py (20 nm) bilayer films.

In Fig. 5.1, AFM images show that the Co/Py bilayer films are continuous. It consists of interconnected grains with average grain size 10–20 nm and the sample roughness of the film varies between 1.7 and 3.1 nm with increasing Py film thicknesses. The surface consists of an arrangement of homogeneously distributed islands which has been formed during the intermediate growth state. The islands are not well separated but seem to be connected due to coalescence.

The room temperature MOKE hysteresis loops measured within a laser spot size of about 50  $\mu\text{m}$  from the Co/Py bilayer films are shown in Fig. 5.2. The coercivity ( $H_C$ ) of the Co (10 nm)/ Py ( $t$ ) films varies systematically as 435, 335, 159 and 132 Oe for  $t = 10, 20, 25,$  and 30 nm, respectively. We mentioned earlier that we intended to enhance the  $H_C$  value of Co base layer by optimizing substrate temperature.

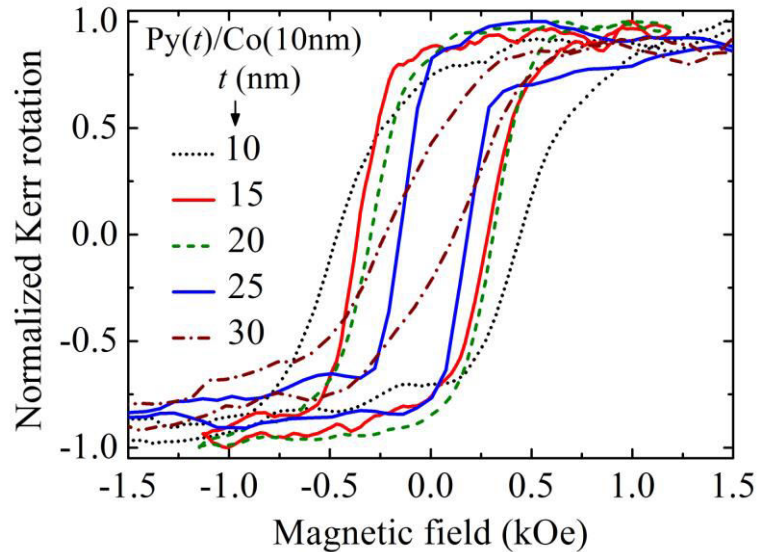


Figure 5.2: Magnetic hysteresis loops for all the Co (10nm)/ Py (10–30nm) bilayer films measured with static MOKE experiment.

Significant increase in  $H_C$  is found in the Co single layer film deposited at around  $500^\circ\text{C}$  substrate temperature ( $H_C = 727\text{ Oe}$ ) as compared with the Co film deposited on a substrate at room temperature ( $H_C = 243\text{ Oe}$ ). The enhanced coercivity of the Co layer in combination with its greater saturation magnetization and exchange stiffness constant is expected to have a greater influence on the exchange spring behavior of the bilayer samples. We observe that bilayers with Py layer thickness  $\leq 25\text{ nm}$  have a more square-like hysteresis loop and the squareness suddenly decreases for Py layer thickness  $>25\text{ nm}$ . The laser spot penetrates about  $12\text{ nm}$  (optical skin depth) down from the surface of the Py layer and thus, the MOKE data indicates that the top  $12\text{ nm}$  of the Py layer is strongly exchange coupled with the Co layer for Py layer thickness up to  $25\text{ nm}$  and beyond that the coupling becomes weaker. The coercive field of the Co (10 nm)/ Py (30 nm) bilayer is  $132\text{ Oe}$ , which is still much greater than a single Py layer, ensuring a significant contribution from the Co layer for the sample with a Py as thick as  $30\text{ nm}$ .

We have further studied thermally excited magnons to understand the effect of the interfacial exchange coupling in our exchange spring bilayers. Figure 5.3 shows the field dependence of BLS spectra for Co (10 nm)/ Py (25nm) sample. A bias magnetic field ( $H$ ) was applied in the plane of the film and the angle of incidence ( $\theta$ ) was chosen as  $45^\circ$ , which results in a magnon wave number  $q = k_i \sin \theta = 1.67 \times 10^7\text{ rad/m}$ .

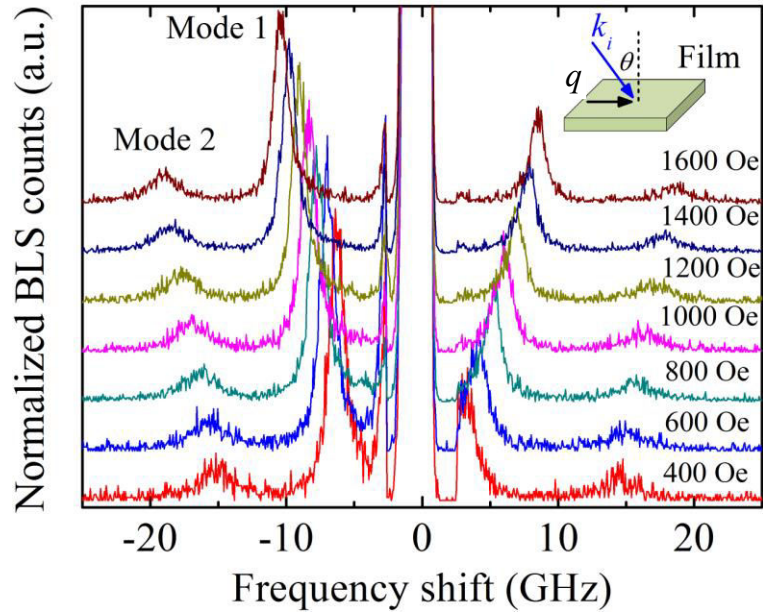


Figure 5.3: BLS spectra for Co (10nm)/ Py (25nm) film at different in-plane bias magnetic fields. Angle of incidence is  $\theta = 45^\circ$ . The measurement geometry is shown in the inset.

The BLS spectra reveal two distinct peaks in the bilayer films. Optical and acoustic spin wave modes were observed previously in a thicker bilayer film Co (100 nm)/ Py (50 nm) by Crew et al. [20]. However, our observed modes have different origin. The peak (-2.7GHz) near zero frequency is due to measurement artifact.

Further measurements reveal that the lower frequency mode has a pronounced dispersion with the in-plane wave vector ( $q$ ) and it corresponds to the surface wave, which propagates in the film plane (Damon-Eshbach mode). On the other hand, negligible dispersion with  $q$  is observed for the higher frequency mode and it is identified as the volume mode, which propagates perpendicular to the surface of the film, also known as the perpendicular standing spin wave (PSSW). Experimental dispersion results of these two modes are shown in one of the insets of Fig. 5.4.

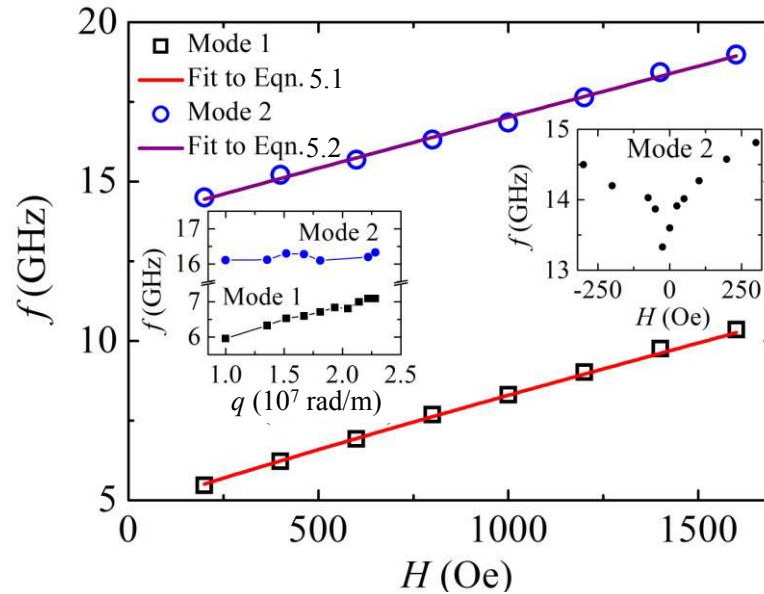


Figure 5.4: Spin wave frequencies of mode 1 and mode 2 as a function of magnetic field for Co (10 nm)/ Py (25 nm) film (symbols) along with the fits (line). Dispersions ( $f(q)$ ) of the two modes have been shown in one of the insets. The symbols correspond to the experimental data while the lines joining the symbols are only guide to the eyes. Other inset shows the field hysteresis of mode 2 in low field regime.

The bias field dependences of the two modes are shown in Fig. 5.4. Frequency of the lower mode becomes very small in low field regime ( $<200$  Oe) and could not be reliably detected using the BLS experiment. Therefore, we concentrated on the higher frequency mode or the PSSW mode for field hysteresis in the low field regime from positive (all layers along the field direction) to negative field direction and it is shown in another inset of Fig. 5.4. A minimum of the frequency was observed at  $-25$  Oe during the field hysteresis, which is a signature of the presence of an exchange coupling between the layers. For fields above  $-25$  Oe the magnetization of the bilayer is parallel with the field direction. Therefore, a quantitative analysis for the bias field dependence of the surface wave frequency can be made by incorporating an effective exchange field ( $H_{ex}$ ) in  $H$  as  $H_{eff} = H + H_{ex}$ . The data were analyzed following the approach of Rezende et al. [24]. The authors have extended the theory of two magnon scattering by Arias and Mills [17] for non-zero wave vector ( $q \neq 0$ ) magnons. Neglecting uniaxial anisotropy field, the frequency of the magnons is given by

$$f = \frac{\gamma}{2\pi} \left\{ \left( H_{eff} + 2\pi M_S q t \sin^2 \varphi + \frac{2A}{M_S} q^2 \right) \times \left( H_{eff} + 4\pi M_{eff} - 2\pi M_S q t + \frac{2A}{M_S} q^2 \right) \right\}^{1/2} \dots\dots(5.1)$$

where  $t$ ,  $\gamma$ ,  $M_S$ ,  $A$  and  $\varphi$  are the thickness, gyromagnetic ratio, saturation magnetization, exchange stiffness constant of Py film and the angle of magnon wave vector in the film plane, respectively. Gyromagnetic ratio is connected to magneto-mechanical ratio  $g$  by  $\gamma = g\mu_B/\hbar$  where  $\mu_B$  is the Bohr magneton and  $\hbar$  is the reduced Planck constant. Surface anisotropy ( $H_S$ ) is included in the effective magnetization ( $M_{eff}$ ) as  $4\pi M_{eff} = 4\pi M_S + H_S$ . For  $\varphi > \varphi_c$ , where the critical angle  $\varphi_c = \sin^{-1} \sqrt{H/(H + 4\pi M_S)}$ , the spin waves are surface waves whereas for  $\varphi < \varphi_c$  they are volume waves. The critical angle in our case is found to be  $26^\circ$  for  $H = 1600$  Oe, which is the maximum field applied in this experiment. The data was fitted with Eqn. 5.1 using  $t = 25$  nm,  $A = 1.3 \times 10^{-6}$  erg/cm and  $4\pi M_S = 10.05$  kG for Py while leaving  $M_{eff}$ ,  $g$  and  $\varphi$  as fitting parameters. The fitting yields  $g = 2.15$ ,  $\varphi = 33^\circ$  and  $4\pi M_{eff} = 5.353$  kG. Larger  $g$  values have been observed before and can be explained by taking the bottom Co layer into account [25], while other parameters have reasonable values. We should mention here that the intensity of the magnon modes decreases with increasing magnetic field and the effect is more pronounced for the low frequency modes compared to the higher frequency modes discussed here. It is also in agreement with the previous observations [20]. The PSSW mode forms along the thickness of the bilayer film and is therefore sensitive to both the parameters for Py and Co layers in the Co (10 nm)/ Py (25 nm) bilayer. Spin configuration varies across the bilayer and a rigorous theoretical model including the spin twist structure will be required for detailed analysis. Nortemann et al. have proposed a semiclassical numerical model for understanding the spin wave frequencies in this type of systems [16]. A qualitative analysis has been performed here assuming the bilayer as an effective single medium with a characteristic effective exchange constant ( $A'$ ) and saturation magnetization ( $M'_S$ ). Subsequently, a model for the PSSW mode is deployed for that single layer film. Although this approach is based on coarse assumptions but it may provide useful and quick information about the long wavelength spin wave energies and the effect of the two coupled layers in a bilayer film [26]. Neglecting uniaxial anisotropy field, the frequency of the PSSW magnons is given by [27]

$$f = \frac{\gamma}{2\pi} \left\{ \left( H_{eff} + \frac{2A'}{M'_S} q_{\perp}^2 + \frac{2A'}{M'_S} q^2 \right) \times \left( H_{eff} + 4\pi M'_{eff} + \frac{2A'}{M'_S} q_{\perp}^2 + \frac{2A'}{M'_S} q^2 \right) \right\}^{1/2} \quad \dots\dots(5.2)$$

Here  $q_{\perp}$  is the wave vector perpendicular to the surface of the film defined as  $q_{\perp} = n\pi/t$ , where  $n$  represents the PSSW mode number and  $t$  is the thickness of the bilayer. For the data in Fig. 5.4, we have used  $t = 35$  nm,  $q = 1.67 \times 10^7$  rad/m and  $g = 2.15$ , while  $M'_S$ ,  $A'$  and  $M'_{eff}$  were used as fitting parameters in Eqn. 5.2. The fit yields,  $4\pi M'_S = 12.202$  kG,  $A' = 1.78 \times 10^{-6}$  erg/cm and  $4\pi M'_{eff} = 4.046$  kG. Interestingly, the value of the exchange constant is close to the weighted average of the exchange constants of the two layers which is  $A' = (t_{py}A_{py} + t_{Co}A_{Co})/(t_{py} + t_{Co})$ . A similar result is also observed in the case of  $M'_S$  value. The effect of coupling between the Py and Co layers is clear from this qualitative picture. A detailed analysis will be of future interest.

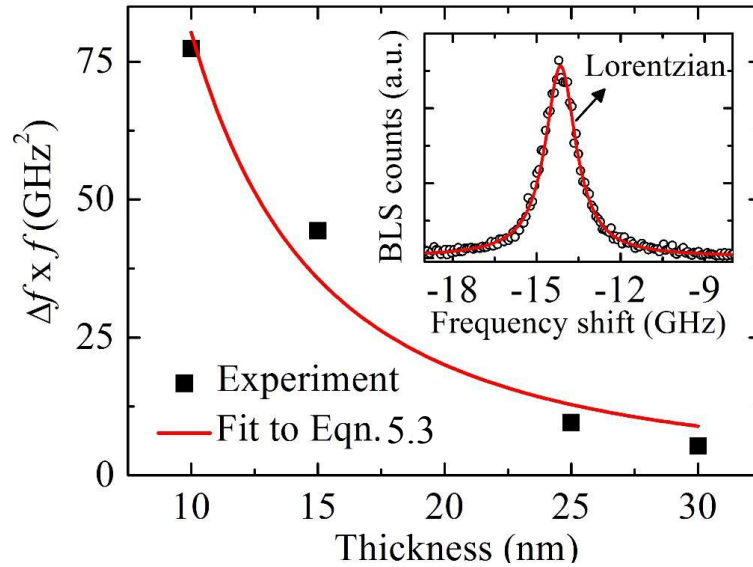


Figure 5.5: Thickness dependence of  $\Delta f \times f$  for Co (10 nm)/ Py ( $t$ ) films (symbols). A fit to Eq. (5.3) has also been shown (line). Inset shows the Lorentzian fit to experimental BLS spectrum obtained for Co (10 nm)/ Py (25 nm) film at  $H = 2800$  Oe.

We further noticed that the BLS linewidths ( $\Delta f$ ) of the frequency peaks ( $f$ ) increase significantly with decreasing Py layer thickness. Interfacial roughness may cause the exchange coupling to fluctuate at the nanoscale regime and the effect is stronger for thinner Py films [28]. This may broaden the linewidths of spin wave peaks as observed in our experiment. We have shown the

variation of  $\Delta f \times f$  as a function of Py thickness ( $t$ ) in Fig. 5.5. Magnon linewidths and peak positions were calculated by fitting the peaks with Lorentzian function (inset of Fig. 5.5). We have extracted the coupling parameter from the magnon linewidth expression as given below [28]

$$\Delta f = \frac{\gamma^2 p \langle A_d \rangle \langle \cos^2 \alpha \rangle 4\pi M_s \xi \left( \frac{J_I}{M_s t} \right)^2}{2\pi D f} \quad \dots\dots(5.3)$$

Here  $p$  is fraction of defects,  $\langle A_d \rangle$  is the surface area,  $\alpha$  is the angle between the moments of the two layers,  $\xi$  is a numerical factor,  $D = 2A/M_s$  and  $J_I$  is the interfacial exchange energy. We fit the data in Fig. 5.5 with Eqn. 5.3 by assuming estimates from AFM data as  $p = 0.3$ ,  $\langle A_d \rangle = 20 \text{ \AA}^2$ , while  $\langle \cos^2 \alpha \rangle$  is assumed as 0.5. Numerical factor  $\xi$  may have small variation with film thickness but assumed as a constant in fitting for simplicity with an average calculated value of 0.55.  $J_I$  is left as fitting parameter. The fit yields  $J_I = 9.39 \text{ erg/cm}^2$ , which is equivalent to a local exchange coupling field  $H_I = J_I/M_s t = 4.69 \text{ kOe}$  for the bilayer with 25 nm Py thickness. This local field is much larger compared to the macroscopic field obtained from the experiment as the measurements are done within about 12 nm from the surface of the film and the exchange field drops exponentially from the interface as it penetrates within the Py layer.

## 5.4. Conclusions

In summary, Brillouin light scattering technique was applied to investigate exchange coupling behavior in Co/Py bilayer films. Coercivity of the bilayer films systematically decreases with increasing Py layer thickness. The coercivity behavior of the bilayers as a function of the deposited Py layer strongly depends on both the mechanism controlling the moment reversal and the phenomena occurring at the soft/hard interface. BLS spectra show the presence of surface and volume modes. Exchange coupling behavior is clearly observed from their analyses as a function of magnetic field. A model based on two magnon scattering is used to quantitatively analyze the linewidths of the spin waves from different bilayer films and interfacial exchange coupling parameter was deduced. Local exchange field was found to be much larger in comparison with measured macroscopic value.

## References

- [1] E. E. Fullerton, J. S. Jiang, M. Grimsditch, *et al.*, “Exchange-spring behavior in epitaxial hard/soft magnetic bilayers,” *Phys. Rev. B* **58**, 12193 (1998).
- [2] E. E. Fullerton, J. S. Jiang, and S. D. Bader, “Hard/soft magnetic heterostructures: model exchange-spring magnets,” *J. Magn. Magn. Mater.* **200**, 392 (1999).
- [3] E. F. Kneller and R. Hawig, “The exchange-spring magnet: a new material principle for permanent magnets,” *IEEE Trans. Magn.* **27**, 3588 (1991).
- [4] R. Skomski and J. M. Coey, “Giant energy product in nanostructured two-phase magnets,” *Phys. Rev. B* **48**, 15812 (1993).
- [5] T. Schrefl, H. Kronmuller, and J. Fidler, “Exchange Hardening in Nano-Structured Permanent Magnets,” *J. Magn. Magn. Mater.* **127**, L273 (1993).
- [6] M. Amato, A. Rettori, and M. G. Pini, “Exchange-spring behavior of hard/soft magnetic multilayers: optimization study of the nanostructure,” *Physica B* **275**, 120 (2000).
- [7] J. M. D. Coey, “Permanent magnetism,” *Solid State Commun.* **102**, 101 (1997).
- [8] R. H. Victora and X. Shen, “Composite media for perpendicular magnetic recording,” *IEEE Trans. Magn.* **41**, 537 (2005).
- [9] R. Pellicelli, C. Pernechele, M. Solzi, *et al.*, “Modeling and characterization of irreversible switching and viscosity phenomena in perpendicular exchange-spring Fe-FePt bilayers,” *Phys. Rev. B* **78**, 184434 (2008).
- [10] G. Asti, M. Ghidini, R. Pellicelli, *et al.*, “Magnetic phase diagram and demagnetization processes in perpendicular exchange-spring multilayers,” *Phys. Rev. B* **73**, 094406 (2006).
- [11] D. C. Crew, R. L. Stamps, H. Y. Liu, *et al.*, “Spin wave excitations in exchange spring Co/CoPt thin film bilayers,” *J. Magn. Magn. Mater.* **272**, 273 (2004).
- [12] D. C. Crew, R. L. Stamps, H. Y. Liu, *et al.*, “Light scattering from spin wave excitations in a Co/CoPt exchange spring,” *J. Magn. Magn. Mater.* **290**, 530 (2005).
- [13] G. Gubbiotti, G. Carlotti, J. Weston, *et al.*, “Asymmetry in the static and dynamic magnetic properties of a weak exchange spring trilayer,” *J. Magn. Magn. Mater.* **286**, 479 (2005).
- [14] S. Tacchi, T. N. A. Nguyen, G. Carlotti, *et al.*, “Spin wave excitations in exchange-coupled [Co/Pd]-NiFe films with tunable tilting of the magnetization,” *Phys. Rev. B* **87**, 144426 (2013).

- [15] S. Pal, S. Barman, O. Hellwig, *et al.*, “Effect of the spin-twist structure on the spin-wave dynamics in  $\text{Fe}_{55}\text{Pt}_{45}/\text{Ni}_{80}\text{Fe}_{20}$  exchange coupled bi-layers with varying  $\text{Ni}_{80}\text{Fe}_{20}$  thickness,” *J. Appl. Phys.* **115**, 17D105 (2014).
- [16] F. C. Nortemann, R. L. Stamps, and R. E. Camley, “Microscopic calculation of spin waves in antiferromagnetically coupled multilayers: Nonreciprocity and finite-size effects,” *Phys. Rev. B* **47**, 11910 (1993).
- [17] R. Arias and D. L. Mills, “Extrinsic contributions to the ferromagnetic resonance response of ultrathin films,” *Phys. Rev. B* **60**, 7395 (1999).
- [18] M. Grimsditch, R. Camley, E. E. Fullerton, *et al.*, “Exchange-spring systems: Coupling of hard and soft ferromagnets as measured by magnetization and Brillouin light scattering (invited),” *J. Appl. Phys.* **85**, 5901 (1999).
- [19] K. J. Kennewell, M. Kostylev, N. Ross, *et al.*, “Magnetization pinning at a Py/Co interface measured using broadband inductive magnetometry,” *J. Appl. Phys.* **108**, 073917 (2010).
- [20] D. C. Crew, K. J. Kennewell, M. J. Lwin, *et al.*, “Optic and acoustic modes measured in a cobalt/Permalloy exchange spring bilayer using inductive magnetometry,” *J. Appl. Phys.* **97**, 10A707 (2005).
- [21] B. Hillebrands, “Modern Techniques for Characterizing Magnetic Materials, eds Y. Zhu,” Kluwer Academic, Boston, (2005).
- [22] S. O. Demokritov, B. Hillebrands, and A. N. Slavin, “Brillouin light scattering studies of confined spin waves: linear and nonlinear confinement,” *Phys. Rep.* **348**, 441 (2001).
- [23] M. Madami, G. Gubbiotti, S. Tacchi, *et al.*, “Chapter Two - Application of Microfocused Brillouin Light Scattering to the Study of Spin Waves in Low-Dimensional Magnetic Systems,” *Solid State Phys.* **63**, 79 (2012).
- [24] S. M. Rezende, F. M. de Aguiar, and A. Azevedo, “Magnon excitation by spin-polarized direct currents in magnetic nanostructures,” *Phys. Rev. B* **73**, 094402 (2006).
- [25] J. P. Nibarger, R. Lopusnik, Z. Celinski, *et al.*, “Variation of magnetization and the Landé  $g$  factor with thickness in Ni–Fe films,” *Appl. Phys. Lett.* **83**, 93 (2003).
- [26] F. C. Nortemann, R. L. Stamps, R. E. Camley, *et al.*, “Effective-medium theory for finite magnetic multilayers: Effect of anisotropy on dipolar modes,” *Phys. Rev. B* **47**, 3225 (1993).

- [27] M. Cottam and D. Lockwood, "Light Scattering in Magnetic Solids," Wiley, New York, (1986).
- [28] S. M. Rezende, A. Azevedo, M. A. Lucena, *et al.*, "Anomalous spin-wave damping in exchange-biased films," Phys. Rev. B **63**, 214418 (2001).

## Chapter 6

# 6. Brillouin light scattering study of $[\text{Co}/\text{Ni}_{80}\text{Fe}_{20}]_r$ multilayers with varying number of bilayer repetition

---

### 6.1. Introduction

The potential impact in the flourishing areas of spintronic devices such as spin valves [1], spin transfer torque devices [2-3], magnetic random access memory [4] and magnonics [4–7] has stimulated considerable interest in the magnetization dynamics in ferromagnetic multilayers. Such systems have been found to display characteristic features in their magnetic properties, which are different from their constituent layers due to (i) interlayer interactions, (ii) interface anisotropies and (iii) different magnetic properties across the layers. In the last decade, there have been intense research activities in studying the magnetization dynamics in magnetic/non-magnetic multilayers [8–12], motivated by the fast evolution of high-density magnetic recording technology. Investigations of several structural and magnetic properties have been reported where magnetic interactions between the layers have been tuned by varying the layer thickness [10], the number of repetitions [9, 13] and also by changing the deposition conditions [14]. Practical magnetic devices require a combination of sensitivity to magnetic fields as well as an ability to control the magnetic state of the device precisely. However, these materials, in general, are plagued by large saturation fields and a magnetic structure that is very difficult to control in miniaturized devices. Therefore, the structures that are being developed for applications tend to be simple devices with metallic magnetic multilayers. Here the absence of a non-magnetic spacer leads to a strong interlayer coupling and thus the surface anisotropies at the interfaces are substantially affected by direct contact [15, 16].

Due to its growing interest, ferromagnetic multilayers including exchange spring systems [17–20] have been widely investigated in recent years. In this article we will focus on ferromagnetic multilayers in general, where the interlayer exchange coupling leads to intriguing spin wave properties. In the literature, there are several studies on ferromagnetic multilayers with perpendicular magnetic anisotropy (PMA) [21–26], where different static and dynamic magnetic

properties have been reported including magnetic domain structure [24], damping [21, 23] and magnetic anisotropy [22, 24–26] which were studied using conventional magnetometry [24, 27], time-resolved magneto-optical Kerr effect (TR-MOKE) [21], ferromagnetic resonance (FMR) [22] and Brillouin light scattering (BLS) spectroscopy [24]. However, to the best of our knowledge, only a few experimental reports on ferromagnetic multilayers with in-plane anisotropy are present [28–31] in the literature. Most of the existing studies in these systems are mainly concerned with Fe/Ni [30, 31] and Co/Fe [28, 29] multilayers where the spin wave (SW) excitations show a strong dependence on the interlayer exchange coupling [31] and interface anisotropy [29], which can be varied by varying the layer thickness [31]. Nevertheless, a thorough study of the magnetic properties and their dependence on different structural and fabrication parameters are yet to be carried out.

Here, we present a comprehensive study of collective spin wave excitations in  $[\text{Co}/\text{Ni}_{80}\text{Fe}_{20}(\text{Py})]_r$  multilayers as a function of the number of bilayer repetition  $r$ . The effect of number of bilayer repetition on the evolution of dynamic magnetic properties has been studied earlier in Ni/Co multilayers with perpendicular magnetic anisotropy [23]. However, no such reports exist on the investigation of magnetization dynamics in all-ferromagnetic multilayers with in plane anisotropy. Here vibrating sample magnetometry (VSM) and BLS spectroscopy have been simultaneously exploited as complementary techniques to make a comparative study between the static and the dynamic magnetic properties of the studied structures. In the BLS spectra, a number of SW modes have been observed, which varied with the number of bilayer repetition. We have explained these multiple modes to be originated from surface and volume contributions with the aid of macrospin modelling. We have also calculated the dependence of the scattering intensity of the volume modes on the associated thickness.

## 6.2. Experimental Details

$[\text{Co}(10\text{ nm})/\text{Py}(10\text{ nm})]_r$  multilayered films with  $r = 1, 2, 3$  and  $4$  were grown onto self-oxidized Si  $[1\ 0\ 0]$  substrates (of dimensions about  $1\text{ cm} \times 1\text{ cm}$ ) at room temperature at a base pressure of  $2 \times 10^{-7}$  Torr, Ar pressure of 5 mTorr and applied dc voltages of 400 V for Co and 350 V for Py. Uniformity in the thickness of the layers was ensured by rotating the substrate at 10 rpm during deposition. The thicknesses of the Co and Py layers were so chosen to have in-plane magnetization of the films. The films were covered with a 5 nm  $\text{SiO}_2$  capping layer to prevent oxidation. The

topography and surface roughness of the films were measured by atomic force microscopy (AFM). The magnetization curves were measured using VSM at room temperature. Thermal magnons in the samples were investigated using BLS spectroscopy in the backscattered geometry [32-33]. The main advantage of BLS is the possibility to observe SWs with varying magnitude and orientation of their wave vectors. The measurements were performed at room temperature in the magnetostatic surface wave geometry (i.e., MSSW or Damon Esbach geometry) using a single-mode solid state laser operated at 532 nm and a Sandercock-type six-pass tandem Fabry–Perot interferometer (FPI) [34]. Here the incident light undergoes inelastic scattering from the magnons owing to the conservation of energy and momentum. Cross polarizations between the incident and the scattered beams were adopted in order to minimize the phonon contribution to the scattered light. The magnetic field  $H$  was applied in the plane of the sample and perpendicular to the plane of light incidence. The BLS spectra were recorded for different values of the wave vector by changing the angle of incidence ( $\theta$ ) of the laser beam. Therefore the orientation of the magnetization is perpendicular to the direction of the transferred wave vector  $q$  of the detected magnons (MSSW geometry). At wave vectors accessible by light-scattering experiments both exchange and dipolar interactions may contribute to the spin wave excitations, and their interplay can be studied.

### 6.3. Results and Discussions

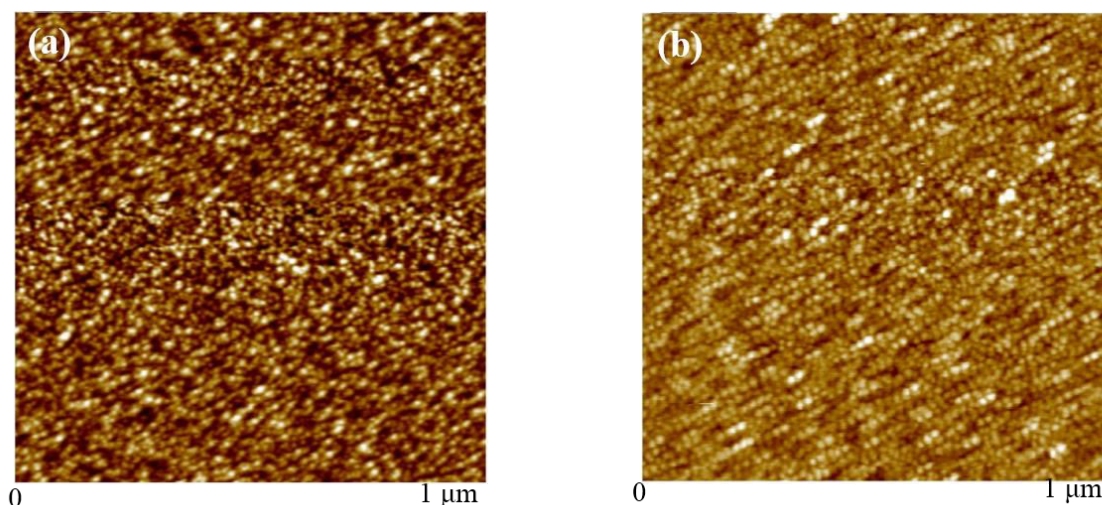


Figure 6.1: AFM images of  $[\text{Co (10 nm)/Py (10 nm)}]_r$  multilayers for a)  $r=1$  and b)  $r=4$ .

The AFM images of  $[\text{Co}/\text{Ni}_{80}\text{Fe}_{20}(\text{Py})]_r$  multilayers are shown in Fig. 6.1 for  $r = 1$  and  $r = 4$ . The results reveal the presence of well inter-connected grains in both cases. However, a marked increase in the average grain size from 13 nm for  $r = 1$  to 24 nm for  $r = 4$  is observed with increasing  $r$ . This indicates improved crystalline structure for higher  $r$ , which eventually determines the magnetic properties as will be discussed later in this article. The magnetization curves of the multilayers, measured at room temperature by VSM, for magnetic field applied parallel to the film plane, is shown in Fig. 6.2.

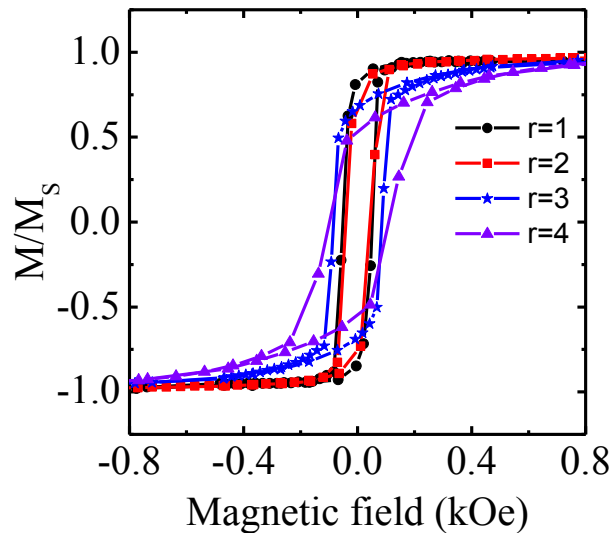


Figure 6.2: Magnetic hysteresis loops of  $[\text{Co} (10 \text{ nm})/\text{Py} (10 \text{ nm})]_r$  multilayers, measured for the magnetic field applied parallel to the film plane. Different cycles refer to samples with different numbers of repetition ( $r$ ).

The results show nearly square shape of the VSM loops, which confirms that the in-plane direction is the easy direction. Here, the increase in coercive field, from 113 to 205 Oe upon increasing  $r$ , signals the increase in the in-plane anisotropy, stabilizing the in-plane orientation of the magnetization.

Figure 6.3a shows the BLS spectra (normalized to the reference beam intensity) for all the samples taken for SW wave vector  $q = 1.1 \times 10^7 \text{ rad/m}$  (angle of incidence  $\theta = 28^\circ$ ). The measurement geometry is shown in the inset. In BLS technique, the magnetic excitations within the sample interact with the incident light resulting in a frequency shifted scattered beam. From the conservation of in-plane wave vector, SW wave vector is given by  $q = 2k_{in} \sin \theta$ .

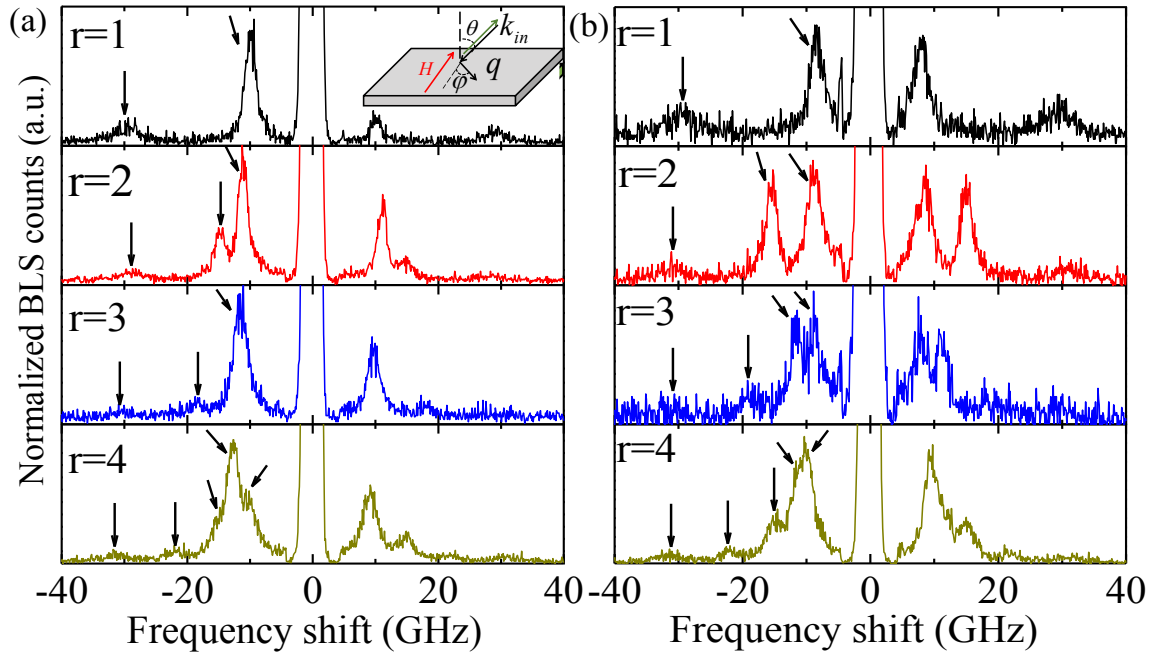


Figure 6.3: BLS spectra for  $[\text{Co (10 nm)/Py (10 nm)}]_r$  multilayers with  $r = 1-4$  taken for (a)  $q = 1.1 \times 10^7$  rad/m and (b)  $q = 0$ . The measurement geometry is shown at the inset of (a) where the parameters are the same as described in the text. The arrows indicate the spin wave peak frequencies.

A bias magnetic field ( $H$ ) of 1000 Oe was applied in the plane of the sample and the free spectral range (which is the scanning range as well) was chosen as 50 GHz by fixing the mirror spacing of FP1 as 3 mm. Therefore, the frequency resolution of the BLS setup, which is limited by the instrumental linewidth, is found to be 0.4 GHz from the width of the elastic peak. The applied field of 1000 Oe is large enough to saturate the sample magnetization within the plane of the sample as evident from Fig. 6.2. The BLS spectra reveal two distinct peaks for  $r = 1$ , whereas for  $r = 2$  and 3, three peaks are found. In contrary, the number of modes for the sample with  $r = 4$  appears to be five. Figure 6.3b shows similar BLS spectra taken at zero wave vector (normal incidence), which corresponds to the Kittel mode. The significance of the Kittel mode lies in the fact that the SW spectra are not affected by the dispersion of the individual mode. Here, the spectra are similar to those in Fig. 6.3a except for  $r = 3$ , where one additional mode has appeared in the spectra. To understand the nature of these modes, wave vector resolved measurements were performed by changing the angle of incidence ( $\theta$ ) of the laser beam *w.r.t.* the sample plane.

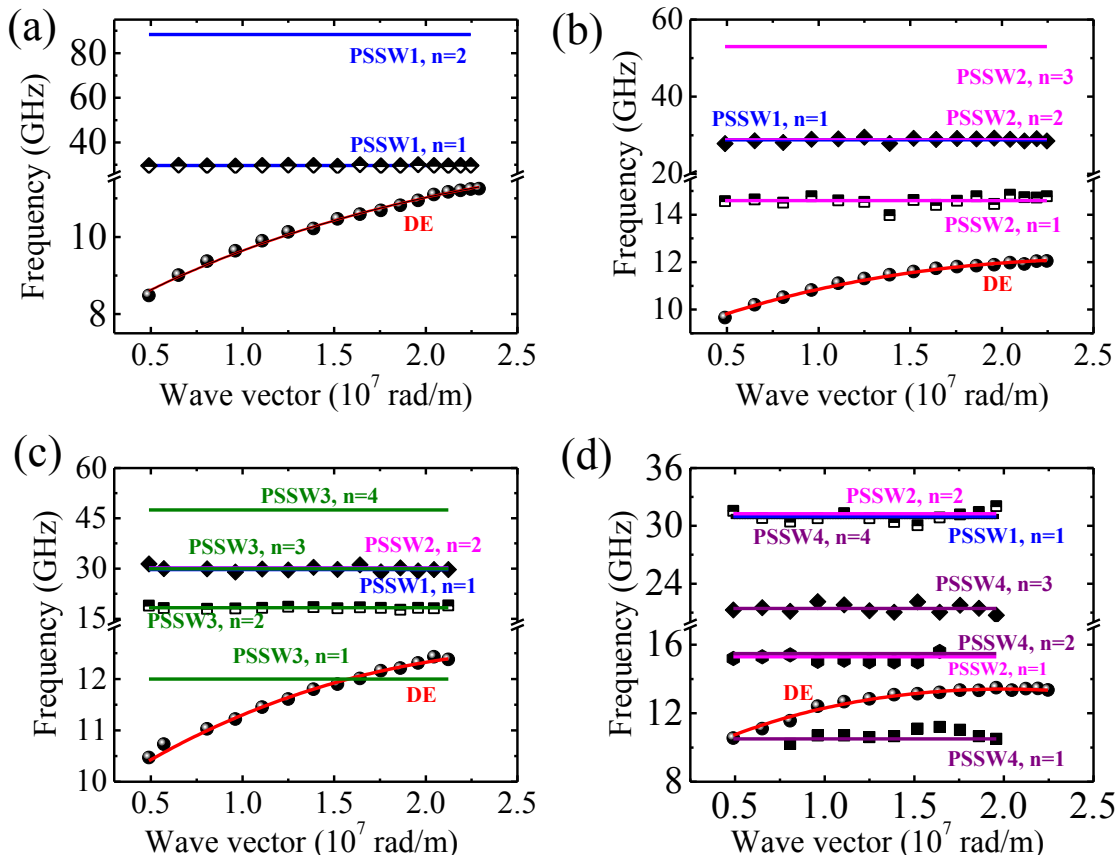


Figure 6.4: Measured spin wave frequencies (symbols) as a function of in-plane wave vector for the  $[\text{Co (10 nm)/Py (10 nm)}]_r$  multilayers with (a)  $r = 1$ , (b)  $r = 2$ , (c)  $r = 3$  and (d)  $r = 4$ , respectively. The solid lines are calculated frequencies.

In Fig. 6.4a–d, the SW frequencies are plotted as a function of the SW wave vector for the samples with  $r = 1, 2, 3$  and  $4$ . Depending on the evolution of mode frequencies with respect to the in-plane wave vector, the detected modes are identified and labeled. The dispersion curves of the modes reveal that the lower frequency mode has a pronounced dispersion with the in-plane wave vector ( $q$ ) and it corresponds to the magnetostatic surface wave, which propagates in the film plane (Damon–Eshbach (DE) mode). This mode can also be identified by its typical non reciprocal nature in Fig. 6.3a. On the other hand, negligible dispersion with wave vector are observed for the higher frequency modes and they are identified as the volume modes, also known as the perpendicular standing spin waves (PSSW). Similar results were also found in other works on ferromagnetic multilayers [29–30]. Note here, that in the BLS spectra (Fig. 6.3a), some of the PSSW modes also show asymmetry in the BLS intensity of Stokes and anti-Stokes sides. This

behavior for PSSW mode is found in other BLS reports as well [11, 29]. However, the detailed understanding of this asymmetry in the PSSW mode is still missing in the literature.

The nature of the SW excitations in these samples can be understood as follows. When two or more ferromagnetic layers are placed in direct contact, a strong coupling between the layers (including dipolar and exchange) is to be expected which affects the dynamic magnetization. This coupling results in a magnetostatic stack surface wave mode, which is localized at the outermost surfaces of the multilayer stack and can be recognized by its typical non reciprocal nature. This mode is affected by the interface anisotropy [29] and its amplitude decreases exponentially away from the surface. On the other hand, the spectrum of the SW propagating perpendicular to the film plane is modified due to the broken translational invariance in the vicinity of the film surfaces. Thus, a quantization effect appears and the wave vector is given by:

$$q_{\perp} = \frac{n\pi}{d} \quad \dots\dots(6.1)$$

where  $d$  is the thickness of the film and  $n = 1, 2, 3, \dots$ , denotes one or more nodes along the perpendicular axis (the number of nodes can be used to label the PSSW). The profile of the dynamic part of the magnetization  $m$  in the  $n$ th mode can be written as follows:

$$m_n(z) = a_n \cdot \cos\left[q_{z,n}\left(z + \frac{d}{2}\right)\right], -\frac{d}{2} < z < \frac{d}{2} \quad \dots\dots(6.2)$$

Equation 6.2 describes a standing mode consisting of two counter propagating waves with quantized wave vectors. We note here that due to the truncation of the cosine function at the film surfaces,  $q_{z,n}$  is not a true wave vector.

To explore the origin of the observed modes for  $r = 1$  and to extract the magnetic parameters, we performed a quantitative analysis using an effective medium approach, where the entire multilayer stack is assumed to be an effective single medium with a characteristic effective exchange constant ( $A$ ) and a saturation magnetization ( $M_S$ ). In earlier studies on ferromagnetic multilayers, the spin wave modes were analyzed considering the magnetic properties of each layer [29, 35-36]. To apply this model, bulk and interfacial properties of each layer as well as appropriate boundary conditions are required. Furthermore, detailed theoretical calculation is needed to identify the origin of modes. The use of this approach is beyond the scope of this paper. The

effective medium approach, on the other hand, was used in earlier investigations on ferromagnetic bilayers [24-25]. Although, the exact estimation of interlayer exchange constant and interface anisotropy is not possible, this approach explains the magnetization dynamics in all-ferromagnetic multilayers reasonably well as will be discussed later in this article. Here, the DE mode was analyzed by using the following expression:

$$f = \frac{\gamma}{2\pi} \left\{ \left( H_{eff} + 2\pi M_s q d \sin^2 \varphi + \frac{2A}{M_s} q^2 \right) \times \left( H_{eff} + 4\pi M_{eff} - 2\pi M_s q d + \frac{2A}{M_s} q^2 \right) \right\}^{1/2} \quad \dots\dots(6.3)$$

where  $\gamma$ ,  $H$ ,  $M_s$ ,  $A$ ,  $d$  and  $\varphi$  are the gyromagnetic ratio, applied magnetic field, saturation magnetization, exchange stiffness constant, thickness of the film and the angle of magnon wave vector in the film plane, respectively. Gyromagnetic ratio is connected to magneto-mechanical ratio  $g$  by  $\gamma = g\mu_B/\hbar$  where  $\mu_B$  is the Bohr magneton and  $\hbar$  is the reduced Planck's constant. Surface anisotropy field ( $H_s$ ) is included in the effective magnetization ( $M_{eff}$ ) as  $4\pi M_{eff} = 4\pi M_s - H_s$ . The data in Fig. 6.4a was fitted with Eq. 6.3 using  $A=1.7 \times 10^{-6}$  erg/cm and  $M_s= 1000$  emu/cc while leaving  $d$ ,  $M_{eff}$ ,  $g$  and  $\varphi$  as fitting parameters. The fitting yields  $\varphi=71^\circ$ ,  $M_{eff}= 540$  emu/cc,  $d = 20$  nm and  $g = 1.86$ .

On the other hand, the frequency for the PSSW mode is given by

$$f = \frac{\gamma}{2\pi} \left\{ \left( H_{eff} + \frac{2A'}{M_s} q_{\perp}^2 \right) \times \left( H_{eff} + 4\pi M_{eff} + \frac{2A'}{M_s} q_{\perp}^2 \right) \right\}^{1/2} \quad \dots\dots(6.4)$$

Here, the wave vector is perpendicular to the surface of the film defined by Eqn 6.1. Using the same parameters as above yields  $d = 20$  nm and  $n = 1$ . This implies that the PSSW mode is confined across the first bilayer thickness. We label these modes as PSSW1 owing to its confinement in a single bilayer. To further justify the validity of our approach, we calculated the frequency of PSSW1 for  $n = 2$  using the same magnetic parameters. The calculated frequency comes out to be larger than 80 GHz, which is beyond our scan range. Therefore, this mode is not expected to be observed, which is in good agreement with our experimental finding. We tried to access higher frequency range by reducing the mirror spacing, but as the amplitude of these modes decreases with the increase in the mode number, this mode could not be detected.

Figure 6.4b demonstrates the dispersion curves for  $r = 2$ . Here also the lowest mode is identified as the DE mode, which after fitting with Eqn. 6.3 yields  $g = 2.1$ ,  $\phi = 56^\circ$ ,  $M_{eff} = 560$

emu/cc and  $d = 23$  nm. The other parameters are kept same as  $r = 1$ . This indicates that the surface mode is still confined in the first (top) bilayer. The other two modes show dispersionless behavior and are identified as PSSW modes. Interestingly, the mode near 15 GHz shows some intensity asymmetry in the Stokes and Anti-Stokes peaks (Fig. 6.3a), which is reversed when the bias field is reversed. This nonreciprocity is not well understood yet and can be a topic of future study. We fitted the PSSW modes with Eqn. 6.4 using the same parameters applied for DE mode. The fitting yields that the mode near 15 GHz is PSSW2 (confined within two bilayers) with  $n = 1$ , whereas the mode near 30 GHz is PSSW2 with  $n = 2$ . It is worth mentioning here, that the latter mode (near 30 GHz) may correspond to PSSW1 with  $n = 1$  as well, similar to the case with  $r = 1$ . Therefore this mode may belong to different harmonics of PSSW1 and PSSW2. As a second step of our investigation, we further calculated the frequency of PSSW2 with  $n = 3$ . The calculations yield that the frequency of PSSW2 with  $n = 3$  lies near 50 GHz. Therefore this mode was not observed due to their low amplitude and consequently the poor signal to noise ratio. The above explanation gives another proof that the assumptions are in support to our observed behavior.

The spectrum for  $r = 3$  is similar to that for  $r = 2$  as presented in Fig. 6.4c. Here also the lowest mode is DE mode, which after fitting with Eqn. 6.3 gives  $g = 2.14$ ,  $\phi = 46^\circ$ ,  $M_{eff} = 650$  emu/cc and  $d = 23$  nm. The fitting parameters reveal that here also the DE mode is confined primarily in the first bilayer. One discernible difference between  $r = 2$  and  $r = 3$  is that the value of  $M_{eff}$  increases with the number of bilayer repeat. Here also, one PSSW mode is observed near 30 GHz, which is identified as PSSW3 (mode confined in three bilayers) with  $n = 3$ . Note here that this mode may be a superposition of three harmonics, namely, PSSW1 with  $n = 1$ , PSSW2 with  $n = 2$  and PSSW3 with  $n = 3$ . The mode near 20 GHz is PSSW3 with  $n = 2$ . Further calculations reveal that PSSW3 with  $n = 1$  lies near 12 GHz. Therefore this mode was observed for low wave vectors (Fig. 6.3b), but not for higher wave vectors where it lies within the tail of the DE mode. Again, the mode PSSW3 with  $n = 4$  (near 47 GHz) was not observed due to similar reason as for  $r = 2$ .

In case of the sample with  $r = 4$ , the number of modes changes to five as shown in Fig. 6.4d. Here, the lowest mode is no longer the DE mode and shows a dispersionless behavior. Rather, the higher frequency mode characterizes the DE mode with the magnetic parameters given by  $g = 1.8$ ,  $\phi = 53^\circ$ ,  $M_{eff} = 828$  emu/cc and  $d = 40$  nm as obtained from fitting with Eqn. 6.3. Therefore, here the DE mode penetrates down to almost two bilayers. By fitting the recorded frequency values

for the other peaks (PSSW modes) we find that the frequencies near 10 GHz and 15 GHz are PSSW4 with  $n = 1$  and  $n = 2$ , respectively. The other two modes observed near 21 GHz and 30 GHz are identified as PSSW4 with  $n = 3$  and  $n = 4$ , respectively. Here also PSSW4 with  $n = 2$  is observed for lower wave vectors only when it is not suppressed by the DE mode (Fig. 6.3b). In addition, the frequency of PSSW4 with  $n = 1$  lies very close to that of PSSW1 with  $n = 1$ , PSSW2 with  $n = 2$  and PSSW3 with  $n = 3$ . Similarly, PSSW4 with  $n = 2$  corresponds to PSSW2 with  $n = 2$ .

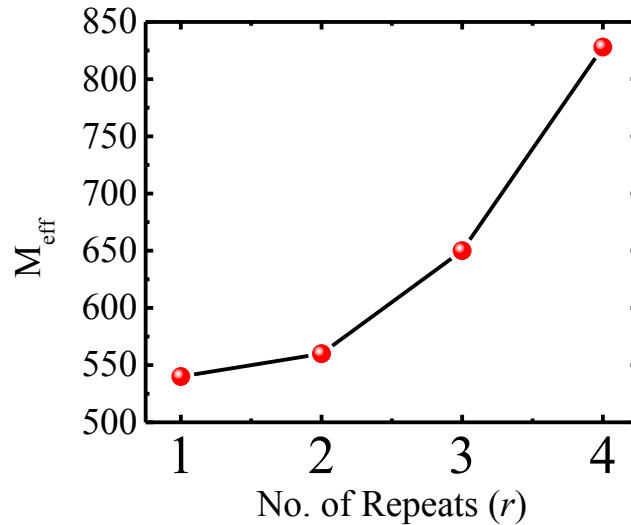


Figure 6.5: Dependence of effective magnetization on the number of repeats ( $r$ ). The line is a guide to the eyes.

The above modeling of the frequency versus wave vector dispersion using an effective medium approach shows that there is an enhancement of the in-plane anisotropy (reflected in the effective magnetization  $M_{eff}$ ) with increasing  $r$ . This is also apparent from the BLS spectra of both the DE mode (Fig. 6.3a) and Kittel mode (Fig. 6.3b) which showed increase in frequency with increasing  $r$ . The variation in  $M_{eff}$  is shown in Fig. 6.5, which is also in qualitative agreement with the VSM results. The reason for this enhancement can probably be attributed to an overall improvement of multilayer quality with increasing  $r$  as is also supported by the AFM results, which in turn improves the in-plane anisotropy. Therefore a detailed study of such systems with higher repeat numbers will be of future interest.

It may further be noted that in case of the PSSW modes with the same mode number, a larger BLS intensity is observed for the modes which are confined in larger number of bilayers and vice versa. This is evident in the BLS spectra of Kittel mode (Fig. 6.3b) where PSSW3 with  $n$

= 1 and PSSW4 with  $n = 1$  are also observed. Consequently, for PSSW1, only the mode with  $n = 1$  is observed whereas for PSSW4, upto  $n = 3$  is observed. In order to interpret this, we have explored the dependence of BLS intensity  $I(d)$  of a PSSW mode on the corresponding thickness  $d$  following the approach of Jorzick et al [37]. As mentioned earlier, the profile of the dynamic part of the magnetization  $m$  in the  $n$ th mode has a cosine like shape (see Eqn. 6.2). Therefore, the intensity, which is essentially determined by the scattering cross-section, can be obtained from

$$I(d) \propto |m_q|^2 = \left| \int_{-d/2}^{d/2} m(z) \cdot \exp(-iqz) dz \right|^2 \quad \dots\dots(6.5)$$

Substituting Eqns. 6.1 and 6.2 in the above equation and performing some analytical calculations, we find that  $I(d)$  is proportional to  $d^2$  which agrees well with our experimental observations.

## 6.4. Conclusions

In conclusion, we have investigated the quasistatic and dynamic magnetic properties of [Co/Py] $_r$  multilayers with a varying number of bilayer repetition  $r$  using VSM and BLS techniques. The VSM results reveal a systematic increase of in-plane anisotropy with increasing repeat number. The BLS results show rich spectra of spin wave modes, which depend strongly on bilayer repeat. The origin of the modes were analyzed in detail using an effective medium approach, which reveals that for each film there is one mode showing a pronounced dispersion with respect to the transferred wave vector, which corresponds to the magnetostatic surface wave (DE) mode confined in upper surface of the stack. The modes showing no noticeable dispersion are interpreted as PSSW modes with different mode numbers. The frequencies of the other PSSW modes with higher mode numbers are calculated and compared with the experimental results. The extracted values of effective magnetization in different samples also mirrors the trend found in VSM results. It is observed that the intensity of the PSSW mode depends on the corresponding thickness and the relation between them has been established. Finally, the tunability of in-plane magnetic anisotropy of these simple ferromagnetic multilayer structures is important for various spintronic and magnonic devices.

## References

- [1] P. S. A. Kumar and J. C. Lodder, "The spin-valve transistor," *J. Phys. D: Appl. Phys.* **33**, 2911 (2000).
- [2] D. C. Ralph and M. D. Stiles, "Spin transfer torques," *J. Magn. Magn. Mater.* **320**, 1190 (2008).
- [3] J. A. Katine and E. E. Fullerton, "Device implications of spin-transfer torques," *J. Magn. Magn. Mater.* **320**, 1217 (2008).
- [4] B. Lenk, H. Ulrichs, F. Garbs, *et al.*, "The building blocks of magnonics," *Phys. Rep.* **507**, 107 (2011).
- [5] V. V. Kruglyak, S. O. Demokritov, and D. Grundler, "Magnonics," *J. Phys. D: Appl. Phys.* **43**, 264001 (2010).
- [6] S. A. Nikitov, P. Tailhades, and C. S. Tsai, "Spin waves in periodic magnetic structures—magnonic crystals," *J. Magn. Magn. Mater.* **236**, 320 (2001).
- [7] S. Pal, J. W. Klos, K. Das, *et al.*, "Optically induced spin wave dynamics in [Co/Pd]<sub>8</sub> antidot lattices with perpendicular magnetic anisotropy," *Appl. Phys. Lett.* **105**, 162408 (2014).
- [8] B. Hillebrands, J. V. Harzer, G. Güntherodt, *et al.*, "Experimental evidence for the existence of exchange-dominated collective spin-wave excitations in multilayers," *Phys. Rev. B* **42**, 6839 (1990).
- [9] S. Hamada, N. Hosoito, T. Ono, *et al.*, "Spin reorientation of the micromagnetic structure in Co/Au multilayer films with moderate perpendicular anisotropy," *J. Magn. Magn. Mater.* **198**, 496 (1999).
- [10] S. Pal, B. Rana, O. Hellwig, *et al.*, "Tunable magnonic frequency and damping in [Co/Pd]<sub>8</sub> multilayers with variable Co layer thickness," *Appl. Phys. Lett.* **98**, 082501 (2011).
- [11] F. D'Orazio, G. Gubbiotti, F. Lucari, *et al.*, "Magnetic and structural properties of Fe/Al multilayers," *J. Magn. Magn. Mater.* **242**, 535 (2002).
- [12] F. Albertini, G. Carlotti, F. Casoli, *et al.*, "Magnetic properties of perpendicularly magnetized Co/Au multilayers," *J. Magn. Magn. Mater.* **240**, 526 (2002).
- [13] G. Gubbiotti, G. Carlotti, F. Albertini, *et al.*, "Dependence of the perpendicular anisotropy in Co/Au multilayers on the number of repetitions," *J. Appl. Phys.* **93**, 7241 (2003).

- [14] G. Gubbiotti, G. Carlotti, F. Albertini, *et al.*, "Influence of annealing on Co/Au multilayers: a structural and magnetic study," *Thin Solid Films*. **428**, 102 (2003).
- [15] R. E. Camley, "Magnetization dynamics in thin films and multilayers," *J. Magn. Magn. Mater.* **200**, 583 (1999).
- [16] P. Grunberg, "Layered magnetic structures in research and application," *Acta mater.* **48**, 239 (2000).
- [17] A. Haldar, C. Banerjee, P. Laha, *et al.*, "Brillouin light scattering study of spin waves in NiFe/Co exchange spring bilayer films" *J. Appl. Phys.* **115**, 133901 (2014).
- [18] S. Pal, S. Barman, O. Hellwig, *et al.*, "Effect of the spin-twist structure on the spin-wave dynamics in Fe<sub>55</sub>Pt<sub>45</sub>/Ni<sub>80</sub>Fe<sub>20</sub> exchange coupled bi-layers with varying Ni<sub>80</sub>Fe<sub>20</sub> thickness," *J. Appl. Phys.* **115**, 17D105 (2014).
- [19] K. Utsumiya, T. Seki, and K. Takanashi, "Magnetic properties of L1<sub>0</sub>-FePt/permalloy exchange-spring films," *J. Appl. Phys.* **110**, 103911 (2011).
- [20] G. Gubbiotti, G. Carlotti, J. Weston, *et al.*, "Asymmetry in the static and dynamic magnetic properties of a weak exchange spring trilayer," *J. Magn. Magn. Mater.* **286**, 479 (2005).
- [21] S. Mizukami, X. Zhang, T. Kubota, *et al.*, "Gilbert Damping in Ni/Co Multilayer Films Exhibiting Large Perpendicular Anisotropy," *Appl. Phys. Express* **4**, 013005 (2011).
- [22] J. M. Shaw, H. T. Nembach, and T. J. Silva, "Damping phenomena in Co<sub>90</sub>Fe<sub>10</sub>/Ni multilayers and alloys," *Appl. Phys. Lett.* **99**, 012503 (2011).
- [23] M. Haertinger, C. H. Back, S. H. Yang, *et al.*, "Properties of Ni/Co multilayers as a function of the number of multilayer repetitions," *J. Phys. D: Appl. Phys.* **46**, 175001 (2013).
- [24] G. Gubbiotti, G. Carlotti, S. Tacchi, *et al.*, "Spin waves in perpendicularly magnetized Co/Ni(111) multilayers in the presence of magnetic domains," *Phys. Rev. B*. **86**, 014401 (2012).
- [25] M. T. Johnson, J. J. de Vries, N. W. E. McGee, *et al.*, "Orientational dependence of the interface magnetic anisotropy in epitaxial Ni/Co/Ni sandwiches," *Phys. Rev. Lett.* **69**, 3575 (1992).
- [26] P. J. H. Bloemen, W. J. M. d. Jonghe, and F. J. A. d. Broeder, "Magnetic anisotropies in Co/Ni (111) multilayers," *J. Appl. Phys.* **72**, 4840 (1992).
- [27] P. J. H. Bloemen and W. J. M. d. Jonge, "Magnetic anisotropy of Co/Ni/Co/Pt multilayers," *J. Magn. Magn. Mater.* **116**, L1 (1992).

- [28] L. Giovannini, S. Tacchi, G. Gubbiotti, *et al.*, “Brillouin light scattering study of exchange-coupled Fe/Co magnetic multilayers,” *J. Phys.: Condens. Matter.* **17**, 6483 (2005).
- [29] F. D’Orazio, F. Lucari, G. Carlotti, *et al.*, “Interface effects on the magnetic properties of exchange coupled Co/Fe multilayers studied by Brillouin light scattering,” *J. Magn. Magn. Mater.* **226**, 1767 (2001).
- [30] H. Litschke, M. Schilberg, T. Kleinefeld, *et al.*, “Spinwave dynamics in FeNi double layers and multilayers,” *J. Magn. Magn. Mater.* **104**, 1807 (1992).
- [31] M. Schilberg, T. Kleinefeld, and B. Hillebrands, “Spin wave dynamics and domain structure in exchange coupled FeNi multilayers,” *J. Magn. Magn. Mater.* **121**, 303 (1993).
- [32] S. O. Demokritov, B. Hillebrands, and A. N. Slavin, “Brillouin light scattering studies of confined spin waves: linear and nonlinear confinement,” *Phys. Rep.* **348**, 441 (2001).
- [33] G. Gubbiotti, S. Tacchi, M. Madami, *et al.*, “Brillouin light scattering studies of planar metallic magnonic crystals” *J. Phys. D: Appl. Phys.* **43**, 264003 (2010).
- [34] J. R. Sandercock, “*Light Scattering in Solids III*, 12 ed.” Springer, Berlin, (1982).
- [35] B. Hillebrands, “Spin-wave calculations for multilayered structures,” *Phys. Rev. B* **41**, 530 (1990).
- [36] B. Hillebrands, “Calculation of spin waves in multilayered structures including interface anisotropies and exchange contributions,” *Phys. Rev. B* **37**, 9885 (1988).
- [37] J. Jorzick, S. O. Demokritov, C. Mathieu, *et al.*, “Brillouin light scattering from quantized spin waves in micron-size magnetic wires,” *Phys. Rev. B* **60**, 15194 (1999).

## Chapter 7

# 7. All-optical study of ultrafast spin dynamics in [Co/Pd]/NiFe exchange spring systems with tunable tilted anisotropy

---

### 7.1. Introduction

Non-uniform magnetic structures, including exchange bias (ferromagnet/antiferromagnet) [1-2] and exchange-spring (ferromagnet/ferromagnet) [3–6] systems, have recently been explored extensively on account of their intrinsic advantages for applications in both permanent magnets and recording media. Exchange-spring (ES) magnets are systems of exchange-coupled hard and soft magnetic layers that behave as a single magnet. Here, the high saturation magnetization ( $M_S$ ) of the soft phase and the high anisotropy ( $H_k$ ) of the hard phase result in a large increase in the maximum energy product. This makes them useful as permanent magnets in energy applications such as engines for generators in miniaturized devices. On the other hand, for spintronic applications, the soft phase is used to improve the writability of the magnetic media, which in turn is stabilized by the magnetic configuration of the hard layer. Consequently, a wealth of research has been devoted to investigate the static and dynamic magnetic properties, including the switching behavior and exchange coupling strength, in ES systems.

In case of ES systems with tilted anisotropy, the hard and soft phases consist of materials with out-of-plane (OOP) and in-plane (IP) anisotropies, respectively. This combination results in a canting of the magnetization of the soft layer with a wide and tunable range of tilt angles. The advantage of such a hybrid anisotropy system is that it is neither plagued by the poor writability and thermal instability of systems with IP anisotropy, nor does it lead to very high switching fields, as in OOP systems. As a result, these materials provide additional degrees of freedom to control the magnetization dynamics in magnetic nanostructures, and hint at potential applications in novel spintronic devices utilizing the spin-transfer torque (STT) effect—such as spin-torque oscillators

(STOs) [7-8] and spin transfer torque magnetoresistive random access memories (STT-MRAMs). In this context, the film surface quality and the interfacial mixing play a crucial role, which in turn affect the overall magnetic response of the system, including the exchange coupling strength. For example, the presence of interfacial defects may lead to an increase in magnetic damping, whereas, the chemical and structural properties of the elemental layers (material properties, layer composition etc.) characterize the spin wave properties.

So far, numerous studies have been performed on such systems where the exchange coupling between the hard and soft layers has been tailored by varying the layer thickness [9-10], layer composition [11], number of repeats [12], and interfacial anisotropy [10]. The literature describes investigations of domain structure and other static magnetic properties for [Co/Pd]/Co [13], [Co/Pd]/NiFe [9,11,13-14], [Co/Pd]/CoFeB [12-13,15], [Co/Pd]-Co-Pd-NiFe [10], [Co/Ni]/NiFe [16] and CoCrPt-Ni [17]—these systems being studied with static magnetometry, magnetic force microscopy (MFM), and micromagnetic simulations. The magnetization dynamics in such systems have also been measured using Brillouin light scattering (BLS) [11,15] and ferromagnetic resonance (FMR) [14] experiments, where the spin wave (SW) modes have been investigated by varying the thickness of the soft layer and changing the configuration of the hard layer. In any process involving magnetization dynamics, the Gilbert damping constant ( $\alpha$ ) plays a key role in optimizing writing speeds and controlling power consumption. For example, in case of STT-MRAM and magnonic devices, low  $\alpha$  facilitates a lower writing current and the longer propagation of SWs, whereas a higher  $\alpha$  is desirable for increasing the reversal rates and the coherent reversal of magnetic elements, which are required for data storage devices.

In this chapter, we present all-optical excitation and detection of magnetization dynamics in [Co (0.5 nm)/Pd (1 nm)]<sub>5</sub>/NiFe ( $t$ ) tilted anisotropy ES systems, with varying soft layer thickness ( $t$ ), using a time-resolved magneto-optical Kerr effect (TR-MOKE) magnetometer. The dynamical magnetic behavior of similar systems has previously been studied using BLS [11] and FMR [14] measurements. However, a detailed study of the precessional magnetization dynamics and relaxation processes in such composite hard/soft systems is yet to be carried out. The advantage of implementing TR-MOKE is that here the magnetization dynamics can be measured on different time scales and the damping is measured directly in the time domain, and is therefore more reliable. We investigate the ultrafast magnetization dynamics over sub-picosecond time scales. The

ultrafast demagnetization is examined and found to change due to the modified spin structure in the soft layer for different  $t$  values. The extracted SW spectra are strongly dependent on  $t$ . An extensive study of the damping coefficient reveals that the extrinsic contribution to the damping is more dominant in the higher thickness regime, while intrinsic mechanisms govern the behavior at lower thicknesses.

## 7.2. Experimental Details

### 7.2.1. Sample Fabrication

The samples were fabricated using dc magnetron sputtering and have the following structure: Ta (5 nm)/Pd (3 nm)/[Co (0.5nm)/Pd (1 nm)]<sub>5</sub>/Ni<sub>80</sub>Fe<sub>20</sub>( $t$ )/ Ta (5 nm), where  $t=4-20$  nm. The chamber base pressure was below  $3 \times 10^{-8}$  Torr, while the Ar work pressure was 2 and 5 mTorr for the Ta, NiFe and Co, Pd layers, respectively. The samples were deposited at room temperature on naturally oxidized Si (100) substrates. The 5 nm Ta seed layer was used to induce fcc-(111) orientation in the Pd layer, which improves the perpendicular magnetic anisotropy of the Co/Pd multilayers; a Ta cap layer was used to avoid oxidation, which has been reported in previous studies [9-10,13]. The layer thicknesses are determined from the deposition time and calibrated deposition rates.

### 7.2.2. Measurement Technique

The surface morphology and the chemical compositions of the thin films were characterized using atomic force microscopy (AFM) and energy dispersive X-ray (EDX) spectroscopy, respectively. The static magnetic properties were investigated using vibration sample magnetometer (VSM) at room temperature, as presented in Fig. 7.1.

To investigate the precessional frequency and damping of these samples, the magnetization dynamics were measured by using an all-optical TR-MOKE magnetometer [18] based on a two color optical pump-probe experiment. The measurement geometry is shown in Fig. 7.2a. The magnetization dynamics was excited by laser pulses of wavelength ( $\lambda$ ) 400 nm (pulse width =100 fs, repetition rate= 80 MHz) of about  $16 \text{ mJ cm}^{-2}$  fluence and probed by laser pulses with  $\lambda= 800$  nm (pulse width = 88 fs, repetition rate= 80 MHz) of about  $2 \text{ mJ cm}^{-2}$  fluence. The pump and probe beams are focused using the same microscope objective with N.A. of 0.65 in a collinear geometry. The probe beam is tightly focused to a spot of about 800 nm on the sample surface and, as a result,

the pump becomes slightly defocused in the same plane to a spot of about 1  $\mu\text{m}$ . The probe beam is carefully aligned at the center of the pump beam with slightly larger spot size. Hence, the dynamic response is probed from a homogeneously excited volume. The bias field was tilted at around  $15^\circ$  to the sample normal (and its projection along the sample normal is referred to as  $H$  in this article) in order to have a finite demagnetizing field along the direction of the pump beam. This field is eventually modified by the pump pulse which induces precessional magnetization dynamics in the samples. The Kerr rotation of the probe beam, back-reflected from the sample surface, is measured by an optical bridge detector using phase sensitive detection techniques, as a function of the time-delay between the pump and probe beams. Figure 7.2b presents typical time-resolved Kerr rotation data from the ES sample with  $t = 7.5$  nm at a bias field  $H = 2.5$  kOe. The data shows a fast demagnetization within 500 fs and a fast remagnetization within 8 ps, followed by a slow remagnetization within 1800 ps. The precessional dynamics appear as an oscillatory signal above the slowly decaying part of the time-resolved Kerr rotation data. This part was further analyzed and a fast Fourier transform (FFT) was performed to extract the corresponding SW modes, as presented in Fig. 7.2c.

The obtained spin wave dynamics was further compared with the results obtained from the BLS technique. BLS measurements were performed in the backscattering geometry, where a monochromatic light of 532 nm wavelength was focused onto the sample surface. The light is then inelastically scattered from thermally excited SWs. Frequencies of the backscattered light were analyzed by a Sandercock-type (3 + 3)-pass Fabry–Perot interferometer. The magnetic field  $H$  was applied in the plane of the sample and perpendicular to the plane of light incidence. The measurements were performed for zero SW wave vector, i.e., the Kittel mode.

## 7.3. Results and Discussions

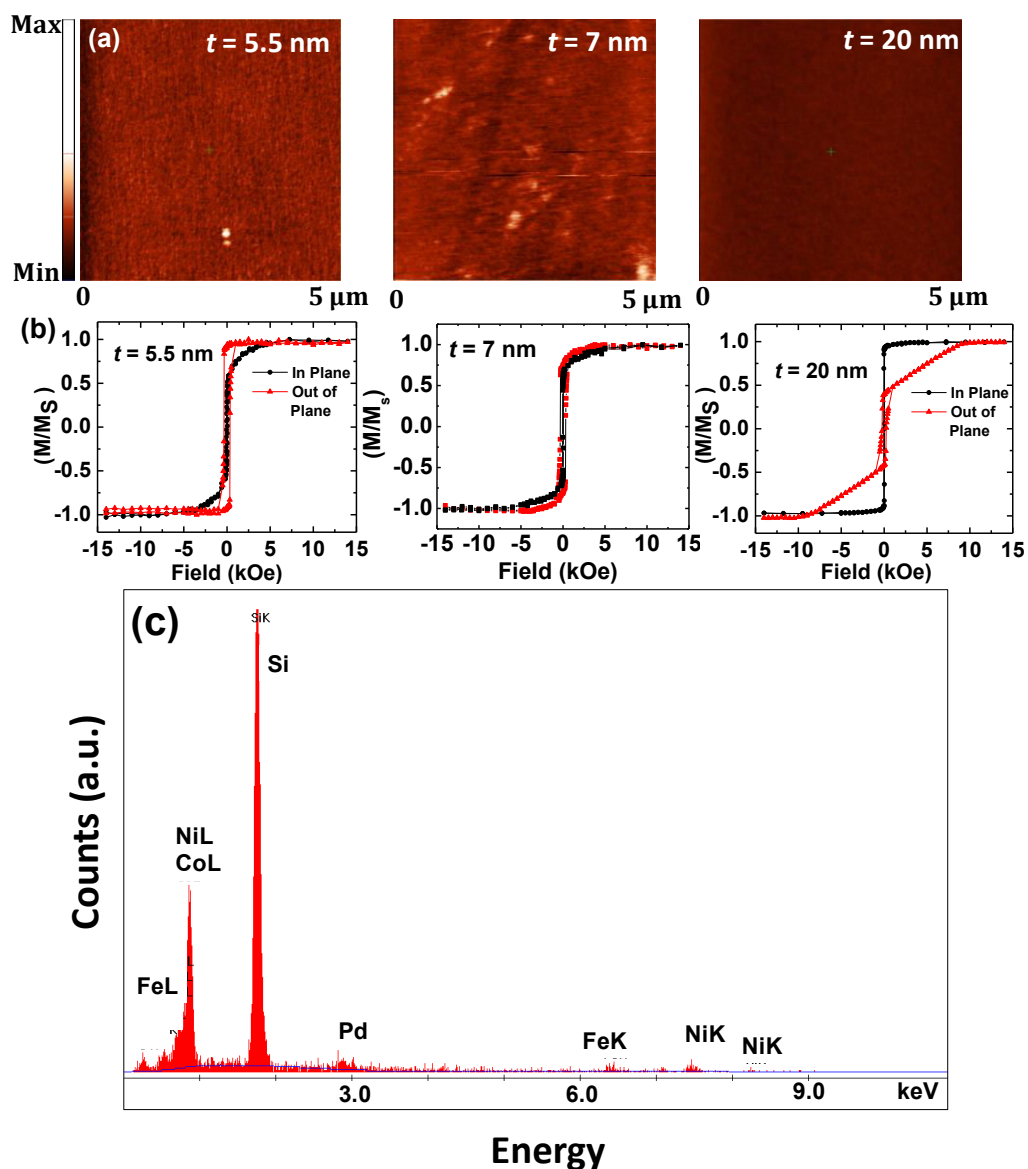


Figure 7.1: (a) In plane AFM images and (b) magnetic hysteresis loops (in-plane and out of plane) for the exchange spring systems with  $t = 5.5$  nm, 7 nm, 20 nm. (c) Typical EDX spectrum of the exchange spring systems.

The AFM images for  $t = 5.5$  nm, 7 nm and 20 nm samples are shown in Fig. 7.1a. The measured root mean square (RMS) roughness was approximately 0.14 nm, 0.16 nm and 0.27 nm, respectively. Figure 7.1b shows the out of plane (OOP) and in-plane (IP) hysteresis loops for the samples with  $t = 5.5$  nm, 7 nm and 20 nm. For  $t = 5.5$  nm, the OOP loop is nearly square with large

remanence, relatively small saturation field, and large coercivity, whereas the IP loop displays characteristic hard axis behavior. This indicates that the thin NiFe layer is rigidly coupled to the Co/Pd MLs during reversal. In contrast, for  $t = 20$  nm, the IP loop shows easy axis behavior, with a decrease in coercivity and saturation field. The OOP loop, interestingly, shows the behavior of a typical two phase system. This indicates a non-uniform spin distribution within the system, as will be shown later in this article. The hysteresis loops for  $t = 7$  nm, show nearly isotropic behavior, signaling a cancellation of the IP and OOP anisotropy, which is intermediate of  $t = 5.5$  nm and  $t = 20$  nm samples. A typical EDX spectrum for one of the samples is presented in Fig. 7.1c. As found from EDX analysis, the Ni: Fe ratio of the top layer is about 80 : 20, which is close to the nominal value.

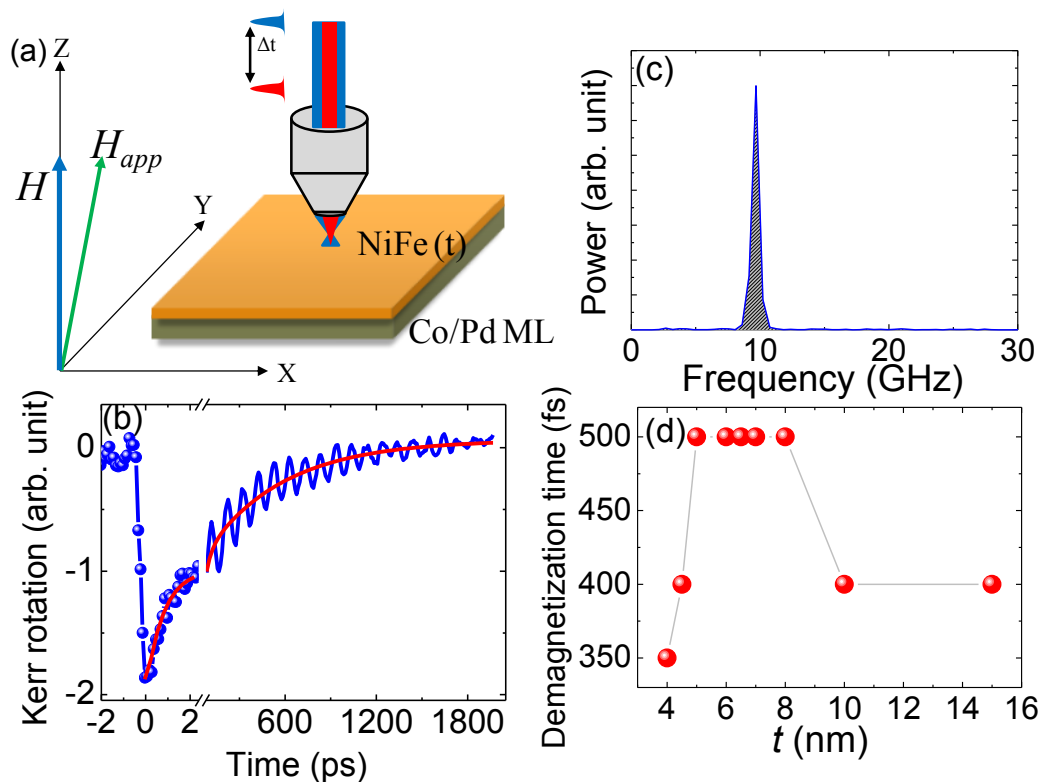


Figure 7.2: (a) Schematic of the two-color pump-probe measurement of the time-resolved magnetization dynamics of exchange-spring systems. The bias field is applied with a small angle to the normal of the sample plane. (b) Typical time-resolved Kerr rotation data revealing ultrafast demagnetization, fast and slow relaxations, and precession of magnetization for the exchange-spring system with  $t = 7.5$  nm at  $H = 2.5$  kOe. (c) FFT spectrum of the background-subtracted time-resolved Kerr rotation. (d) Variation of demagnetization time with  $t$ .

In order to closely observe the ultrafast demagnetization and fast remagnetization, we recorded the transient MOKE signals for delay times up to 30 ps at a resolution of 50 fs. In Fig. 7.2d, the demagnetization times are plotted as a function of  $t$ . We observe that the demagnetization is fastest in the thinnest NiFe layer ( $t=4$  nm) and increases sharply with the increase in  $t$ , becoming constant at 500 fs at  $t=5$  nm. At  $t=10$  nm, it decreases drastically to 400 fs and remains constant for further increases in  $t$ . For  $t < 5$  nm, the laser beam penetrates to the Co/Pd layer. In this regime, the large spin-orbit coupling of Pd enhances the spin-flip rate, resulting in a faster demagnetization process. As  $t$  increases, the top NiFe layer is primarily probed. Here, the spin configuration across the NiFe layer, which is further affected by the competition between the IP and the OOP anisotropies of the NiFe and [Co/Pd] layers, governs the demagnetization process. Qualitatively, ultrafast demagnetization can be understood by direct transfer of spin angular momentum between neighboring domains [19-20], which may be explained as follows: for  $t > 8$  nm, the magnetization orientation in the NiFe layer varies over a wide range of angles across the film thickness, where the magnetization gradually rotates from nearly perpendicular at the Co/Pd and NiFe interface to nearly parallel to the surface plane in the top most NiFe layer. Such a spin structure across the NiFe layer thickness can be seen as a network of several magnetic sublayers, where the spin orientation in each sublayer deviates from that of the neighboring sublayer. This canted spin structure accelerates the spin-flip scattering between the neighboring sublayers and thus results in a shorter demagnetization time, similar to the work reported by Vodungbo *et al.* [19]. On the other hand, for  $5 \text{ nm} < t < 8 \text{ nm}$ , the strong out-of plane anisotropy of the Co/Pd layer forces the magnetization in the NiFe film towards the direction perpendicular to the surface plane, giving rise to a uniform spin structure. The strong coupling reduces the transfer rate of spin angular momentum and causes the demagnetization time to increase. Investigating the variation of the precessional dynamics with  $t$ , we further recorded the time-resolved data for a maximum duration of 2 ns at a resolution of 10 ps.

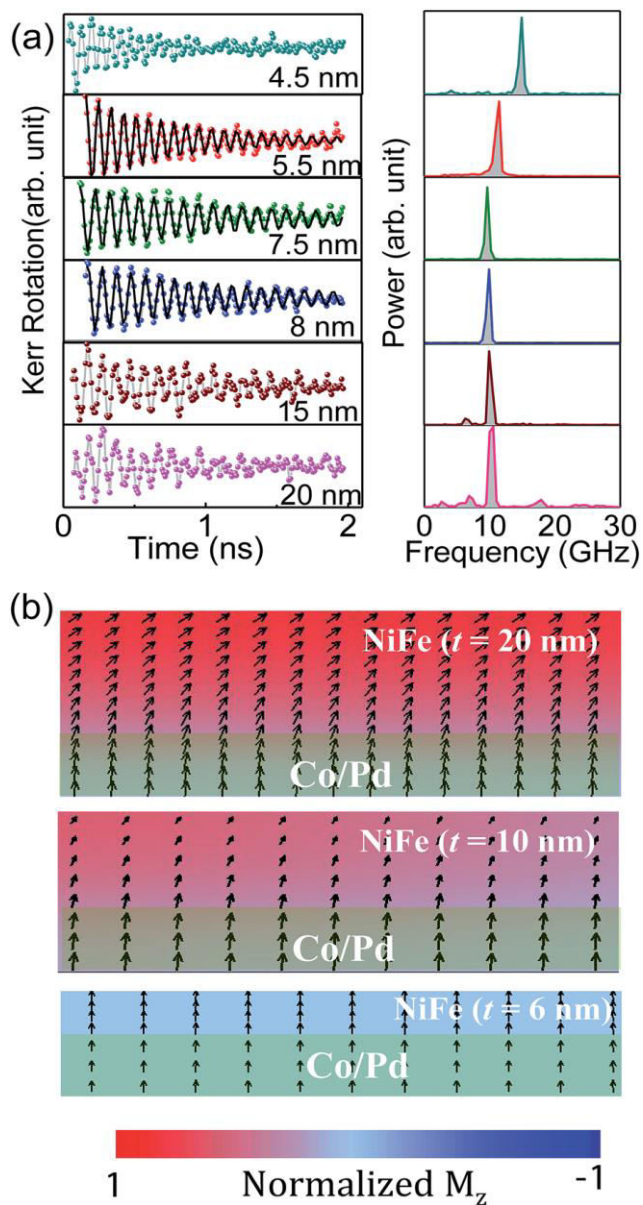


Figure 7.3: (a) Background-subtracted time-resolved Kerr rotation and the corresponding FFT spectra for samples with different  $t$  values at  $H = 2.5$  kOe. The black lines show the fit according to Eqn. 7.1. (b) Simulated static magnetic configurations for samples with  $t = 20$ ,  $10$ , and  $6$  nm with a bias field  $H = 2.5$  kOe in the experimental configuration. The simulated samples are not to scale. The color map is shown at the bottom of the figure.

Figure 7.3a shows the background subtracted time-resolved Kerr rotation data for different values of  $t$  at  $H = 2.5$  kOe and the corresponding FFT power spectra. Four distinct peaks are observed in the power spectrum of  $t = 20$  nm, which reduces to two for  $t = 15$  nm. This is probably due to the

relative decrease in the non-uniformity of the magnetization across the NiFe thickness, which agrees with the variation in the demagnetization time, as described earlier. To confirm this, we simulated the static magnetic configurations of these samples in a field of  $H = 2.5$  kOe using the LLG micromagnetic simulator [21]. Simulations were performed by discretizing the samples in arrays of cuboidal cells with two dimensional periodic boundary conditions applied within the sample plane. The simulations assume the Co/Pd multilayer as an effective medium [22] with saturation magnetization  $M_S = 690$  emu/cc, exchange stiffness constant  $A = 1.3 \times 10^{-6}$  erg/cm and anisotropy constant  $K_{ul} = 5.8$  Merg  $\text{cm}^{-3}$  along the (001) direction, while the material parameters used for the NiFe layer were  $M_S = 800$  emu/cc,  $A = 1.3 \times 10^{-6}$  erg/cm, and  $K_{ul} = 0$  [23]. The interlayer exchange between Co/Pd and NiFe is set to  $1.3 \times 10^{-6}$  erg/cm and the gyromagnetic ratio  $g = 18.1$  MHz/Oe is used for both layers. The Co/Pd layer was discretized into cells of dimension  $5 \times 5 \times 2$  nm<sup>3</sup> and the NiFe layer was discretized into cells of dimension  $5 \times 5 \times 1$  nm<sup>3</sup>. The results are presented in Fig. 7.3b for  $t = 20, 10,$  and  $6$  nm samples. The non-uniform spin structure is prominent in the NiFe layer of the  $t = 20$  nm sample, which modifies the SW spectrum of this sample, giving rise to the new modes [23]. With the reduction of  $t$ , the spin structure in the NiFe layer gradually becomes more uniform, while at  $t = 7.5$  nm it is completely uniform over the whole thickness profile. Hence, for low values of  $t$ , the power spectra show a single peak due to the collective precession of the whole stack.

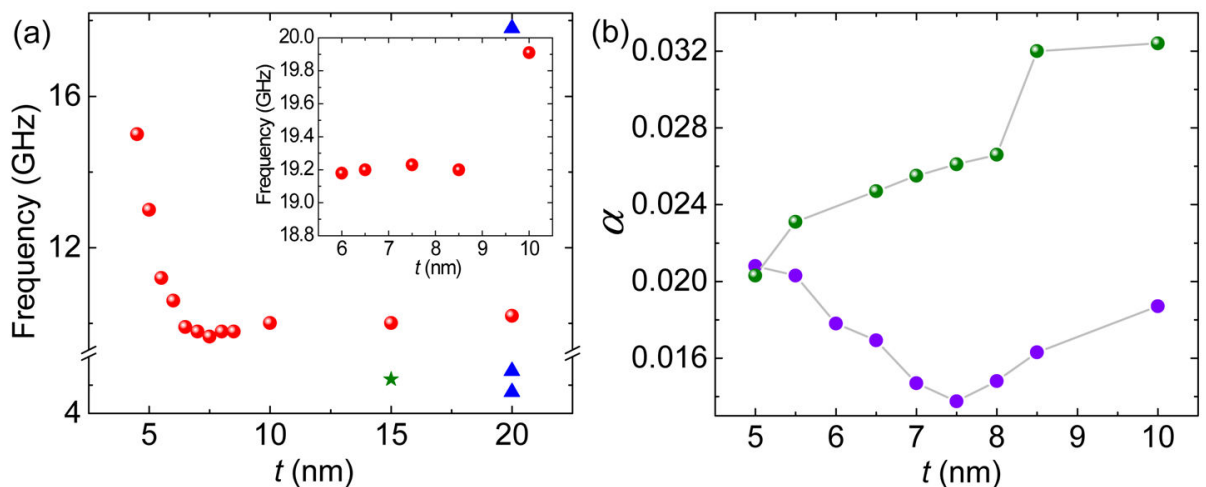


Figure 7.4: (a) Dependence of spin wave frequency on NiFe layer thickness ( $t$ ) at a magnetic field of 2.5 kOe. The inset shows the frequency dependence on  $t$  when the magnetic field (of 2.5 kOe) is applied in-plane, as obtained from BLS measurements. (b) Evolution of Gilbert damping constant as a function of  $t$  at  $H = 1.3$  kOe (green circles) and 2.5 kOe (violet circles).

The variation in precession frequency with  $t$  is plotted in Fig. 7.4a. The frequency of the most intense mode shows a slow decrease down to  $t = 7.5$  nm, below which it increases sharply down to the lowest thickness  $t = 4.5$  nm, exhibiting collective precessional dynamics. This mode is basically the uniform mode of the system and follows Kittel's equation [24]. The variation in frequency depicts the evolution of the effective anisotropy from OOP to IP with increasing  $t$ , which is in agreement with previously reported results [14]. For lower  $t$ , the system displays an OOP easy axis, owing to the strong OOP anisotropy of the Co/Pd multilayer. This is manifested as a sharp increase in the frequency with decreasing  $t$  below 7.5 nm. For greater thicknesses, the effect of the perpendicular anisotropy of the Co/Pd multilayer gradually decreases and the effect of the in-plane NiFe becomes more prominent. These two anisotropies cancel near  $t = 7.5$  nm, resulting in a minimum frequency, as shown in Fig. 7.4a. In the inset of Fig. 7.4a, the frequency vs.  $t$  plot measured using BLS technique is presented. In BLS measurements a magnetic field of 2.5 kOe (same in magnitude as in TR-MOKE measurements) is applied in the plane of the samples and the frequencies are recorded at zero wave vector (Kittel mode). The results reveal an increase in the frequency with increasing  $t$ . This, in turn, implies an enhancement of the IP anisotropy with increasing  $t$ , which is in complement with the TR-MOKE results.

To extract the damping coefficients, the time domain data was fitted with an exponentially damped harmonic function given by Eqn. 7.1.

$$M(t) = M(0)e^{-\frac{t}{\tau}} \sin(2\pi ft - \phi) \quad \dots\dots\dots(7.1)$$

where the relaxation time  $\tau$  is related to the Gilbert damping coefficient  $\alpha$  by the relation  $\tau = 1/(2\pi f\alpha)$ . Here,  $f$  is the experimentally obtained precession frequency and  $\phi$  is the initial phase of the oscillation. The fitted data for various values of  $t$  is shown by the solid black lines in Fig. 7.3a. We did not extract the values of  $\alpha$  for  $t = 15$  and 20 nm due to the occurrence of multimode oscillations, which may lead to an erroneous estimate of the damping. The extracted  $\alpha$  values are plotted against  $t$  in Fig. 7.4b for two different field values of  $H$  of 2.5 and 1.3 kOe. The evolution of  $\alpha$  as a function of  $t$  depends significantly on  $H$ , as can be seen from the figure. This is because of the different mechanisms responsible for determining the damping in different samples, as will be discussed later.

An interesting trend in the  $\alpha$  vs.  $t$  plot is observed for  $H = 2.5$  kOe. For  $10 \text{ nm} \leq t \leq 7.5 \text{ nm}$ ,  $\alpha$  decreases with decreasing  $t$  and reaches a minimum value of about 0.014 for  $t = 7.5 \text{ nm}$ . Below this thickness,  $\alpha$  increases monotonically and reaches a value of about 0.022 for the lowest thickness. This variation of  $\alpha$  is somewhat correlated with the variation of precession frequency with thickness. In the thinner regime, we probe both the NiFe layer and a fraction of the Co/Pd multilayer and the relative contribution from the latter increases as  $t$  decreases. The occurrence of a single mode oscillation points towards a collective precession of the stack, which may be considered as a medium with effective magnetic parameters consisting of both NiFe and Co/Pd layers. The variation in damping may be related to the variation in the anisotropy of the material. The competing IP and OOP anisotropies of the NiFe and Co/Pd layers lead to the appearance of a minimum in the damping. The damping in this system may have multiple contributions, namely (a) dephasing of the uniform mode in the spin-twist structure [25] (b) interfacial d-d hybridization at the Co/Pd interface [22], and (c) spin pumping into the Pd layers [26]. The first is an extrinsic mechanism and is dominant in samples with higher NiFe thicknesses, while the other two mechanisms are intrinsic damping mechanisms. For  $t > 7.5 \text{ nm}$ , due to the non-uniformity of the spin distribution, the dominant mode undergoes dynamic dephasing and the damping thus increases compared to the magnetically uniform samples. With the increase in NiFe thickness, the non-uniformity of spin distribution and the consequent mode dephasing across its thickness increases, leading to an increase in the damping value. Hence, in samples with higher  $t$  values, dephasing is the dominant mechanism, while at lower  $t$  values—i.e., when the contribution from the Co/Pd multilayer is dominant—the spin-orbit coupling and spin pumping effects dominate. At intermediate  $t$  values, the extrinsic and intrinsic effects compete with each other, leading to a minimum in the damping. However, the damping increases monotonically with  $t$  in a lower field of  $H = 1.3$  kOe. For a deeper understanding of this effect, we have measured  $\alpha$  as a function of precession frequency  $f$ .

Figure 7.5a and b show the variation of  $\alpha$  with  $f$ . Two different regimes in the thickness are presented in (a) and (b) to show the rate of variation more clearly.

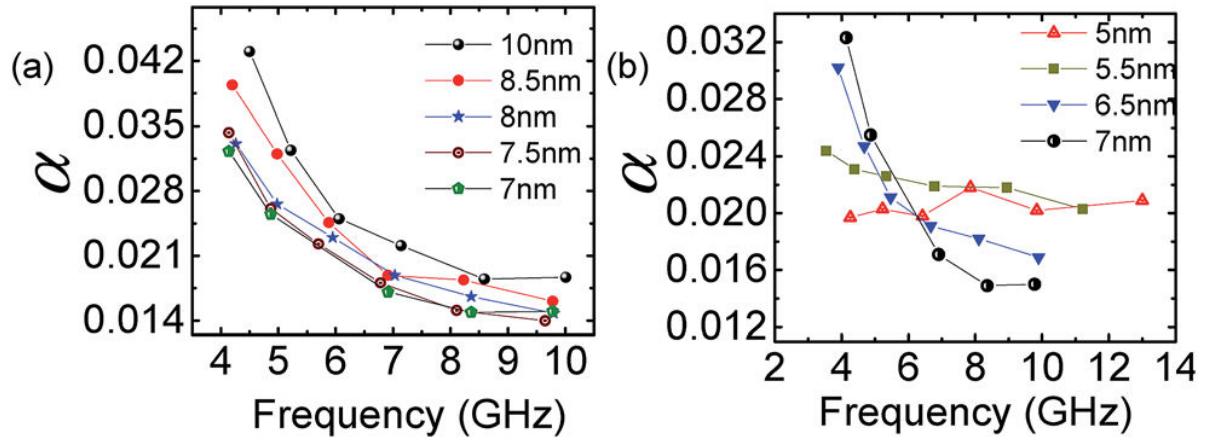


Figure 7.5: Dependence of Gilbert damping coefficient on soft layer thickness ( $t$ ) for (a) 7–10 nm and (b) 5–7 nm, respectively.

For  $10\text{ nm} \leq t \leq 7\text{ nm}$ ,  $\alpha$  decreases strongly with the increase in  $f$  and the rate of variation remains nearly constant with  $t$ . This is the signature of extrinsic damping generated by the non-uniform spin distribution. However, for  $t = 6.5\text{ nm}$ , the rate falls drastically and for  $t \leq 5.5\text{ nm}$ ,  $\alpha$  becomes nearly independent of  $t$ , which indicates that purely intrinsic damping is operating in this regime. This confirms the competition between two different types of damping mechanisms in these samples.

The study demonstrates that various aspects of ultrafast magnetization dynamics—namely demagnetization time, precession frequency, number of modes, and damping—are influenced by the spin distribution in the soft magnetic layer, as well as by the properties of the hard layer. By changing the thickness of the soft layer, the relative contributions of these factors can be tuned effectively. This enables efficient control of the damping and other magnetic properties over a broad range, and will hence be very useful for potential applications in spintronic and magnonic devices.

## 7.4. Conclusions

In summary, we have employed the time-resolved MOKE technique to measure the evolution of ultrafast magnetization dynamics in exchange-coupled  $[\text{Co/Pd}]_5/\text{NiFe}(t)$  multilayers, with varying NiFe layer thicknesses, by applying an out-of-plane bias magnetic field. The coupling of a high-

anisotropy multilayer with a soft layer allows broad control over the spin structure, and consequently other dynamic magnetic properties which are strongly dependent on  $t$ . The ultrafast demagnetization displayed a strong variation with  $t$ . The reason for this was ascribed to the chiral-spin-structure-dependent spin-flip scattering in the top NiFe layer, as well as to interfacial 3d–4d hybridization of Co/Pd layer. The precessional dynamics showed multiple spin wave modes for  $t = 20$  nm and 15 nm, whereas a single spin wave mode is observed for thinner NiFe layers following the change in the magnetization profile with decreasing  $t$ . The precession frequency and the damping show strong variation with the thickness of the NiFe layer. The changes in frequency are understood in terms of the modification of the anisotropy of the system, while the variation in damping originates from the competition between intrinsic and extrinsic mechanisms, which are somewhat related to the anisotropy. The observed dynamics will be important for understanding the utilization of tilted anisotropy materials in devices such as spin transfer torque MRAM and spin-torque nano-oscillators.

## References

- [1] R. E. Camley, B. V. McGrath, R. J. Axtal, *et al.*, “Magnetization dynamics: A study of the ferromagnet/antiferromagnet interface and exchange biasing,” *J. Vac. Sci. Technol. A* **17**, 1335 (1999).
- [2] M. C. Weber, H. Nembach, S. Blomeier, *et al.*, “All-optical probe of magnetization dynamics in exchange biased bilayers on the picosecond timescale,” *Eur. Phys. J. B* **45**, 243 (2005).
- [3] A. Haldar, C. Banerjee, P. Laha, *et al.*, “Brillouin light scattering study of spin waves in NiFe/Co exchange spring bilayer films,” *J. Appl. Phys.* **115**, 133901 (2014).
- [4] D. C. Crew and R. L. Stamps, “Ferromagnetic resonance in exchange spring thin films,” *J. Appl. Phys.* **93**, 6483 (2003).
- [5] J. S. Jiang, E. E. Fullerton, M. Grimsditch, *et al.*, “Exchange-spring behavior in epitaxial hard/soft magnetic bilayers,” *J. Appl. Phys.* **58**, 12193 (1998).
- [6] T. J. Fal, K. L. Livesey and R. E. Camley, “Domain wall and microwave assisted switching in an exchange spring bilayer,” *J. Appl. Phys.* **109**, 093911 (2011).

- [7] Y. Zhou, C. L. Zha, S. Bonetti, *et al.*, “Spin-torque oscillator with tilted fixed layer magnetization,” *Appl. Phys. Lett.* **92**, 262508 (2008).
- [8] Y. Zhou, C. L. Zha, S. Bonetti, *et al.*, “Microwave generation of tilted-polarizer spin torque oscillator,” *J. Appl. Phys.* **105**, 07D116 (2009).
- [9] T. N. A. Nguyen, Y. Fang, V. Fallahi, *et al.*, “[Co/Pd]-NiFe exchange springs with tunable magnetization tilt angle,” *Appl. Phys. Lett.* **98**, 172502 (2011).
- [10] T. N. A. Nguyen, N. Benatmane, V. Fallahi, *et al.*, “[Co/Pd]<sub>4</sub>-Co-Pd-NiFe spring magnets with highly tunable and uniform magnetization tilt angles,” *J. Magn. Magn. Mater.* **324**, 3929 (2012).
- [11] S. Tacchi, T. N. A. Nguyen, G. Carlotti, *et al.*, “Spin wave excitations in exchange-coupled [Co/Pd]-NiFe films with tunable tilting of the magnetization,” *Phys. Rev. B* **87**, 144426 (2013).
- [12] T. N. A. Nguyen, R. Knut, V. Fallahi, *et al.*, “Depth-Dependent Magnetization Profiles of Hybrid Exchange Springs,” *Phys. Rev. Appl.* **2**, 044014 (2014).
- [13] T. N. A. Nguyen, V. Fallahi, Q. T. Le, *et al.*, “Investigation of the Tunability of the Spin Configuration Inside Exchange Coupled Springs of Hard/Soft Magnets,” *IEEE Trans. Magn.* **50**, 2004906 (2014).
- [14] L. Tryputen, F. Guo, F. Liu, *et al.*, “Magnetic structure and anisotropy of [Co/Pd]<sub>5</sub>-NiFe multilayers,” *Phys. Rev. B* **91**, 014407 (2015).
- [15] S. Tacchi, T. N. A. Nguyen, G. Gubbiotti, *et al.*, “[Co/Pd]-CoFeB exchange spring magnets with tunable gap of spin wave excitations,” *J. Phys. D: Appl. Phys.* **47**, 495004 (2014).
- [16] S. Chung, S. M. Mohseni, V. Fallahi, *et al.*, “Tunable spin configuration in [Co/Ni]-NiFe spring magnets,” *J. Phys. D: Appl. Phys.* **46**, 125004 (2013).
- [17] D. Navas, J. Torrejon, F. B’oeron, *et al.*, “Magnetization reversal and exchange bias effects in hard/soft ferromagnetic bilayers with orthogonal anisotropies,” *New J. Phys.* **14**, 113001 (2012).
- [18] A. Barman and A. Haldar, "Solid State Physics Vol. 65, eds E. Camley Robert & L. Stamps Robert (pp.1-108)," Academic Press, (2014).
- [19] B. Vodungbo, G. Julien, G. Lambert, *et al.*, “Laser-induced ultrafast demagnetization in the presence of a nanoscale magnetic domain network,” *Nat. Commun.* **3**, 999 (2012).

- [20] B. Koopmans, G. Malinowski, F. D. Longa, *et al.*, “Explaining the paradoxical diversity of ultrafast laser-induced demagnetization,” *Nat. Mater.* **9**, 259 (2010).
- [21] M. R. Scheinfein, LLG Micromagnetics Simulator, available: <http://www.llgmicro.home.mindspring.com/>.
- [22] S. Pal, B. Rana, O. Hellwig, *et al.*, “Tunable magnonic frequency and damping in [Co/Pd]<sub>8</sub> multilayers with variable co layer thickness,” *Appl. Phys. Lett.* **98**, 082501 (2011).
- [23] S. Pal, S. Barman, O. Hellwig, *et al.*, “Effect of the Spin-Twist Structure on the Spin-Wave Dynamics in Fe<sub>55</sub>Pt<sub>45</sub>/Ni<sub>80</sub>Fe<sub>20</sub> Exchange Coupled Bi-layers with varying Ni<sub>80</sub>Fe<sub>20</sub> Thickness,” *J. Appl. Phys.* **115**, 17D105 (2014).
- [24] C. Kittel, “On the Theory of Ferromagnetic Resonance Absorption,” *Phys. Rev.* **73**, 155 (1948).
- [25] A. Barman and S. Barman, “Dynamic dephasing of magnetization precession in arrays of thin magnetic elements,” *Phys. Rev. B* **79**, 144415 (2009).
- [26] Y. Tserkovnyak, A. Brataas and G. E. W. Bauer, “Enhanced Gilbert damping in thin ferromagnetic films,” *Phys. Rev. Lett.* **88**, 117601 (2002).

## Chapter 8

# 8. Investigation of Magnonic Band Structure in Co/Pd Stripe Domain System

---

### 8.1. Introduction

The potential of spin waves (SWs) to excite, transmit, store, and retrieve electric signals as well as to perform logical operations has fueled a new spectrum of research in the wave-based signal processing technology [1-4]. Usually, magnonic crystals (MC), *i.e.* arrays of nanoscale magnetic stripes [5], dots [6], antidots [7], etched grooves or pits [8], periodic variations of the internal magnetic field [9] and saturation magnetization by ion implantation [10], are employed to control the flow of SWs. Magnetostatic surface SWs or the Damon–Eshbach (DE) SW modes, which propagate perpendicular to the in-plane (IP) magnetization direction, are promising in this context because of their large group velocities ( $v_g$ ) and low attenuation. Consequently, significant progress has been made towards the practical realization of magnonic devices in terms of the on-chip generation, directional channeling, detection and manipulation of SWs. However, to realize the experimental geometry, a large magnetic field has to be applied to enforce the magnetization perpendicular to the SW propagation direction. This is a major obstacle to the implementation of a MC into a practical device. A way out is to use the Oersted field generated from an underlying current-carrying stripe [11-12], which is still plagued by the problem of generation of waste heat which increases with increasing data processing speed. Moreover, the fabrication of periodic nanostructures involves high-precision electron-beam lithography which is very complex and expensive. An alternative approach to overcome these fundamental drawbacks is to take recourse to the spin dynamics in the remanent state, which is more suitable for nanoscale device applications, as it does not require any stand-by power once initialized.

In the literature, only few reports exist on the magnetization dynamics for systems with an inhomogeneous magnetization distribution containing domains and domain walls. Most commonly studied is a periodic or non-periodic distribution of magnetic units of up and down domains (parallel, labyrinthine, bubble-like domains) [13-19], separated by negligibly thin, one-

dimensional domain walls. Such domains appear in magnetic thin films with a perpendicular anisotropy smaller than the demagnetizing energy if the film thickness is higher than a critical value  $t_c$ , which is, in turn, dependent on the perpendicular anisotropy constant, saturation magnetization and the exchange constant. The morphology of the domains and consequently the spin dynamics are strongly affected by the field history, allowing for a broad range of tunability. Moreover, just recently the topic of SWs propagation within domain walls, as an ultra-narrow waveguides is intensively studied by the magnonic community, however, mostly theoretically in magnetic systems with strong Dzyaloshinskii-Moriya interaction [20-23]. There are only a few examples of experimentally realized systems presenting SW propagation within domain wall [24].

The study on the magnetic properties of stripe domain systems (array of parallel up and down domains) was pioneered by Kittel [25], where the formation of stripe domains was predicted for films thicker than the magnetic domain width. After that, a multitude of theoretical [26-27] and experimental [14, 28-30] studies have been carried out in this direction for a broad variety of magnetic systems, where the evolution, morphology and interaction between the stripe domains are addressed. Experimentally, the formation of a stripe domain structure is characterized as a function of film thickness, applied magnetic field, annealing temperature, film composition, etc., using magnetic force microscopy (MFM), magneto-optical Kerr effect (MOKE), X-ray diffraction, for NiFe [31-32], Co [33-34], CoFeSiB [35], FeSiB [36-37], FeCoAlON [38], FeCoZr [39], FePd [40] films. Nevertheless, only few measurements have been reported so far on the dynamical properties of magnetization, which used ferromagnetic resonance (FMR) [40-42] and Brillouin light scattering (BLS) [14, 43] techniques. The results reveal that the consecutive domains give rise to periodically modulated internal magnetic field, which introduces a partial reflection of the propagating SW at the stripe domain boundaries. The feature of rotational magnetic anisotropy is also evidenced, which is associated with the reorientation of the stripes. These results triggered the possibility towards achieving reconfigurable magnetic properties by tailoring the intricate interaction between the consecutive stripes as well as the magnetocrystalline anisotropy in these systems.

In this chapter, we aim at developing a combined understanding of the static and dynamic magnetic properties of the parallel stripe domain structure in Co/Pd multilayered systems. The study of magnetic multilayers with high perpendicular magnetic anisotropy (PMA) is motivated to a large extent by industrial importance of these films, *e.g.*, in patterned magnetic media [44],

spin transfer torque magnetoresistive random access memory (STT-MRAM) [45] and magnonic crystals [46]. In these systems, the interface anisotropy (because of the broken symmetry), combined with  $d-d$  hybridization at the ferromagnet/nonmagnet interfaces, are responsible for the onset of PMA, and consequently of a stripe domain structure, for film thickness greater than a critical value. Moreover, the proximity effect, along with the magnetic coupling between the layers leads to magnetic properties unreachable to standard single-layer systems. These effects get further modified in presence of stripe domain. In this context, a deep understanding of the magnetic coupling between the constitutive layers at larger stack thickness and the impact of stripe domain on the static and dynamic properties become of crucial interest. So far, the quasistatic properties of the domain structure have been investigated for FeNi/Co [47], FePd [7, 48], Fe/Cu [49], Co/Cu/(Fe/Ni)/Cu(001) [50] and Co/Au [51] multilayers. However, the dynamic SW properties are still unexplored.

Here we have investigated the static and dynamic magnetic properties in Co/Pd multilayers with stripe domains by using MFM, vibrating sample magnetometry (VSM) and Brillouin light scattering (BLS) spectroscopy. Our first goal is to examine how this stable spin configuration manifests itself on the dynamic response. For that, the SWs were measured in saturated as well as in remanent state (*i.e.* in presence of stripe domain) and their wave vector dispersions are analyzed and compared. We have further studied the evolution of the SW band structure by changing the relative orientation between the SW wave vector and the domains. Micromagnetic simulations are employed to calculate both eigenvalues (mode frequencies) and eigen vectors (mode profiles) of the SWs. The results proclaim that the SW propagation is similar to that in a one-dimensional (1D) magnonic crystal, which can be significantly reconfigured by varying the wave vector orientation. Furthermore, this system serves as a possible prototype for magnon-based data transfer devices, with the advantage of non-volatile operation, energy efficient computing, ease of fabrication and control on SW frequency and velocity.

## 8.2. Experimental Details

The multilayered sample was deposited using DC magnetron sputtering and has the following structure: Ta (15) /Pd (30) / [Co (10) /Pd (7)]<sub>25</sub> /Pd (20), where the numbers denote the thickness in Å. For deposition we used a multi-source confocal sputter up geometry with a source/substrate distance of 0.1-0.15 m. During deposition, the substrate was rotated for uniformity at about 3 Hz

and was kept at room temperature using a low Argon pressure of 3mTorr. Co was sputtered at 250 W with a deposition rate of 0.7 Å/sec and Pd was sputtered at 100 W with a deposition rate of ~2 Å/sec. Given the low Ar pressure used during deposition, the film is relatively smooth, with sharply defined interfaces [52].

To obtain the aligned stripe domain structure, the saturating magnetic field was applied within the film plane (arbitrary direction, as the films are [111] out-of-plane (OOP) textured and IP isotropic) followed by an IP AC demagnetization (preferred alignment of the domains is along the applied field direction), *i.e.* the IP field is switched back and forth between positive and negative polarity starting above the saturation field strength down to about a few Oersted, where the field amplitude is reduced about 1% in each step. As a result, we obtain an aligned parallel magnetic stripe domain state similar to an array of artificial stripe wires, *i.e.* a magnonic crystal. The magnetization curves (IP and perpendicular to the plane) were measured using VSM at room temperature. The domain images at the remanent state were recorded by magnetic force microscopy (MFM). BLS measurements in the 180° backscattered geometry were employed to investigate the wave vector dispersions of the thermal magnons. This technique relies on an inelastic light scattering process due to interaction between incident photons and magnons. Monochromatic laser light (wavelength  $\lambda = 532$  nm) from a solid state laser was focused on the sample surface. As the laser beam is inelastically scattered from the magnons, due to conservation of momentum, the magnitude of the IP transferred wave vector  $q$  depends on the incidence angle of light  $\theta$  according to:  $q = (4\pi/\lambda)\sin\theta$ . The direction of magnon wave vector  $q$  lies along the intersection of the scattering plane and the film plane. Cross polarizations between the incident and the scattered beams were adopted in order to minimize the phonon contribution to the scattered light. Subsequently, the frequencies of the scattered light are analyzed using a Sandercock-type six-pass tandem Fabry-Perot interferometer (JRS Scientific Instruments) [53]. One set of measurements was carried out in the demagnetized state in presence of the stripe domains for  $q$  parallel and perpendicular to the stripe axis. This was accomplished by rotating the sample around the film normal, *i.e.* varying the angle  $\varphi$  between  $q$  and stripe axis. In another measurement set, the sample was saturated applying a strong IP magnetic field ( $H = 3.5$  kOe) and the wave vector dispersion was taken in the DE geometry ( $q \perp H$ ).

## 8.3. Micromagnetic Simulations

To validate the experimental results and to understand the physical character of the resonant modes we exploited micromagnetic simulations (MSs) by means of open-source gpu-accelerated MuMax3 program [54] solving full Landau-Lifshitz equation using time domain finite difference method. MSs primarily were used to relax the stable stripe domain pattern of comparable lattice constant as obtained experimentally, to compute dispersion relations for the uniformly IP magnetized structure and the stripe domain pattern, and, finally, to visualize resonant mode profiles. In MSs we assumed effective homogeneous material parameters in the whole structure. The saturation magnetization and anisotropy constant were set to the values obtained from the VSM measurements (as will be discussed later), i.e.  $M_S=970$  emu/cc, and  $K_u=1.9\times 10^6$  erg/cm<sup>3</sup>. To fit MSs results with the BLS data, we had to assume an anisotropic exchange constant [55-57], with  $A_{ex,IP}=1.45\times 10^{-6}$  erg/cm and  $A_{ex,OOP}=1.05\times 10^{-6}$  erg/cm along the IP and out-of-plane (OOP) directions, respectively.

### 8.3.1. Discretization

MS were performed for the system of thickness  $L_z=42.5$  nm, discretized with the unit cell of dimensions being much smaller than the exchange length or width of the domain walls. It was  $1\times 1\times L_z/16$  nm<sup>3</sup> or  $2\times 1\times L_z/16$  nm<sup>3</sup>. At the lateral edges of the simulated structure, which dimensions were chosen to obtain dispersion with sufficient resolution, periodic boundary conditions were assumed. To shorten the simulation time, the lateral dimensions of the simulated structures were varied depending on the magnetic configuration and direction of SWs propagation with respect to the domain walls (DWs) (the coordinate axes are shown in Fig. 8.1c). In the case of SWs propagating in a uniformly magnetized film it was  $5\ \mu\text{m} \times 0.1\ \mu\text{m}$ . In the case of SWs propagating across DWs in the stripe domain structure it was  $0.1\ \mu\text{m} \times 25A$ , where  $A$  is the relaxed stripe domain pattern lattice constant. For magnetic parameters used in the MSs it was  $A=100$  nm. Finally, for SWs propagating parallel to the DWs, along the  $x$ -axis, it was  $5\ \mu\text{m} \times 2A$ .

### 8.3.2. Stripe Domain Pattern Relaxation

To obtain a stable stripe domain pattern following algorithm of relaxation was applied. In order to accelerate simulations and to obtain stripe domains along the  $x$ -axis, one unit cell with periodic

boundary conditions along the  $x$ -axis and periodic boundary conditions along the  $y$ -axis were assumed. Along the  $y$ -axis a sufficiently large number of unit cells should be assumed to enable relaxation of dozens of stripe domains.

In the first stage of the MSs, the system was in-plane magnetized by a high magnetic field strength parallel to the  $x$ -axis. Then, the field strength was reduced (in MSs we assumed field steps of value  $\Delta H= 250$  Oe) and the magnetic configuration was slightly perturbed by a dynamic impulse of the orthogonal magnetic field (parallel to the  $z$ -axis) and again relaxed. This procedure was repeated till the external field strength was reduced to  $H=0$ . At the end, a stripe domain pattern is obtained. In the last stage, the system was stretched along the  $x$ -axis and cut to desired dimensions, before starting the SW dynamic simulations.

### 8.3.3. Dispersion Relation and Resonant Mode Profiles Calculation

The SWs dispersion relation and modes profiles were calculated according to Ref. [58]. In the first stage a stripe domain pattern was perturbed by a small amplitude dynamic magnetic field of broad band frequency and wave vector spectra. The dispersion relations were computed by transforming the time dependent OOP magnetization component into frequency and wave vector space using two dimensional fast Fourier transformation (FFT). Obtained results are presented in a form of color maps where color intensities correspond to the OOP component of the magnetization and relate to the intensities obtained in measurements. Resonant mode profiles are presented as a distribution of the amplitude and phase of the OOP dynamic magnetization component ( $m_z$ ), a component to which BLS is sensitive to.

## 8.4. Results and Discussions

The stripe domain patterns as measured by MFM in the demagnetized states are shown in Fig. 8.1a. After IP AC demagnetization, we observe well-defined parallel stripe domains aligned along the IP demagnetization direction. The half period of the pattern is  $A/2 \approx 60$  nm ( $A$  being the lattice constant), which is comparable to the thickness of the entire stack (42.5 nm). As mentioned in the introduction, the broken translational symmetry at the Co/Pd interfaces, combined with the  $d-d$  hybridization is responsible for the PMA in this structure, which favors an OOP magnetization.

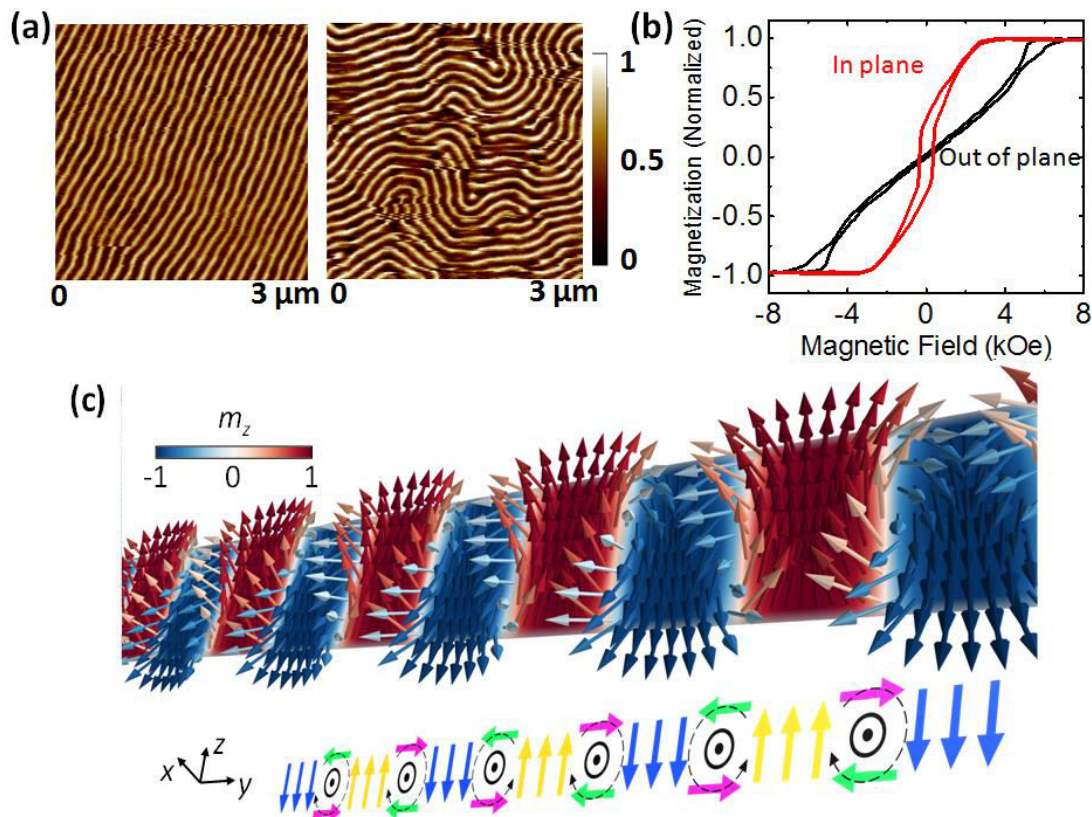


Figure 8.1: (a) MFM image in the demagnetized state showing the parallel (left panel) and labyrinth (right panel) stripe domains of the Co/Pd multilayered system, obtained after IP and OOP AC demagnetization, respectively. (b) Magnetic hysteresis loops of the multilayers with IP and OOP applied magnetic fields. (c) The domain configuration (cross-sectional view) obtained from micromagnetic simulations. Arrows correspond to the magnetization vector and colors spanning between blue and red correspond to the OOP component of the magnetization. The bottom panel schematically visualizes static magnetization with clockwise and anticlockwise domain walls. The  $x$  and  $z$  axes are assumed to be parallel to domain walls and multilayered system thickness, respectively.

The tendency of the magnetization to rotate OOP, however, is hindered by the presence of the magnetic charges on the surface of the film, which contributes to the magnetostatic energy (shape anisotropy). The competition between the PMA and the thin-film shape anisotropy leads to domains with up and down magnetization perpendicular to the film plane [30]. The features of stripe domain pattern depend on the respective thicknesses of the layers, the number of repetitions of the Co/Pd bilayer, and the amplitude of the anisotropy field. Basically, the magnetic domains occur when the gain in magnetostatic energy due to the domain structure is bigger than the energy

required to form the domain walls. A quality factor is defined, as given by,  $Q = \frac{K_u}{2\pi M_s^2}$ , where  $K_u$  is OOP anisotropy energy density while  $M_s$  is saturation magnetization. For a moderate value of the quality ratio,  $Q \leq 1$ , a ground state with a stripe domain structure is favored.

The static magnetometry results for applied field along IP and OOP directions are shown in Fig. 8.1b. The higher saturating field ( $\sim 7.5$  kOe) observed on the OOP hysteresis loop suggests that the magnetization is primarily in the sample plane. The IP hysteresis loop marks two distinct magnetization phases: an IP component, which quickly reverses at fields close to the coercive field, and a linear approach to saturation (starting at around  $H \approx 1500$  Oe), due to the perpendicularly magnetized stripe domains, whose magnetization progressively rotates under the application of an IP magnetic field. The coercivity is approximately 0.7 kOe and the remanent magnetization is around 30%, revealing that the magnetization vector is tilted *w.r.t.* the OOP direction. The magnetization reversal curve for OOP magnetic field, on the other hand, is characterized by domain nucleation, propagation, and annihilation characteristics of labyrinth domain structure [15]. As discussed in Ref. 15, the parallel domains are robust and stable under small OOP field exposures up to about  $\pm 3-4$  kOe, *i.e.*, within the linear region of the OOP hysteresis loop. In this range, only the relative width of up versus down domains is altered by the out-of-plane field although the overall domain topology is preserved. Figure 8.1a (right panel) shows the MFM image taken after demagnetizing the film with perpendicular applied field, which confirms the labyrinth domain formation. The saturation magnetization and the uniaxial anisotropy constant associated with the PMA were both estimated from the hysteresis curves as  $M_s = 970$  emu/cc, and  $K_u = 1.9 \times 10^6$  erg/cm<sup>3</sup> [59]. These values give a quality factor  $Q = 0.3$ .

We first describe the BLS measurements of the wave vector dispersion of thermal SWs after saturating the sample magnetization by applying an IP field  $H = 3.5$  kOe. The measurement geometry is shown in Fig. 8.2a, where the transferred IP wave vector is perpendicular to direction of magnetization, *i.e.* DE geometry. Figure 8.2g shows measured SW frequency peaks (solid symbols, labelled with M) as a function of  $q$ , together with a typical spectrum taken at  $q = 1.2 \times 10^7$  rad/m (Fig. 8.2d). We observed two dispersive modes where the mode M1 (M2) shows a maximum (minimum) at  $q_g = 1 \times 10^7$  rad/m, leading to a frequency gap of 3 GHz.

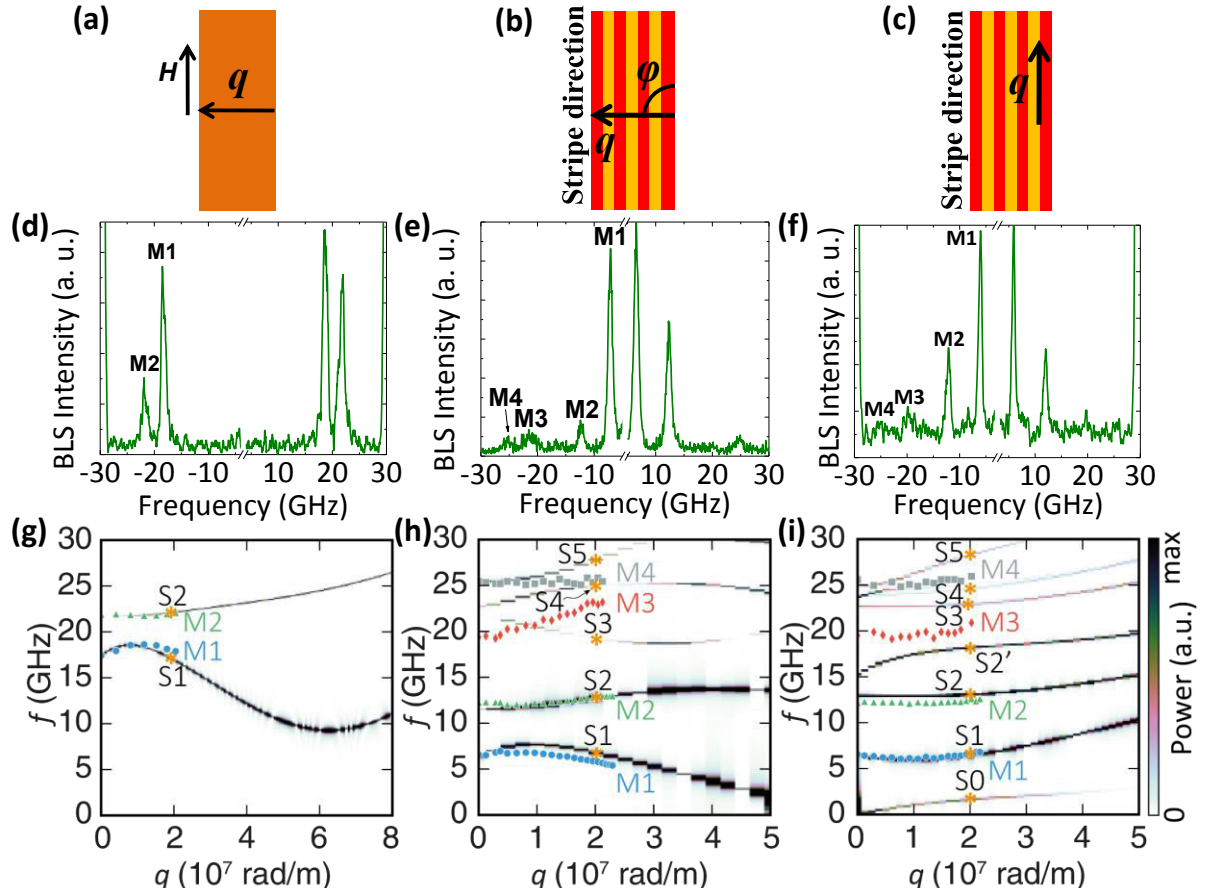


Figure 8.2: (a)-(c) The measurement geometries for the saturated state,  $\phi=90^\circ$  in (a) and (b), and  $\phi=0^\circ$  in (c). (d)-(f) Corresponding typical BLS spectra at  $q=1.2 \times 10^7$  rad/m and (g)-(i) dispersion curves. Measured in BLS dispersions and modes are labeled with M and marked with the color points in (g)-(i). Simulation results are shown by the gray scale map, the orange stars labeled with S represent modes visualized in Fig. 8.3.

To validate the experimental results and to understand the physical character of the resonant modes we exploited micromagnetic simulations. The simulated mode frequency in dependence on the wave vector is presented by the gray scale map in Fig. 8.2g (marked with label S), which agree well with the experimental results. Further, we investigated the physical nature of the modes. Figure 8.3a displays the corresponding power and phase maps of the SW modes at  $q=2 \times 10^7$  rad/m. The result reveals the mode M1 (S1) extends across the volume of the sample, however with increasing localization of the amplitude at the bottom surface of the film as the wave number increases. This points at the DE character of the mode, although with non-monotonic dispersion. The former is also accorded by the marked Stokes/anti-Stokes asymmetry of the mode in the BLS spectrum, which can be reversed by simply reversing the direction of the magnetic

field. We attribute this unusual non-monotonicity to the PMA, as confirmed with the analytical model [60], which reproduces the BLS as well as the micromagnetic simulation dispersion relations. The mode M2 (S2) is a perpendicular standing spin wave (PSSW) excitation of the exchange character with the one nodal plane in the middle of the film (Fig. 8.3a).

In the next step, we investigated how the SW dynamics are modified in presence of a stripe domain structure. Figure 8.1c presents the cross-sectional view of the simulated stripe domain structure where the magnetic state is shown with the arrows and OOP component of the magnetization by a red-white-blue colormap and arrows' color. Clearly, it consists of basic up and down domains, with a spatial periodicity of about  $A=100$  nm which is in reasonable agreement (slightly under-estimated) with the experimental MFM images. These domains are separated by complex twisted domain walls (DW), as given by the not fully vertical arrows of colors different than saturated dark red and dark blue being present in the middle part of each domain, where the magnetization is exactly parallel to the  $z$ -axis.

Note that, the DW occupies a significant region in each spatial period, so that the magnetization profile in each domain deviates from its rectangular shape. For the DWs, interestingly, two main features are evidenced as follows. i) The magnetization profile in the DW depicts a Neel-wall like character at the film surfaces, which eventually rotates towards the direction parallel to the DW axes when moved away from the surface (Bloch-wall like) [see schematic representation of domain structure in Fig. 8.1c (lower panel)]. ii) At the same time, it evolves into a twisted pattern around the DW axis (cork-screw type) [61], which is clockwise or anti-clockwise for alternate DWs (see Fig. 8.1c). Consequently, the resultant magnetization inside the DW is directed IP along the DW axis. This spin configuration is different from the closure domain structure reported earlier for single layered films. In fact, the spin structure is governed by the minimization of total energy and as reported in Ref. [27], the dipolar interaction between consecutive domains is minimal when the magnetization vector stays in the DW plane. This is easily conceivable because the IP magnetic component of the wall should be in the same direction as the magnetic field that was applied during the formation of the stripes, which means in the IP AC demagnetization process we align the IP components of the domain walls rather than the perpendicular domains themselves.

In Figs. 8.2h and 8.2i, we have plotted the resonant frequencies versus  $q$  at  $H=0$ , for  $q$  perpendicular ( $\varphi=90^\circ$ ) and parallel ( $\varphi=0^\circ$ ) to the stripe domain axis, respectively. The solid symbols represent the measured values, while the simulated frequencies are shown by the color

map. The typical BLS spectra (Figs. 8.2e and 8.2f) are characterized by the presence of four peaks, however, with different frequency versus wave number dependences for the orthogonal directions of  $q$ , which merge to the same frequencies as  $q$  approaches zero. The increase in the number of peaks as compared to the saturated state signals results from the periodical spin texture. In case of SWs propagation across DWs those magnetization non-uniformities are treated as regular scattering centers, which are provided by the domain boundaries, similar to the geometric magnetic boundaries of a lithographically patterned magnonic crystal. In case of SWs propagating parallel to the DWs those inhomogeneities are treated as different channels defined by different magnetization orientation. In both cases periodicity is crucial to collect strong enough BLS signal from the SW excitations.

For  $\varphi=90^\circ$ , the corresponding SW frequencies exhibit pronounced dispersion with  $q$ , together with characteristic band gaps (Fig. 8.2h). The width of the lower band gap is larger than the frequency gap observed for the saturated state (see Fig. 8.2g). Good agreement between experimental and simulation results is visible for M1 (S1) and M2 (S2), whereas the frequency of S3 in simulations is shifted up with respect to BLS result M3. Simulations show also, that the horizontal dispersion line M4, being related to the mode with two nodal lines across the thickness S4 (see Fig. 8.3b), is hybridized with the other dispersive mode S5. In BLS measurements there is no indication for the hybridization. To explain those discrepancies we note that the lattice constant of the stripe domains in micromagnetic simulations is 100 nm while from MFM images we got around  $A=120$  nm. Therefore, in the sample the Brillouin zone boundary is at smaller wave number than in micromagnetic simulations. It means that M3 band, being two times folded-back M2 band to the 1<sup>st</sup> Brillouin zone, should be shifted down with respect to the frequency obtained in the simulations. Moreover, its next folding at  $q=0$  should hybridize with the horizontal M4 band for very large wave numbers being above measured range. The analysis of the modes (see Fig. 8.3b) supports this explanation. Modes S2 and S3, have the same origin in PSSW with one nodal line, whereas horizontal S4 is the first band from another family of PSSWs with two nodal lines across the thickness.

On the other hand, for  $\varphi=0^\circ$ , the dispersion is repressed and all the modes exhibit similar frequency evolution—see Fig. 8.2i. Very good agreement between BLS (M1, M2) and simulation (S1 and S2) results for the first two bands is found, also the fourth band (M4 with S4) match well, apart from the small wave numbers. The spatial distribution of the modulus of the dynamic

magnetization, as will be discussed in the next paragraph, illustrates that the modes primarily reside in the DWs and at the top and bottom surfaces of the structure. This implies that in absence of external magnetic fields, the IP magnetostatic field trapped in the direction of the DW axis actually acts as the driving field for the SW propagation. In that sense, the  $\varphi=90^\circ$  and  $\varphi=0^\circ$  cases can effectively be termed as the DE geometry and the backward volume magnetostatic SW geometry, although they have different physical origin than in homogeneously magnetized films.

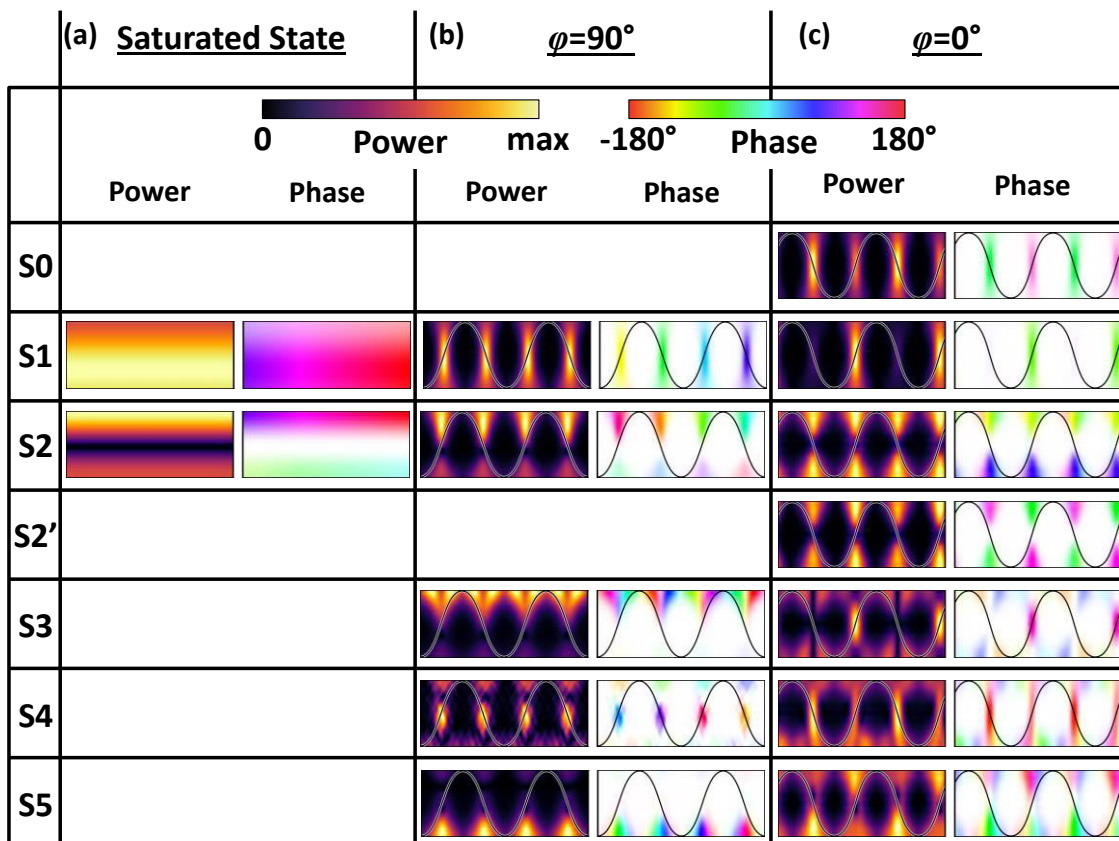


Figure 8.3: The amplitude and phase maps of  $m_z$  for different SW modes (as marked with orange stars in Fig. 8.2) calculated at  $q=2 \times 10^7$  rad/m for the saturated state (a), and domain structure with  $\varphi=90^\circ$  (b) and  $\varphi=0^\circ$  (c). The corresponding color scale is shown at the top of the figure. Dark solid lines in (b) and (c) correspond to the OOP component of the static magnetization at the top surface of the structure.

The nature of the above SW excitations can be better understood by carefully looking at the relevant cross-sectional spin precession profiles, which are depicted in Figs. 8.3b and c, for the two experimental geometries shown in Figs. 8.2b and c, respectively. The solid black lines represent static  $m_z$  component at the top surface of the domain structure indicating the up and down domains for reference. For  $\varphi=90^\circ$  geometry (Fig. 8.3b), the amplitude of the SW modes are

localized mainly in the DWs. This confirms that the SW modes investigated in BLS are primarily related to the IP component of the static magnetization. In particular, the mode profiles are characterized by one or more distinct nodal planes, which are indeed close to those reported earlier for 1D MC, prepared by periodic patterning of magnetic material [62-63]. The mode profiles for  $\varphi=0^\circ$  are similar to  $\varphi=90^\circ$ , except that the amplitude is concentrated in alternate DWs, typical of backward volume modes in MCs [64]. These facts prove the equivalence of our stripe domain structure with the previous MCs.

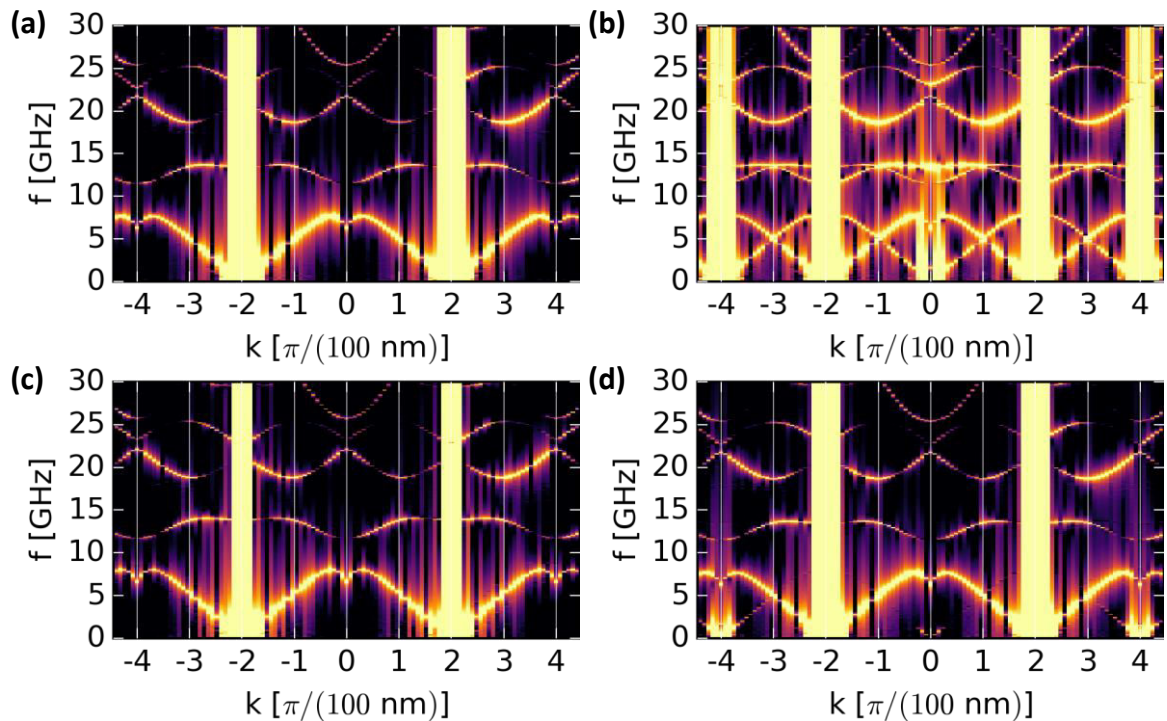


Figure 8.4: Dispersion relation obtained from MSs for the DE configuration in the stripe domain structure without external magnetic field (a), (b) and with external magnetic field of 0.01 T and 0.005 T along the  $x$ -axis (parallel to the domains) and  $z$ -axis (perpendicular to the film plane) in (c) and (d), respectively. In (b) the aggregated dynamics from all three magnetization components is used in the calculation of the dispersion relation, whereas in all other figures only OOP magnetization component was used. In order to visualize as much as possible SWs resonances, the power of the presented signals is shown in logarithmic scale.

In order to investigate the periodicity of the magnonic properties, we have calculated the dispersion relation of the SWs propagating perpendicular to the DWs in a wide range of the wave vector, as is shown in Fig. 8.4a. In these simulations only the  $m_z$  component of the magnetization

vector was taken into account. The dispersion relation has a periodicity of  $2\pi/A$ . This means that for the  $z$  component of the SW amplitude the periodicity is determined by the size of a single domain. However, when the  $x$  component of the magnetization is taken into account (the component parallel to the domain walls) as well (Fig. 8.4b), the additional branches appear in the spectra and the dispersion relation acquires a periodicity of  $\pi/A$ . External magnetic field applied perpendicular to the plane of the film breaks the symmetry between the magnetic domains oriented up and down and the periodicity  $\pi/A$  in the dispersion relation is introduced in the MSs also when only calculated from the  $m_z$  component of the magnetization vector. In Fig. 8.4d this is visible for the 1<sup>st</sup> band – the additional branch of the weak intensity appears in the 2<sup>nd</sup> Brillouin zone. The magnetic field applied along the DWs does not change the dispersion relation (Fig. 8.4c).

We have further found a dispersion line at low frequency (S0 for  $\varphi=0^\circ$ , see Fig. 8.2i) with the linear slope approaching zero-frequency when  $q$  goes to zero and the S1 branch for  $\varphi=90^\circ$  (Fig. 8.2h) decreasing to zero at  $q=2\pi/A$ . The magnetization dynamics related to those modes is mostly related to the OOP component of the magnetization. Moreover, the character of that mode, *i.e.*, how all three components of the magnetization oscillate together, suggests that profile of that mode displays the DW oscillation (See Fig. 8.5). This points at a Goldstone mode connected with the DW oscillations [65].

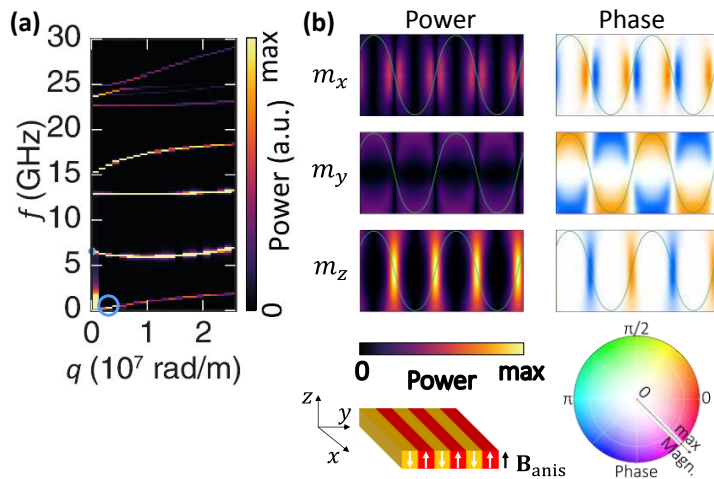


Figure 8.5: (a) Dispersion relation obtained from MSs for the SW propagating along domains (along the  $x$ -axis). (b) The amplitude and phase of SWs from the first band at the wave number close to zero  $q \approx 0$ , marked by blue circle in (a).

Finally, we elucidate the salient magnetic properties of the Co/Pd multilayered system, as it evolves from the uniformly saturated state to the stripe domain configuration. One sees that the dispersion characteristics, magnonic bandgap width and position are controllable by the external applied field and the orientation of the SW wave vector. In particular, the evolution of the SW modes and the mode profiles from the uniformly saturated state to the stripe domain state resemble the transformation of magnonic properties from unpatterned continuous thin films to a periodically patterned 1D MC. Essentially, the periodicity of the IP magnetization (inside the DW) promotes a periodic potential, which subsequently leads to a scattering of the SWs. To confirm this, we have investigated the nature of spin waves in case of labyrinth stripe domain sample. Figure 8.6 presents the recorded BLS spectra for few wave vectors. The following features are observed: i) on the contrary to the case of aligned stripe, here the data is noisier. ii) The mode M1 is split for lower  $q$  values. We find that except for the shoulder mode of M1, no other mode shows any pronounced change with  $q$ . iii) The asymmetry of the BLS intensities in the Stokes and Anti Stokes sides is not significantly affected with changing  $q$ . iv) Modes M3 and M4 are not observed in the spectra. All these characteristics stand for the disorder in the spin orientation on case of labyrinth domain sample and show that the magnonic band structure obtained for aligned stripe domains arises primarily from the periodicity of the spin topography. Overall, once the domain structure is formed, this system does not require any external power for SW propagation and thereby can serve as a building block for the practical realization of energy efficient magnonic devices operating in the microwave frequency range.

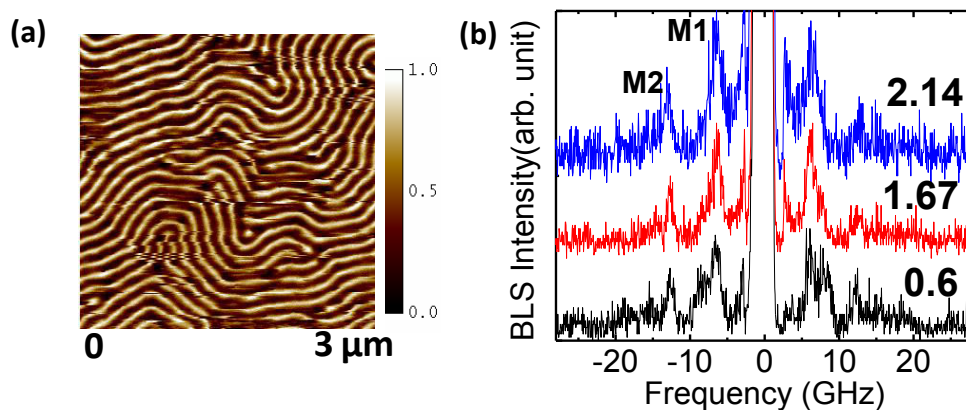


Figure 8.6: (a) MFM image of the labyrinth stripe domain sample. (b) The BLS spectra taken at different values of the in-plane transferred wave vector  $q$  (denoted in units of  $10^7$  rad/m) for labyrinth stripe domain sample. The mode numbers are assigned in accordance with the aligned stripe domain sample.

## 8.5. Conclusions

In conclusion, the quasistatic and dynamic magnetic properties of Co/Pd multilayered films characterized by magnetic stripe domains at remanence have been investigated both experimentally and using micromagnetic simulations. The signature of the stripe domains are clearly observed in the MFM and VSM results. The dynamical magnetic properties were analyzed by studying the wave vector dispersion of the SWs, by means of BLS technique. In the saturated state, two dispersive SW modes are observed, which are identified as the bulk mode and a surface mode of the system. Demagnetizing the film with an AC IP applied field gives rise to an anisotropic remanent state of parallel (rather than a labyrinth) stripe domains aligned along the demagnetization field direction. Micromagnetic simulations reveal the presence of cork-screw type twisted domain walls, with its resultant magnetization directed along the DW axis. The spatial periodicity of this magnetization serves as a periodic potential for SW propagation, in a similar manner as for a laterally confined geometry, *e.g.*, magnonic crystals. As a result, the number of SW modes increases in the BLS spectra and the dispersion depends strongly on the IP angle  $\varphi$  due to the IP anisotropy induced by the parallel alignment of the stripe domains. Analysis of amplitude and phase maps of the resonant modes further illustrates that the dynamics of the system is dominated by the magnetization of periodic DWs, yielding mode profiles close to those of a 1D MC. Due to simple, uniform design, such structures are free from fabrication defects and structural non-uniformities, such as edge roughness. Finally, the observed tunability of the magnonic properties opens a new route towards low energy units for magnonic computing, such as microwave filters, splitters and waveguide structures.

### References

- [1] A. A. Serga, A. V. Chumak, and B. Hillebrands, “YIG magnonics,” *J. Phys. D. Appl. Phys.* **43**, 264002 (2010).
- [2] B. Lenk, H. Ulrichs, F. Garbs, *et al.*, “The building blocks of magnonics,” *Phys. Rep.* **507**, 107 (2011).
- [3] M. Krawczyk and D. Grundler, “Review and prospects of magnonic crystals and devices with reprogrammable band structure,” *J. Phys. Condens. Matter.* **26**, 123202 (2014).
- [4] A. Khitun, D. E. Nikonov, M. Bao, *et al.*, “Feasibility study of logic circuits with a spin wave bus,” *Nanotechnology.* **18**, 465202 (2007).

- [5] Z. K. Wang, V. L. Zhang, H. S. Lim, *et al.*, “Nanostructured magnonic crystals with size-tunable bandgaps,” *ACS Nano*. **4**, 643 (2010).
- [6] G. Gubbiotti, G. Carlotti, T. Okuno, *et al.*, “Brillouin light scattering investigation of dynamic spin modes confined in cylindrical Permalloy dots,” *Phys. Rev. B*. **68**, 184409 (2003).
- [7] S. Neusser, B. Botters, and D. Grundler, “Localization, confinement, and field-controlled propagation of spin waves in Ni<sub>80</sub>Fe<sub>20</sub> antidot lattices,” *Phys. Rev. B*. **78**, 054406 (2008).
- [8] A. V. Chumak, A. A. Serga, B. Hillebrands, *et al.*, “Scattering of backward spin waves in a one-dimensional magnonic crystal,” *Appl. Phys. Lett.* **93**, 022508 (2008).
- [9] L. Bai, M. Kohda, and J. Nitta, “Observation of spin wave modes depending on a tunable periodic magnetic field,” *Appl. Phys. Lett.* **98**, 172508 (2011).
- [10] B. Obry, P. Pirro, T. Bracher, *et al.*, “A micro-structured ion-implanted magnonic crystal,” *Appl. Phys. Lett.* **102**, 202403 (2013).
- [11] K. Vogt, F.Y. Fradin, J.E. Pearson, *et al.*, “Realization of a spin-wave multiplexer,” *Nat. Comm.* **5**, 3727 (2014).
- [12] K. Vogt, H. Schultheiss, S. Jain, *et al.*, “Spin waves turning a corner,” *Appl. Phys. Lett.* **101**, 042410 (2012).
- [13] J. Choi, J. Wu, C. Won, *et al.*, “Magnetic Bubble Domain Phase at the Spin Reorientation Transition of Ultrathin Fe/Ni/Cu(001) Film,” *Phys. Rev. Lett.* **98**, 207205 (2007).
- [14] S. Tacchi, S. Fin, G. Carlotti, *et al.*, “Rotatable magnetic anisotropy in a Fe<sub>0.8</sub>Ga<sub>0.2</sub> thin film with stripe domains: Dynamics versus statics,” *Phys. Rev. B*. **89**, 024411 (2014).
- [15] O. Hellwig, G. P. Denbeaux, J. B. Kortright, *et al.*, “X-ray studies of aligned magnetic stripe domains in perpendicular multilayers,” *Physica B*. **336**, 136 (2003).
- [16] H. Stoll, A. Puzic, B. V. Waeyenberge, *et al.*, “High-resolution imaging of fast magnetization dynamics in magnetic nanostructures,” *Appl. Phys. Lett.* **84**, 3328 (2004).
- [17] F. G. Aliev, A. A. Awad, D. Dieleman, *et al.*, “Localized domain-wall excitations in patterned magnetic dots probed by broadband ferromagnetic resonance,” *Phys. Rev. B* **84**, 144406 (2011).
- [18] K. Perzmaier, M. Buess, C. H. Back, *et al.*, “Spin-Wave Eigenmodes of Permalloy Squares with a Closure Domain Structure,” *Phys. Rev. Lett.* **94**, 057202 (2005).

- [19] C. W. Sandweg, S. J. Hermsdoerfer, H. Schultheiss, *et al.*, “Modification of the thermal spin-wave spectrum in a Ni<sub>81</sub>Fe<sub>19</sub> stripe by a domain wall,” *J. Phys. D: Appl. Phys.* **41**, 164008 (2008).
- [20] X. Xing and Y. Zhou, “Fiber optics for spin waves,” *NPG Asia Mater.* **8**, e246 (2016).
- [21] W. Yu, J. Lan, R. Wu, *et al.*, “Magnetic Snell's law and spin-wave fiber with Dzyaloshinskii-Moriya interaction,” *Phys. Rev. B* **94**, 140410(R) (2016).
- [22] F. G. Sanchez, P. Borys, R. Soucaille, *et al.*, “Narrow Magnonic Waveguides Based on Domain Walls,” *Phys. Rev. Lett.* **114**, 247206 (2015).
- [23] J. Lan, W. Yu, R. Wu, *et al.*, “Spin-Wave Diode,” *Phys. Rev. X* **5**, 041049 (2015).
- [24] K. Wagner, A. Kákay, K. Schultheiss, *et al.*, “Magnetic domain walls as reconfigurable spin-wave nanochannels,” *Nat. Nanotechnol.* **11**, 432 (2016).
- [25] C. Kittel, “Physical Theory of Ferromagnetic Domains,” *Rev. Mod. Phys.* **21**, 541 (1949).
- [26] M. C. Ambrose and R. L. Stamps, “Magnetic stripe domain pinning and reduction of in-plane magnet order due to periodic defects in thin magnetic films,” *J. Magn. Magn. Mater.* **344**, 140 (2013).
- [27] Y. Yafet and E. M. Gyorgy, “Ferromagnetic strip domains in an atomic monolayer,” *Phys. Rev. B.* **38**, 9145 (1988).
- [28] A. Ovadia, I. B. Puchalska, and J. P. Jakubovics, “Stripe domains in obliquely deposited Co-Au films,” *J. Magn. Magn. Mater.* **54**, 851 (1986).
- [29] G. Leaf, H. Kaper, M. Yan, *et al.*, “Dynamic Origin of Stripe Domains,” *Phys. Rev. Lett.* **96**, 017201 (2006).
- [30] O. Hellwig, J. B. Kortright, A. Berger, *et al.*, “Domain structure and magnetization reversal of antiferromagnetically coupled perpendicular anisotropy films,” *J. Magn. Magn. Mater.* **319**, 13 (2007).
- [31] N. Amos, R. Fernandez, R. Ikkawi, *et al.*, “Magnetic force microscopy study of magnetic stripe domains in sputter deposited Permalloy thin films,” *J. Appl. Phys.* **103**, 07E732 (2008).
- [32] J. McCord, B. Erkartal, T. v. Hofe, *et al.*, “Revisiting magnetic stripe domains — anisotropy gradient and stripe asymmetry,” *J. Appl. Phys.* **113**, 073903 (2013).
- [33] F. Tang, D. L. Liu, D. X. Ye, *et al.*, “Magnetic properties of Co nanocolumns fabricated by oblique-angle depositio,” *J. Appl. Phys.* **93**, 4194 (2003).

- [34] M. Hehn, S. Padovani, K. Ounadjela, *et al.*, “Nanoscale magnetic domain structures in epitaxial cobalt films,” *Phys. Rev. B* **54**, 3428 (1996).
- [35] J. Yoon, S.-y. Park, Y. Jo, *et al.*, “Dense stripe domains in a nanocrystalline CoFeSiB thin film,” *Curr. Appl. Phys.* **9**, 688 (2009).
- [36] M. Coisson, F. Vinai, P. Tiberto, *et al.*, “Magnetic properties of FeSiB thin films displaying stripe domains,” *J. Magn. Magn. Mater.* **321**, 806 (2009).
- [37] M. Coisson, C. Appino, F. Celegato, *et al.*, “Magnetization processes in sputtered FeSiB thin films,” *Phys. Rev. B* **77**, 214404 (2008).
- [38] D. Wu, T. Jin, Y. Lou, *et al.*, “Understanding the dense stripe domains in soft magnetic film,” *Appl. Surf. Sci.* **346**, 567 (2015).
- [39] F. Luo, F. Zheng, G. Yin, *et al.*, “Approximate Solution of the Magnetostatic Property of FeCoZr Thin Films with Stripe Domain,” *Appl. Phys. Express.* **6**, 073003 (2013).
- [40] N. Vukadinovic, H. L. Gall, J. B. Youssef, *et al.*, “Magnetization dynamics and relaxation in epitaxial FePd thin films with a stripe domain structure,” *Eur. Phys. J. B.* **13**, 445 (2000).
- [41] J. Wei, Z. Zhu, C. Song, *et al.*, “Annealing influence on the exchange stiffness constant of Permalloy films with stripe domains,” *J. Phys. D: Appl. Phys.* **49**, 265002 (2016).
- [42] U. Ebels, L. Buda, K. Ounadjela, *et al.*, “Ferromagnetic resonance excitation of two-dimensional wall structures in magnetic stripe domains,” *Phys. Rev. B* **63**, 174437 (2001).
- [43] S. S. Ha, J. Yoon, S. Lee, *et al.*, “Spin wave quantization in continuous film with stripe domains,” *J. Appl. Phys.* **105**, 07D544 (2009).
- [44] O. Hellwig, A. Berger, T. Thomson, *et al.*, “Separating dipolar broadening from the intrinsic switching field distribution in perpendicular patterned media,” *Appl. Phys. Lett.* **90**, 162516 (2007).
- [45] R. Sbiaa, H. Meng, and S. Piramanayagam, “Materials with perpendicular magnetic anisotropy for magnetic random access memory,” *Phys. Stat. Solidi RRL* **5**, 413 (2011).
- [46] S. Pal, J. W. Klos, K. Das, *et al.*, “Optically induced spin wave dynamics in [Co/Pd]<sub>8</sub> antidot lattices with perpendicular magnetic anisotropy,” *Appl. Phys. Lett.* **105**, 162408 (2014).
- [47] R. Bruc̃as, H. Hafermann, M. I. Katsnelson, *et al.*, “Magnetization and domain structure of bcc Fe<sub>81</sub>Ni<sub>19</sub>/Co(001) superlattices,” *Phys. Rev. B* **69**, 064411 (2004).

- [48] G. Beutier, G. v. d. Laan, K. Chesnel, *et al.*, “Characterization of FePd bilayers and trilayers using soft x-ray resonant magnetic scattering and micromagnetic modeling,” *Phys. Rev. B.* **71**, 184436 (2005).
- [49] A. Bauer, G. Meyer, T. Crecelius, *et al.*, “Magnetic stripe domains in ultrathin films and their transformation in magnetic fields,” *J. Magn. Magn. Mater.* **282**, 252 (2004).
- [50] Y. Z. Wu, C. Won, A. Scholl, *et al.*, “Magnetic Stripe Domains in Coupled Magnetic Sandwiches,” *Phys. Rev. Lett.* **93**, 117205 (2004).
- [51] O. Donzelli, D. Palmeri, L. Musa, *et al.*, “Perpendicular magnetic anisotropy and stripe domains in ultrathin Co/Au sputtered multilayers,” *J. Appl. Phys.* **93**, 9908 (2003).
- [52] O. Hellwig, T. Hauet, T. Thomson, *et al.*, “Coercivity tuning in Co/Pd multilayer based bit patterned media,” *Appl. Phys. Lett.* **95**, 232505 (2009).
- [53] J. R. Sandercock, "Light Scattering in Solids III, eds M. Cardona and G. Guntherodt (pp. 173-)," Springer, Berlin, (1982).
- [54] A. Vansteenkiste, J. Leliaert, M. Dvornik, *et al.*, “The design and verification of MuMax3,” *AIP Advances.* **4**, 107133 (2014).
- [55] V. Kambersk, P. d. Haan, J. Simsova, *et al.*, “Domain wall theory and exchange stiffness in Co/Pd multilayers,” *J. Magn. Magn. Mater.* **158**, 301 (1996).
- [56] D. M. Schaadt, R. Engel-Herbert, and T. Hesjedal, “Effects of anisotropic exchange on the micromagnetic domain structures,” *Phys. Stat. Sol. B.* **244**, 1271 (2007).
- [57] P. Manchanda, R. Skomski, P. K. Sahota, *et al.*, “Multiscale micromagnetism of Co-Pd multilayers,” *J. Appl. Phys.* **111**, 07C724 (2012).
- [58] J. Rychly, P. Gruszecki, M. Mruczkiewicz, *et al.*, “Magnonic crystals — prospective structures for shaping spin waves in nanoscale,” *Low Temp. Phys.* **41**, 959 (2015).
- [59] M. T. Johnson, P. J. H. Bloemen, F. J. A. d. Broeder, *et al.*, “Magnetic anisotropy in metallic multilayers,” *Rep. Prog. Phys.* **59**, 1409 (1996).
- [60] B. A. Kalinikos, M. P. Kostylev, N. V. Kozhus, *et al.*, “The dipole-exchange spin wave spectrum for anisotropic ferromagnetic films with mixed exchange boundary conditions,” *J. Phys.: Condens. Matter.* **2**, 9861 (1990).
- [61] R. Hertel and J. Kirschner, “Magnetization reversal dynamics in nickel nanowires,” *Physica B.* **343**, 206 (2004).

- [62] S. Saha, R. Mandal, S. Barman, *et al.*, “Tunable Magnonic Spectra in Two-Dimensional Magnonic Crystals with Variable Lattice Symmetry,” *Adv. Funct. Mater.* **23**, 2378 (2013).
- [63] F. J. Buijnsters, A. Fasolino, and M. I. Katsnelson, “Zero modes in magnetic systems: General theory and an efficient computational scheme,” *Phys. Rev. B.* **89**, 174433 (2014).
- [64] M. L. Sokolovskyy and M. Krawczyk, “The magnetostatic modes in planar one-dimensional magnonic crystals with nanoscale sizes,” *J. Nanopart. Res.* **13**, 6085 (2011).
- [65] K.-S. Lee, D.-S. Han, and S.-K. Kim, “Physical Origin and Generic Control of Magnonic Band Gaps of Dipole-Exchange Spin Waves in Width-Modulated Nanostrip Waveguides,” *Phys. Rev. Lett.* **102**, 127202 (2009).

## Chapter 9

# 9. Width dependent transition of quantized spin wave modes in Ni<sub>80</sub>Fe<sub>20</sub> square nanorings

---

### 9.1. Introduction

Nanomagnets feature prominently in a number of applications, including magnetic storage, logic, and memory devices [1–3]. Magnetic recording is a field of increasing interest and technological development driven by the quest of ever increasing storage density and improved design of readwrite heads [3]. One of the most promising approaches to new storage architecture is the use of patterned recording media where the recording layer is fabricated as an ordered array of magnetic dots, each one storing a single bit of information [4]. An important feature of a memory device is that the hard layer should have two remanent states and the switching process must be simple and reliable. For submicron magnetic elements, only in very few cases with well-defined anisotropies does the reversal take place via a coherent rotation of the magnetization. Recent studies show that magnetic ring structures have two kinds of magnetic states: a flux closure or vortex state, and an onion state in which each half of a ring has the same moment orientation, forming head-to-head and tail-to-tail domain walls where the opposite fluxes meet. Thus, either of the two orientations of the onion state or the two different chiralities of the vortex state can be used as two memory states in the storage layer [5]. In addition, the magnetization dynamics of rings magnetized in the onion state shows a large richness in its spin wave modes, which shows its potential for future logic, memory and data storage devices. Eigenmodes in magnetic confined structures form standing spin wave patterns if the coherence length of the spin wave is larger than the dimensions of the confining structure. Here, quantization of spin waves takes place not only due to the confinement in radial and azimuthal directions in the so-called equatorial regions (where the spins are parallel to the ring edge in onion state) but also in spin wave wells in the so-called pole regions (where the spins are perpendicular to the ring edge) created by the demagnetizing

field at the finite edges of the ring [6–11]. However, a major problem associated with a symmetrical ring is the difficulty in pinning the magnetic domain walls in certain places without which, both magnetic “poles” of the onion state will rotate simultaneously and the reversed onion state is reached without the intermediate vortex state. In order to achieve the stability, square [12–16], rectangular [17–18], triangular [19] and elliptical rings [9, 20–23] and off-centered asymmetrical circular magnetic rings [24] have been proposed as an alternative to circular magnetic rings.

So far, extensive research has been carried out on the static properties of micron and nanosize circular, square, and asymmetric circular ring magnets, mainly using the magneto-optical Kerr effect (MOKE) [15, 17, 20], magnetic force microscopy (MFM) [25], local Hall effect techniques [26], and diffracted MOKE [13, 16]. Magnetization dynamics has also been studied using micro-focused Brillouin light scattering [6–9, 18, 21], ferromagnetic resonance [10–11] and time-resolved MOKE (TR-MOKE) [11] in circular [6–8], elliptical [9, 21], rectangular [18] and triangular rings [19]. While the static magnetic properties of arrays of square rings have been reported in literature, studies of their magnetization dynamics have not been reported so far. The spin dynamics in square magnetic ring is of special interest because the domain wall pinning may lead to a significant change in the spin wave modes with the change in ring width and quantized spin wave modes may be observed.

This chapter focuses on all-optical excitation and detection of magnetization dynamics in square shaped  $\text{Ni}_{80}\text{Fe}_{20}$  (Py) nanorings using a TR-MOKE microscope. The fast Fourier transform (FFT) spectra showed a number of eigen modes, which are strongly dependent on the ring width. We explain these multiple modes to be originated from width dependent inhomogeneity in the internal field and quantization effect with the help of micromagnetic simulations.

## 9.2. Experimental Details

Arrays covering  $20 \times 20 \mu\text{m}^2$  area, each with 20 nm thick Py square rings arranged on a square lattice were fabricated on self-oxidized Si (100) substrates using a combination of electron beam lithography and electron beam evaporation. The nominal inner diameters of the rings were fixed at 300 nm while the ring width  $w$  was varied as 300 nm, 200 nm, and 100 nm in this experiment. The edge-to-edge separation was fixed at 200 nm. The surface topography of the samples is

measured by scanning electron microscope, while the static magnetic configurations of the samples are measured by MFM. The ultrafast magnetization dynamics of the samples are measured by using a custom built TR-MOKE microscope based upon a two-color collinear pump-probe setup [27]. The bias field was tilted at a  $15^\circ$  angle from the plane of the sample ( $H$ =component of the bias field along the horizontal edge) to have a finite demagnetizing field along the direction of the pump pulse ( $\lambda=400$  nm, pulse width~100 fs), which is eventually modified by the pump pulse to induce precessional magnetization dynamics within the samples. The Kerr rotation angle of the probe beam ( $\lambda=800$  nm, pulse width~80 fs) is measured as a function of the time-delay between the pump and probe beams. The spot size of focused pump and probe beams are around  $1\ \mu\text{m}$  and  $800$  nm, respectively. Hence, in these measurements, one ring was probed while being placed within the array.

### 9.3. Results and Discussions

Figure 9.1a represents a typical time-resolved Kerr rotation for the ring with  $w=300$  nm when  $H=550$  Oe is applied parallel to the horizontal edge of the ring array. The corresponding static magnetic configuration shows an onion state superposed on a flower state, reminiscent of a square shaped confined magnetic element as shown later in this article. The data shows an ultrafast demagnetization within 500 fs and a bi-exponential decay with decay constants of 1.4 ps and 34.7 ps, respectively; corresponding to spin lattice interaction and transfer of energy to the substrate and the surroundings [28]. The precessional dynamics appears as an oscillatory signal on top of the slowly decaying time-resolved Kerr rotation. The background subtracted Kerr rotation data is shown in Fig. 9.1b. The FFT is performed after subtracting the bi-exponential background to find out the corresponding power spectrum. Figure 9.1c shows the scanning electron micrographs of all the samples. The samples show some deviation in the shape and size (up to  $\pm 10\%$ ) as compared to the nominal dimensions. The deviation in size and shape as obtained from the micrographs will be included in the micromagnetic simulations, although the detailed edge roughness and deformations cannot be precisely included in the finite difference method based micromagnetic simulations.

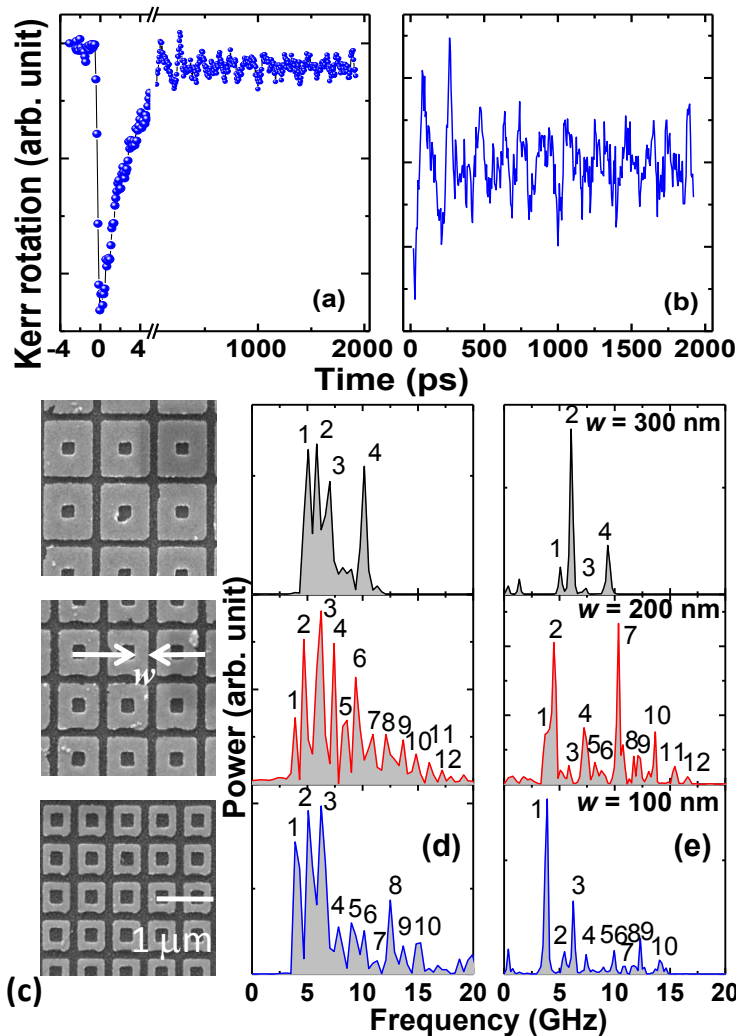


Figure 9.1: (a) Typical time-resolved Kerr rotation data revealing ultrafast demagnetization, fast and slow relaxations, and precession of magnetization for Py square ring array with ring width  $w=300$  nm at  $H=550$  Oe. (b) Background subtracted time-resolved Kerr rotation. (c) Scanning electron micrographs of the ring arrays of different ring width. (d) Experimental and (e) simulated FFT spectra.

Figure 9.1d shows the spin wave spectra for Py square rings with different width at  $H=550$  Oe. A clear variation in the spin wave spectrum is observed with varying ring width. For  $w=300$  nm, four clear modes are observed while for  $w=200$  nm, a drastic change occurs in the spectrum with twelve clear modes appearing between 3 and 17 GHz. Such a large number of modes were not reported previously for ferromagnetic nanoring [7–9, 11]. However, for  $w=100$  nm, the number of modes reduces to ten and the modes lie in between 3 and 15 GHz. Quantization of spin waves has been reported earlier for circular, oval, rectangular, and triangular rings in radial and azimuthal

directions [8] as well as in polar and equatorial regions. The quantization condition was found to vary as a function of ring dimension [8, 10], applied magnetic field [6, 21], and relative orientation of the magnetic field [18-19] with respect to the ring array. In our case, variation in the ring width controls the static magnetic configuration within the ring structure, which leads to different quantization conditions as explained later in this article.

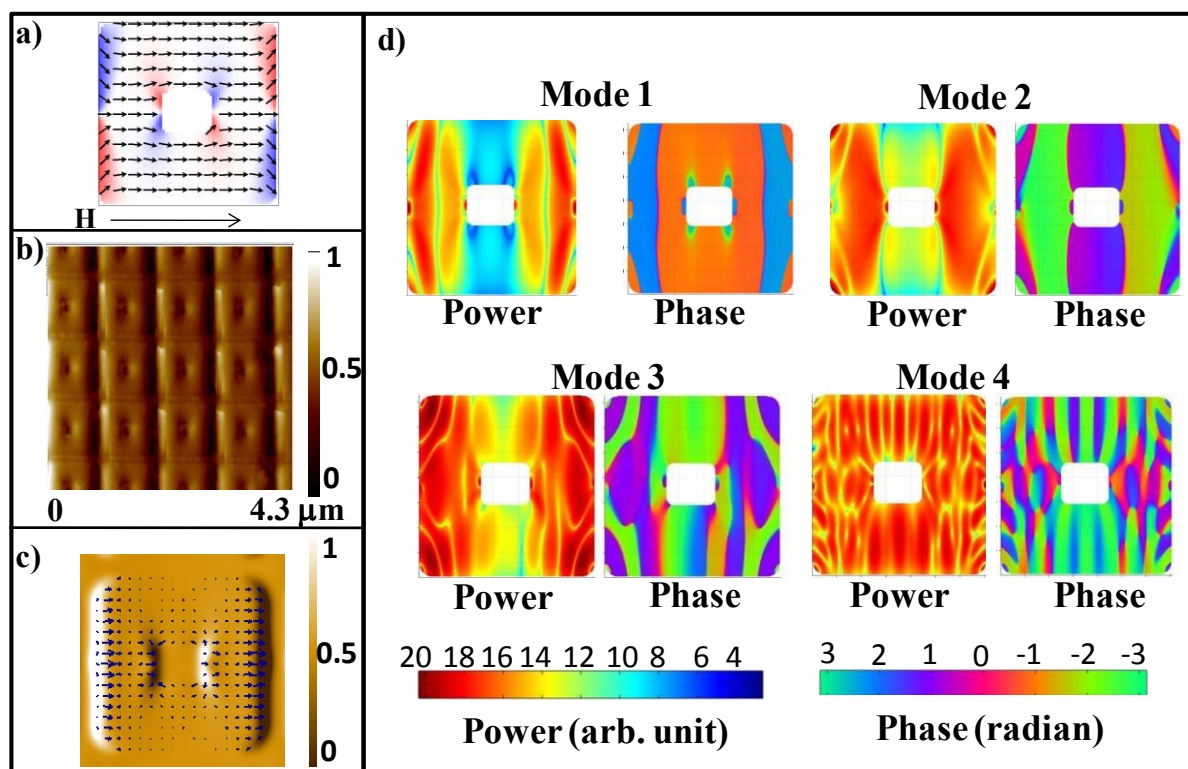


Figure 9.2: (a) Static magnetic configuration of a single ring with  $w=300$  nm at  $H=550$  Oe. The component of magnetization perpendicular to the bias magnetic field is represented by a blue-white-red colormap. (b) MFM image of this nanoring array in presence of  $H=550$  Oe. (c) Simulated MFM image. (d) Simulated power and phase maps of the observed resonant modes. The color maps for the power and phase distributions are shown at the bottom of (d).

To understand the dynamics, we performed micromagnetic simulations on single ring element using the OOMMF software [29]. Further test simulations on arrays of  $3 \times 3$  rings showed similar spin wave spectra with only a small change in the relative intensities as well as negligible inter-ring stray magnetic fields, which allowed us to use a single element simulation. Calculations were done by dividing the nanorings into arrays of cuboidal cells of dimension  $2 \times 2 \times 20$  nm<sup>3</sup> and material parameters for Py were used as gyromagnetic ratio  $\gamma=18.5$  MHz/Oe, anisotropy field  $H_k=0$ ,

saturation magnetization  $M_S=860$  emu/cc, and exchange stiffness constant  $A = 1.3 \times 10^{-6}$  erg/cm. The optical excitation in the experimental sample is simulated as an out-of-plane effective pulsed magnetic field [30]. Figure 9.1e shows the simulated spin wave spectra for all three samples. The simulations qualitatively reproduce the experimentally observed features, although the exact values of the frequencies and relative intensities are not reproduced. In order to visualize the spatial characters of different modes, we have calculated the power and phase maps of the modes by using a home-built code [31]. Figure 9.2a shows the simulated static magnetic configuration in the ground state for the sample with  $w=300$  nm. Here,  $H=550$  Oe is applied parallel to the horizontal edge of the ring. The static magnetic state shows an onion state superposed on a flower state for the given applied field with significant amount of demagnetized regions near the external and internal vertical boundaries of the ring as shown by a blue-white-red colormap. These demagnetized regions, in combination with the magnetization state, will determine the spin wave mode profiles. The MFM image and the corresponding micromagnetic simulation results are presented in Figs. 9.2b and c, which also confirms the simulation result. The power and phase maps show that all the modes are quantized modes where quantization is in the direction parallel to the bias magnetic field (backward volume (BV) modes). The two lower frequency modes are confined near the pole regions (the vertical arms in this case) where the ring edges are perpendicular to the applied field. The demagnetizing fields due to the edges reduce the effective magnetic field and the corresponding mode frequencies. The spatial profiles of mode 3 and mode 4 show that they have similar characters as mode 1 and mode 2 with higher quantization number. However, these modes reside not only in the pole region, but also in the equatorial region where the ring arms are parallel to the direction of the applied field and where the internal field (which is defined as the sum of the Zeeman and demagnetizing fields) is approximately uniform and equal to the value of the external field  $H$ .

In case of circular ring in an onion state, there are essentially two families of modes; (i) “bulk” modes mainly localized in the equatorial regions and (ii) modes localized close to the pole regions of the ring where the internal magnetic field is inhomogeneous [6-7, 10, 11]. Each of these sectors can accommodate different kinds of excitations including quantized and localized modes. The spin dynamics of triangular ring is also similar. However, our observed mode profiles for  $w=300$  nm do not follow a similar trend. Instead, the mode profiles resemble the extended and quantized modes of antidot lattices with similar dimensions [30] apart from the modes with high

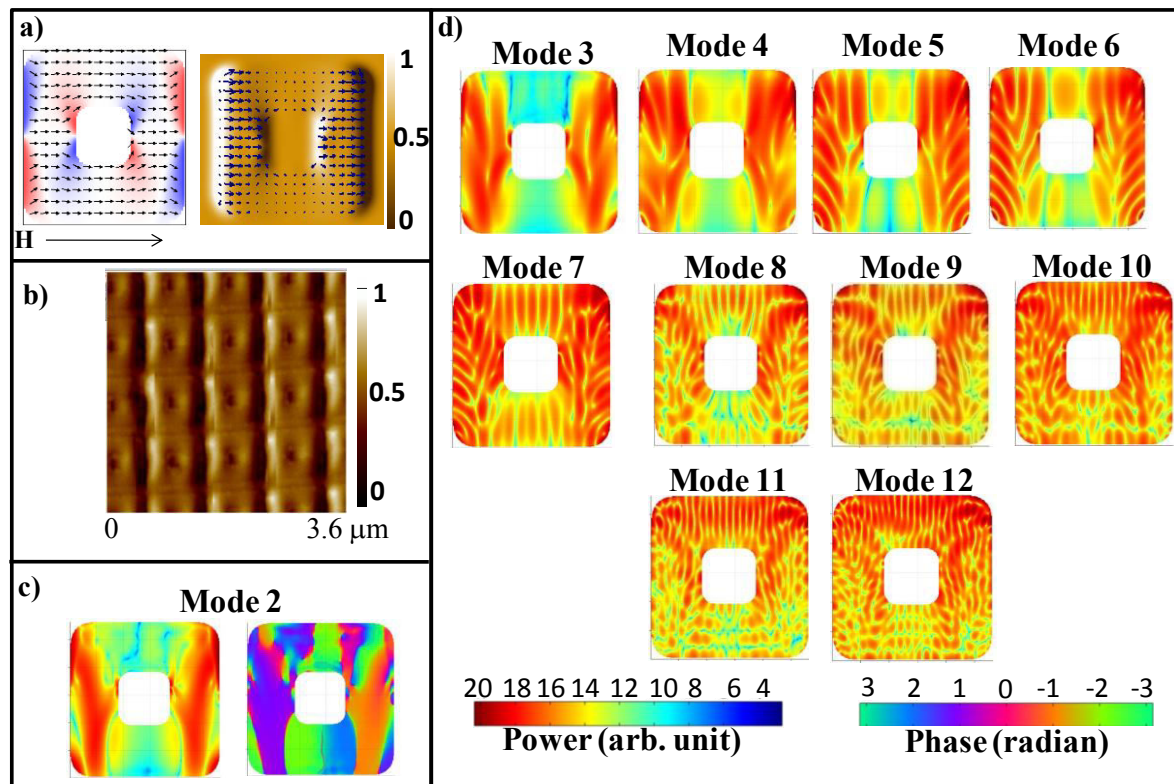


Figure 9.3: (a) The simulated static magnetic configuration (left panel) and simulated MFM image (right panel) of a single nanoring with  $w=200$  nm at  $H=550$  Oe. (b) Experimental MFM image. (c) Power and phase maps for mode 2. (d) Simulated power maps corresponding to the resonant peaks from mode 3 to mode 12. The colormap for power and phase distributions are shown at the bottom of (d).

quantization number. In case of a nanoring, the finite external boundaries are probably responsible for the increase in quantization number.

The profiles of some selected modes for the nanoring with  $w=200$  nm are shown in Fig. 9.3. Here, the static magnetic configuration (Fig. 9.3a) is similar to that for  $w=300$  nm. However, the onion state is dominant over the flower state. The frequency spectrum also demonstrates different kinds of modes, which were not present in the nanoring with  $w=300$  nm. Here, we found that the lower frequency excitations (mode 1 to mode 3) are clearly localized in the pole regions (two vertical arms of the ring), where the internal field is minimum. In addition, the relative phases of the modes are opposite at the two pole regions. Figure 9.3c presents the power and phase maps for mode 2. The power maps for the other modes are presented in Fig. 9.3d. Mode 4 also resides near the pole region, but it is a quantized mode, exhibiting nodal planes perpendicular to the

magnetic field direction (BV mode). The other modes (mode 5 to mode 12) have similar character as mode 4 with gradually increasing quantization number. However, these modes also have an azimuthal character (mixed modes), exhibiting nodal planes perpendicular to the local direction of the static magnetization. The quantized azimuthal modes lie near the outer edges of the square ring, whereas the BV modes reside away from the outer edges. We label these modes as  $(m, n)$ -mixed, where  $m$  specifies the number of azimuthal nodal planes and  $n$  is the number of nodal planes along the external field direction. Another feature of these modes is that their quantization number (both  $m$  and  $n$ ) goes very high ((53, 25)-mixed for mode12). Azimuthal modes are already exhibited by circular and elliptical rings, but with much lower quantization number [8, 10-11].

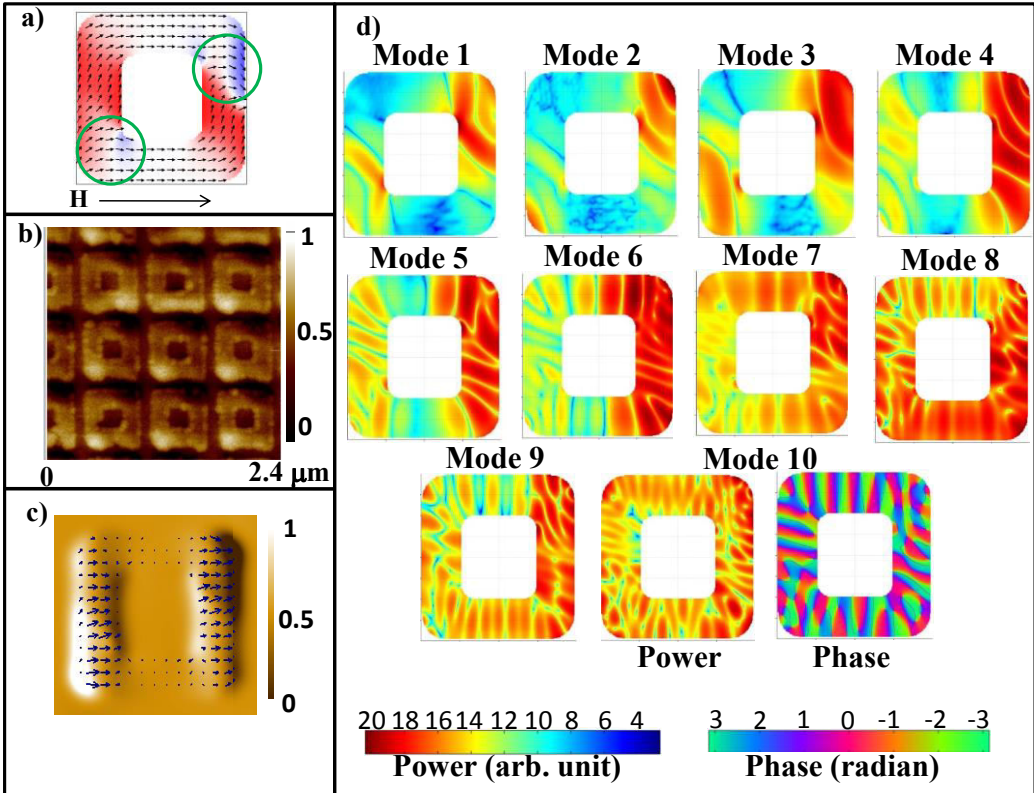


Figure 9.4: (a) Static magnetic configuration of the ring with  $w=100$  nm at  $H=550$  Oe. The circles denote the pole regions. (b) Experimental and (c) simulated MFM image of the ring array, respectively. (d) Simulated power maps corresponding to the resonant peaks in the FFT spectra. The simulated phase profile of mode10 is also shown in lower panel. The colormap for power and phase distributions are shown at the bottom of (d).

Figure 9.4 shows the mode profiles for the nanoring with  $w=100$  nm. In contrast to the other two nanorings, here the magnetization exhibits pronounced onion state. Moreover, the poles are also

shifted towards the corners as indicated by the green circles in Fig. 9.4a. This distinctive feature is also present in both experimental and simulated MFM results (Figs. 9.4b and c, respectively). Here, the spins at the outer and inner edges of the two vertical arms are parallel to each other barring the pole regions, where they are either converging or diverging. This can be attributed to the competition between the demagnetizing field and the shape anisotropy field (caused by the reduced width) due to which the spins tend to align along the respective arms. The power maps for different modes and phase map of mode 10 are presented in Fig. 9.4d. It shows that the lower frequency modes (mode 1-mode 3) reside at the pole region (near the diagonal) and they are also quantized along the diagonal. The higher frequency modes (mode 4 to mode 10) are quantized azimuthal modes. Here, the modes with relatively lower azimuthal nodes are observed in two vertical arms of the ring. As the quantization number increases, the spatial profiles of the modes advance to the horizontal arms of the ring. Here, also the quantization number goes up to very high value (near 42) starting from 12.

To understand the role of inter-ring magnetostatic coupling on the spin dynamics, we have further calculated the magnetostatic field distributions of the simulated magnetostatic field for each ring array. Here a  $3 \times 3$  array of each ring element is simulated by using LLG Micromagnetic simulator [32]. We first simulated the static magnetic configurations of all the samples. After that, the static field distributions are calculated under virtual dynamic environment. The cell discretization and the material parameters were kept same as that of oommf simulations. The results are presented in Fig. 9.5a. It is clear that the ring elements have negligible interaction which also agrees well with our assumption that the dynamics of the square ring arrays is mainly due to that of single ring. Line-scans of the simulated magnetostatic fields at the positions of the lattices as indicated by horizontal dashed lines in Fig. 9.5a are also calculated and presented in the lower panel (Fig. 9.5b). Here the overall internal fields inside the rings is shown to decrease from 9.8 kOe to around 5.5 kOe as the ring width decreases from 300 nm to 100 nm. The above variation of the internal fields of the ring elements in various rings is responsible for the variation in the frequency spectra.

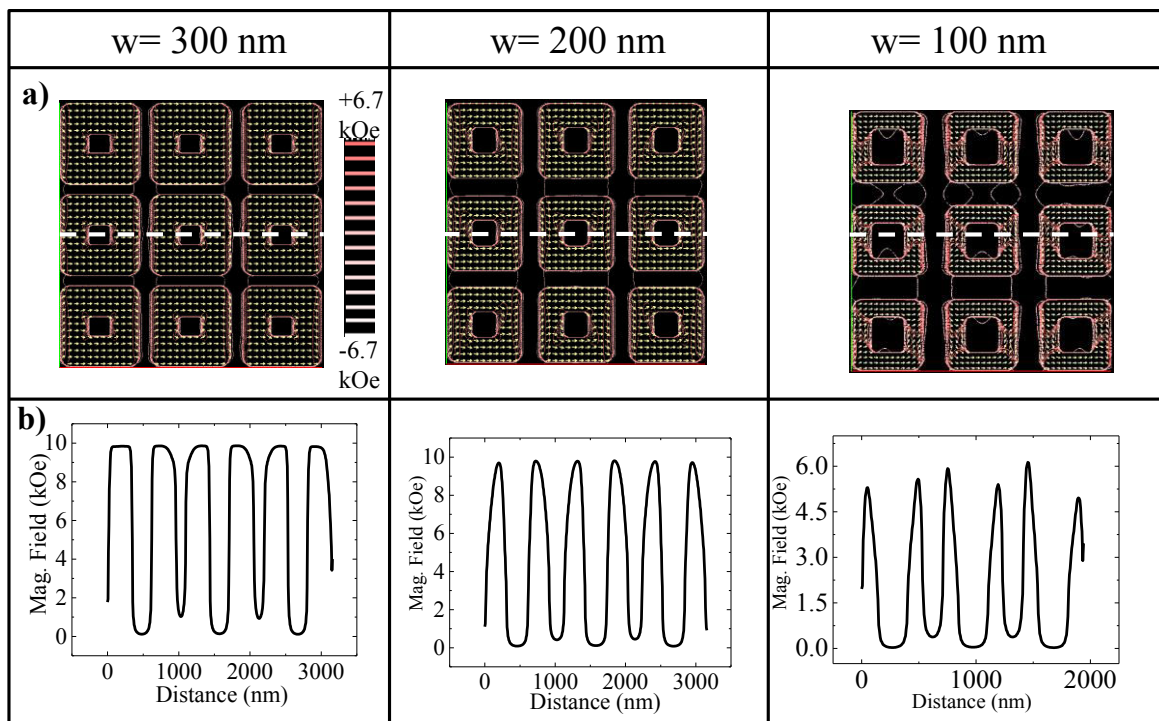


Figure 9.5: (a) Contour maps of the simulated magnetostatic stray field distribution and (b) line scans of simulated magnetostatic fields from various ring arrays as obtained from the positions indicated by horizontal dashed lines in (a).

## 9.4. Conclusions

In conclusion, we have studied the internal-field driven ultrafast magnetization dynamics of Py square nanorings with varying ring width. Rich spectra of quantized spin waves are observed for these samples, which depend strongly on the width of the ring. The micromagnetic simulations qualitatively reproduced all the modes present in the frequency spectra. The simulated power and phase maps show that the ring with the largest width (300 nm) exhibits quantization along the direction of the external magnetic field, whereas the ring with smallest width (100 nm) shows azimuthal quantization. The ring with 200 nm width contains mixed modes with quantization along both the external field and the azimuthal direction. The transition between different types of

quantized modes within the nanoring by varying ring width is attributed to the inhomogeneity of the internal field, which shows a transition from an "onion state superimposed on a flower state" to "pronounced onion state" as the ring width decreases. The simulated magnetostatic fields within the nanoring arrays show that the elements are mostly non-interacting. The tunability of different types of quantized spin wave modes with ring width will be useful for the future applications of ferromagnetic nanorings in high speed storage and memory devices and for microwave applications.

## References

- [1] O. Hellwig, A. Berger, T. Thomson, *et al.*, "Separating dipolar broadening from the intrinsic switching field distribution in perpendicular patterned media," *Appl. Phys. Lett.* **90**, 162516 (2007).
- [2] A. Imre, G. Csaba, L. Ji, *et al.*, "Majority Logic Gate for Magnetic Quantum-Dot Cellular Automata," *Science* **311**, 205 (2006).
- [3] S. Tehrani, E. Chen, M. Durlam, *et al.*, "High density submicron magnetoresistive random access memory (invited)," *J. Appl. Phys.* **85**, 5822 (1999).
- [4] T. Thomson, G. Hu, and B. D. Terris, "Intrinsic Distribution of Magnetic Anisotropy in Thin Films Probed by Patterned Nanostructures," *Phys. Rev. Lett.* **96**, 257204 (2006).
- [5] V. Metlushko, U. Welp, V. Vlasko-Vlasov, *et al.*, "Arrays of nano-rings for magnetic storage applications," in *Proceedings of the 2nd IEEE Conference on Nanotechnology, IEEE-NANO (2002)*, p. 63.
- [6] F. Montoncello, L. Giovannini, F. Nizzoli, *et al.*, "Magnetization reversal and soft modes in nanorings: Transitions between onion and vortex states studied by Brillouin light scattering," *Phys. Rev. B* **78**, 104421 (2008).
- [7] H. Schultheiss, C. W. Sandweg, B. Obry, *et al.*, "Dissipation characteristics of quantized spin waves in nano-scaled magnetic ring structures," *J. Phys. D: Appl. Phys.* **41**, 164017 (2008).
- [8] H. Schultheiss, S. Schafer, P. Candeloro, *et al.*, "Observation of Coherence and Partial Decoherence of Quantized Spin Waves in Nanoscaled Magnetic Ring Structures," *Phys. Rev. Lett.* **100**, 047204 (2008).

- [9] C. G. Tan, H. S. Lim, Z. K. Wang, *et al.*, “Quantization of spin waves in oval-shaped nanorings,” *J. Magn. Magn. Mater.* **320**, 475 (2008).
- [10] F. Giesen, J. Podbielski, and D. Grundler, “Mode localization transition in ferromagnetic microscopic rings,” *Phys. Rev. B* **76**, 014431 (2007).
- [11] I. Neudecker, M. Klaui, K. Perzlmaier, *et al.*, “Spatially Resolved Dynamic Eigenmode Spectrum of Co Rings,” *Phys. Rev. Lett.* **96**, 057207 (2006).
- [12] A. Libal, M. Grimsditch, V. Metlushko, *et al.*, “Control of magnetic vortex chirality in square ring micromagnets,” *J. Appl. Phys.* **98**, 083904 (2005).
- [13] P. Vavassori, M. Grimsditch, V. Novosad, *et al.*, “Magnetization switching in Permalloy square ring magnets,” *J. Appl. Phys.* **93**, 7900 (2003).
- [14] D. R. Lee, J. W. Freeland, G. Srajer, *et al.*, “Domain-specific magnetization reversals on a Permalloy square ring array,” *J. Appl. Phys.* **95**, 7016 (2004).
- [15] A. V. Goncharov, A. A. Zhukov, V. V. Metlushko, *et al.*, “In-plane anisotropy of coercive field in permalloy square ring arrays,” *J. Appl. Phys.* **99**, 08Q508 (2006).
- [16] P. Vavassori, M. Grimsditch, V. Novosad, *et al.*, “Metastable states during magnetization reversal in square permalloy rings,” *Phys. Rev. B* **67**, 134429 (2003).
- [17] Y. Ren and A. O. Adeyeye, “Magnetic spin states and vortex stability control in elongated Ni<sub>80</sub>Fe<sub>20</sub> nanorings,” *J. Appl. Phys.* **105**, 063901 (2009).
- [18] F. S. Ma, V. L. Zhang, Z. K. Wang, *et al.*, “Magnetic-field-orientation dependent magnetization reversal and spin waves in elongated permalloy nanorings,” *J. Appl. Phys.* **108**, 053909 (2010).
- [19] J. Ding, M. Kostylev, and A. O. Adeyeye, “Broadband ferromagnetic resonance spectroscopy of permalloy triangular nanorings,” *Appl. Phys. Lett.* **100**, 062401 (2012).
- [20] L. J. Chang, C. Yu, T. W. Chiang, *et al.*, “Magnetic interaction in nanometer line width elliptical ring arrays,” *J. Appl. Phys.* **103**, 07C514 (2008).
- [21] M. Madami, F. Montoncello, G. Capuzzo, *et al.*, “Experimental Evidence of Field-Induced Localization of Spin Excitations in NiFe Elliptical Rings by Micro-Focused Brillouin Light Scattering,” *IEEE Trans. Magn.* **46**, 1531 (2010).
- [22] M. Madami, S. Tacchi, G. Gubbiotti, *et al.*, “Spin Modes in Elliptical Nanorings in the Vortex State: Two-Dimensional Mapping by Micro-Focused Brillouin Light Scattering,” *IEEE Trans. Magn.* **46**, 199 (2010).

- [23] M. Hara, J. Shibata, T. Kimura, *et al.*, "Rotational dynamics of paired nano-domain walls confined in an elliptical ring," *J. Magn. Magn. Mater.* **310**, 2451 (2007).
- [24] T. M. Nguyen and M. G. Cottam, "Spin-wave excitations in arrays of asymmetric ferromagnetic nanorings," *J. Appl. Phys.* **103**, 07C503 (2008).
- [25] J. Wang, A. O. Adeyeye, and N. Singh, "Magnetostatic interactions in mesoscopic Ni<sub>80</sub>Fe<sub>20</sub> ring arrays," *Appl. Phys. Lett.* **87**, 262508 (2005).
- [26] M. Steiner and J. Nitta, "Control of magnetization states in microstructured permalloy rings," *Appl. Phys. Lett.* **84**, 939 (2004).
- [27] A. Barman and A. Haldar, "Solid State Physics Vol. 65, eds E. Camley Robert & L. Stamps Robert (pp.1-108)," Academic Press, (2014).
- [28] A. Laraoui, J. Venuat, V. Halte, *et al.*, "Study of individual ferromagnetic disks with femtosecond optical pulses," *J. Appl. Phys.* **101**, 09C105 (2007).
- [29] M. Donahue and D. G. Porter, "OOMMF User's guide, Version 1.0," NIST Interagency Report No. 6376, National Institute of Standard and Technology, Gaithersburg, MD, URL: <http://math.nist.gov/oommf/> (1999).
- [30] R. Mandal, S. Saha, D. Kumar, *et al.*, "Optically Induced Tunable Magnetization Dynamics in Nanoscale Co Antidot Lattices," *ACS Nano* **6**, 3397 (2012).
- [31] D. Kumar, O. Dmytriiev, S. Ponraj, *et al.*, "Numerical calculation of spin wave dispersions in magnetic nanostructures," *J. Phys. D: Appl. Phys.* **45**, 015001 (2012).
- [32] M. R. Scheinfein, LLG Micromagnetics Simulator, available: <http://www.llgmicro.home.mindspring.com/>.

## Chapter 10

# 10. Reconfigurable spin wave propagation in pseudo one-dimensional nanoscale magnonic crystal

---

### 10.1. Introduction

Periodically patterned arrays of magnetic elements in the submicron scale [1-6] are attracting wide interest since last decade, because of both the unique features of magnetism in low-dimensional systems and their potential applications in the design of magnetic storage [7], memory [8], sensors [9] and spin based signal processing and logic devices [10-13]. The Photonic crystals, which are artificial electromagnetic dielectric materials with periodically modulated refractive index, have already found practical applications in optoelectronics. Magnonic crystals (MCs) [11, 14] can be regarded as the magnetic counterpart of photonic crystals with spin waves (SWs) acting as information carriers. In fact, since the wavelength of SWs is several orders of magnitude shorter than that of electromagnetic waves of the same frequency in photonic crystals, MC offers better perspectives towards miniaturization of microwave devices. Based on their design, MCs exhibit a characteristic Bragg scattering, leading to the formation of bandgap regions of the SW spectrum in which SW propagation is prohibited [15-17]. The number and properties of the bandgaps can be tuned by controlling material and structural parameters [18-19] as well as the strength of the bias magnetic field. This allows for the reliable and active manipulation of the propagation properties of SWs and makes MCs potentially useful in microwave resonators, filters and switches operating in the GHz frequency range. Also, the significant reduction of SW group velocity in the vicinity of magnonic bandgaps can be exploited for designing frequency dependent delay lines. To this end, understanding of the interplay between shape and intrinsic anisotropy, as well as the influence of dipolar coupling in these laterally confined magnetic structures is of paramount importance for any desired application.

Hitherto, intensive research has been carried out to investigate the spin wave dynamics in one-[16, 18-21], two-[3-6, 22-25] and three-dimensional [26-27] arrays of magnetic nanostructures of different shapes and compositions, which were studied using various methods ranging from analytical (such as the plane wave method (PWM)) and computational (using micromagnetic simulations) methods to experimental means using Brillouin light scattering (BLS), ferromagnetic resonance (FMR) and time-resolved magneto-optical Kerr effect (TR-MOKE) techniques. These structures can be broadly subdivided into three groups: (i) an array of interacting ferromagnetic dots [3, 5, 22-24], where the dynamical coupling between the dots is due to magnetostatic interaction between the SW modes excited in the single dot. (ii) Array of periodic holes in a ferromagnetic thin film or antidot lattice [6, 28-29]. Here the formation of the magnonic band structure is determined by the periodicity of the demagnetizing field around the holes in the film plane. In some cases the holes can also be filled with another ferromagnetic material (bicomponent MC) [25], where all the effects mentioned above are present and the additional dipolar and exchange interaction between the two materials give additional control parameters over the magnonic bandgap and propagation velocity. (iii) One dimensional periodic waveguides in the form of microstrips, with periodically modulated compositions and structures [15, 18-20, 30]. All of these investigations point towards a wide range of manipulation of magnonic properties and have opened the pathway for tailoring the dispersion of high-frequency SWs in a much wider class of magnonic systems than considered so far.

Here, we introduce a pseudo one-dimensional (1D) magnonic crystal formed by an array of asymmetric sawtooth-shaped waveguides (ASWs) and studied their magnonic band structure by experimental and theoretical methods. The topic of periodic SW waveguides studied so far include microscopic waveguide with periodically bent sections [31], periodic arrays of nanostrips [19], waveguide with variable edges [16-17] or thickness [32], ferromagnetic stripe microstructured using localized ion implantation [33] or a periodic bias magnetic field [34] and one-dimensional comb-like structures [35]. In these cases, the allowed and forbidden SW modes were governed by the periodic variation of dipolar coupling, magnetization or internal magnetic field. In our present study, the MC offers a periodic modulation of both dipolar coupling and internal magnetic field in two perpendicular directions, thereby enhancing the number of magnetic parameters to control the magnonic band structure. Here, we used Brillouin light scattering (BLS) technique to investigate the magnonic band structures and mode properties of the ASW array. We

study how the magnonic bandgaps can be significantly reconfigured by rotating an applied magnetic field by twenty degrees *w.r.t.* the spin wave propagation channel. In a real on-chip magnonic circuit, all the processing units are integrated along with a pre-defined path for data flow. Therefore, to achieve a band tunability by slightly rotating the bias field is more feasible as far as the practical implementation is concerned, as compared to rotating the entire system or changing the physical structuring. The plane wave method (PWM) was employed to reproduce and analyze the mode characteristics. Here the edge corrugation basically engineers the edge potential wells of the stripes, which can be used to control the mode coupling in miniature magnonic waveguides. Our findings show that this system may serve as a possible prototype for tunable SW waveguide and SW signal processor, which are important components for magnonic device.

## 10.2. Experimental Details and Definition of Measurement Geometries

A  $72\mu\text{m} \times 72\mu\text{m}$  array of 30 nm thick (nominal) ASWs made of polycrystalline permalloy ( $\text{Ni}_{80}\text{Fe}_{20}$ ) was fabricated on thermally oxidized silicon substrate by means of e-beam lithography, electron-beam evaporation and lift-off process. For that, Si (001) substrate covered with 100 nm  $\text{SiO}_2$  was spin-coated with bilayer polymethyl methacrylate (PMMA 495K and 950K) positive tone e-beam resist. On these resist coated substrate, using high resolution e-beam lithography, corrugated nano-stripe pattern was defined followed by development in methyl isobutyl ketone (MIBK) and isopropyl alcohol (IPA), MIBK:IPA :: 1:3, solution. Following this, on this substrate, using e-beam evaporation (base pressure =  $3 \times 10^{-8}$  Torr) we deposited 30 nm thick  $\text{Ni}_{80}\text{Fe}_{20}$  at a deposition rate of 0.2 Å/s. A 2 nm thick  $\text{SiO}_2$  was deposited over the  $\text{Ni}_{80}\text{Fe}_{20}$  using rf sputter deposition technique (base pressure  $2 \times 10^{-7}$  Torr, deposition under Ar pressure = 5 mTorr, deposition rate = 0.3 Å/S, rf power = 60 W). Subsequently, the lift off was done in acetone using ultrasonic agitation to obtain the well defined  $\text{Ni}_{80}\text{Fe}_{20}$  ASW array. The scanning electron microscopy (SEM) image of the final structure is shown in Fig. 10.1a. The length of each stripe is 72  $\mu\text{m}$  (average width: 350 nm) and the nominal distance between the central axes of two consecutive stripes ( $a$ ) is 800 nm. Since, the edges of each stripe were patterned in an asymmetric sawtooth-like structure, this gives rise to an additional periodicity along the stripe axes (*i.e.*,  $y$ -

axis), to the otherwise 1D array of simple magnetic stripes with the periodic variation of dipolar stray field along the z-direction.

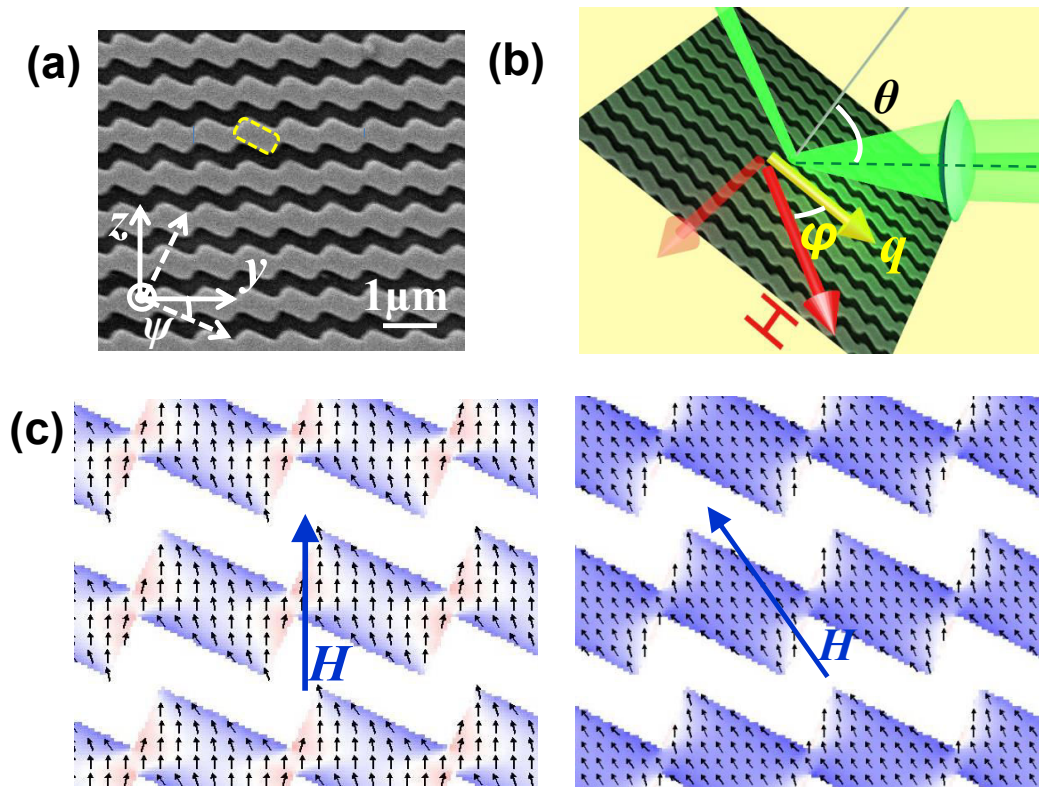


Figure 10.1: (a) Scanning electron microscope (SEM) image of the studied ASW array. The co-ordinate axes are shown by the white arrows. The unit cell considered for PWM calculations is marked by dashed box. (b) Schematic of the BLS measurement geometry used, showing the incident and scattered light beams and the in-plane angle  $\varphi$  between the magnon wave vector  $q$  and applied magnetic field  $H$ , with both vectors lying in the sample plane. (c) Simulated static magnetic configurations (shown in red-white-blue colour map) for  $\varphi = 90^\circ$  and  $\varphi = 70^\circ$  configurations (left and right panel, respectively) for  $H = 850$  Oe. The magnetic field direction is shown by blue arrows.

Note that, due to the asymmetry in the corrugated edges, the edge to edge spacing between two ASWs is constant along the stripe, restricting the periodicity in dipolar stray field along y-direction. In that sense, the chosen system may be termed as pseudo 1D MC, which features two different 1D MCs in two perpendicular directions. The lattice constant ( $a$ ) and Brillouin zone (BZ) edge ( $\pi/a$ ) along y-direction are 800 nm and  $3.9 \times 10^7$  rad/m, respectively.

BLS experiments were performed in the backscattering configuration for measurement of dispersion characteristics of thermal magnons in this structure. This technique relies on inelastic

light scattering process due to interaction between incident photons and magnons. Monochromatic laser light (wavelength  $\lambda = 532$  nm, power = 130 mW) from a solid state laser was focused on the sample surface. The diameter of the laser spot was about  $40 \mu\text{m}$ , hence smaller than the array dimensions. As the laser beam is inelastically scattered from the magnons, due to conservation of momentum, the magnitude of the in-plane transferred wave vector  $q$  depended on the incidence angle of light  $\theta$  according to  $q = (4\pi/\lambda) \sin\theta$ . Cross polarizations between the incident and the scattered beams were adopted in order to minimize the phonon contribution to the scattered light. Subsequently, the frequencies of the scattered light are analyzed using a Sandercock-type six-pass tandem Fabry-Perot interferometer (JRS Scientific Instruments). There, a frequency shift is observed along with the laser frequency taking into account energy and momentum conservation. The measurement geometry is shown in Fig. 10.1b. Throughout the experiment, the direction of the wave vector ( $q$ ) was enforced to be parallel to the stripe, *i.e.*,  $y$ -direction, by making the stripe axes parallel to the light scattering plane (see Fig. 10.1b) and the BLS spectra were recorded for upto two Brillouin Zones (BZs), *i.e.*,  $q \sim 8 \times 10^7$  rad/m. The sample was subjected to an in-plane magnetic field of  $H = 850$  Oe during the measurement, which can be rotated by an angle  $\varphi$  with the ASW axis (*i.e.*, along  $q$ ) using a precision rotary mount. In this work, we adopted two values of  $\varphi$  of  $90^\circ$  (also known as Damon Esbach geometry) and  $70^\circ$ , which correspond to two different magnetic configurations, as will be discussed later.

### 10.3. Theoretical Approach

We calculated the spectrum of magnonic excitations of the ASW array using the plane wave method (PWM). This method is a popular tool because of its conceptual simplicity and its applicability to any type of lattice and any shape of scattering centers. We solve the Landau–Lifshitz (LL) equation, *i.e.*, the equation of motion of the magnetization vector  $\mathbf{M}(\mathbf{r}, t)$ , under the impact of effective magnetic field  $\mathbf{H}_{\text{eff}}$ , which has primarily three contributions: a uniform and constant applied magnetic field  $\mathbf{H}$ , the exchange field  $\mathbf{H}_{\text{ex}}$  and the magnetostatic field  $\mathbf{H}_{\text{ms}}$ . In the linear approximation, the component  $M_S(\mathbf{r})$  of the magnetization vector parallel to the static magnetic field is constant in time, and its magnitude is much greater than that of the perpendicular components  $\mathbf{m}(\mathbf{r}, t)$ , *i.e.*,  $|\mathbf{m}(\mathbf{r}, t)| \ll M_S(\mathbf{r})$ , with  $\mathbf{M}(\mathbf{r}, t) = M_S(\mathbf{r})\hat{z} + \mathbf{m}(\mathbf{r}, t)$ . In a magnetically inhomogeneous medium (like a MC), the spatial inhomogeneity of the material parameters

(exchange constant, spontaneous magnetization) as well as the magnetostatic field must be taken into account. Subsequently, we perform the Fourier transformation to map all the periodic functions (in space and time), including the static and dynamic parts of the magnetic fields and magnetization components, to the reciprocal space using Bloch's theorem [36]. In that way the PWM transforms the LL equation into an infinite set of algebraic equations, which leads to an eigenvalue problem. In order to find the eigenvalues (frequencies of SWs) and eigen vectors (amplitude of the dynamical component of the magnetization vector) the Fourier series have to be limited to finite number of elements. The eigen value problem is then solved with standard numerical routines.

Here, we considered the lattice structure forming of permalloy and air, with two lattice vectors given by,  $\mathbf{a1}=a\mathbf{y}$  and  $\mathbf{a2}=a\mathbf{z}$ . For the calculation, we assumed the magnetic field to be always oriented along the z-axis, *i.e.*, for  $\varphi =90^\circ$  geometry along the vertical line and for  $\varphi =70^\circ$  geometry along the line anticlock-wise-rotated by  $\psi= 20^\circ$ . We thus rotated the in-plane components of the co-ordinate system in clockwise direction consistent with a rotation of the magnetic field (Fig. 1a). Therefore, in generalized form, the lattice vector becomes a superposition of two primitive vectors, given by  $\mathbf{a1}=a \cos\psi \mathbf{y} +a \sin\psi \mathbf{z}$  and  $\mathbf{a2}= -a \sin\psi \mathbf{y} +a \cos\psi \mathbf{z}$ , where  $\psi=0^\circ$  ( $20^\circ$ ) for  $\varphi =90^\circ$  ( $70^\circ$ ).

In the reciprocal space, the dynamic components of magnetization and magnetostatic field are expressed using the Bloch's theorem, *i.e.*, as a product of a plane-wave envelope function and a periodic function:

$$m(\mathbf{r}) = \sum m_q(\mathbf{G})e^{i(\mathbf{q}+\mathbf{G})\cdot\mathbf{r}} \quad \dots\dots\dots(10.1)$$

where  $\mathbf{G} = (G_y, G_z)$  denotes the reciprocal lattice vector of the considered structure; in the case of the ASW array, we get  $\mathbf{G} = \frac{2\pi}{a} (n_y \cos\psi - n_z \sin\psi, n_y \sin\psi + n_z \cos\psi)$ ,  $n_y$  and  $n_z$  being integers. The Bloch wave vector  $\mathbf{q} = (q_y, q_z)$ , in this case, lies along the stripe axis. So it reads as  $\mathbf{q} = [|\mathbf{q}| \cos\psi, |\mathbf{q}| \sin\psi]$ .

Being a periodic function of position in the MC, the saturation magnetization ( $M_S$ ) and the squared exchange length ( $l_{ex}^2 = \sqrt{\frac{2A}{\mu_0 M_S^2}}$ ,  $A$  is exchange constant) can be mapped onto the reciprocal space using the Fourier transformation formulas:

$$M_s(r) = \sum_G M_s(G) e^{iG \cdot r} \quad \dots\dots\dots(10.2)$$

$$I_{ex}^2(r) = \sum_G I_{ex}^2(G) e^{iG \cdot r} \quad \dots\dots\dots(10.3)$$

where the Fourier co-efficients  $M_s(G)$  and  $I_{ex}^2(G)$  were determined analytically. To simplify the problem, we assumed each ASW as a periodic sequence of tilted (at  $25^\circ$  angle with respect to y-axis) rectangular elements (with nominal dimensions  $800 \text{ nm} \times 400 \text{ nm}$ ), serially connected with each other with small overlap (see Fig. 10.1a). This way, the ASW array is reduced to a 2D lattice of tilted rectangles minus the overlapped region. Although the inter-element exchange should be considered for more accurate calculation, the large size of the elements *w.r.t.* the exchange length of permalloy ensures that the main contribution to the collective dynamics originates from the collective dipolar field. The chosen material parameters corresponding to permalloy are saturation magnetization  $M_s=860 \text{ emu/cc}$ , exchange constant  $A=1.3 \times 10^{-6} \text{ erg/cm}$ ,  $g = 2$ , while, small non-zero values of  $M_s$  and  $A$  were assigned to the air gap to avoid any non-physical frequency values. A satisfactory convergence of numerical solutions of the eigenvalue problem is obtained by taking 882 plane waves.

## 10.4. Results and Discussions

Figure 10.1c shows the static magnetic configurations of the sample with  $\varphi = 90^\circ$  and  $70^\circ$  (the left and right panels, respectively), simulated using OOMMF software [37], by dividing the samples into cuboidal cells of  $4 \times 4 \times 30 \text{ nm}^3$  volume. For  $\varphi = 90^\circ$ , the static magnetic state reveals a series of ‘S’ states with the demagnetized regions near the edges of each stripe, as shown by the y-component of magnetization encoded using blue-white-red colormap. The  $\varphi = 70^\circ$  configuration, on the other hand, shows a series of leaf states where the magnetization lies along the diagonal of each element. Here, the demagnetized regions pervade only near the smaller edge of the rectangular element and are less pronounced as compared to the  $\varphi = 90^\circ$  case. The modification in the local magnetization states changes the dipolar coupling between the elements, which eventually determines the SW character, as will be shown later.

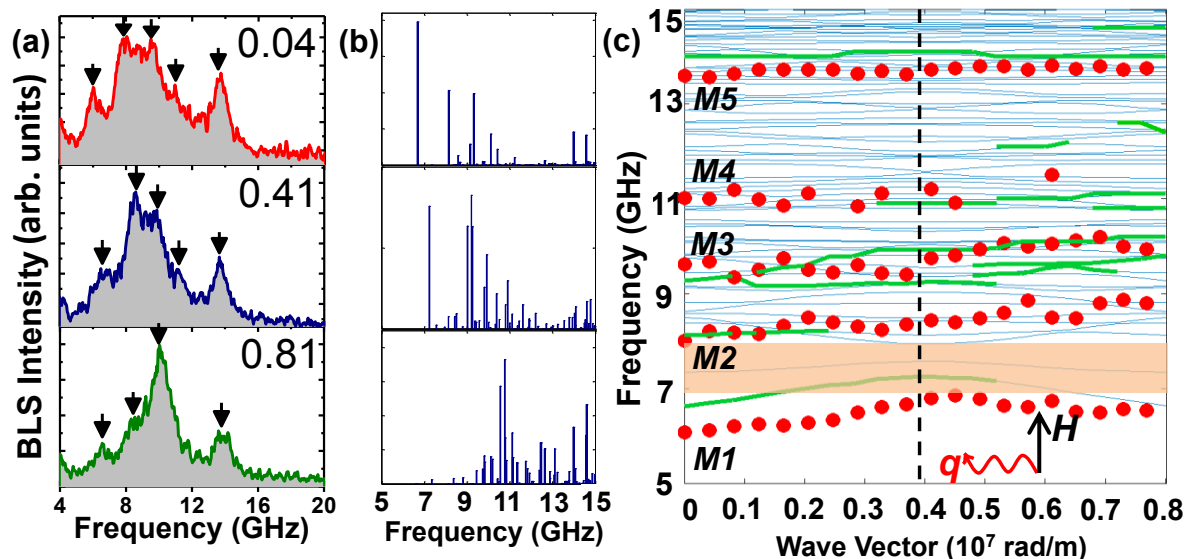


Figure 10.2: (a) The Stokes side of BLS spectra taken at different values of the in-plane transferred wave vector  $q$  (denoted in units of  $10^7$  rad/m) for  $\varphi = 90^\circ$  geometry. The spectra are horizontally flipped for convenience. The SW peaks are indicated by the arrows. (b) Relative values of BLS intensities as calculated by PWM for different values of  $q$  given in (a). (c) Magnonic band structure in  $\varphi = 90^\circ$  geometry. Thin blue lines are PWM results. Bold green lines emphasize intense excitations as predicted by PWM. Red solid circles represent peaks in the BLS spectra. The dashed vertical line is the boundary of first BZ. The bandgap is shown by shaded region.

For the geometry with  $\varphi = 90^\circ$ , the wave vector evolution of spin wave frequencies, together with few representative BLS spectra (measured and calculated) are presented in Fig. 10.2. The calculated intensities were determined from the square of the modulus of the fundamental harmonics of magnetization in PWM, which is proportional to the signal strength detected in BLS. In Fig. 10.2c, the rich magnonic band structure of the ASW array, as obtained from PWM calculations for two BZs, is shown by the blue lines, where the magnonic bands with predicted large scattering cross sections are emphasized by bold green lines. The experimental data (red solid circles) are overlaid on the calculated dispersion, which is in good agreement with the latter. In the experiment, the BLS spectra are characterized by the presence of five well-defined modes (Fig. 10.2a). Amongst them, modes M1, M2 and M3 are dispersive modes, while M4 and M5 do not significantly depend on  $q$ . In addition, at wave vector near  $\pi/a$  (*i.e.*, the edge of the 1<sup>st</sup> BZ), mode M1 undergoes Bragg diffraction, inducing the opening of a band gap of width  $\sim 1$  GHz. The value of this gap depends upon the lattice dimensions and the cross-talk between the consecutive ASWs.

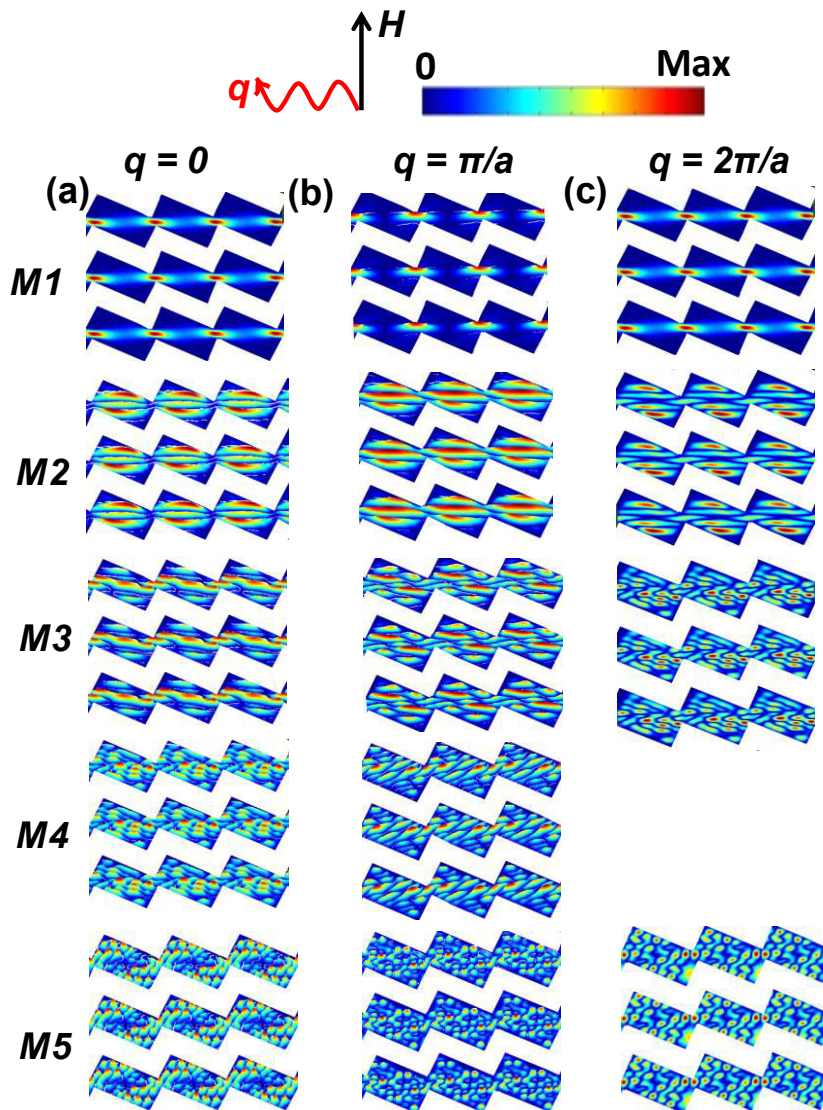


Figure 10.3: Spatial profiles of the selected modes for (a)  $q=0$  and (b)  $q=\pi/a$  and (b)  $q=2\pi/a$  for the geometry with  $\varphi=90^\circ$ .

In order to get a closer insight into the wave scattering mechanisms, we have calculated the SW mode profiles, *i.e.*, modulus of the amplitude of the  $x$ -component of the dynamic magnetization, of the relevant experimental modes. The spatial profiles of these modes are shown for  $q=0$ ,  $q=\pi/a$  and  $q=2\pi/a$  (*i.e.*, in the center and the edges of the BZs) in Fig. 10.3a, b and c, respectively. Starting from the mode profile of M1 at  $q=0$  (Fig. 10.3a), we find that this mode is an extended mode along the ASW axes, although with a non-uniform profile along the stripe axes. A correlation between this profile with the corresponding magnetic configuration shown in Fig. 10.1c

emphasizes that this mode actually resides where the local magnetization is parallel to the external applied field, i.e., the so-called barrier or center mode of a magnetic stripe [39]. In case of a uniform magnetic stripe the modes are governed by the spatially inhomogeneous internal magnetic field formed by the edge potential wells due to demagnetizing effects, forming the well modes and barrier mode at the edge and central regions respectively. As the width of the stripe is scaled down, the well mode and the barrier mode starts to couple, which may create noise in the propagating signal. The corrugation at the edges lifts the demagnetized regions away from the propagation channel, thereby impedes the edge modes from occurring. In other words, the corrugation can control the extent of the edge modes, which will be useful for decoupling the center mode in miniaturized magnonic devices. The spatial profiles of the higher frequency modes M2 and M3 show that they are also quantized extended modes, with quantization number of 3 and 8, respectively, the nodal planes being perpendicular to  $H$ . The modes M4 and M5, on the other hand, show a high degree of hybridization, recognized by the presence of nodal planes in both parallel and perpendicular directions to the local magnetic field. Interestingly, the mode profiles of M4 and M5 foster tunneling nodal planes through the rectangular elements, still they do not exhibit any systematic dispersion with  $q$  (see Fig. 10.2c). The reason can be ascribed to the very high quantization number of these modes, which reduces the dynamic dipolar coupling between the rectangular elements, thereby prohibiting the mode propagation.

As we move to the mode profiles for  $q = \pi/a$  (Fig. 10.3b), we observe a significant reduction in the extended character of M1. This is expected because at the BZ edge, as mentioned earlier, its dispersion undergoes a change from positive slope to negative slope. This substantially minimizes its group velocity ( $v = d(2\pi f)/dq$ ) at the BZ edge, i.e., its propagating character. The corresponding profiles for M2 and M3, on contrary, show a more pronounced tunneling at the BZ boundary. The modes M4 and M5 continue to show an extended nature, with a slight change in their hybridization characteristics.

With further increase in  $q$ , we see substantial changes in the profiles of M1, M2 and M3. At the second BZ boundary (Fig. 10.3c), mode M1 regains its extended character, due to the aforementioned reason. The mode M2 and M3, on the other hand, evolves into a profile with higher quantization number. Basically, in case of quantized modes with high degree of quantization, the wave vector dispersion is associated with their growth in terms of nodal planes.

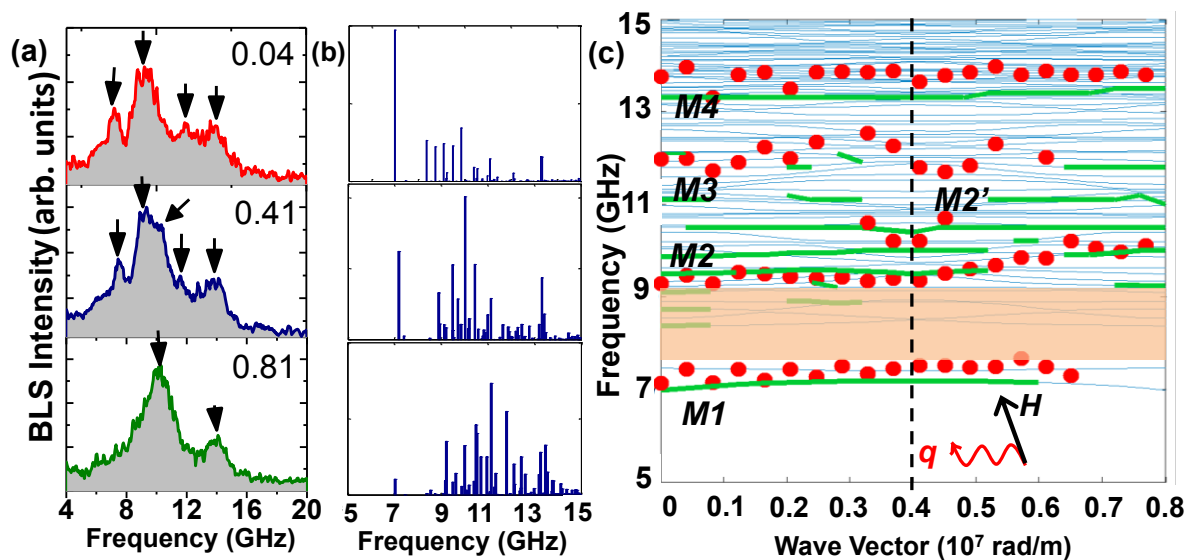


Figure 10.4: (a) The Stokes side of BLS spectra taken at different values of the in-plane transferred wave vector  $q$  (denoted in units of  $10^7$  rad/m) for  $\varphi = 70^\circ$  geometry. The spectra are horizontally flipped for convenience. The SW peaks are indicated by the arrows. (b) Relative values of BLS intensities as calculated by PWM for different values of  $q$  given in (a). (c) Magnonic band structure in  $\varphi = 70^\circ$  geometry. Thin blue lines are PWM results. Bold green lines emphasize intense excitations as predicted by PWM. Red solid circles represent peaks in the BLS spectra. The dashed vertical line is the boundary of first BZ. The bandgap is shown by shaded region.

In Fig. 10.4, the experimental and calculated frequencies are presented for  $\varphi = 70^\circ$ . Note that, for both values of  $\varphi$ , the calculated band structure exhibits mirror symmetry *w.r.t.* the boundary of the first BZ. This signifies that the wave vector is always along one symmetry direction, *i.e.*, along the axes of ASW. As seen from Fig. 10.4a, primarily four modes are observed in the BLS spectra for  $\varphi = 70^\circ$ . As compared to the  $\varphi = 90^\circ$  geometry, here the frequencies of the modes are shifted to higher value, except M4. This trait can be attributed to the reduced demagnetized regions for  $\varphi = 70^\circ$ , which enhances the internal magnetic field inside the stripe. Moreover, a suppression of spin wave propagation is seen for M1, *i.e.*, the group velocity is close to zero. The mode M2, on the other hand, has first an almost constant frequency up to about  $\pi/a$  and then it is dispersive, *i.e.*, has a finite slope as a function of  $q$ . This leads to a marked increase in the bandgap width ( $\sim 1.8$  GHz) as well as an upshift in its frequency position. The dispersive character of M2 is reproduced in the PWM results, except for the fact that the mode with highest BLS intensity (see Fig. 10.4b) is at larger frequency than M2. In addition, although experimentally the mode M2 evolves continuously

with  $q$ , theoretically, the evolution of the predicted BLS intensity jumps to another frequency branch. Our findings on SW propagation and bandgap features are different from the results reported earlier for strongly interacting magnetic stripe array, where the wave vector (of constant magnitude) was rotated in azimuthal direction, while keeping the direction of  $H$  fixed [38].

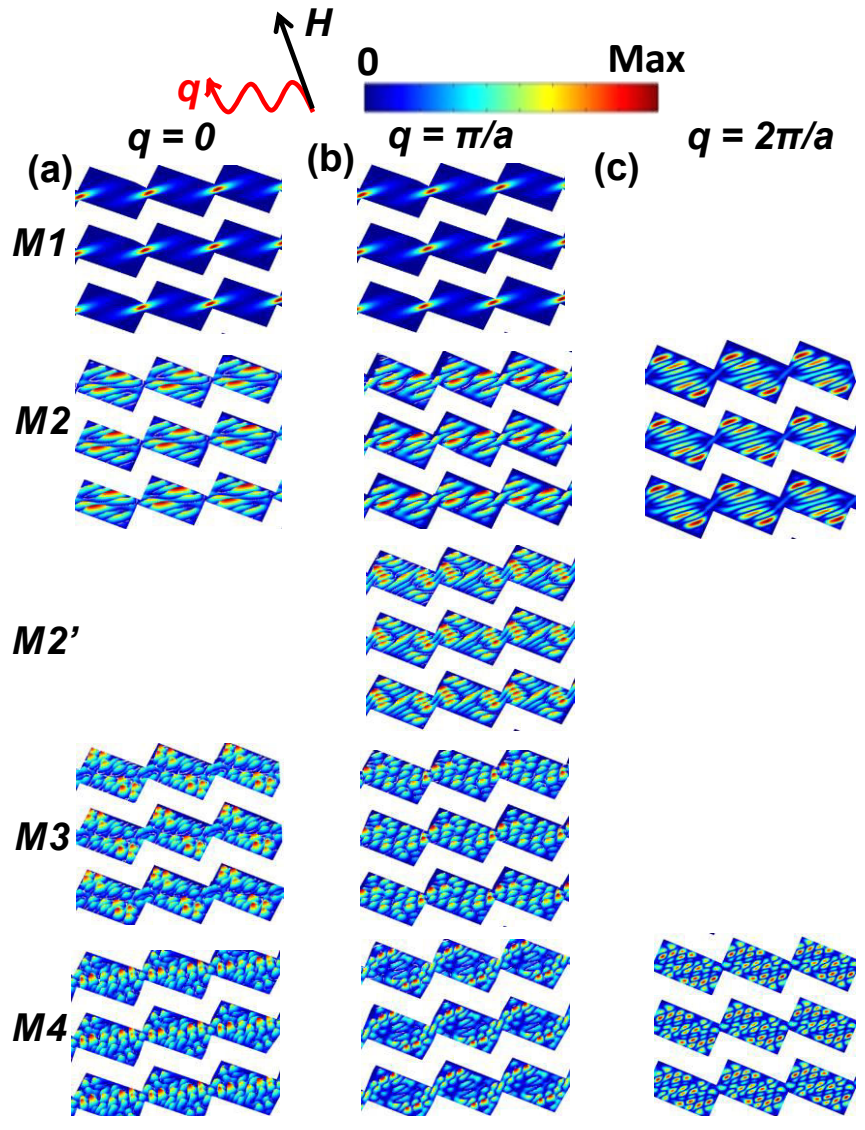


Figure 10.5: Spatial profiles of the selected modes for (a)  $q = 0$  and (b)  $q = \pi/a$  and (b)  $q = 2\pi/a$  for the geometry with  $\varphi = 70^\circ$ .

Inspection of the spatial spin-precession profiles of the experimentally observed modes, presented in Fig. 10.5 (Fig. 10.5a, b and c for  $q = 0$ ,  $q = \pi/a$  and  $q = 2\pi/a$ , respectively), reveals that here the mode M1 is a quantized mode with mode number one, the nodal plane being perpendicular to the

external field direction. Moreover, the profile of M1 for  $\varphi = 70^\circ$  evidence a weaker coupling of magnetic excitations between the constituent elements, thereby weakening the SW propagation (see Fig. 10.5a). As for M2, it is a quantized mode with quantization number 8, similar to M3 in case of  $\varphi = 90^\circ$  geometry. Nevertheless, its nodal planes are confined in the rectangular elements at  $q=0$ , then it extends substantially across the inter element channels giving rise to a propagating behavior, at the edge of first BZ. At the second BZ boundary, the mode profile attains a higher quantization degree. All these trends is consistent with the dispersion behavior observed experimentally, where initially its eigen frequency is nearly independent of  $q$ , which takes a positive slope as  $q$  approaches the BZ. The other high frequency modes are complex hybridized modes, which show a very high quantization number and have similar properties as for the geometry of  $\varphi = 90^\circ$ .

The above results demonstrate an active method of magnonic band engineering in ASW array by merely rotating an external magnetic field *w.r.t.* the in-plane wave vector. In a practical integrated magnonic circuit, the external bias field to drive the magnons is provided either by external fields coming from a permanent magnet, or by the oersted field created by a current through a loop which also requires a cooling system. Therefore to orient the magnetic field in a different direction is an easier way (one can possibly make two current carrying lines corresponding to the two magnetic field orientations and send same magnitude of current through one of them at a time) compared to increasing the field value or rotating the entire magnonic circuit. The variation in the magnetic field direction essentially leads to a modulation in the profile of periodically varying SW channel, which subsequently determines the SW frequency dispersion. Figuratively, the SW energy incident on each rectangular element is partly reflected because the SW width profile does not fit into the narrow waveguide section at the junction of two elements. This property can be implemented in dynamic SW filter and SW waveguides. Besides, the magnonic bands can be further tuned by changing the structural parameters of each ASW, *e.g.*, the dimensions of rectangular elements, the interaction between the ASWs (an increase in cross-talk results in reduction of bandgap), the orientation and magnitude of magnetic field and the symmetry of corrugation.

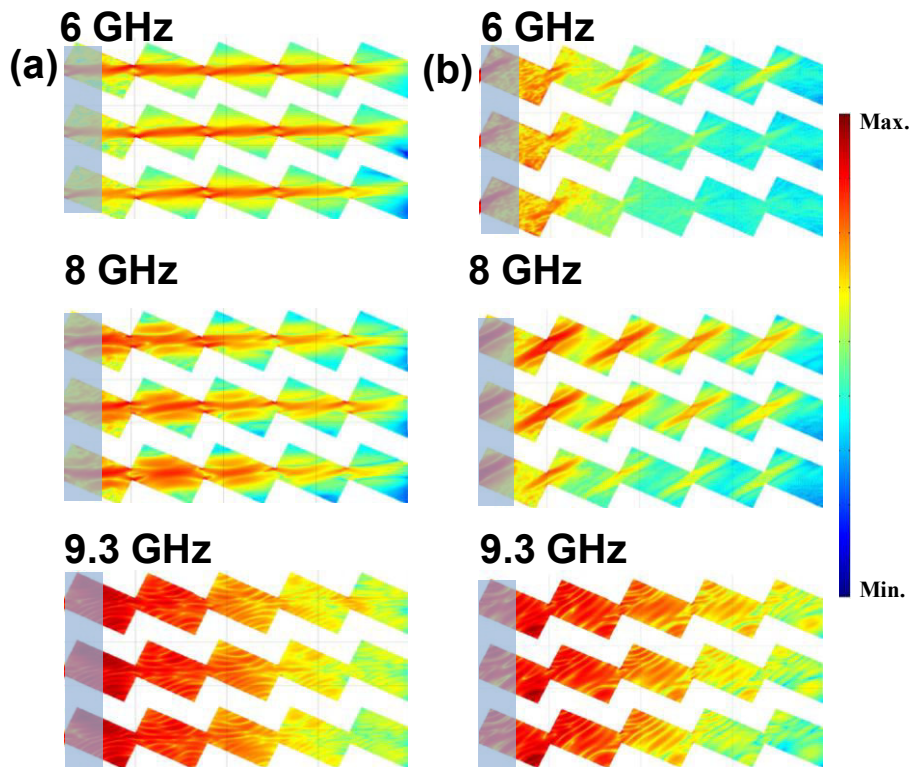


Figure 10.6: Amplitude profiles of different spin wave modes excited locally at the shaded region for (a)  $\varphi = 90^\circ$  and (b)  $\varphi = 70^\circ$  geometry.

Figure 10.6 provides an exemplary demonstration of how the SW propagation can be manipulated in the ASW array. For that, the SW response to microwave excitation was simulated for the two  $\varphi$  values. Using oommf software, SWs were launched at the left end of the considered structure through a 400 nm wide region. For excitation we used a time varying field of sinc profile (frequency window 30 GHz) applied along the stripe axes. Figure 10.6a and b show the mode profiles at different SW frequencies for  $\varphi = 90^\circ$  and  $\varphi = 70^\circ$  respectively. The results reveal that the transmission of the nodal planes at 6 GHz and 8 GHz is blocked when  $\varphi$  changes from  $90^\circ$  to  $70^\circ$ . On contrary, at 9.3 GHz, the nodal planes are able to pass through for both values of  $\varphi$ . This asserts the use of ASW array as a frequency dependent dynamic filter. It is noteworthy, that for 6 GHz in Fig. 10.6a, the non-uniformity of the SW amplitude is not that pronounced, as it was in the PWM results (Fig. 10.3a). Therefore we infer that the obtained non uniformity is a result of the pinned boundary condition inherent in PWM.

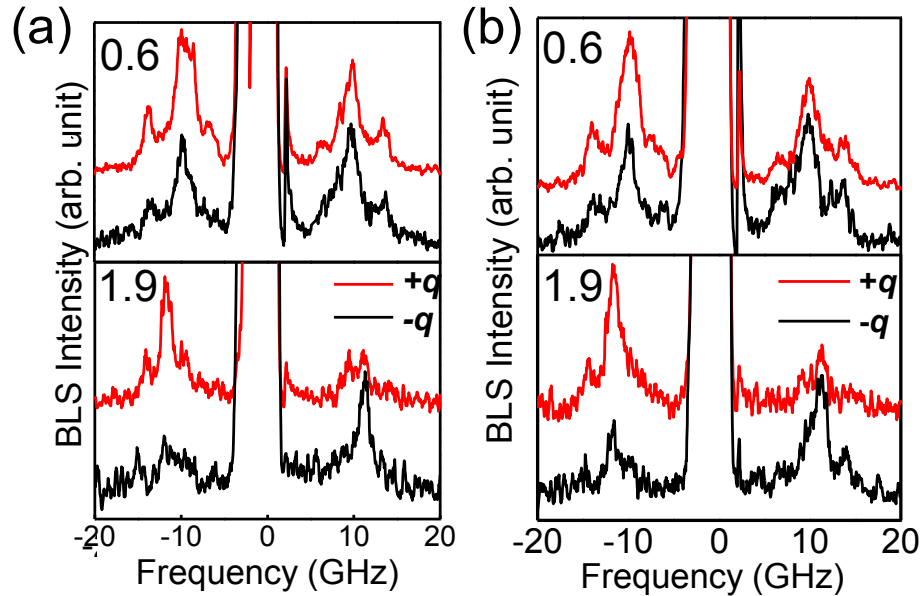


Figure 10.7: BLS spectra measured at two different values of the in-plane transferred wave vector  $q$  (denoted in units of  $10^7$  rad/m) for (a)  $\varphi = 90^\circ$  and (b)  $\varphi = 70^\circ$  geometry. The spectra in red and black stand for two counter propagating directions of wave vector.

Because of the lack of mirror symmetry in this system, one may expect some impression of non-reciprocal SW behaviour *w.r.t* the counter propagating wave vectors. The non-reciprocal behaviour was indeed predicted for a corrugated stripe (having mirror symmetry about its axis) with lower dimensions [40]. To verify that in our case, we have measured the BLS spectra for two magnitudes of wave vectors of counter propagating SWs. The results are presented in Fig. 10.7a and 10.7b for  $\varphi = 90^\circ$  and  $\varphi = 70^\circ$  respectively. Surprisingly, even for higher  $q$  ( $= 1.9 \times 10^7$  rad/m), negligible asymmetry is observed for both  $\varphi$  values. We speculate that the reason lies in the internal field profile. When the SW propagates along either positive or negative direction, it simultaneously perceives the profile of small and large arms of the rectangular element. Another possible reason may be the feature dimensions, which is too large for any chirality to be visible. Nevertheless, a thorough investigation of the non-reciprocal behavior is of future interest.

## 10.5. Conclusions

In conclusion, we have presented a combined experimental and theoretical study of the reconfigurable magnonic excitations in a pseudo one-dimensional magnonic crystal composed of asymmetric sawtooth waveguide (ASW) arrays, by varying the angle ( $\varphi$ ) between the wave vector (directed along ASW axes) and magnetic field. The switching of the magnetic field from  $\varphi = 90^\circ$  to  $\varphi = 70^\circ$  results in a transition in the internal magnetic field distribution, from ‘S’ state to ‘leaf’ state. Consequently, the magnonic band structure for  $\varphi = 90^\circ$  supports propagating SW modes and is characterized by a pronounced magnonic bandgap. The frequency and size of the gap is effectively modified by varying  $\varphi$  to  $70^\circ$ . Further calculations of the spatial mode profiles reveal that the edge potential well modes can be effectively tuned by manipulating the edge corrugation. All these observations are important from a fundamental scientific viewpoint as well as in terms of magnonics where the tunability of spin waves is considered for magnetic nanodevices operating in the GHz frequency regime.

## References

- [1] A. O. Adeyeye and N. Singh, “Large Area Patterned Magnetic Nanostructures,” *J. Phys. D: Appl. Phys.* **41**, 153001 (2008).
- [2] J. Y. Cheng, C. A. Ross, V. Z.-H. Chan, *et al.*, “Formation of a Cobalt Magnetic Dot Array Via Block Copolymer Lithography,” *Adv. Mater.* **13**, 1174 (2001).
- [3] G. Gubbiotti, G. Carlotti, T. Okuno, *et al.*, “Brillouin Light Scattering Investigation of Dynamic Spin Modes Confined in Cylindrical Permalloy Dots,” *Phys. Rev. B.* **68**, 184409 (2013).
- [4] V. V. Kruglyak, A. Barman, R. J. Hicken, *et al.*, “Precessional Dynamics in Microarrays of Nanomagnets,” *J. Appl. Phys.* **97**, 10A706 (2005).
- [5] B. Rana, D. Kumar, S. Barman, *et al.*, “Detection of Picosecond Magnetization Dynamics of 50 Nm Magnetic Dots Down to the Single Dot Regime,” *ACS Nano.* **5**, 9559 (2011).
- [6] R. Mandal, S. Saha, D. Kumar, *et al.*, “Optically Induced Tunable Magnetization Dynamics in Nanoscale Co Antidot Lattices,” *ACS Nano.* **6**, 3397 (2012).

- [7] O. Hellwig, A. Berger, T. Thomson, *et al.*, “Separating Dipolar Broadening from the Intrinsic Switching Field Distribution in Perpendicular Patterned Media,” *Appl. Phys. Lett.* **90**, 162516 (2007).
- [8] S. Tehrani, E. Chen, M. Durlam, *et al.*, “High Density Submicron Magnetoresistive Random Access Memory (Invited),” *J. Appl. Phys.* **85**, 5822 (1999).
- [9] S. H. Chung, A. Hoffmann, S. D. Bader, *et al.*, “Biological Sensors Based on Brownian Relaxation of Magnetic Nanoparticles,” *Appl. Phys. Lett.* **85**, 2971 (2004).
- [10] A. A. Serga, A. V. Chumak, and B. Hillebrands, “Yig Magnonics,” *J. Phys. D: Appl. Phys.* **43**, 264002 (2010).
- [11] B. Lenk, H. Ulrichs, F. Garbs, *et al.*, “The Building Blocks of Magnonics,” *Phys. Rep.* **507**, 107 (2011).
- [12] A. Haldar and A. O. Adeyeye, “Deterministic Control of Magnetization Dynamics in Reconfigurable Nanomagnetic Networks for Logic Applications,” *ACS Nano.* **10**, 1690 (2016).
- [13] D. B. Carlton, N. C. Emley, E. Tuchfeld, *et al.*, “Simulation Studies of Nanomagnet-Based Logic Architecture,” *Nano Letters.* **8**, 4173 (2008).
- [14] S. A. Nikitov, P. Tailhades, and C. S. Tsai, “Spin Waves in Periodic Magnetic Structures—Magnonic Crystals,” *J. Magn. Magn. Mater.* **236**, 320 (2001).
- [15] Z. K. Wang, V. L. Zhang, H. S. Lim, *et al.*, “Nanostructured Magnonic Crystals with Size-Tunable Bandgaps,” *ACS Nano.* **4**, 643 (2010).
- [16] F. Ciubotaru, A. V. Chumak, N. Y. Grigoryeva, *et al.*, “Magnonic Band Gap Design by the Edge Modulation of Micro-Sized Waveguides,” *J. Phys. D: Appl. Phys.* **45**, 255002 (2012).
- [17] K. S. Lee, D. S. Han, and S. K. Kim, “Physical Origin and Generic Control of Magnonic Band Gaps of Dipole-Exchange Spin Waves in Width-Modulated Nanostrip Waveguides,” *Phys. Rev. Lett.* **102**, 127202 (2009).
- [18] A. V. Chumak, A. A. Serga, B. Hillebrands, *et al.*, “Scattering of Backward Spin Waves in a One-Dimensional Magnonic Crystal,” *Appl. Phys. Lett.* **93**, 022508 (2008).
- [19] G. Gubbiotti, S. Tacchi, G. Carlotti, *et al.*, “Collective Spin Modes in Monodimensional Magnonic Crystals Consisting of Dipolarly Coupled Nanowires,” *Appl. Phys. Lett.* **90**, 092503 (2007).

- [20] M. P. Kostylev, G. Gubbiotti, J.-G. Hu, *et al.*, “Dipole-Exchange Propagating Spin-Wave Modes in Metallic Ferromagnetic Stripes,” *Phys. Rev. B* **76**, 054422 (2007).
- [21] A. V. Chumak, P. Pirro, A. A. Serga, *et al.*, “Spin-Wave Propagation in a Microstructured Magnonic Crystal,” *Appl. Phys. Lett.* **95**, 262508 (2009).
- [22] V. V. Kruglyak, P. S. Keatley, A. Neudert, *et al.*, “Imaging Collective Magnonic Modes in 2d Arrays of Magnetic Nanoelements,” *Phys. Rev. Lett.* **104**, 027201 (2010).
- [23] S. Saha, R. Mandal, S. Barman, *et al.*, “Tunable Magnonic Spectra in Two-Dimensional Magnonic Crystals with Variable Lattice Symmetry,” *Adv. Funct. Mater.* **23**, 2378 (2013).
- [24] J. M. Shaw, T. J. Silva, M. L. Schneider, *et al.*, “Spin Dynamics and Mode Structure in Nanomagnet Arrays: Effects of Size and Thickness on Linewidth and Damping,” *Phys. Rev. B* **79**, 184404 (2009).
- [25] M. Krawczyk, S. Mamica, M. Mruczkiewicz, *et al.*, “Magnonic Band Structures in Two-Dimensional Bi-Component Magnonic Crystals with in-Plane Magnetization,” *J. Phys. D: Appl. Phys.* **46**, 495003 (2013).
- [26] J. R. Vivas, S. Mamica, M. Krawczyk, *et al.*, “Investigation of Spin Wave Damping in Three-Dimensional Magnonic Crystals Using the Plane Wave Method,” *Phys. Rev. B* **86**, 144417 (2012).
- [27] M. Hänze, C. F. Adolff, B. Schulte, *et al.*, “Collective Modes in Three dimensional Magnonic Vortex Crystals,” *Sci. Rep.* **6**, 22402 (2016).
- [28] M. Kostylev, G. Gubbiotti, G. Carlotti, *et al.*, “Propagating Volume and Localized Spin Wave Modes on a Lattice of Circular Magnetic Antidots,” *J. Appl. Phys.* **103**, 07C507 (2008).
- [29] S. Tacchi, B. Botters, M. Madami, *et al.*, “Mode Conversion from Quantized to Propagating Spin Waves in a Rhombic Antidot Lattice Supporting Spin Wave Nanochannels,” *Phys. Rev. B* **86**, 014417 (2012).
- [30] J. Topp, J. Podbielski, D. Heitmann, *et al.*, “Internal Spin-Wave Confinement in Magnetic Nanowires Due to Zig-Zag Shaped Magnetization,” *Phys. Rev. B* **78**, 024431 (2008).
- [31] V. S. Tkachenko, A. N. Kuchko, M. Dvornik, *et al.*, “Propagation and Scattering of Spin Waves in Curved Magnonic Waveguides,” *Appl. Phys. Lett.* **101**, 152402 (2012).
- [32] A. V. Chumak, A. A. Serga, S. Wolff, *et al.*, “Design and Optimization of One-Dimensional Ferrite-Film Based Magnonic Crystals,” *J. Appl. Phys.* **105**, 083906 (2009).

- [33] B. Obry, P. Pirro, T. Bracher, *et al.*, “A Micro-Structured Ion-Implanted Magnonic Crystal,” *Appl. Phys. Lett.* **102**, 202403 (2013).
- [34] L. Bai, M. Kohda, and J. Nitta, “Observation of Spin Wave Modes Depending on a Tunable Periodic Magnetic Field,” *Appl. Phys. Lett.* **98**, 172508 (2011).
- [35] H. Al-Wahsh, A. Akjouj, B. Djafari-Rouhani, *et al.*, “Large Magnonic Band Gaps and Defect Modes in One-Dimensional Comblike Structures,” *Phys. Rev. B.* **59**, 13 (1999).
- [36] M. Krawczyk and H. Puzskarski, “Plane-Wave Theory of Three-Dimensional Magnonic Crystals,” *Phys. Rev. B.* **77**, 054437 (2008).
- [37] M. Donahue and D. G. Porter, "OOMMF User's guide, Version 1.0," NIST Interagency Report No. 6376, National Institute of Standard and Technology, Gaithersburg, MD, URL: <http://math.nist.gov/oommf/>, (1999).
- [38] M. Kostylev, P. Schrader, R. L. Stamps, *et al.*, “Partial Frequency Band Gap in One-Dimensional Magnonic Crystals,” *Appl. Phys. Lett.* **92**, 132504 (2008).
- [39] V. E. Demidov, S. O. Demokritov, K. Rott, *et al.*, “Nano-Optics with Spin Waves at Microwave Frequencies,” *Appl. Phys. Lett.* **92**, 232503 (2008).
- [40] H. -G. Piao, J.-H. Shim, M. Yang, *et al.*, “Selective Behavior of Spin Wave Propagation in Asymmetrically Modulated Ferromagnetic Nanowires,” *IEEE Trans. Magn.* **51**, 11 (2015).

## Chapter 11

# 11. Effects of adjacent layers on the structure and magnetization dynamics of Co-Fe-Al-Si Heusler alloy thin films

---

### 11.1. Introduction

The development of magnetoelectronic devices [1–3] is becoming an immense practical need for contemporary magnetic information storage and processing technology. Inspired by this quest, the research on spintronics aims at the growth and integration of new materials with unique, specifically tailored magnetic properties. In this aspect, Heusler alloys (HA) are important primarily due to their high spin polarization, magnetic anisotropy and small intrinsic Gilbert damping [4] which make them ideal candidates to realize a low current density for current induced magnetization reversal [5] and a high spin polarized current source for giant and tunnel magnetoresistance devices [6-7] used in magnetoresistive random access memories (MRAM) and in microwave components for spintronic applications. The composition of full HA is  $X_2YZ$ , where X and Y are transition metal elements and Z is a group III, IV, or V element. This composition has spurred interest because of the resulting electronic structure which shows an asymmetry in the spin split band structure [8]: while the majority spin band exhibits a metallic behavior, the minority electrons show a semiconducting behavior. Such half metallic band structure suppresses the spin flip processes and hence reduces the damping of magnetization precession. The electronic structure of HA compounds can further be tuned by alloying with a fourth element, which in turn modifies the structural and magnetic properties, providing a new way of designing materials with tailored characteristics.

Interestingly, the magnetic and structural properties of HA compounds are strongly influenced by the crystalline structure and the degree of chemical order which depend on the substrate material, as well as other deposition conditions [9]. It is thus imperative to investigate and control the magnetization dynamics of HA films by varying different structural properties and

deposition parameters. So far, extensive research has been carried out on  $\text{Ni}_2\text{MnSn}$  [10],  $\text{Co}_2\text{FeSi}$  [11-12],  $\text{Co}_2\text{MnSi}$  [13–15],  $\text{Co}_2\text{FeAl}$  [8-9, 16] and  $\text{Co}_2\text{CrAl}$  [17] compounds where the magnetic properties have been studied by varying the film thickness, substrate material and deposition parameters including annealing temperature and target composition. Amongst them, the spin dynamics in cobalt based HA compounds are of special interest because of their high spin polarization at the Fermi level (therefore providing large tunneling magnetoresistance (TMR)), high Curie temperature and very low magnetic damping parameter. Besides the ternary compounds, Co based quaternary HA compounds are also important where the Fermi level is further tuned leading to higher spin polarization. Hitherto, the magnetization dynamics and its dependence on different structural properties has been studied for Co–Cr–Fe–Al [18-19], Co–Fe–Mn–Si [20-21] and Co–Fe–Al–Si [6, 22-23] HA compounds using time resolved magneto optical Kerr effect (TR-MOKE), ferromagnetic resonance (FMR) and Brillouin light scattering (BLS) techniques.

In this chapter, we report a comprehensive study of collective spin wave excitations in CFAS compounds and their variation with different top (capping)-layers and under-layers. CFAS exhibits a high spin polarization (above 0.9) with the weakest temperature dependence among all known half-metals, and, therefore, may lead to the development of new families of spintronic devices with better performance. In earlier reports on CFAS compounds the spin polarization phenomena associated with TMR and giant magnetoresistance (GMR) effects [6, 22, 24] have been widely investigated. Further, the structural and static magnetic properties were studied by varying the gas pressure [25], annealing temperature [23] and film thickness [4]. In these cases, Ag [22, 24], Cr [6], MgO [7, 23] were taken as underlayer and Ru [6-7, 22–24] was used as top layer. However, the investigation of the ultrafast magnetization dynamics and its dependence on the top and under-layers have not yet been addressed. Here, we have used atomic force microscopy (AFM), transmission electron microscopy (TEM), Xray diffraction (XRD), vibrating sample magnetometry (VSM), combined with Brillouin light scattering (BLS) spectroscopy, to perform a correlative analysis between structural and static and dynamic magnetic properties of CFAS thin films grown on MgO (001) substrates. The XRD results reveal a transition from B2 to A2 ordered phase for different samples. Systematic studies of static and dynamic magnetization also show significant changes in the magnetic properties including the spin wave mode frequencies and

magnetic anisotropy. Moreover, the extracted damping parameter shows a broad tunability with varying chemical order.

## 11.2. Experimental Details

Three sets of CFAS thin films (30 nm in thickness) were prepared on MgO (001) single crystal substrates using an ultrahigh vacuum magnetron sputtering system with a base pressure lower than  $10^{-8}$  Torr. The substrates were cleaned first with acetone, then with isopropyl alcohol and finally with deionized water in an ultrasonic bath before being loaded into the sputtering chamber. Next, the substrates were baked in situ at 600° C for 30 minutes and cooled to room temperature (RT). For one set of the samples, a 20 nm thick Ag layer was grown on the substrate at RT by DC sputtering under an argon pressure of 3 mTorr. The Ag layer was then annealed at 300° C for 30 minutes and cooled to RT before the deposition of the CFAS layer. The applied DC power and the duration for the deposition was 40W and 3 min 20 s, respectively for the deposition of Ag layer. The distance between substrate and sputtering target was 16 cm. The CFAS thin film was deposited subsequently from a stoichiometric Co–Fe–Al–Si (Co: 50.0%, Fe: 25.0%, Al: 12.5%, and Si: 12.5%) target. For CFAS, the applied DC power and the duration of deposition were 60 W and 40 min, respectively. The samples were then annealed at 500° C for 30 minutes and cooled to RT before the deposition of the capping-layer. For the other two sets of samples, a 20 nm thick Cr buffer layer followed by a 20 nm thick Pt layer were deposited on the substrates at RT. The DC power used for both Cr and Pt layer deposition was 60W while the duration of deposition was 20 min and 7 min and 30 s for Cr and Pt, respectively. The Cr/Pt under-layer was then annealed at 600° C for 30 minutes and cooled to RT before the deposition of the CFAS layer. The samples were then also annealed at 500° C for 30 minutes and cooled to RT before the deposition of the cap layers. We label these samples as S1 (with Ag under-layer), S2 and S3 (with Cr/Pt under-layer). Finally, a 2 nm thick MgO (RF power: 120 W; duration: 10 min) layer was deposited to cap S1 and S3, while S2 was capped with a Ru layer (DC power: 60 W; duration: 30 s) of 4 nm thickness. Therefore, the stacking structure of S1, S2 and S3 are the following:

S1: Sub MgO/Ag (20 nm)/CFAS (30 nm)/MgO (2 nm),

S2: Sub MgO/Cr (20 nm)/Pt (20 nm)/CFAS (30 nm)/Ru (4 nm),

S3: Sub MgO/Cr (20 nm)/Pt (20 nm)/CFAS (30 nm)/MgO (2 nm).

The materials for the substrate and underlayers were chosen based on their lattice matching with CFAS, while the thicknesses were chosen so that the values should be suitable to allow for proper formation of the layers, taking into account aspects such as stress relaxation. MgO was chosen as one of the capping layers because in real MTJ devices, MgO is used as the tunnel barrier and grown on top of the ferromagnetic CFAS layer. Hence, it is reasonable to mimic our sample structure as realistic as possible. The MgO thickness was also chosen to be similar to the thickness used in MTJ devices. However, MgO is susceptible to degradation by moisture. Hence, a well-established protective cap layer, Ru, was also used for one of the samples.

The surface morphology and structural properties were characterized using AFM, TEM and XRD methods. The static magnetic properties were investigated using VSM at room temperature. BLS spectroscopy in the backscattered geometry was employed to study the magnetization dynamics, in particular the spin wave frequency and linewidth. Here, a laser beam from a diode pumped, frequency doubled Nd:YVO<sub>4</sub> laser with a wavelength of  $\lambda = 532$  nm is incident on the magnetic sample and inelastically scattered from the spin waves. During this interaction, magnons are created or annihilated following the conservation of energy and momentum. The frequencies of the scattered light are then analyzed using a Sandercock-type sixpass tandem Fabry–Perot interferometer (FPI) [26]. The different wave vectors of spin waves can be selected by changing the angle of incidence of the beam, owing to the relation  $q = 2k_i \sin\theta$ , where  $q$  and  $k_i$  are the wave vectors of the spin wave and the incident beam, respectively, and  $\theta$  is the angle of incidence. The external magnetic field  $H$  was applied in the so-called magnetostatic surface wave geometry, wherein  $H$  is applied in the plane of the sample and is perpendicular to the plane of light incidence (i.e.  $H \perp q$ ).

### 11.3. Results and Discussions

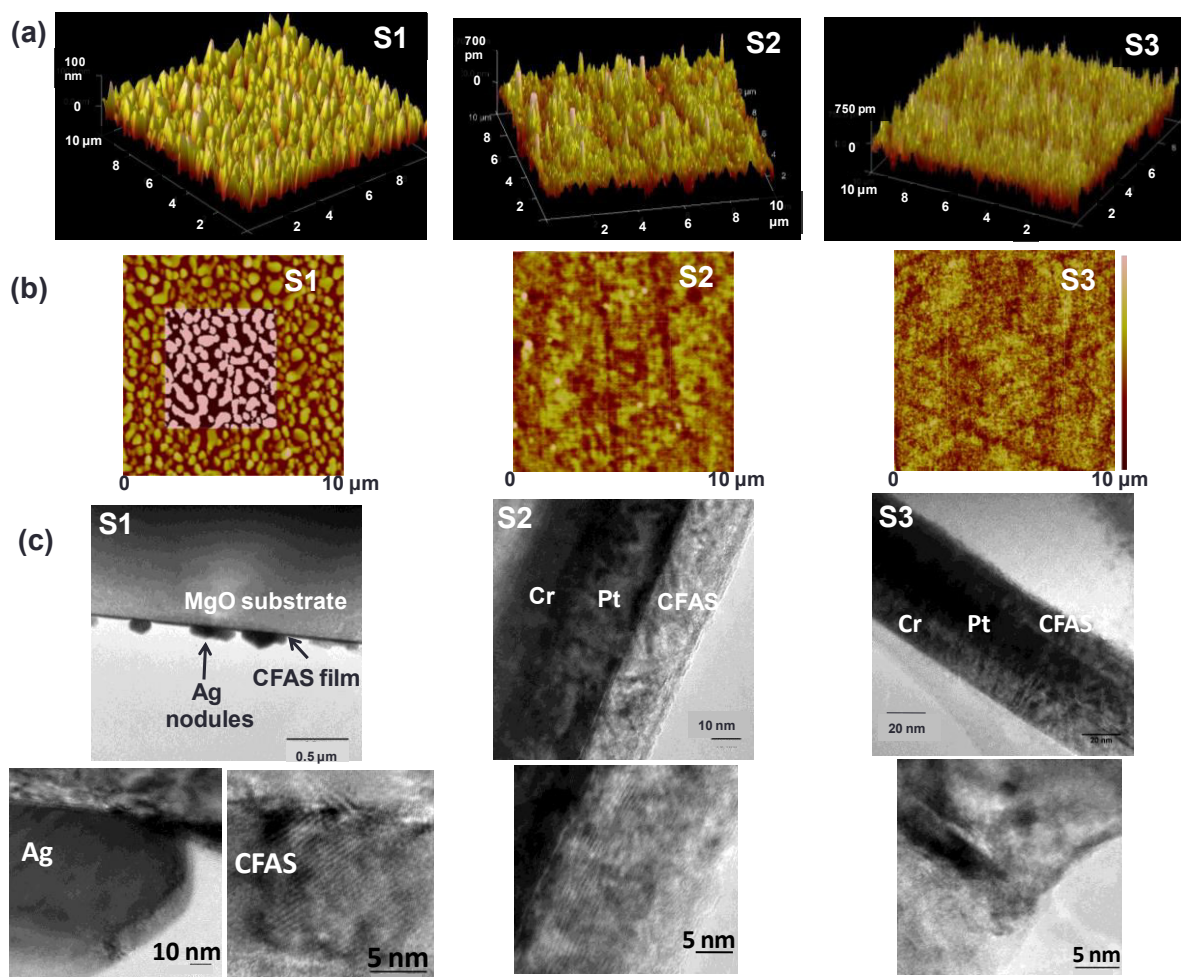


Figure 11.1: (a) Three-dimensional and (b) in-plane view of AFM images for S1, S2 and S3. (c) Cross-sectional TEM images for all three samples. The lower panels show high resolution images of the diffraction fringes of CFAS films.

The AFM images for the respective samples are shown in Fig. 11.1a and b. The measured root mean square (RMS) roughness was approximately 0.2 nm for S2 and S3. However, S1 had significantly higher roughness of 33 nm. These values are listed in Table 11. 1. The high roughness of the sample S1 is probably due to the diffusion of Ag from the under-layer to the top of the film stack after enabling the formation of a desirable crystal structure in the magnetic thin film [27]. This is further revealed in the cross-sectional TEM image (Fig. 11.1c). On the other hand, no such diffusion of under-layer material into the CFAS film is observed in S2 and S3, giving rise to a reasonable low surface roughness of these samples. The cross-sectional TEM images confirm that

the samples have good crystalline quality throughout the layers and have good quality interfaces (Fig. 11.1c). The XRD data for the CFAS sample series are shown in Fig. 11.2. The characteristic peaks of CFAS are shown by arrows. In addition to that, several other peaks corresponding to MgO, Ag, Pt, Cr, CrPt, Ru are observed, which are marked by various symbols. Some peaks remain unidentified, which are also marked in Fig. 11.2a. The XRD pattern of sample S1 contains CFAS (002) as well as CFAS (004) peaks, indicating (001)-oriented growth on the MgO surface. The presence of the CFAS (002) peak indicates an ordered B2 structure. In contrast, for S2 and S3, the CFAS (420) peak is observed, which corresponds to the disordered A2 phase. We notice here that sample S2 also exhibits the (002) peak but with a very low intensity. Hence, we can state that the ratio  $I_{002}/I_{004}$  of the integrated intensities of the (002) and (004) peaks decreases from S1 to S3, indicating a decrease in the degree of chemical order from the ordered B2 phase towards the disordered A2 phase. Note here, that the CFAS (004) and CFAS (002) reflections in S2 is shifted as compared to that of S1. This can be attributed to the growth of CFAS layer over the respective under-layers. The lattice mismatch between Ag and CFAS (in S1) results in out-of-plane contraction, while the lattice mismatch between Pt and CFAS (in S2) results in out-of-plane expansion. This may result in the shift in those peaks in the XRD pattern.

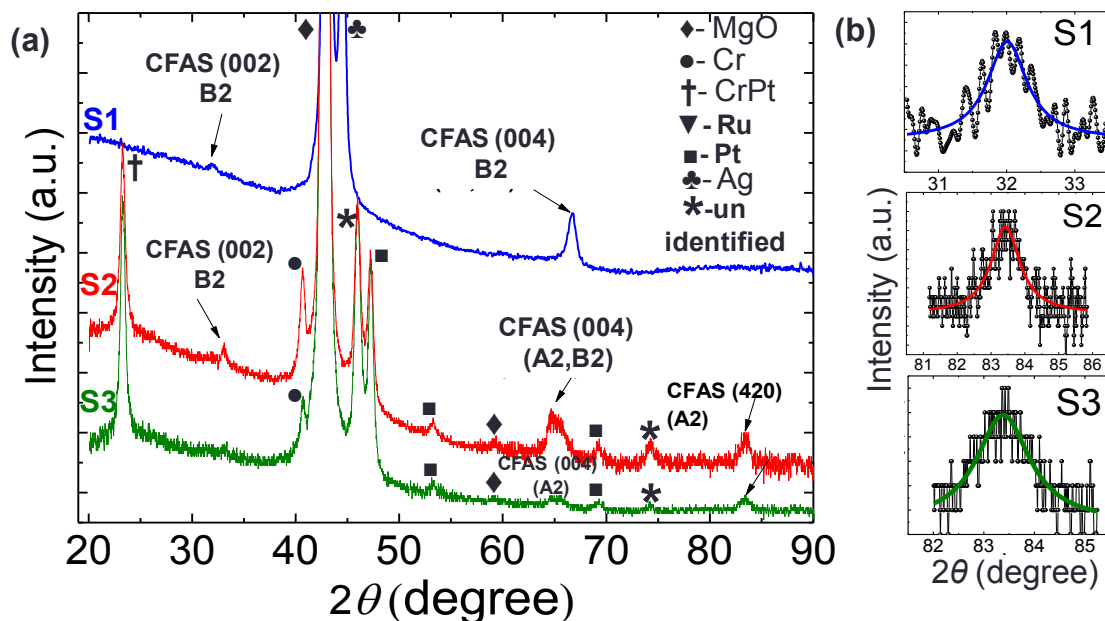


Figure 11.2: (a) XRD patterns for all three samples. The arrows indicate the CFAS peaks, while peaks corresponding to other materials are indicated by symbols. (b) Lorentzian fit to the characteristic CFAS peaks of S1, S2 and S3 which is used in the text to find out the crystallite size of the CFAS thin films.

We have further estimated the crystallite size of the thin films by modelling the characteristic B2 and A2 peaks of the CFAS samples with the Debye–Scherrer equation, given by:

$$\tau = \frac{0.9\lambda}{\beta \cos \theta} \quad \dots\dots(11.1)$$

where  $\tau$  is the mean size of the ordered (crystalline) domains,  $\lambda$  is the X-ray wavelength,  $\beta$  is the full width at half maximum (FWHM) of the characteristic peak and  $\theta$  is the respective Bragg angle. The obtained values are 11 nm, 10 nm and 8 nm for S1, S2 and S3, respectively. The crystallite size for S1 to S3 indicates overall good crystalline quality in all three samples.

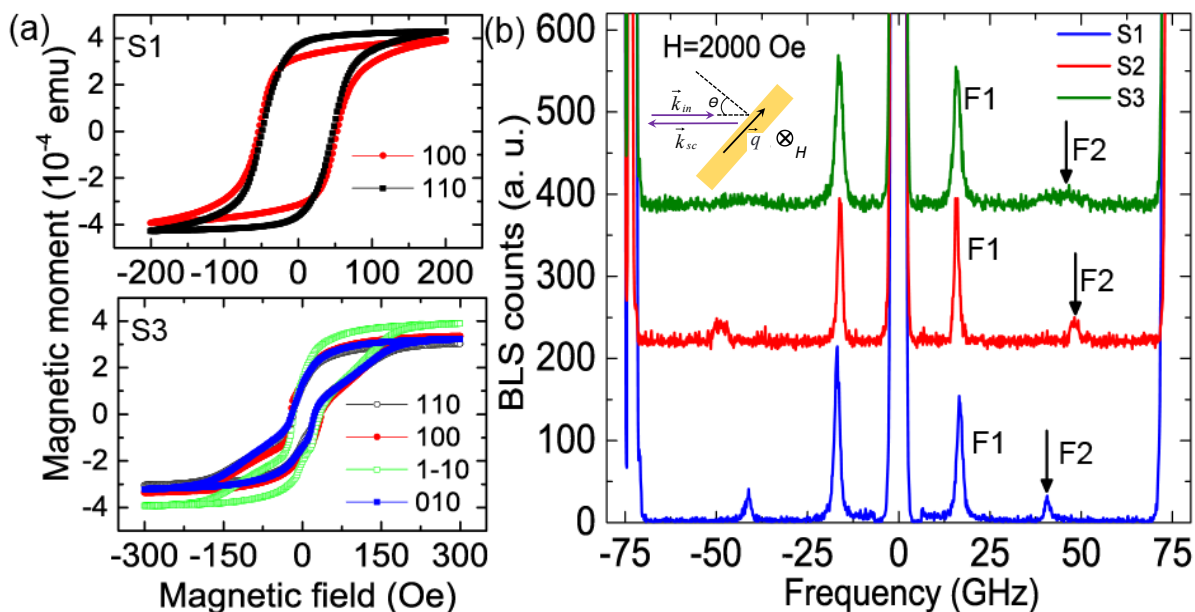


Figure 11.3: (a) Magnetic hysteresis loops of S1 (upper panel) and S3 (lower panel), measured for magnetic field applied parallel to the film surface, at various angles with respect to the edges of the MgO substrate ([100] and [010]). The results for S3 are also representative of S2. (b) Typical BLS spectra of all samples taken for  $q = 0$  at  $H = 2$  kOe. The arrows indicate the peak frequencies of PSSW modes. The measurement geometry is shown in the inset.

The magnetometry measurements on the CFAS films were performed using VSM at room temperature. Figure 11.3a shows magnetization versus applied magnetic field curves for magnetic fields applied in the plane of the films along the [100] and [110] crystallographic orientations. The properties and the shape of the reversal curves allow us to make qualitative conclusions on the magnetic behavior of the samples. Here the hysteresis curves change from a nearly coherent reversal for S1 to a multistage reversal for S2 and S3. This variation (which is independent of the

field orientation) can be due to the change of the domain wall structure in the CFAS thin films, induced by different interface roughness at different capping and under-layers. The interface roughness gives rise to domain wall pinning, which is different for different adjacent layers. Moreover, for S1, a distinct fourfold symmetry is observed as the magnetic field is applied in different directions within the plane of the film, as apparent from the variation of normalized remanent magnetizations ( $M_r/M_s$ ), with the easy and hard axes lying parallel to the [110] and [100] axes, respectively. On the other hand, the reversal curves for S2 and S3 show a uniaxial anisotropy. We attribute this to two possible reasons: (i) the different degrees of chemical ordering in those samples and (ii) the tensile stress formed due to the lattice mismatching of the film with the adjacent layers along with the growth morphology. The average magnetization at saturation for all samples from VSM measurements has been found to be  $M_s = 530$  emu/cc. The  $M_s$  value is lower than the typical value of approximately 1000 emu/cc [28], which can be attributed to the formation of magnetic dead layer during the multiple annealing and cooling steps. To calculate  $M_s$ , the magnetization was divided by the volume of the magnetic thin film, where the volume of the thin film was taken as the product of the area and the nominal thickness of the measured thin film. Hence, the nominal thickness over-estimated the thickness of the magnetic thin film due to the dead layer, resulting in an under-estimation of the  $M_s$ .

In order to capture the complete magnetization dynamics as well as to obtain the magnetic parameters, we have further studied thermally excited magnons by BLS spectroscopy. In a continuous film, various modes are expected to propagate with wave vectors in the plane of the film. Schematically, for the direction of magnetization aligned perpendicular to the in-plane wave vector  $q$ , two types of spin wave modes are observed: (i) surface spin waves for in-plane propagation, the so-called Damon–Eshbach mode (DE mode), which consists of a dipolar dominated wave and is characterized by its exponential decay across the film thickness leading to its non-reciprocity, and (ii) the bulk spin waves which are excitations of the whole magnetic system (often called standing spin waves (SSW)) and are exchange-dominated modes with a frequency strongly depending on the film thickness. Figure 11.3b shows the BLS spectra (normalized to the reference beam intensity) for all the samples taken for zero wave vector (angle of incidence  $\theta = 0^\circ$ ), which corresponds to the Kittel mode. A bias magnetic field ( $H$ ) of 2 kOe was applied in the plane of the sample and the scanning range was chosen as 75 GHz by fixing the mirror spacing of FPI as 2mm. The geometry of the experiment is shown in the inset of Fig. 11.3b.

**Table 11.1: Material parameters obtained for different samples**

| Sample | Chemical Ordering | Surface Roughness (rms) | Grain Size | g    | $M_S$ (emu/cc) | A ( $\mu\text{erg/cm}$ ) | $H_{K2}$ (Oe) ( $2K_2/M_S$ ) | $H_{K4}$ (Oe) ( $K_4/M_S$ ) | Gilbert damping ( $\alpha$ ) |
|--------|-------------------|-------------------------|------------|------|----------------|--------------------------|------------------------------|-----------------------------|------------------------------|
| S1     | B2                | 33 nm                   | 11 nm      | 2.25 | 883            | 2.5                      | 0                            | 29.5                        | 0.002                        |
| S2     | B2 and A2         | 0.17 nm                 | 10 nm      | 2.25 | 883            | 2.5                      | 45                           | 2                           | 0.003                        |
| S3     | A2                | 0.21 nm                 | 8 nm       | 2.25 | 854            | 2.5                      | 19                           | 4                           | 0.006                        |

The significance of the Kittel mode lies in the fact that the spin wave spectra are solely dominated by the magnetic parameters and dispersion of the individual mode does not come into play. The applied field of 2 kOe is large enough to saturate the sample magnetization within the plane of the sample as evident from Fig. 11.3a. As shown in Fig. 11.3b, two peaks corresponding to spin wave modes can be observed both in the Stokes and anti-Stokes regimes for all samples. The lower and higher frequency peaks correspond to the Kittel mode and perpendicular standing spin wave (PSSW), respectively, as shown by the evolution of their mode frequencies with respect to the in-plane wave vector and applied magnetic field, which will be discussed later. A quick inspection of the spin wave spectra for all three samples shows a significant change in the frequency of the PSSW mode for different samples. This can be understood as a variation in the internal magnetic field profile, caused by the variation in interface effects of different top-layers and under-layers. As noticed above, this tendency was found in the VSM results as well, where a variation in the switching behavior was observed. On the other hand, the frequencies of the Kittel mode are nearly the same for all samples, in support of the similar  $M_S$  values found for all samples from VSM measurements. Nevertheless, the small difference is caused by the variation in anisotropy fields, as shown in Fig. 11.4.

The typical dependences of mode frequencies at  $q = 0$  for varying the bias field as well as in-plane azimuthal angle are shown in Fig. 11.4a and 11.4b, respectively. The frequency of the Kittel mode (F1), in the presence of magnetic anisotropy, is given by Eqn. 11.2:

$$f = \frac{\gamma}{2\pi} \left( \left[ H + \frac{2K_2}{M_S} \cos 2\varphi - \frac{4K_4}{M_S} \cos 4\varphi \right] \left[ H + 4\pi M_S + \frac{2K_2}{M_S} \cos^2 \varphi - \frac{K_4}{M_S} (3 + \cos 4\varphi) \right] \right)^{\frac{1}{2}} \dots\dots(11.2)$$

Where  $\gamma$ ,  $H$ ,  $M_S$ ,  $\varphi$ ,  $K_2$ , and  $K_4$  are the gyromagnetic ratio, applied magnetic field, saturation magnetization, angle between applied bias field and the [100] direction, and the uniaxial and fourfold anisotropy constants, respectively. On the other hand, the frequency for the PSSW mode (F2) is given by:

$$f = \frac{\gamma}{2\pi} \left( \left[ H + \frac{2K_2}{M_S} \cos 2\varphi - \frac{4K_4}{M_S} \cos 4\varphi + \frac{2A}{M_S} q_{\perp}^2 \right] \left[ H + 4\pi M_S + \frac{2K_2}{M_S} \cos^2 \varphi - \frac{K_4}{M_S} (3 + \cos 4\varphi) + \frac{2A}{M_S} q_{\perp}^2 \right] \right)^{\frac{1}{2}} \dots\dots(11.3)$$

Here, the wave vector is perpendicular to the surface of the film and defined by

$$q_{\perp} = \frac{n\pi}{d} \dots\dots(11.4)$$

where  $d$  is the thickness of the film and  $n = 1, 2, 3..$ , denoting one or more nodes along the perpendicular axis.

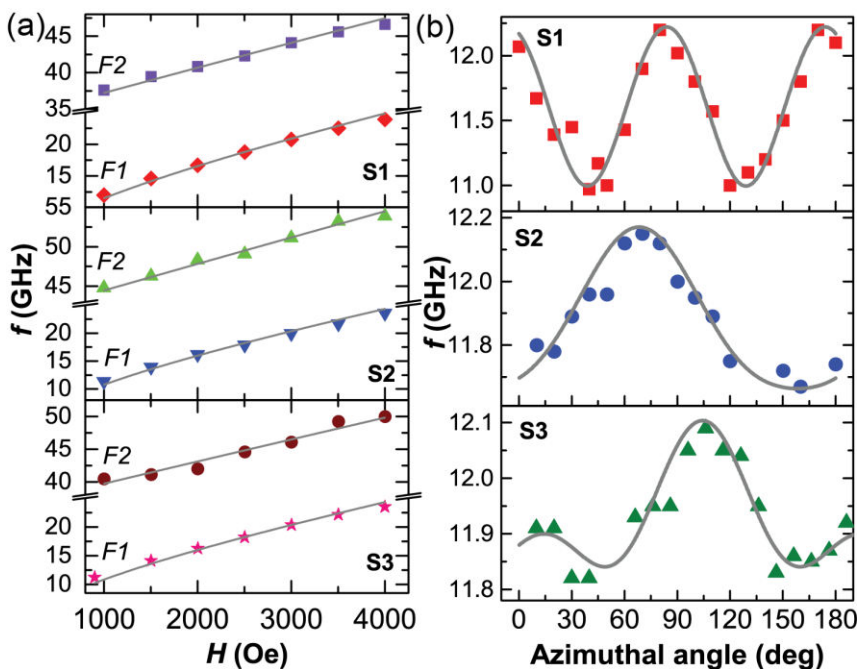


Figure 11.4: (a) Evolution of the frequencies (symbols) of the Kittel mode (F1) and PSSW mode (F2) with respect to the bias magnetic field. (b) Dependence of F1 on the azimuthal angle of the applied bias magnetic field. The solid lines correspond to fits to Eqn. 11.2 and 11.3 for F1 and F2, respectively.

The spin wave spectra were also recorded as a function of in-plane wave vector  $q$  at a magnetic field of 2 kOe (Fig. 11.5). In this case, the frequency of the lower frequency mode F1 exhibits pronounced dispersion (DE mode in this case) and is given by:

$$f = \frac{\gamma}{2\pi} \left( \left[ H + \frac{2K_2}{M_s} \cos 2\varphi - \frac{4K_4}{M_s} \cos 4\varphi + 2\pi M_s q d \sin^2 \psi \frac{2A}{M_s} q^2 \right] \left[ H + 4\pi M_s + \frac{2K_2}{M_s} \cos^2 \varphi - \frac{K_4}{M_s} (3 + \cos 4\varphi) - 2\pi M_s q d + \frac{2A}{M_s} q^2 \right] \right)^{\frac{1}{2}} \dots\dots(11.5)$$

Where  $\psi$  is the angle between  $q$  and  $H$ . The higher frequency mode F2 follows Eqn. 11.3 and is dispersionless, as expected. By simultaneously fitting all data to the respective equations presented above, the Landé  $g$ -factor ( $g$ ), the saturation magnetization ( $M_s$ ) the exchange stiffness constant ( $A$ ) and the anisotropy fields are extracted and are presented in Table 11.1. Note that each of the fitted parameters is determined rather independently from a particular experimental dependence or feature, making the fit reliable and providing results with a relatively small error ( $\sim \pm 5\%$ ). While the fitted value of  $g$  and exchange constant  $A$  are the same for all samples, the angular behavior of the mode frequencies is governed by a fourfold anisotropy for S1 and a uniaxial anisotropy superposed on a fourfold anisotropy for S2 and S3, in agreement with the VSM results. The presence of the fourfold anisotropy for all samples indicates that this is directly correlated with the crystal structure. As a result, the anisotropy increases for improved crystal structure and vice versa. On the other hand, the uniaxial anisotropies in S2 and S3 are presumably stemmed from film structure in the vicinity of the interfaces, as reported previously for CFAS and Co2FeAl [4, 9] thin films. There are many possible origins of such magnetic anisotropy, including the formation of an interface alloy, formation of anisotropic interfacial bonds and anisotropic strain relaxation.

We now turn to the dependence of the Gilbert damping constant ( $\alpha$ ) for different samples. In any process involving magnetization dynamics, the Gilbert damping constant is one key indicator to optimize writing speeds and reduce power consumption. The analysis of the

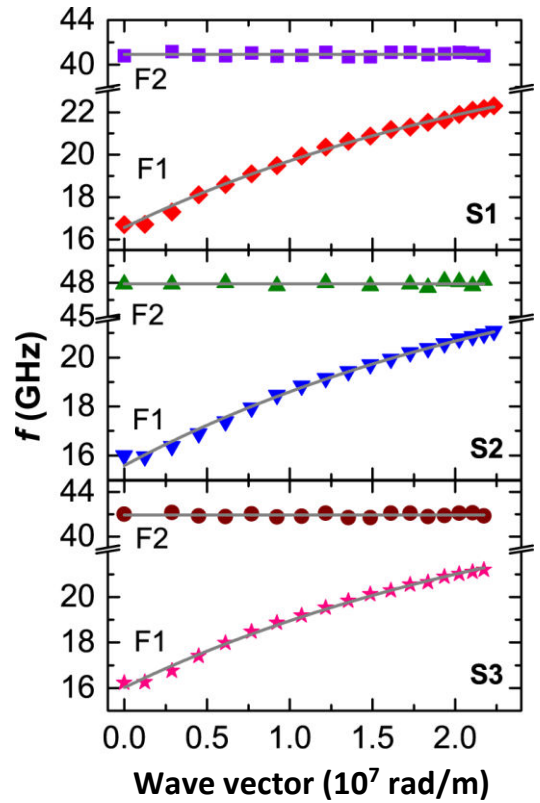


Figure 11.5: Measured spin wave frequencies (symbols) as a function of in-plane wave vector at a magnetic field of 2 kOe. The solid lines are calculated frequencies.

variation of the half width at half maximum (HWHM ( $\Delta H$ )) versus the frequency ( $f$ ) of the  $q=0$  mode allows for quantifying  $\alpha$  for different samples, using the following Eqn. 11.6 [25]:

$$\Delta H(f) = \frac{2\pi\alpha f}{\sqrt{3}\gamma} + \Delta H_0 \quad \dots\dots(11.6)$$

This linewidth is caused by two mechanisms: the intrinsic damping of the magnetization and extrinsic contributions (such as inhomogeneities, surface defects, two magnon scattering, mosaicity, etc.) given by the first and second terms, respectively, in the above equation. In Fig. 11.6, the measured linewidth (HWHM) of the  $q = 0$  mode is plotted as a function of the mode frequency for all three CFAS films.

To obtain this, the frequency swept magnon linewidths ( $\Delta f$ ) were extracted by fitting the BLS peaks with the Lorentzian function. Subsequently, this is converted to field swept linewidth following the method described in Ref. [29]. It is worth mentioning here that the linewidth data

are not deconvoluted to remove the contribution for instrumental broadening, because the instrumental broadening will be uniformly present in all the BLS signals and thus it will not change our interpretation.

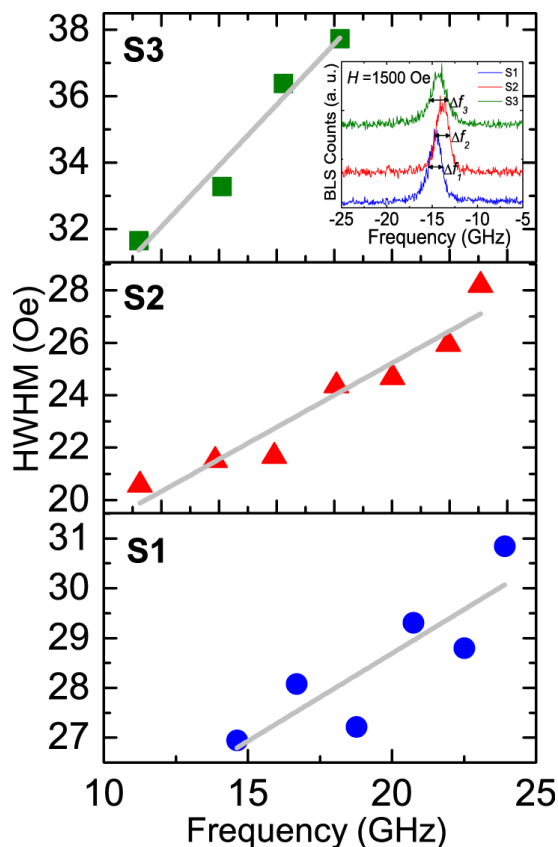


Figure 11.6: Linewidth of the  $q = 0$  mode as a function of the mode frequency for different samples. Inset shows typical anti-Stokes peaks for all three samples, taken for  $q = 0$  at  $H = 1500$  Oe.

The  $\alpha$  values, as extracted from the slopes of the linear fitting of each data set in Fig. 11.6 are 0.002, 0.003 and 0.006 for S1, S2 and S3, respectively, showing a pronounced tunability. The  $\alpha$  value obtained for S1 is comparable to that found in earlier works on Co based HA samples, with optimized annealing temperature, HA layer thickness and chemical composition [4, 5, 9]. However, our study is unique in a sense that we have achieved a broad tunability in  $\alpha$  without tampering any parameter of the CFAS layer. This tunability is attributed to the variation in the structural order (which is dependent on the adjacent layers) and shows great spintronics application potential. Furthermore, a qualitative comparison of the typical anti-Stokes peaks for all three samples, taken for  $q = 0$  at  $H = 1500$  Oe, is presented in the inset of Fig. 11.6. This reveals an increase in the peak linewidth from S1 to S3, reminiscent of the presence of interface defects in

S2 and S3, as mentioned before. The above results suggest that different capping-layers and under-layers result in significantly different effects on the surface morphology, crystal structure, magnetic anisotropy and Gilbert damping parameter. The different morphology can be attributed to different surface energy and melting point of the under-layers. Surface energy and melting point are important factors that influence various surface phenomena including faceting, roughening, crystal growth, and surface segregation during annealing. Such as in the case of S1, the surface forms granular islands, while S2 and S3 maintain continuous, smooth surfaces. This is due to the low melting point (961° C) of Ag which leads to a lower ordering temperature. On the other hand, the high melting point of Pt (1768° C) and Cr (1907° C) and high surface energy allow S2 and S3 to stay continuous. Besides that, the thermal expansion stress arising from the different coefficients of thermal expansion of different layers can also play a role for the chemical ordering of CFAS films, which, together with the previous reason, eventually determines the magnetic properties. Overall, suitable under-layer and capping-layer are essential to use CFAS films in various magnetic devices because they can affect the morphology, microstructure, and magnetic properties of the films greatly.

## 11.4. Conclusions

In this work, we show that the chemical ordering, static magnetic properties and magnetization dynamics of the sputtered CFAS thin films can be effectively controlled by changing the capping layer and under-layer. The AFM, TEM and XRD results present a lowering in surface roughness, as well as in the degree of chemical ordering (from B2 to A2), as the sample is changed from S1 to S3 by varying the capping-layer and under-layer. The magnetometry measurements obtained for different field orientations reveal the presence of fourfold anisotropy for S1, but a uniaxial anisotropy for S2 and S3. BLS spectroscopy has been used to investigate the thermal spin waves in these films. The spin wave modes were identified as DE mode and PSSW modes from the analysis of angular, field and wave vector dependent measurements, and the relevant magnetic parameters were extracted. The origin of the fourfold anisotropy is ascribed to the structural ordering and the uniaxial anisotropy is attributed to the interfacial defects. The Gilbert damping coefficient is also obtained from the  $q = 0$  mode in the BLS spectra and is found to increase with the decrease in chemical ordering. The lowest damping coefficient obtained for S1 was 0.002. The observed structural and magnetic properties can be well explained in terms of the melting point of

the under-layers and thermal expansion stress at the interfaces. Finally, our findings will be useful for selecting proper adjacent layers of CFAS thin films for various spintronic and magnonic applications.

## References

- [1] A. Khitun, M. Bao and K. L. Wang, “Magnonic logic circuits,” *J. Phys. D: Appl. Phys.* **43**, 264005 (2010).
- [2] P. S. A. Kumar and J. C. Lodder, “The spin-valve transistor,” *J. Phys. D: Appl. Phys.* **33**, 2911 (2000).
- [3] S. Tehrani, E. Chen, M. Durlam, *et al.*, “High density submicron magnetoresistive random access memory (invited),” *J. Appl. Phys.* **85**, 5822 (1999).
- [4] M. Belmeguenai, H. Tuzcuoglu, M. S. Gabor, *et al.*, “Co<sub>2</sub>FeAl Heusler thin films grown on Si and MgO substrates: Annealing temperature effect,” *J. Appl. Phys.* **115**, 043918 (2014).
- [5] L. M. Loong, P. Deorani, X. Qiu, *et al.*, “Investigating and engineering spin-orbit torques in heavy metal/ Co<sub>2</sub>FeAl<sub>0.5</sub>Si<sub>0.5</sub>/ MgO thin film structures,” *Appl. Phys. Lett.* **107**, 022405 (2015).
- [6] R. Shan, H. Sukegawa, W. H. Wang, *et al.*, “Demonstration of Half-Metallicity in Fermi-Level-Tuned Heusler Alloy Co<sub>2</sub>FeAl<sub>0.5</sub>Si<sub>0.5</sub> at Room Temperature,” *Phys. Rev. Lett.* **102**, 246601 (2009).
- [7] H. Sukegawa, W. Wang, R. Shan, *et al.*, “Spin-polarized tunneling spectroscopy of fully epitaxial magnetic tunnel junctions using Co<sub>2</sub>FeAl<sub>0.5</sub>Si<sub>0.5</sub> Heusler alloy electrodes,” *Phys. Rev. B* **79**, 184418 (2009).
- [8] S. Mizukami, D. Watanabe, M. Oogane, *et al.*, “Low damping constant for Co<sub>2</sub>FeAl Heusler alloy films and its correlation with density of states,” *J. Appl. Phys.* **105**, 07D306 (2009).
- [9] M. Belmeguenai, H. Tuzcuoglu, M. S. Gabor, *et al.*, “Co<sub>2</sub>FeAl thin films grown on MgO substrates: Correlation between static, dynamic, and structural properties,” *Phys. Rev. B* **87**, 184431 (2013).

- [10] J. Dubowika, I. Goscianska, K. Z. H. Glowinski, *et al.*, “Epitaxial Growths and Magnetization Dynamics of Ni<sub>2</sub>MnSn Heusler Alloy Films,” *Acta Phys. Pol. A* **121**, 1121 (2012).
- [11] O. Gaier, J. Hamrle, S. Trudel, *et al.*, “Exchange stiffness in the Co<sub>2</sub>FeSi Heusler compound,” *J. Phys. D: Appl. Phys.* **42**, 232001 (2009).
- [12] D. Steil, O. Schmitt, R. Fetzner, *et al.*, “Ultrafast magnetization dynamics in Co-based Heusler compounds with tuned chemical ordering,” *New J. Phys.* **16**, 063068 (2014).
- [13] H. B. Huang, X. Q. Ma, C. P. Zhao, *et al.*, “Micromagnetic study of high-power spin-torque oscillator with perpendicular magnetization in half-metallic Heusler alloy spin valve nanopillar under external magnetic fields,” *J. Magn. Magn. Mater.* **373**, 10 (2015).
- [14] H. B. Huang, X. Q. Ma, Z. H. Liu, *et al.*, “Modelling high-power spin-torque oscillator with perpendicular magnetization in half-metallic Heusler alloy spin valve nanopillar,” *J. Alloys Compd.* **597**, 230 (2014).
- [15] Y. Liu, L. R. Sheldford, V. V. Kruglyak, *et al.*, “Optically induced magnetization dynamics and variation of damping parameter in epitaxial Co<sub>2</sub>MnSi Heusler alloy films,” *Phys. Rev. B* **81**, 094402 (2010).
- [16] M. S. Gabor, T. Petrison Jr, C. Tiusan, *et al.*, “Magnetic and structural anisotropies of Co<sub>2</sub>FeAl Heusler alloy epitaxial thin films,” *Phys. Rev. B* **84**, 134413 (2011).
- [17] E. Sasioğlu, L. M. Sandratskii, P. Bruno *et al.*, “Exchange interactions and temperature dependence of magnetization in half-metallic Heusler alloys,” *Phys. Rev. B* **72**, 184415 (2015).
- [18] J.-P. Wustenberg, D. Steil, S. Alebrand, *et al.*, “Ultrafast magnetization dynamics in the half-metallic Heusler alloy Co<sub>2</sub>Cr<sub>0.6</sub>Fe<sub>0.4</sub>Al,” *Phys. Status Solidi B* **248**, 2330 (2011).
- [19] O. Gaier, J. Hamrle, S. Trudel, *et al.*, “Brillouin light scattering study of Co<sub>2</sub>Cr<sub>0.6</sub>Fe<sub>0.4</sub>Al and Co<sub>2</sub>FeAl Heusler compounds,” *J. Phys. D: Appl. Phys.* **42**, 084004 (2009).
- [20] T. Seki, H. Yako, T. Yamamoto, *et al.*, “Spin torque-induced magnetization dynamics in giant magnetoresistance devices with Heusler alloy layers,” *J. Phys. D: Appl. Phys.* **48**, 164010 (2015).
- [21] T. Sebastian, Y. Kawada, B. Obry, *et al.*, “All-optical characterization of the spintronic Heusler compound Co<sub>2</sub>Mn<sub>0.6</sub>Fe<sub>0.4</sub>Si,” *J. Phys. D: Appl. Phys.* **48**, 164015 (2015).

- [22] T. Furubayashi, K. Kodama, H. Sukegawa, *et al.*, "Current-perpendicular-to-plane giant magnetoresistance in spin-valve structures using epitaxial  $\text{Co}_2\text{FeAl}_{0.5}\text{Si}_{0.5}/\text{Ag}/\text{Co}_2\text{FeAl}_{0.5}\text{Si}_{0.5}$  trilayers," *Appl. Phys. Lett.* **93**, 122507 (2008).
- [23] W. Wang, H. Sukegawa, R. Shan, *et al.*, "Preparation and characterization of highly L21-ordered full-Heusler alloy  $\text{Co}_2\text{FeAl}_{0.5}\text{Si}_{0.5}$  thin films for spintronics device applications," *Appl. Phys. Lett.* **92**, 221912 (2008).
- [24] T. M. Nakatani, T. Furubayashi, S. Kasai, *et al.*, "Bulk and interfacial scatterings in current-perpendicular-to-plane giant magnetoresistance with  $\text{Co}_2\text{Fe}(\text{Al}_{0.5}\text{Si}_{0.5})$  Heusler alloy layers and Ag spacer," *Appl. Phys. Lett.* **96**, 212501 (2010).
- [25] L. Jin, H. Zhang, X. Tang, *et al.*, "Tuning the Magnetization Dynamics in Sputtered  $\text{Co}_2\text{FeAl}_{0.5}\text{Si}_{0.5}$  Heusler Alloy Thin Film by Gas Pressure," *IEEE Trans. Magn.* **50**, 1 (2014).
- [26] R. Mock, B. Hillebrands, and J. R. Sandercock, "Construction and performance of a Brillouin scattering set-up using a triple-pass tandem Fabry-Perot interferometer," *J. Phys. E.* **20**, 656 (1987).
- [27] E. Yang, D. E. Laughlin and J.-G. Zhu, "Buffer Layers for Highly Ordered L10 FePt-Oxide Thin Film Granular Media at Reduced Processing Temperature," *IEEE Trans. Magn.* **46**, 2446 (2010).
- [28] H. Sukegawa, S. Kasai, T. Furubayashi, *et al.*, "Spin-transfer switching in an epitaxial spin-valve nanopillar with a full-Heusler  $\text{Co}_2\text{FeAl}_{0.5}\text{Si}_{0.5}$  alloy," *Appl. Phys. Lett.* **96**, 042508 (2010).
- [29] S. S. Kalarickal, P. Krivosik, M. Wu, *et al.*, "Ferromagnetic resonance linewidth in metallic thin films: Comparison of measurement methods," *J. Appl. Phys.* **99**, 093909 (2006).

## Chapter 12

# 12. Summary and outlook

---

### 12.1. Summary

In this PhD research study, we have investigated the quasistatic and dynamic magnetization properties in structured ferromagnetic materials at submicron scale. The motivation for such research is to promote the potential of spin wave devices for future data storage and information processing technology. Here, we have primarily dealt with the fundamental spin wave properties in layered and patterned structures, which are relevant in terms of spin wave waveguides and magnetic data recording. The samples are prepared by different techniques such as ultra high vacuum magnetron sputtering, electron beam lithography and electron beam evaporation. The preliminary characterizations of the samples were performed by the X-ray diffraction (XRD), scanning electron microscopy (SEM), transmission electron microscopy (TEM), atomic force microscopy (AFM) and energy dispersive X-ray spectroscopy (EDX). The static magnetic properties were studied using magnetic force microscopy (MFM), magneto-optical Kerr effect magnetometry (MOKE) and vibrating sample magnetometry (VSM). The time-resolved (from femtosecond to nanosecond time scale) and wave vector resolved magnetization dynamics were investigated by home-built time-resolved magneto-optical Kerr effect (TR-MOKE) microscope and Brillouin Light Scattering (BLS) technique, respectively. The experimental results are modeled and analyzed by solving the Landau-Lifshitz-Gilbert (LLG) equation for the respective system using macrospin formalism, micromagnetic simulations and plane wave method.

We have investigated the spin wave dynamics in Permalloy ( $\text{Ni}_{80}\text{Fe}_{20}$ , Py)/Cobalt(Co) exchange spring bilayer thin films using BLS experiment. The strong exchange coupling at the interface of soft NiFe layer and hard Co layer makes it a composite system having magnetic properties different from elemental layers. The interfacial coupling is manifested as a monotonic decrease in coercivity in the magnetic hysteresis loops with increasing Py thickness. The BLS measurements performed for different values of the applied external field helps to identify the observed spin wave (SW) modes as surface and volume modes. The analysis of the BLS line

widths of the observed resonant modes based on a two magnon scattering model enables to quantify the local interfacial exchange coupling strength, which was much larger in comparison with measured macroscopic value.

Next, we have studied  $[\text{Co/Py}]_r$  multilayered systems with fixed elemental layer thickness, but with varying repetition number  $r$ . The increase in the number of interfaces enhances the effective magnetization of the system, which is reflected in the magnetization reversal curves as well as in the trend of resonant SW modes. Interestingly, the BLS results featured rich spectra of spin wave modes, consisting of magnetostatic surface wave mode as well as standing waves formed across the sub-layers. The number and frequencies of the standing wave modes were strongly dependent on  $r$  and the number of sub-layers they belong to. Moreover, the relative BLS intensities of the standing waves were determined to be inversely proportional to the square of corresponding thickness, which agree with the experimental findings.

The top soft layer in an exchange spring system finds another degree of freedom when it is coupled with a magnetic hard layer having high anisotropy perpendicular to its plane. The magnetization of the soft layer is now tilted which can be controlled by varying its thickness. In case of  $[\text{Co/Pd}]/\text{Py}$  multilayers, the chiral spin texture across the Py layer gives rise to a network of magnetic domains having gradually changing spin orientation. This effectively modifies the dynamic magnetic properties including the spin flip scattering based demagnetization phenomena, resonant SW modes and magnetic damping. Basically, for lower Py thickness, the hard Co/Pd layer dominates over the magnetic properties of the Py layer, which is not so strong in higher thickness range. In the intermediate thickness, there is a competition between the out-of-plane and in-plane anisotropies of the hard and soft layers, respectively. Consequently, two clear regimes in terms of magnetic damping are observed: an extrinsic effect dominated damping for Py thickness greater than 7.5 nm and vice versa.

The interfacial anisotropy at the Co/Pd interfaces, together with the d-d hybridization, is responsible for the high perpendicular magnetic anisotropy in Co/Pd multilayer. This supports the occurrence of exotic stripe domain system at remanence above a critical thickness, due to its competition with the demagnetizing field caused by the magnetic charges at the film surfaces. As opposed to the saturated state, the periodic domains lead to the formation of anisotropic periodic scattering potential for the SWs. The resultant anisotropic dispersion characteristics are studied for

two different orientations of the SW wave vector. We found that the resonant modes primarily reside at the domain walls, where the resultant in-plane magnetization is favored. Furthermore, the resonant mode profiles resemble that of a magnonic crystal, although without any physical patterning.

The conventional magnonic crystal was investigated for arrays of square magnetic nanorings by varying the ring width. The localization and the quantization of the resonant SW modes have a pronounced dependence on the distribution of the static and dynamic demagnetizing fields, which is controlled by the geometry as well as the dimensions of the elements. In particular, it is the combination of the demagnetizing effect with the shape anisotropy at the ring arms, which yields the magnetic configuration from a flower state for the widest ring to an onion state for the narrowest ring. As a result, the nature of the SW modes showed a transition in the quantization characteristics: while the ring with the largest width exhibited quantization along the direction of the external magnetic field, the ring with smallest width showed azimuthal quantization.

Unlike the square ring array, the array of sawtooth waveguide lacks the configurational symmetry, which is the root of tunable magnonic band structure in this system. We have performed a combined experimental and theoretical study of the reconfigurable magnonic band structure for two different angles between the fixed spin wave direction and the applied magnetic field and found that the spin wave propagation can be blocked for selected frequency values just by turning the magnetic field. The spin wave mode profiles show that the corrugation prohibits the edge potential wells from coming in the propagation channel, and can be engineered by controlling the extent of corrugation. Overall, the idea of tuning the SW propagation by merely rotating the magnetic field is important from a fundamental scientific viewpoint as well as in terms of magnonics where the tunability of spin waves is considered for magnetic nanodevices operating in the GHz frequency regime.

In case of Heusler compounds, the magnetic response is an overall impact of the interaction of the atomic magnetic moments with the chemical bonding amongst the elements. For thin films, the atomic bonding, and consequently the magnetic behavior can be tailored by controlling the interfacial stress with its adjacent layers at the time of annealing. This effectively manipulates different surface phenomena including faceting and crystal growth, which is dependent on the adjacent layer material. We found, for CFAS Heusler alloy, a change in the internal magnetic

configuration by changing the combination of top and bottom layers, which primarily affect the magnetic anisotropy, damping parameter and the frequency of the volume mode. To obtain tunable magnetic properties without tampering any parameter of the magnetic layer will be interesting for different spintronic applications.

## 12.2. Future Perspectives

In the previous chapters, we have discussed the tunability of SW properties as an effect of interfacial interactions or due to the change in the demagnetizing field profile. Next, we plan for experimental visualization of the propagating SWs under various magnetic potentials. For that purpose, we have developed a space resolved micro-BLS set up in our laboratory (the description of the set up is given in chapter 3). The micro-BLS increases the optical resolution of the BLS experiment, thereby enables a two dimensional imaging of SW amplitude across the magnonic device.

When a SW is excited in a nano-scale magnetic element, it generates dynamic dipolar field (dynamic stray field) outside the element. If we consider two magnonic waveguides (WGs) placed beside each other, the SW launched in one WG will induce some excitation in the other. The amplitude and phase of the induced excitation will depend upon the distance between the WGs. We expect that the amplitude and phase of the induced mode is controllable via the presence of a third waveguide. Effectively, here two WGs will act as input channels whereas the output (which is the superposition of the two induced excitations) will be extracted from the third one. This may lead to one kind of magnonic logic where the logic operation can be controlled by changing the distance between the WGs.

One of the salient features of SW as compared to optical waves is its anisotropic propagation. When a SW of a particular frequency is launched in a magnetic medium, it follows the phase fronts of that frequency, which is, in turn, a reflection of the iso-frequency contour in reciprocal space. The propagation of SW is basically determined by the group velocity, which is perpendicular to the iso-frequency contour at a certain wave vector. Even for a planar magnetic film, these contours are not isotropic. Therefore, the SWs do not follow a circular phase front. The

study of this anisotropic propagation will be further interesting in case of magnonic crystal. Here, depending on the distribution of the scattering centres, different magnonic bands will have different propagation characteristics. These characteristics will be modified for different frequencies, amplitude as well as direction of magnetic field. Hence the frequency dependent SW propagation in case of different 2D MCs calls for a thorough research which may lead to a novel way of frequency dependent SW channeling.

In case of Co/Pd multilayered system featuring stripe domains at remanence, we have observed that the magnonic excitations are primarily concentrated at the domain walls. By giving a line excitation to the system, it is compulsive to follow the propagating SWs with wave vectors parallel or perpendicular to the domain walls. Because the consecutive domain walls have opposite chirality, we expect that the SWs propagating parallel to the domain wall will have non-reciprocal characteristics, which will be reverted for alternate domain walls, i.e., SWs in alternate domain walls will propagate in opposite directions. There are several advantages of implementing stripe domain waveguides in magnonic technology. Firstly, the absence of external magnetic field means low power consumption for signal processing. Secondly, since the lattice constant of the periodic domains is very small ( $\sim 100$  nm), a number of propagation channels (i.e. domain walls) can be accommodated in a single waveguide. Furthermore, the difference in dispersion characteristics for wave vector parallel and perpendicular to the domain wall may lead to exotic SW channeling behavior in 2D film. This can be measured by launching SWs from a narrow excitation window (point excitation).